Lipid Peroxidation Mechanisms and Their Contribution to Ferroptosis

Quynh Do

A dissertation

submitted in partial fulfillment of the

requirements for the degree of

Doctor of Philosophy

University of Washington

2022

Reading Committee

Libin Xu, Chair

Rheem Totah

Miklos Guttman

Program Authorized to Offer Degree

Medicinal Chemistry

University of Washington

Abstract

Lipid Peroxidation Mechanisms and Their Contribution to Ferroptosis

Quynh Do

Chair of the Supervisory Committee:

Libin Xu

Medicinal Chemistry

The attack of reactive oxygen species (ROS) on reactive lipids leads to free radical chain reactions with molecular oxygen, a process termed lipid peroxidation. Increased lipid peroxidation is associated with many human diseases, including cancer, diabetes, neurodegenerative diseases, and, more recently, cell death. The rate-determining step in lipid peroxidation reactions is usually the propagation step in which the peroxyl radical can undergo either hydrogen(H)-atom transfer or peroxyl-radical addition reaction. The rate constants of the H-atom transfer process for several reactive lipids and sterols have been measured using the peroxyl radical clock method. However, no method was available to study the peroxyl-radical addition reaction. In this dissertation, I aim to elucidate lipid peroxidation mechanisms and their relevance in ferroptosis, a form of regulated cell death driven by lipid peroxidation of polyunsaturated fatty acids (PUFAs). In this work, I modified the original linoleate-based peroxyl radical clock to enable the measurement of both the H-atom transfer and peroxyl-radical addition reactions in the propagation step. The new probe was

then applied to study lipid peroxidation mechanism and kinetics for a variety of biologically important lipids, including conjugated fatty acids, sterols, coenzyme Q10, and lipophilic vitamins, such as vitamin D_3 and A, for the first time. Next, I elucidated the effects of various unsaturated lipids in sensitizing ferroptosis. I then sought to elucidate the mechanism underlying the potency of the different ferroptosis-inducing conjugated and nonconjugated PUFAs. Next, I investigated the relevance of ER stress and unfolded protein response in ferroptosis execution. Finally, I summarize all the findings of this collective work and propose how research in this area can continue to expand.

Acknowledgements

Despite the challenges I encountered during grad school, when I look back at my journey, I am grateful to have this experience because I have learned and grown so much during this time. Therefore, I would like to thank all of those who have helped me growth into the person and the scientist that I am today.

First, I would like to thank my advisor, Dr. Libin Xu, for choosing me for the peroxyl radical clock project, for letting me grow the project further into exploring ferroptosis, and for his tremendous support along the way. As a mentor, Libin are always available to answer my questions. I am grateful that he is always open to listen to my ideas and let me carry out experiments that I am interested in. I am especially grateful for his support during the time when I was struggling with my mental health. Without his kindness and support, I would not have been able to finish my grad school journey.

I would also like to thank my thesis committee members: Dr. Rheem Totah, Dr. Mike Guttman, and Dr. Terry Kavanagh. Their insightful feedbacks and suggestions have helped me tremendously in the developing my project.

I would also like to acknowledge my industry mentor, Dr. Josh Pearson, for his support and guidance. Thank to Josh, I have learned what it means to be a good and humble scientist. Thank to him, I realized my dream and goal of becoming a mentor myself and being able to support younger of scientists in the future.

I would also like to thank the members of the Xu Lab - Dr. Ryan Seguin, Dr. Rutan Zhang, Amy Li, Tianwei Shen, Vanessa Lopez, Emily Pruitt, Marie Brzoska, Noelle Reimers, Lixin Zhu, Ryan Nguyen, Gavin Hooper, and Angela Guo – for your support and for contributing into my projects in various way.

I also want to thank my parents for their support and sacrifice so I can be where I am today in life. They had a good life in Vietnam with good jobs and a good home, but they were willing to give up their comfortable life to move to the US so I could have a better education.

Lastly, I would like to thank my significant other Stuart and my boys, Genji and Huey, for being my biggest support in grad school and in life. I know it has not been easy having a partner that is constantly stressed out, but you have always had my back through thick and thin. Thank you for taking care of me and for making the best cups of Americano which helped me tremendously in finishing my writings.

TABLE OF CONTENTS

LIST OF FIGURES

LIST OF TABLES

Chapter 1. Introduction

1.1 The Study of Free Radical Lipid Peroxidation Mechanism, Kinetics, and Product Distribution Using Radical Clocks

1.1.1 The Free Radical Chain Oxidation Mechanism

Despite the crucial role of molecular oxygen in cell metabolism and energy production, the imbalance between pro-oxidative and anti-oxidative cellular processes can lead to increased levels of reactive oxygen species, a state generally called 'oxidative stress'. Oxidative stress can result in lipid, protein, and DNA damage and alter cell proliferation, differentiation, or metabolism (*1*). Lipids are among the primary targets of attack by reactive oxygen species (ROS), leading to subsequent free radical chain reactions with molecular oxygen, termed lipid peroxidation. Since lipids are essential components of the cell membrane, lipid peroxidation is associated with multiple human conditions and diseases (*2-4*), including atherosclerosis (*5*), diabetes (*6*), cancer (*7, 8*), neurodegenerative disorders (*9-11*), and certain cholesterol biosynthesis disorders (*12*). More recently, lipid peroxidation was discovered to be associated with ferroptosis, a regulated form of cell death that is morphologically, biochemically, and genetically distinct from other types of cell death, such as apoptosis, necrosis, cuprotosis, and autophagy (*13-15*). More importantly, non-enzymatic free radical-mediated lipid peroxidation, or autoxidation, was found to be the key effector in the induction of ferroptosis (*16-18*).

Lipid autoxidation mechanism, kinetics, and product distribution have been studied intensively for decades (*2, 4, 19, 20*). The autoxidation process occurs via a three-step mechanism: initiation, propagation, and termination (**Figure 1.1**) (*2, 4*). The rate-limiting step in this mechanism is the propagation step in which the lipid peroxyl radical can undergo two types of reactions, including hydrogen (H)-atom transfer (HAT) and peroxyl-radical addition (PRA). In the

HAT reaction, the peroxyl radical abstracts an H-atom from another lipid or oxidizable substrate, generating a lipid hydroperoxide, while in the PRA reaction, the peroxyl radical adds to a "C=C" double bond. This PRA product can either undergo intramolecular homolytic substitution (S_Hi) to form an epoxide or react with another molecular oxygen to form a new peroxyl radical. Both the HAT and PRA reactions generate new radicals that can continue the free radical chain oxidation by reacting with another lipid molecule or oxidizable substrate.

1.1.2 The Conventional Radical Clock Method to Study Lipid Peroxidation Mechanism and Kinetics

The direct measurement of HAT rate constants, k_H, for a variety of organic substrates requires the knowledge of the rates of polymerization (R_p), initiation (R_i), and termination (R_t); however, R_t can only be determined using the rotating-sector method, which is not widely available (*21-23*). On the other hand, radical clock, which utilizes a known rate constant of a unimolecular reaction to measure an unknown rate constant of a competing bimolecular reaction, is a more convenient method to indirectly measure k_H (*24-27*). Specifically, a linoleate-based peroxyl radical clock, which utilizes the competition between the β-fragmentation reactions with known rate constants and the bimolecular HAT reaction, was developed to measure k_H for a variety of lipids, including polyunsaturated fatty acids (PUFAs) and sterols (**Figure 1.2**) (*24-27*). Particularly, the reaction between linoleate and molecular oxygen can generate peroxyl radicals at either the 9- or 13- position of the carbon chain. These 9- or 13-peroxyl radicals can then undergo HAT to yield either 9-*trans,cis*(*tc*)- or 13-*tc*-hydroperoxide products, which are termed HPODEs, or they can also undergo the competing β-fragmentation reaction, leading to 13-*trans,trans*(*tt*)- and 9-*tt*-HPODEs. Therefore, linoleate peroxyl radicals, with known rate constants for β-fragmentation, can be used to "clock" the unknown rate constants of HAT reactions via the following equation:

$$\frac{[tc\text{−HPODEs}]}{[tt\text{−HPODEs}]} = \frac{[9\text{−}tc\text{−HPODEs} + 13\text{−}tc\text{−HPODEs}]}{[9\text{−}tt\text{−HPODEs} + 13\text{−}tt\text{−HPODEs}]} = \frac{k_{\mathrm{H}}[\mathrm{Substrate}]}{214} + 0.16$$

Here, 214 and 0.16 are β-fragmentation and linoleate concentration-dependent constants (*24*). Based on the measurements using the peroxyl radical clock methods, cholesterol was found to be a moderately oxidizable lipid with a k_{H} of 11 M^{-1} s^{-1} at 37 °C, but 7-dehydrocholesterol (7-DHC), a biosynthetic precursor of cholesterol and vitamin D_3 (*28, 29*), was found to be the most reactive lipid molecule so far, with a k_{H} of 2260 M^{-1} s^{-1} (*25*).

While the HAT reaction mechanism and rate constants have been studied extensively via the radical clock method, there are no methods established to measure the rate constants for the PRA reaction, k_{add}. Therefore, the development and optimization of a peroxyl radical clock that can simultaneously measure both k_{H} and k_{add} are needed.

1.2 Ferroptosis

1.2.1 Early Observations and the Discovery of Ferroptosis

Based on the recommendations of the Nomenclature Committee on Cell Death, there is a distinction between accidental and regulated cell death (*30*). Accidental cell death (necrosis) results from severe physical, chemical, and mechanism insults and is irreversible by molecular interventions. In contrast, regulated cell death is controlled by intrinsic cellular mechanisms and, thus, can be modulated pharmacologically and genetically. Programmed cell death is a subset of regulated cell death that occurs in normal physiological contexts. Apoptosis was the first regulated and programmed cell death to be characterized. Since then, other types of regulated cell death have been identified, including necroptosis (*31*), pyroptosis (*32*), and, more recently, ferroptosis (*13*) and cuprotosis (*15*).

Prior to the official "discovery" of ferroptosis, this type of cell death, along with its associated molecular mechanisms, was observed in various studies. For example, as early as the

1950s, in a series of studies conducted by Harry Eagle *et al.*, the depletion of only cysteine, out of 13 amino acids examined, was identified to result in the depletion of glutathione (GSH) and the inhibition of growth and proliferation of mammalian cells (*33-35*). In the following years, it was found that cysteine deprivation-induced cell death could be suppressed by iron chelators and lipophilic antioxidants, such as α-tocopherol and idebenone (*36-40*). Importantly, ROS and free radicals were recognized as the drivers of the cell death described in these studies. On the other hand, glutathione peroxidase 4 (GPX4), which was isolated for the first time from pig liver in 1982 (*41*), was identified as the only peroxidase isoform that can convert the toxic membrane phospholipid hydroperoxides into the corresponding non-toxic alcohol (*42, 43*). Thus, GPX4 plays an essential role in the cellular antioxidant network and protects cells from lipid peroxidation-induced damages (*44-47*). Importantly, in 2008, the Conrad group discovered that GPX4 inactivation led to increased lipid peroxidation, which was modulated in parts by the function of the enzyme 12/15-lipoxygenase, and, subsequently, an unrecognized mode of cell death (*48*). Another example related to this type of cell death is ceramide-induced cell death in human glioma cells, which was reported to be dependent on the generation of ROS and lipid peroxidation (*49*). However, despite the identification of ROS, free radicals, and lipid peroxidation as the central drivers of cell death, most of the lethal mechanisms observed in these various studies were not recognized as a distinct type of cell death from apoptosis until later.

In 2003, in a high-throughput screen by the Stockwell lab to identify small molecules that can selectively induce cell death in *HRAS* mutant engineered cell lines, eradicator of RAS-transformed cells, or erastin, was identified (*50*). Later, RAS-selective lethal 3, or RSL3, was identified in a larger screen (*51*). Notably, both erastin and RSL3 induce a form of non-apoptotic cell death that depends on the cellular levels of iron and the lethal accumulation of lipid peroxides

(*51, 52*). In 2012, Dixon *et al.* officially coined the term *ferroptosis* to describe the erastin- and RSL3-induced cell death (*13*). In this study, ferroptosis was found to be morphologically, genetically, and pharmacologically different from other forms of cell death. Specifically, while staurosporine-induced apoptosis exhibited chromatin condensation and margination, smaller and denser mitochondria and increased membrane density were observed in erastin-induced cell death. In addition, apoptosis-specific inhibitors failed to rescue erastin-induced cell death. Furthermore, staurosporine-induced apoptosis and erastin-induced cell death were found to be regulated by distinct genetic networks. Currently, ferroptosis is acknowledged as a distinct form of regulated cell death tightly associated with iron-dependent lipid peroxidation (*53*).

1.2.2 The Hallmarks of Ferroptosis

1.2.2.1 Ferroptosis is Iron Dependent

In the 2012 study, Dixon *et al*. observed that only the addition of exogenous iron sources, but not with other metal ions, could potentiate erastin-induced lethality and that the iron chelator deferoxamine could suppress cell death (*13*). Thus, these observations led them to name this form of cell death *fer*roptosis. In addition, supplementing the cells with iron-bound transferrin sensitizes cells to erastin-induced ferroptosis (*54*). In contrast, silencing the *TFCR* gene encoding for the transferrin receptor, which facilitates the uptake of transferrin-iron complexes into the cells, was shown to rescue cells from erastin lethality (*51, 54*).

The exact mechanism by which iron potentiates cells to ferroptosis is unknown. However, it has been suggested that iron plays multiple roles in ferroptosis. For example, free intracellular iron can participate in the initiation of non-enzymatic lipid peroxidation. Specifically, under normal physiological conditions, the cellular iron level is tightly regulated. Most iron is stored in the iron storage protein ferritin, bound in the FeS clusters, or ligated in heme. On the other hand,

there is a pool of cytosolic labile iron that is free to participate in redox reactions known as "Fenton chemistry" (*55*). In these redox reactions, labile ferrous iron can react with lipid hydroperoxide, forming ferric iron and a hydroxyl radical (**Figure 1.3**). Ferric iron can then react with another lipid hydroperoxide, regenerating ferrous iron and forming a peroxyl radical. Both the hydroxyl and peroxyl radicals formed in this reaction are highly reactive and, thus, can initiate and propagate the free radical chain oxidation of lipids. Therefore, an increase in intracellular iron level can lead to the accumulation of lipid peroxides and potentiate cells to ferroptosis. Indeed, the degradation of the iron storage protein ferritin and the iron exporter protein ferroportin via ferritinophagy, an autophagic process, leads to increased cytosolic labile iron level and ferroptosis sensitivity (*54, 56, 57*). In addition, the silencing of iron metabolism master regulator *IREB2* results in alterations in iron uptake and metabolism, the expression of storage-related genes, such as *TFRC, ISCU, FTH1*, and *FTL*, and a reduction in ferroptosis sensitivity (*13*).

In addition to catalyzing the non-enzymatic lipid peroxidation via Fenton chemistry, iron can also contribute to ferroptosis by acting as the cofactor of phospholipid peroxide-generating enzymes, including lipoxygenase (LOX) and P450s, and as the key component of metabolic enzymes that can lead to the generation of cellular ROS (*58*).

1.2.2.2 Loss of Lipid Peroxide Repair Promotes Ferroptosis

Due to the substantial generation of ROS and constantly being under high levels of oxidative stress (*59*), certain cancer cell lines rely heavily on the functions of the components in the cellular antioxidant network for their proliferation and survival. Thus, the inhibition of the antioxidant enzyme GPX4, the only GPX isoform that can detoxify membrane phospholipid hydroperoxides into lipid alcohols (*14, 60*), by the two small molecules erastin and RSL3 can lead to the accumulation of lipid peroxidation and, subsequently, ferroptosis. Specifically, erastin

inhibits system x_c^-, an antiporter that functions in the import of extracellular cystine into the cells, leading to a decrease in the level of cellular cysteine, which is the precursor of GSH biosynthesis (*14*). Since GSH is the cofactor essential for the functions of GPX4, the depletion of GSH resulting from the inhibition of system x_c^- leads to the inactivation of GPX4 and the induction of ferroptosis. In addition, in some cell lines, the transsulfuration pathway can be utilized for the biosynthesis of cysteine from methionine (*61*). Therefore, the upregulation of the transsulfuration pathway can lead to resistance to erastin-induced ferroptosis (*62*).

At the same time, RSL3 covalently binds to the active site and directly inhibits the function of GPX4 (*63*). More recently, the protein ferroptosis suppressor protein 1 (FSP1), which reduces coenzyme Q10 (CoQ10) into its antioxidative quinol form, was discovered as another important antioxidant enzyme that acts in parallel to GPX4 to inhibit ferroptosis (*64, 65*). In addition, iFSP1, a potent inhibitor of FSP1, was identified to selectively induce ferroptosis in GPX4-knockout cell lines that overexpress FSP1 (*65*). In short, lipid peroxidation is suppressed, and ferroptosis is inhibited when there is an overexpression of the antioxidant enzymes. In contrast, the loss of function of the antioxidant networks leads to the accumulation of lipid peroxidation and promotes ferroptosis.

1.2.2.3 Ferroptosis is Driven by the Autoxidation of Esterified PUFAs

PUFAs have been established as the key lipid species that drive ferroptosis. For example, when various cancer cells were treated with different exogenous lipid species, the nonconjugated PUFAs, including linoleic acid (LA) and arachidonic acid (AA), were shown to sensitize cells to ferroptosis (*63*). Due to their weak allylic C-H bonds, LA and AA are susceptible to lipid peroxidation and, thus, can promote ferroptosis. Indeed, when the bis-allylic H atom is replaced with deuterium, both erastin- and RSL3-induced cell death are inhibited (*63*). In contrast, cells that

are supplemented with the monounsaturated fatty acid oleic acid (OA), which has low reactivity to lipid peroxidation (*2*), are resistant to ferroptosis (*66*).

Importantly, the PUFAs must be activated and incorporated into the membrane phospholipids to exert their lethality. Specifically, the endogenous phosphatidylethanolamines (PEs) containing one arachidonoyl (20:4) or one adrenyl (22:4) PUFA tail were identified as primary lipid species that drive RSL3-induced ferroptosis (*67*). Other glycerol-derived lipids that have been found to contribute to ferroptosis include phospholipids with two PUFA tails (*68*), PUFA-containing ether lipids (*69*), and 2-arachidonoyl glycerol (*70*). In addition, the removal of the oxidized PUFA tails by phospholipase A_2 group VI (iPLA2β) suppresses p53-driven ferroptosis (*71*). These findings suggest that both free non-oxidized and oxidized PUFAs are not the drivers of ferroptosis. Instead, PUFAs must be membrane-bound and remain in the lipid membrane after undergoing peroxidation to drive ferroptosis. Thus, the enzymes involved in the activation and incorporation of PUFAs into membrane phospholipids, such as acyl-CoA synthetase long-chain family member 4 (ACSL4) and lysophosphatidylcholine acyltransferase 3 (LPCAT3), play essential roles in the induction of ferroptosis. Indeed, the deletion or inactivation of ACLS4 and LPCAT3 promotes a ferroptosis-resistant state (*67, 72-74*), and the overexpression of ACSL4 sensitizes cells to ferroptosis (*72*). However, it should be noted that ACSL4 was recently shown to be a context-specific ferroptosis regulator rather than a universal one (*66*). Specifically, ACSL4 was found to be more important to ferroptosis induced by direct GPX4 inhibition than cysteine deprivation. Besides ACSL4, ACSL1 and ACL3 were also found to regulate ferroptosis in some contexts (*75-77*).

For some time, the enzymatic lipid peroxidation of PUFAs catalyzed by LOXs was considered the driver of ferroptosis. Specifically, early studies found that cell death induced by the

depletion of GSH can be suppressed by the deletion of 12/15-LOX in mouse embryonic fibroblasts (*48*). In addition, small molecule inhibitors of LOX enzymes were shown to induce resistance to erastin-induced lethality (*63, 78, 79*). However, it has been implicated that LOX functions in ferroptosis are context-dependent and are more important to erastin-induced than RSL3-induced ferroptosis. Indeed, genetic silencing of LOX enzymes only leads to the inhibition of erastin-induced ferroptosis but does not affect RSL3 lethality (*63*). In addition, disruption of the *Alox15* gene encoding for 15-LOX enzyme failed to rescue *gpx4-/-* lethality in acute renal mice and cell models (*78*), $CD8^+$ T cells (*80*), and mice embryonic fibroblasts (*81*). Furthermore, it should be noted that the LOX inhibitors commonly used in studying ferroptosis, such as zileuton, nordihydroguaiaretic acid (NDGA), and PD146176, were shown to be good radical trapping antioxidants (RTAs) (*17*) and, thus, can inhibit the non-enzymatic lipid peroxidation and prevent ferroptosis. In addition, it was suggested that vitamin E and liproxstatin-1 (Lip-1), a ferroptosis-specific inhibitor (*78*), suppress ferroptosis by binding to and inhibiting the functions of 15-LOX (*67*). However, vitamin E is a lipophilic antioxidant, and Lip-1 was shown to protect cells from ferroptosis as a radical-trapping agent (*16*). Together, the data above provides evidence that non-enzymatic reactions are the key driver of the propagation of lipid peroxidation in the lipid membrane leading to ferroptosis. On the other hand, LOX can contribute to the ferroptosis sensitivity by converting esterified PUFAs into lipid hydroperoxides that participate in the ferroptosis initiation phase via the Fenton reactions with ferrous irons.

In summary, during the initiation phase of ferroptosis, PUFAs are activated and incorporated into membrane phospholipids (**Figure 1.4**). Then, during the execution phase, when the detoxification functions of the cellular antioxidant networks are impaired, the PUFA tails of

membrane phospholipid undergo lipid autoxidation, leading to the accumulation of lipid oxidation products. Once the pool of oxidation products reaches a certain threshold, ferroptosis is induced.

1.2.3 Canonical Mechanisms of Ferroptosis Induction

As the only peroxidase that can detoxify lipid hydroperoxides from the biological membranes, GPX4 plays a central role in the modulation of ferroptosis. Therefore, the canonical ferroptosis inducers are considered those that can either directly or indirectly affect the levels or functions of GPX4. The chemical structures of the canonical ferroptosis inducers mentioned in this section are shown in **Figure 1.5**.

1.2.3.1 Inhibition of System x_c^-

System x_c^- is a Na^+-independent antiporter that imports a cystine molecule, the major extracellular form of cysteine, into the cells in exchange for a glutamate molecule from inside the cells. System x_c^- is comprised of the 12-pass transmembrane transporter subunit SLC7A11 and the single-pass transmembrane regulatory subunit SLC3A2 (*82, 83*). The first discovered ferroptosis-inducing compound, erastin (*50*), induces ferroptosis by binding to and inhibiting the activity of system x_c^- (*13*). System x_c^- inhibition by erastin leads to the intracellular depletion of cysteine and, subsequently, both the reduced and oxidized forms of GSH (*84*). As the essential co-factor of GPX4, the deprivation of GSH leads to the impairment of GPX4, leading to the lethal accumulation of lipid peroxidation. Therefore, erastin can be considered an indirect inhibitor of GPX4. More potent analogs of erastin, including piperazine erastin and imidazole ketone erastin, which have improved water solubility and metabolic stability, have been developed (*14, 85*). In addition, the FDA-approved drugs, including sulfasalazine and sorafenib, were found to be inhibitors of system x_c^-, and thus, can act as ferroptosis inducers (*84, 86-88*).

1.2.3.2 Direct GPX4 Inhibition

(1*S*,3*R*)-RSL3, or RLS3, is the second discovered ferroptosis inducer (*51*). The chloroacetamide moiety of RSL3 covalently modifies the nucleophilic selenocysteine in the active site of GPX4 and directly inhibits its activity, leading to the accumulation of lipid peroxidation and toxic oxidation products and, eventually, cell death (*63*). Other chloroacetamide-containing direct inhibitors of GPX4, such as ML162, were identified in additional screening assays (*14, 89*). Nitroisoxazole-containing compounds, such as ML210, can also act as direct inhibitors of GPX4 (*89, 90*).

1.2.3.3 Other Indirect GPX4 Inhibition Mechanisms

In a systematic study conducted to identify metabolic regulators of ferroptosis, CIL56 and FIN56 were identified as small-molecule ferroptosis inducers (*91*). CIL56 and FIN56 treatments result in the simultaneous depletion of GPX4 protein through post-translational degradation and lipophilic antioxidants, such as coenzyme Q10, via the inhibition of squalene synthase in the mevalonate pathway. While FIN56 is a specific ferroptosis inducer, CIL56 induces ferroptosis at low concentrations and necrotic, non-suppressible lethality at higher concentrations. Statin drugs, such as cerivastatin, atorvastatin, and simvastatin, can also act as ferroptosis inducers by suppressing the biosynthesis of GPX4 and inhibiting the mevalonate pathway via the inhibition of HGM-CoA reductase, leading to the depletion of CoQ10 (*91-94*). Another recently discovered ferroptosis inducer is the endoperoxide $FINO_2$ which oxidizes iron to promote lipid peroxidation and inactivates GPX4 (*95, 96*). Other compounds, including buthionine sulfoximine (BSO), acetaminophen, artesunate, and cisplatin, which lead to the depletion of GSH, can indirectly inhibit the enzymatic activity of GPX4 and potentiate ferroptosis (*14, 97-99*).

1.2.4 Examples of Molecular Modulators of Ferroptosis

Since the discovery of ferroptosis, various molecular modulators of ferroptosis have been identified. For example, ACSL4 and LPCAT3 are involved in the activation and incorporation of PUFAs into membrane phospholipids to potentiate ferroptosis (*72, 73*). In addition, the silencing of the *PHKG2* gene, which encodes the catalytic subunit of the phosphorylase complex, leads to iron depletion and suppresses erastin-induced cell death in HT-1080 cell line (*63*). Furthermore, in a 2019 study, the transcription factor BYB domain and CNC homolog 1 (BACH1) was identified as a ferroptosis promoter (*100*). Specifically, BACH1 represses the transcription of genes involved in GSH biosynthesis and metabolism of intracellular labile iron, including glutamate-cysteine ligase modifier subunit (*GCLM*), solute carrier, family 7 member 11 (*SLC7A11*), ferritin heavy chain 1 (FTH1), ferritin light chain 1 (*FTL1*), and solute carrier family 40 member 1 (*SLC40A1*). Therefore, the activation of BACH1 leads to the depletion of GSH and the increase in the levels of intracellular labile iron, both of which increase ferroptosis sensitivity. Another modulator of ferroptosis, heme oxygenase-1 (HO-1), was shown to play conflicting roles in ferroptosis. Particularly, HO-1 degrades hemes and releases free iron, potentiating cells to ferroptosis (*101, 102*). On the other hand, the degradation of heme by HO-1 also releases the radical scavengers biliverdin and bilirubin. In addition, HO-1 is also one of the transcriptional targets of the antioxidant-responsive elements (AREs), which are activated by the KEAP1-NRF2 pathway. Thus, HO-1 can also function as a ferroptosis suppressor (*103, 104*). Moreover, it was suggested that increasing the expression of ferritin and ferroportin via the inhibition of BACH1, which reduces the levels of intracellular labile iron, would allow HO-1 to function effectively as an antioxidant enzyme (*100*).

The p53 protein was found to exert its tumor suppressor functions via the induction of ferroptosis (*105*). Particularly, p53 suppresses the expression of SLC7A11, which is the transporter subunit of system x_c^-. In addition, the upregulation of the glutaminase enzyme GLS2, a target of p53, was shown to contribute to p53-dependent ferroptosis (*106, 107*). In a genome-wide, CRISPR-Cas9-mediated suppressor screening, cytochrome P450 oxidoreductase was identified as a ferroptosis promoter, which could be due to their ability to donate electrons to cytochrome P450 enzymes that can promote lipid peroxidation (*108*). On the other hand, two additional GPX4-independent ferroptosis suppressors, GCH1 and DHODH, were reported. Specifically, GCH1 inhibits ferroptosis via the generation of the lipophilic antioxidant tetrahydrobiopterin (BH_4), the increase in the abundance of reduced CoQ10, and the depletion of esterified PUFAs (*68, 109*). Meanwhile, DHODH reduces mitochondrial CoQ10 to its quinol form and, thus, acts as a mitochondrial suppressor of ferroptosis (*110*).

1.2.5 Small-molecule Ferroptosis Inhibitors

The chemical structures of the ferroptosis inhibitors mentioned in this section are shown in **Figure 1.6**. Since ferroptosis is driven by non-enzymatic lipid peroxidation, the inhibition of the propagation step in the free radical chain oxidation by RTAs would lead to the suppression of ferroptosis. For example, the endogenous lipophilic antioxidant CoQ10, which is reduced to the active form by the enzyme FSP1, and tetrahydrobiopterin (BH_4), which is a metabolic derivative formed from the enzyme GCH1, were found to be a potent ferroptosis suppressor (*64, 65, 68, 109, 111*). In addition, supplementing the cells with α-tocopherol, which is considered Nature's premier lipid-soluble RTA, and other lipophilic antioxidants, such as Trolox and butylated hydroxytoluene, were shown to inhibit ferroptosis (*13, 51, 112*). Furthermore, Lip-1 and Fer-1, which were identified through high-throughput screening assays to identify small-molecule ferroptosis-

specific inhibitors (*13, 78*), were shown to be good RTAs in solution (*16*). Being aromatic amines, Lip-1 and Fer-1 are both weaker RTAs than a-tocopherol in organic solution. However, in liposomes, Lip-1 and Fer-1 are excellent RTAs and are much more potent than a-tocopherol in inhibiting ferroptosis, owing to their weak N-H bonds. Particularly, since amines are weak hydrogen bond donors, they do not participate in strong hydrogen bonding interaction with the phospholipid headgroups. Thus, the H atoms of amines are readily available for abstraction, leading to the inhibition of the autoxidation process. In addition, the reactions between aminyl and peroxyl radicals give rise to nitroxides that can trap multiple radicals. Therefore, these are the key factors contributing to the excellent potency of aminic RTAs as ferroptosis inhibitors. Indeed, amine-containing compounds, including diarylamines and phenoxazine, are highly effective RTAs in the lipid bilayer and potent inhibitors of ferroptosis (*113, 114*). Furthermore, nitroxide-based compounds, such as XJB5-131, TEMPO, and phenoxazine-N-oxyl, were reported to be ferroptosis suppressors (*115, 116*). Moreover, LOX inhibitors, such as zileuton, NDGA, and PD146176, were shown to inhibit ferroptosis via their radical-trapping properties (*17*). In addition to RTAs, ferroptosis can also be suppressed via the inhibition of autoxidation initiation by iron chelators, including deferoxamine and ciclopirox (*13*).

Another strategy to inhibit ferroptosis is to reduce the number of oxidizable substrates in the lipid membrane. For example, the pharmacological inhibition of ACSL4 by thiazolidinedione compounds, including rosiglitazone, pioglitazone, and troglitazone, leads to the reduction in the activation of PUFAs into membrane phospholipids and, subsequently, ferroptosis suppression (*72, 73, 117*). Alternatively, supplementing the cells with deuterated LA at bis-allylic positions increases ferroptosis resistance due to the reduced reactivity of the C-D bond (*63*). Furthermore, the addition of exogenous OA leads to a ferroptosis-resistant state (*77*). Even though the exact

mechanism of ferroptosis resistance of OA is not confirmed, it is speculated that the incorporation of OA into the cellular membranes would reduce the number of peroxidation-reactive PUFAs and, thus, mitigate the lipid peroxidation process within the lipid bilayers.

1.2.6 The Contributions of Different Subcellular Organelles to Ferroptosis

1.2.6.1 Plasma Membrane

Previously, oxidized lipid tails were shown to undergo reorientation to protrude into the aqueous phase, leading to a reduction in membrane thickness (*118*). Such reorientation then leads to changes in the lipid bilayer's physical properties, such as decreased membrane fluidity and increased membrane permeability, resulting in disrupted ion gradients (*118-121*). In the context of ferroptosis, molecular dynamic simulation of lipid membrane undergoing peroxidation showed that increased lipid peroxidation in the membrane led to increased membrane thinning and curvature as well as membrane damage through micelle formation (*122*). More recently, it was determined that pore formation, increased cell swelling and calcium influx, and, eventually, cell rupture are the late events in the cell death progress of ferroptosis (*123, 124*). In addition, the plasma membrane isoform of FSP1 was shown to protect cells from RSL3-induced ferroptosis, and the inhibition of ferroptosis by monounsaturated fatty acids was suggested to result from the suppression of plasma membrane peroxidation, emphasizing the importance of the plasma membrane in the execution of ferroptosis (*64, 65, 77*), Interestingly, ferroptosis was shown to propagate between neighboring cells independently from cell rupture, possibly via the release of oxidized lipids into the extracellular space (*123*).

1.2.6.2 Endoplasmic Reticulum

Recently, it was shown that before lipid peroxidation propagates to the plasma membrane, at which the late events in ferroptosis happen, it first occurs at the cell interior (*66*). Therefore,

other subcellular organelles represent critical sites where lethal lipid peroxidation happens. As the site where most eukaryotic membrane proteins start their lives, the endoplasmic reticulum (ER) lipid bilayers need to adapt to the differences in transmembrane spanning domain length of the proteins destined for different organelles to avoid hydrophobic mismatch (*125, 126*). Specifically, the ER requires a thinner membrane with increased fluidity and decreased surface charge. Therefore, the ER membrane has high PUFA content since the kink in their tails increases the fluidity of the lipid bilayer. As a result, the ER membrane is prone to lethal lipid peroxidation and, thus, has been suggested as the most critical site of lipid peroxidation during ferroptosis (*53*).

Indeed, lipid hydroperoxides were shown to accumulate predominantly in the ER compartment in RSL3-treated cells (*67*). Additionally, in a study utilizing alkyne-tagged ferrostatin analogs using stimulated Raman scattering microscopy to image the localization of ferroptosis inhibitors, the accumulation of such compounds in the ER was shown to be sufficient to inhibit ferroptosis, while their localization in lysosomes and mitochondria did not affect ferroptosis sensitivity (*127*). In addition, the ER was reported to increase in viscosity and become more acidified during ferroptosis (*128, 129*), which indicates increased lipid peroxidation and accumulation of reactive oxidation products (*130-132*). Furthermore, the inhibitors of system x_c^-, including erastin and sorafenib, were shown to significantly upregulate the ER stress response (*84, 133*). Together, these data are the evidence that highlights the important role of the ER in ferroptosis.

1.2.6.3 Mitochondria

Currently, there is a debate about whether mitochondrion is an essential subcellular organelle in ferroptosis. Evidence supporting its role in ferroptosis includes the observation of smaller mitochondria with increased membrane density and loss of structural integrity in erastin-

treated cells, and that mitochondria-specific nitroxides are more potent ferroptosis inhibitors than non-specific nitroxides (*13, 112*). In addition, the mitochondrial DHODH and mitochondrial CoQ10 can also rescue cells from ferroptosis (*110*). Previously, the mitochondria-targeted antioxidant MitoQ was shown to be much less effective in rescuing GPX4 knockout-induced cell death than the membrane-targeted antioxidant DecylQ (*78*), which may indicate that mitochondria are not essential to ferroptosis. However, GPX4 is highly enriched in the mitochondrial intermembrane space (*134*) while MitoQ primarily targets the mitochondria matrix (*135*). Therefore, it is possible that MitoQ did not accumulate at the location of lipid hydroperoxide buildup. Additionally, glutaminolysis, which is responsible for the degradation of glutamine in the mitochondria to generate cellular energy, and its associated enzyme GSL2 as well as the tricarboxylic acid cycle, have been shown to sensitize cells to ferroptosis (*54, 136, 137*). Moreover, doxorubicin-induced ferroptosis was shown to be mitochondria-dependent (*102, 138*).

On the other hand, several studies have suggested that the presence of mitochondria is not necessary for ferroptosis. For example, it was reported that lipid peroxidation accumulation and ferroptosis could still happen in mitochondria-deficient cells (*127*). In addition, several nitroxide-based compounds lacking mitochondria-specific moiety can potently rescue cells from ferroptosis (*116*). Importantly, it was shown that the role of mitochondria in ferroptosis is more relevant in cysteine deprivation-induced than direct GPX4 inhibition-induced cell death (*137*).

1.2.6.4 Peroxisomes

Even though the accumulation of lipid peroxidation in peroxisome has not been examined during ferroptosis, peroxisomes can contribute to the induction of ferroptosis via the biosynthesis of ether lipids. Specifically, ether phospholipids and their peroxisome-driven biosynthesis have been implicated as drivers of ferroptosis (*69, 139*). In addition, the loss of the gene *FAR1* encoding

for fatty acyl-CoA reductase 1 (FAR1) can protect cells from RSL3-induced cell death (*109*). However, it should be noted that, recently, disruption of the gene *APGS* encoding for alkylglycerone phosphate synthase (AGPS), an enzyme required for the synthesis of ether lipids, was found to have little effect on the lethality of erastin2 and RSL3 (*66*). This result suggests that the role of APGS-dependent ether lipid synthesis and, in general, peroxisomes in ferroptosis may be context-dependent.

1.2.6.5 Lysosomes

Ferritinophagy is an autophagic process in which ferritin is degraded in the lysosome, leading to the release of iron into intracellular space and increased ferroptosis sensitivity (*54, 57*). In addition, it was shown that ROS was constitutively generated in lysosomes during ferroptosis, and the autophagy/lysosomal inhibitors, including bafilomycin A1, 3-methyladenine, and PepA-Me, could inhibit lysosomal ROS generation as well as ferroptotic cell death (*140*). Thus, lysosomes are suggested to contribute to ferroptosis as iron reservoirs. However, the accumulation of Fer-1 in lysosomes was shown to not contribute to its ability to suppress ferroptosis (*127*). In addition, in a different study, bafilomycin A1 and 3-methyladenine were found to be ineffective in inhibiting ferroptosis (*13*). Therefore, additional studies are needed to elucidate whether lysosomes are essential to ferroptosis induction.

1.2.6.6 Lipid Droplets

The role of lipid droplets in ferroptosis is controversial due to their dual functions in modulating the availability of PUFAs to be incorporated into the membrane (*141*). Specifically, lipid droplets can sequester PUFAs away from the membrane and, thus, reduce ferroptosis sensitivity. Evidence supporting the protective role of lipid droplets includes the observations that the inhibition of diacylglycerol acyltransferase, an essential enzyme in lipid droplet synthesis,

leads to increased oxidative stress and lethality in both stem cell niche and acidified tumors (*142, 143*). In addition, lipid droplet biogenesis stimulated by phospholipase A_2 was shown to promote the survival of triple-negative breast cancer cells (*144*).

On the other hand, lipolysis mediated by the enzyme adipose triglyceride lipase (ATGL) can release PUFAs from lipid droplets (*141*). Thus, lipid droplets can also act as the reservoirs of PUFAs for phospholipid synthesis. Indeed, ATGL depletion leads to a reduction in PUFA-dependent cell death (*144*). In addition, the incorporation of PUFAs into lipid droplets was reported to promote ferroptosis sensitivity in recent studies (*75, 145, 146*). Furthermore, the viscosity of lipid droplets was shown to increase during erastin and RSL3-induced ferroptosis while remaining unchanged upon the addition of both erastin in the presence of Fer-1 (*147*), suggesting an accumulation of lipid peroxidation and oxidation products within lipid droplets during ferroptosis (*130-132*). In line with this observation, imidazole ketone erastin (IKE) was reported to induce both the reduction in the levels of phospholipids and triacylglycerides (TAGs) while upregulating the expression of ATGL (*148*), suggesting that the increase in oxidized PUFA tails on TAGs promote ATGL-mediated lipolysis of lipid droplets. Additional studies also implicate that TAGs stored within lipid droplets can undergo lipid peroxidation (*149, 150*). Thus, lipid droplets may be additional sites where lipid peroxidation happens, contributing to the induction and progression of ferroptosis.

1.2.7 Biological Functions of Ferroptosis

Ferroptosis has been suggested to play a role in tumor suppression, especially via the functions of p53. Particularly, p53 suppresses the transcription of system x_c^- subunit SCL7A11 in both *in vitro* and *in vivo* models, leading to the subsequent depletion of GSH, the inactivation of GPX4, and the induction of ferroptosis (*105, 151*). In addition, the tumor-suppressive mechanisms

involving MLL4, BAP1, and NSF1 are related to ferroptosis (*152-154*). Moreover, a diet rich in PUFAs was shown to promote tumor suppression via the induction of ferroptosis (*143*).

In addition to tumor suppression, ferroptosis is implicated in immune functions. Specifically, the cytokine interferon-γ produced by $CD8^+$ T cells upregulates the expression of ACSL4 while downregulates the expression of SLC7A11, resulting in tumor cell ferroptosis (*155, 156*). Importantly, excess AA was detected in the tumor microenvironment, suggesting that the combination between endogenous PUFAs and interferon-γ may represent a natural ferroptosis-dependent tumor suppression mechanism. Furthermore, the cytokines interleukin (IL)-4 and IL-3 can suppress the expression of GPX4 in kidney, lung, heart, and spleen cells, leading to the accumulation of AA metabolites, which are key inflammatory intermediates (*157*). Additionally, GPX4 is suggested to play a role in immune surveillance by modulating the levels of immunomodulatory lipid metabolites and the cellular ferroptosis-sensitivity state (*158*). Ferroptosis has also been suggested to be involved in normal development and aging processes across different species (*159-161*).

1.2.8 Therapeutic Implications of Ferroptosis

1.2.8.1 Therapeutic Implications of Ferroptosis Inhibitors

Increased oxidative stress and lipid peroxidation are implicated in various diseases, such as acute kidney injury (*162, 163*), periventricular leukomalacia (PVL), which is a form of white matter brain injury commonly found in premature infants (*164, 165*), and Huntington disease (*166-168*). Therefore, ferroptosis is suggested to be the mechanism underlying these pathologies, and the ferroptosis inhibitors can be utilized as therapeutics. Indeed, Fer-1 and Lip-1, which are ferroptosis-specific inhibitors, were shown to be effective therapeutics in these disease models (*78, 169, 170*). In addition, treatments using lipid peroxidation inhibitors, including iron chelators and

RTAs, can prevent cell death in models of loss of oligodendrocytes (*171*), R6/2 Huntington neurons (*172*), and cardiomyopathy (*102*), while the inhibition of glutaminolysis has been shown to protect against brain hemorrhage, ischemia/reperfusion-induced heart, and kidney damage in experimental models (*54, 170, 173, 174*). Furthermore, ferroptosis inhibition via the hypocholesterolemic drug probucol, selenium delivery, and the mitochondria-targeted nitroxide XJB-5-131 was shown to be effective in models of glutamate toxicity, stroke, and traumatic brain injury, respectively (*115, 175, 176*).

1.2.8.2 Therapeutic Implications of Ferroptosis Inducers

The applications of ferroptosis inducers in cancer have been investigated extensively. For example, the system x_c^- inhibitor IKE was shown to induce ferroptosis and mitigate tumor growth in mice lymphoma xenografts (*148*). In addition, the deletion of the gene *SLC7A11* was reported to slow the growth of a mouse genetic model of pancreatic cancer (*177*). Furthermore, certain diffuse large B cell lymphoma (DLBCL) cell lines have defective transsulfuration pathways and, thus, rely on the activity of system x_c^- for the import of cystine/cysteine into the cells (*86, 178*). On the other hand, renal cell carcinomas (RCCs), especially chromophobe RCCs, have elevated cellular iron levels and, thus, are susceptible to lipid peroxidation (*179*). These results suggest that these cancer cell lines are highly sensitive to ferroptosis. In fact, DLBCL and RCCs were identified to be particularly susceptible to ferroptosis in a sensitivity profiling in 177 cancer cell lines (*14*). Therefore, ferroptosis inducers may be effective therapeutics for these cancer types. Indeed, the system x_c^- inhibitor sulfasalazine potently inhibits the growth of lymphomas with low expression levels of SLC7A11 (*86, 180*). In addition, sorafenib, an approved treatment for advanced RCCs, is another system x_c^- inhibitor and can induce ferroptosis (*84*). Ferroptosis can also be applied as therapies in aggressive cancers that have undergone epithelial-to-mesenchymal transition and

cancer therapy-resistant cells (*93, 181-183*). Additionally, ferroptosis inducers can be utilized in radiotherapy and immunotherapy (*184-186*).

1.3 Summary and Dissertation Overview

Even though both the HAT and PRA mechanisms contribute to the rate-determining propagation steps of the free radical oxidation mechanism, the conventional radical clock method only accounts for the HAT mechanism. Without considering the contribution of the peroxyl addition reaction to the overall rate constant of the propagation step, one would not be able to fully understand the complex nature of the lipid peroxidation mechanism and its biological effects. To fill this gap, chapter 2 of this dissertation discusses the development, validation, and application of a new peroxyl radical clock approach that can simultaneously measure both the HAT and PRA rate constants and elucidate the lipid peroxidation mechanism of various oxidizable substrates, including biologically important lipids.

In the remaining chapters of this dissertation, we focus primarily on investigating the relationship between lipid peroxidation mechanism and kinetics and its modulatory effects on ferroptosis, a type of regulated cell death driven by the iron-dependent autoxidation of PUFAs that have been activated and incorporated into cellular membranes. Previous studies have shown that exogenous lipids, including OA, LA, AA, EPA, DHA, α-eleostearic acid, punicic acid, 7-DHC, and vitamin D_3, can modulate ferroptosis sensitivity in various cancer cell lines (*63, 77, 143, 146, 187-190*). However, a systematic study is lacking to compare the modulatory effects of different exogenous lipids in the same cell lines. Therefore, in chapter 3, we present the first systematic investigation of the extent to which various exogenous lipids affect ferroptosis induction in ferroptosis-sensitive cell lines. We also explain the observed ferroptosis modulatory effects based on the lipid peroxidation mechanism and kinetics elucidated in chapter 2. Chapter 4 focuses on

investigating the mechanisms underlying the ferroptosis induction by conjugated PUFAs, which are the lipid species that we discovered to be particularly reactive towards PRA reactions and can act as a potent noncanonical ferroptosis inducer. The results from this chapter also provide some insights into the contributions of different subcellular organelles to ferroptosis and the molecular events that happen during the ferroptosis execution phase. In Chapter 5, the RNA-seq and pathway analysis results for the conjugated PUFAs from Chapter 4 are compared to the publicly available RNA-seq data of other ferroptosis inducers to elucidate whether different ferroptosis inducers cause common gene expression pathway changes. Finally, Chapter 6 summarizes the important finding and conclusions from this collective work and suggests how to expand research in this area.

Figures

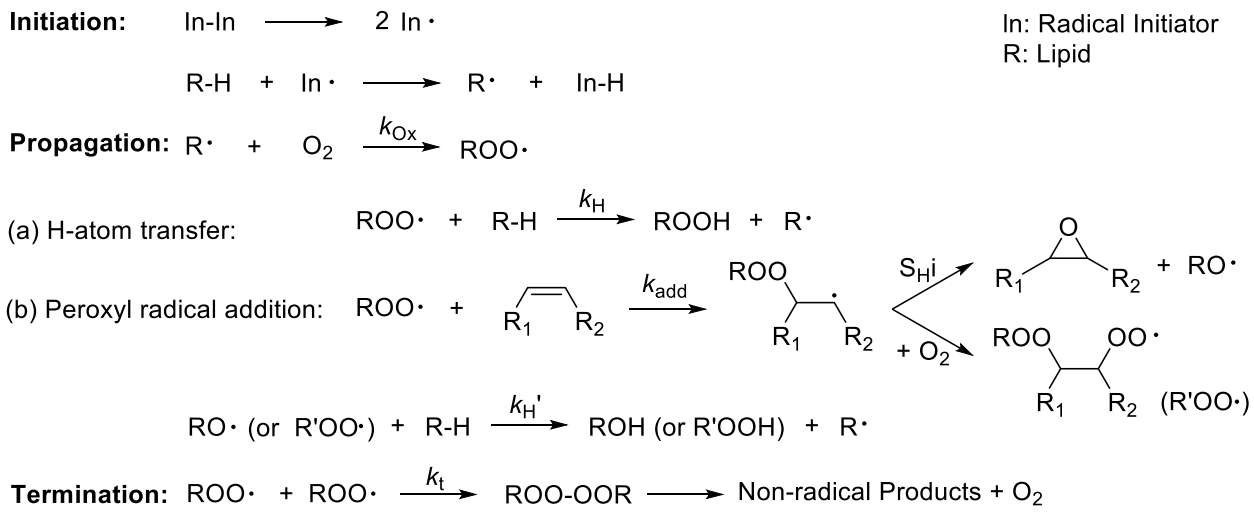

Figure 1.1 Free radical chain oxidation mechanism of lipids.

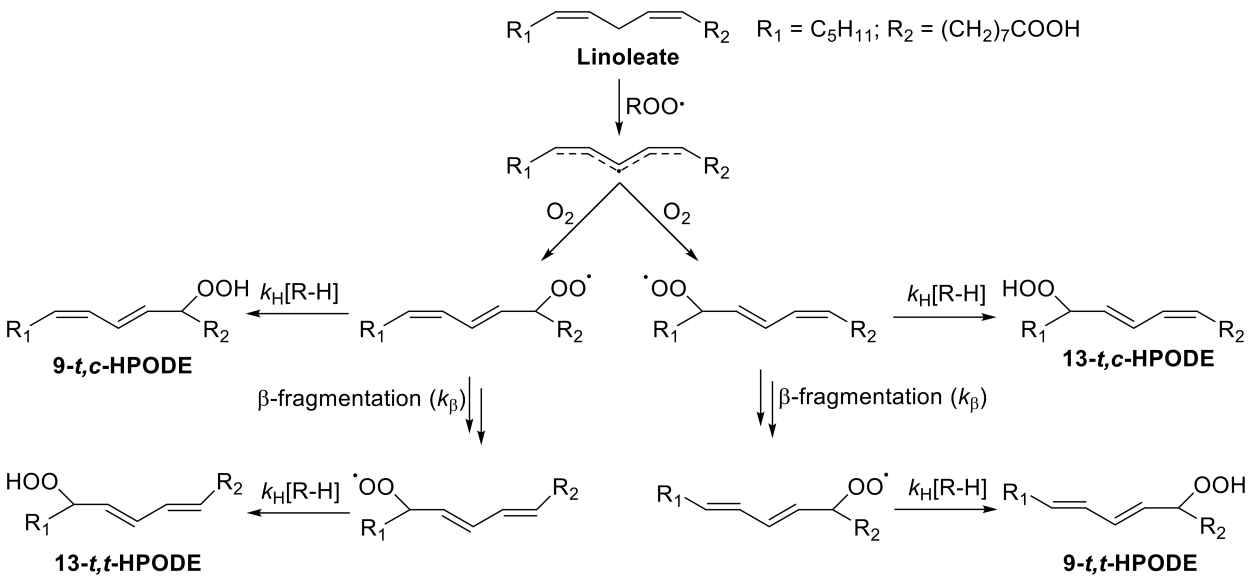

Figure 1.2 The original linoleate peroxyl radical clock (*24*).

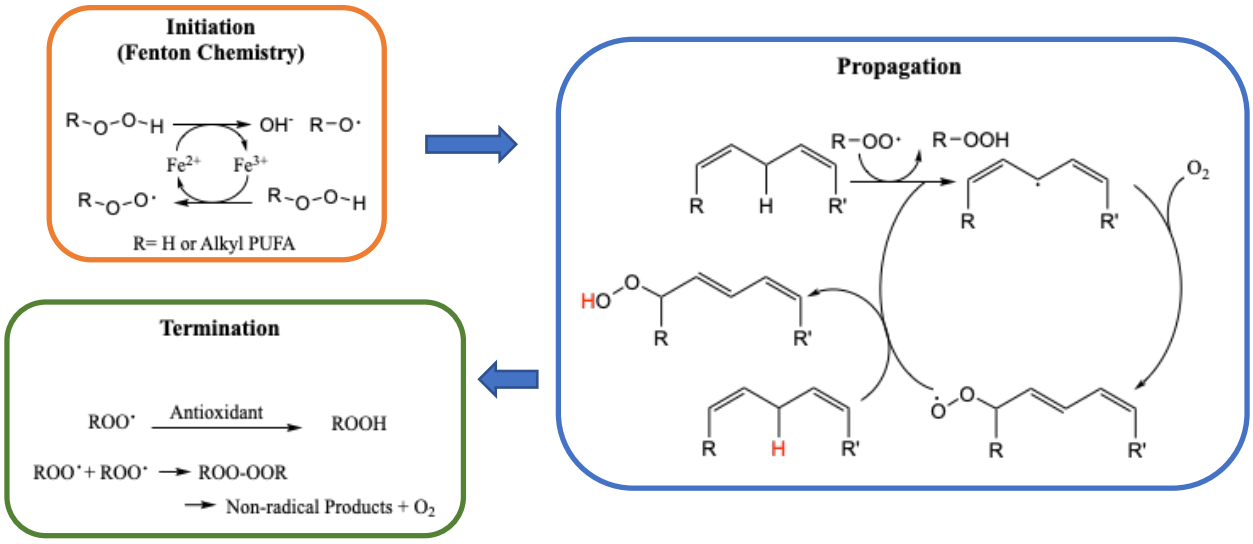

Figure 1.3 The initiation of the nonenzymatic free radical chain oxidation via Fenton chemistry.

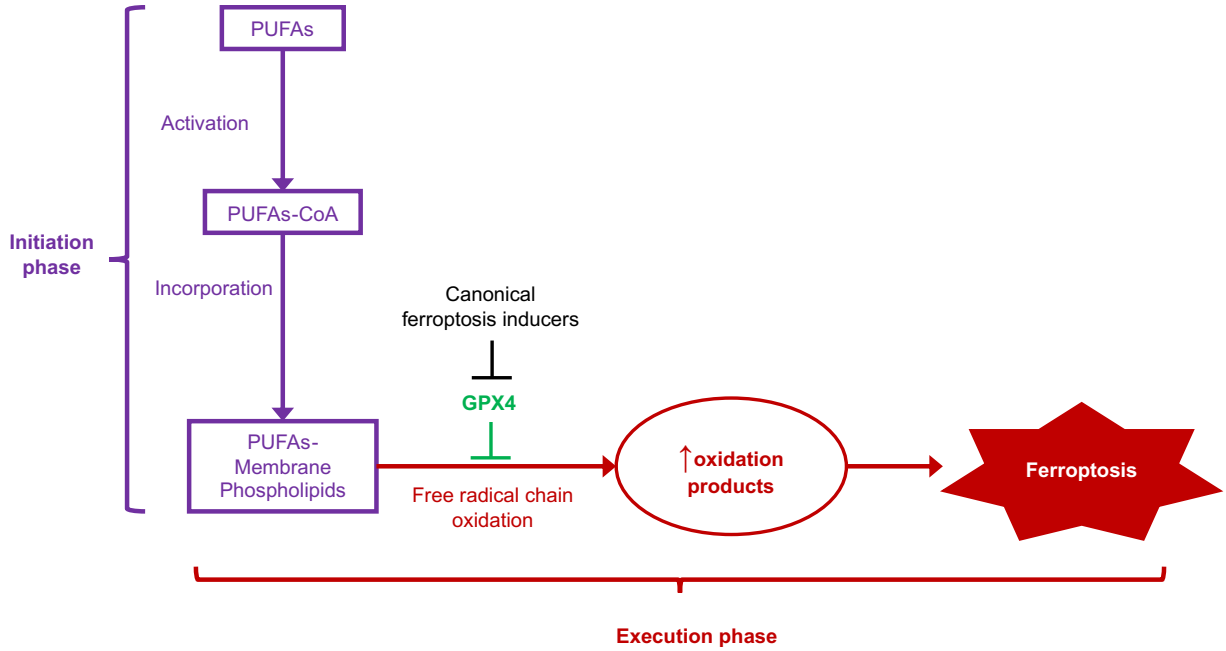

Figure 1.4 Free radical-mediated lipid peroxidation drives ferroptosis.

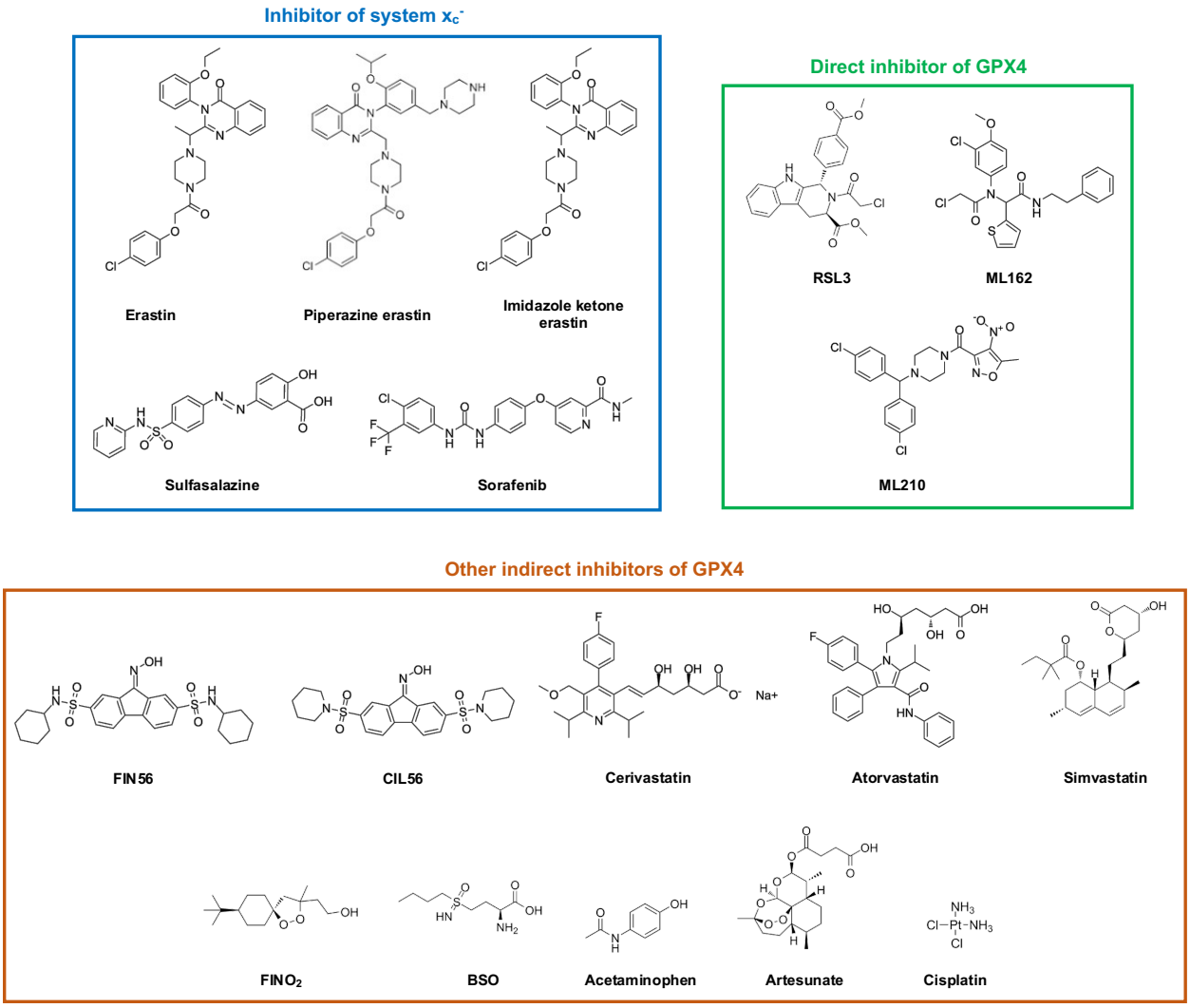

Figure 1.5 Chemical structures of ferroptosis canonical inducers.

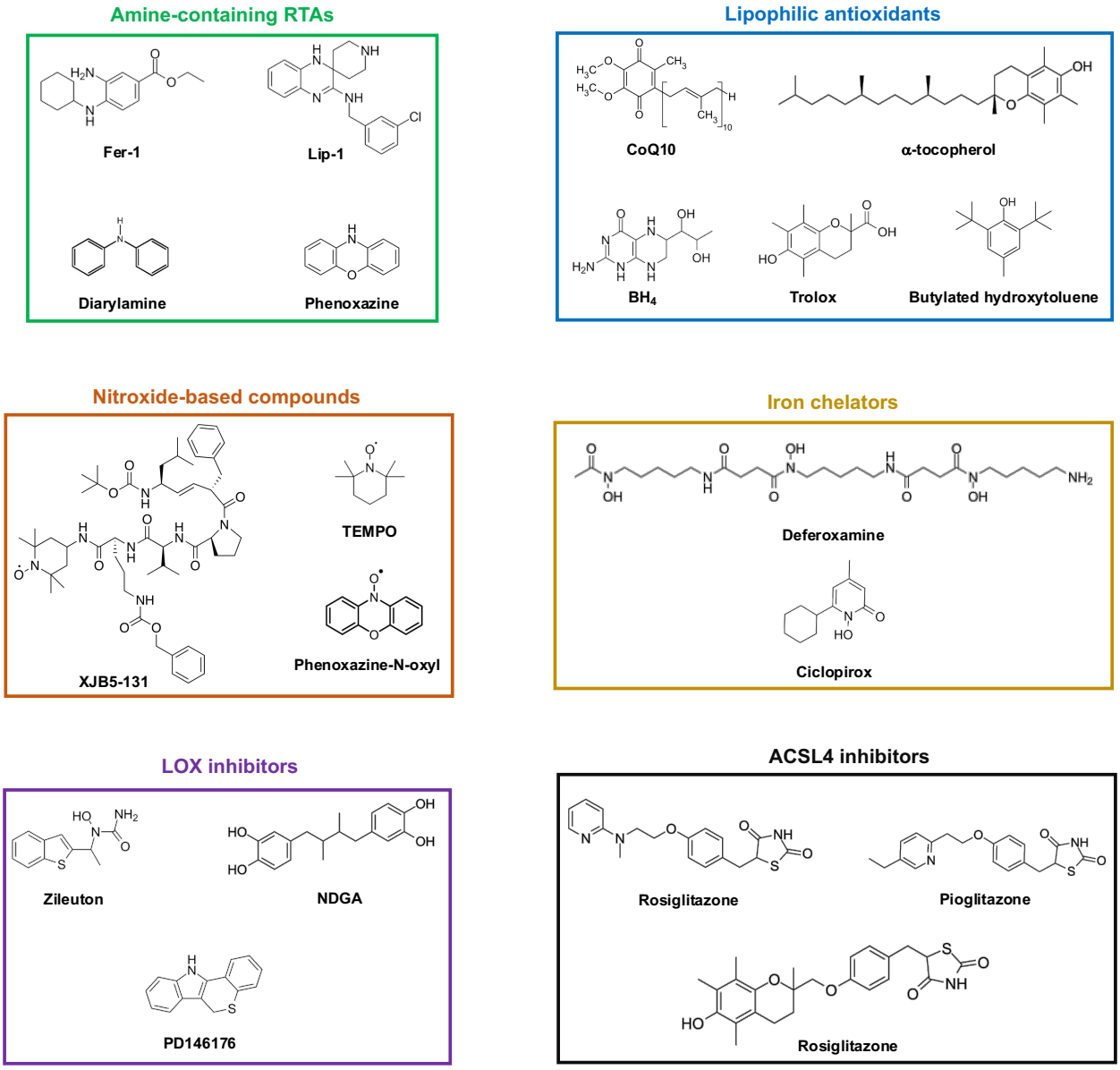

Figure 1.6 Chemical structures of small-molecule ferroptosis inhibitors.

Chapter 2. The Development and Validation of a New Peroxyl Radical Clock Approach to Delineate Peroxidation Mechanism and Kinetics

Portions of this chapter have been adapted and reproduced with permission from:

Quynh Do, David D. Lee, Andrew N. Dinh, Ryan P. Seguin, Rutan Zhang, and Libin Xu. Development and Application of a Peroxyl Radical Clock Approach for Measuring Both Hydrogen-Atom Transfer and Peroxyl Radical Addition Rate Constants. *J. Org. Chem,* 86 (**2021**) 153–168.

2.1 Introduction

Autoxidation is a term used describe the non-enzymatic reaction between a lipid molecule and molecular oxygen. Autoxidation occurs via a three-step mechanism including: initiation, propagation, and termination (*2*) (see **Figure 1.1**). The rate-limiting step in this mechanism is the propagation step in which the lipid peroxyl radical can undergo two types of reaction including hydrogen(H)-atom transfer (HAT) and peroxyl-radical addition (PRA). In the HAT reaction, the peroxyl radical will receive a H-atom from another lipid or oxidizable substrate generating a lipid hydroperoxide (ROOH). Meanwhile, in the PRA reaction, the peroxyl radical can be added into a double bond. This addition product can then either undergoes intramolecular homolytic substitution (S_Hi) to form an epoxide or reacts with another molecular oxygen to form new peroxyl radical products. Since both the H-atom transfer and peroxyl-radical addition reactions generate new radicals that can continue to react with another lipid molecule or oxidizable substrate, lipid peroxidation can also be considered free radical chain oxidation reaction.

The rate constant of H-atom transfer reaction, k_H, for a variety of lipids and oxidizable substrates has been studied intensively utilizing the linoleate peroxyl radical clock (see **Figure 1.2**) (*24*). However, there were no methods available to measure the rate constants for the PRA

reaction, k_{add}. Epoxides, one of the addition products, were identified among the oxidation products from sterols, such as cholesterol and 7-DHC (*12, 191, 192*). In addition, intramolecular PRA reactions were discovered to occur in cardiolipins with multiple linoleate chains, once one chain is oxidized to linoleate peroxyl radical (*193*). These results suggest that PRA also contributes significantly to the propagation step and thus, its rate constants should also be considered in the study of lipid peroxidation kinetics. This is a major gap in the field that this study aims to fill. The sum of k_H and k_{add}, also defined as the total propagation rate constant (k_p) of lipid peroxidation of a substrate, can also be measured with the inhibited autoxidation method using a set of calibrated reference inhibitors (*194*). However, this method cannot differentiate between the two rate constants, either. To be able to fully understand the complex nature of the lipid peroxidation mechanism, kinetics, and products, we modified the current linoleate peroxyl radical clock to account for the contribution of the PRA reaction (**Figure 2.1**).

We report here the development of a new analytical approach based on the original linoleate-based peroxyl radical clock, which enables the simultaneous measurement of the rate constants of both HAT and PRA reactions. We first explain the design of the new peroxyl radical clock approach. We then apply this new approach to elucidate the values of k_H and k_{add} for a variety of substrates, including para- and meta-substituted styrenes, double bond-substituted styrenes, conjugated dienes with methyl substituent at different positions, cyclic compounds, and biologically important lipids (**Figure 2.2**). Based on these results, we will discuss the factors that affect the contribution of each reaction to the overall propagation step. In the end, we will discuss the limitations of the new approach.

2.2 Results

2.2.1 Design of the New Peroxyl Radical Clock.

Our new approach was developed based on the autoxidation of methyl linoleate (MeLn) as its mechanism is well studied. In addition, our preliminary studies had shown that the high-performance liquid chromatography (HPLC) chromatograms of MeLn-based oxidation products had better separation compared to that of linoleic acid, which enables better product analysis. To elucidate the values of k_H and k_{add}, it is crucial to capture all the linoleate-derived peroxide products by fully reducing the hydrogen peroxyl group in HPODEs from the HAT reaction and the alkyl peroxyl group in addition products from PRA reaction. We used the co-oxidation reaction of MeLn and styrene in benzene to examine different reducing agents and conditions because styrene can only undergo PRA reactions (see Experimental Procedures Section).

After the peroxidation reaction, the reaction mixture was split into two halves. While the first half was analyzed directly, the second half was reduced prior to analysis. This ratio between the total reduced-oxidized products and the total non-reduced oxidation products is expected to be equal to or larger than one if all the oxidation products are fully reduced. Even though triphenylphosphine was commonly used in the classic radical clock approach as a reducing agent (*24, 25*), we found that it was not strong enough to reduce all the linoleate-derived products, particularly those from the PRA reactions, which are endoperoxides and sometimes in the form of peroxide polymers (*2*). Attempts using sodium borohydride under various conditions were also unsuccessful, leading to the ratios between the concentration of reduced and non-reduced oxidation products that are less than one. We found that the complete reduction of all oxidation products could only be achieved using the strong reducing agent, lithium aluminum hydride ($LiAlH_4$). It should be noted here that $LiAlH_4$ reduces both the peroxyl bonds and the ester moiety in MeLn to

alcohols. Importantly, these diols are a completely new set of products from the oxidation of linoleate that have never been characterized before as readouts for radical clocks. We termed these linoleate-derived alcohols, or hydroxyoctadecadienols, HODOLs (structures shown in **Figure 2.3**).

Our new peroxyl radical clock approach can be summarized into two main steps: to measure the sum of k_H and k_{add} and to determine the ratio of k_{add}/k_H (**Figure 2.3**). The sum of k_H and k_{add}, which equals to k_p, can be elucidated via plotting the ratio [*tc*-HODOLs]/[*tt*-HODOLs] at different substrate concentrations. Specifically, when an oxidizable substrate can undergo both HAT and PRA reactions, the ratio [*tc*-HODOLs]/[*tt*-HODOLs] will be mediated by the competition from the HAT, β-fragmentation, and PRA reactions. Therefore, k_p can now be calculated from eq 1:

$$\frac{[tc\text{−HODOLs}]}{[tt\text{−HODOLs}]} = \frac{k_p[\text{Substrate}]}{214} + 0.16 \text{ (eq 1)}$$

On the other hand, the ratio k_{add}/k_H could be elucidated by plotting the ratio between the concentration of the total HODOLs, which are reduced oxidation products derived from both the HAT and PRA reactions, termed $HODOL_{total}$, and of the total HPODEs, which are non-reduced oxidation products derived from only the HAT reaction, termed $HPODE_{total}$, at different substrate concentrations. Thus, eq 2 describes the ratio $[HODOL_{total}]/[HPODE_{total}]$ as a function of substrate concentration.

$$\frac{[\text{HODOL}_{\text{total}}]}{[\text{HPODE}_{\text{total}}]} = \frac{k_{\text{MeLn}}[\text{MeLn}]+k_H[\text{Substrate}]+k_{\text{add}}[\text{Substrate}]}{k_{\text{MeLn}}[\text{MeLn}]+k_H[\text{Substrate}]} = \frac{k_{\text{add}}[\text{Substrate}]}{k_{\text{MeLn}}[\text{MeLn}]+k_H[\text{Substrate}]} + 1$$

$$= \frac{k_H\frac{k_{\text{add}}}{k_H}[\text{Substrate}]}{k_{\text{MeLn}}[\text{MeLn}]+k_H[\text{Substrate}]} + 1 = \frac{k_H\frac{k_{\text{add}}}{k_H}[\text{Substrate}]}{18.7+k_H[\text{Substrate}]} + 1 \text{ (eq 2)}$$

Here, k_{MeLn} represents the total propagation rate constant of MeLn, which is 62 M^{-1} s^{-1} as measured by the rotating-sector method (*23*). In addition, [MeLn], which is fixed at 0.3 M, is the concentration of MeLn used to set up the radical clock experiment. Therefore, the term k_{MeLn}[MeLn] is a constant that is equal to 18.7 s^{-1}. By fitting the [Substrate] vs [$HODOL_{total}$]/[$HPODE_{total}$] curve to eq 2 using Prism software, we could obtain the value of k_{add}/k_H. Now, the individual value for each rate constant could be solved from the sum and the ratio of k_H and k_{add}. An example on the determination of k_p, k_{add}, and k_H values from the [Substrate] vs [*tc*-HODOLs]/[*tt*-HODOLs] and [Substrate] vs [$HODOL_{total}$]/[$HPODE_{total}$] plots for 1,3-cyclohexadiene (1,3-CHD), a substrate that can undergoes both reactions, is shown in **Figure 2.4a**. When a substrate can only undergo HAT reaction, such as 1,4-CHD, eq 2 would be rewritten as eq 3, and the linear fit of the [Substrate] vs [$HODOL_{total}$]/[$HPODE_{total}$] data would give a slope close to 0 (**Figure 2.4b**). In this case, the value of k_H would be reported as the value of k_p. In contrast, when PRA is predominant compared to HAT, such as in the oxidation of styrene (Sty), eq 3 would become eq 4 and the linear fit of [Substrate] vs [$HODOL_{total}$]/[$HPODE_{total}$] data would give a non-zero slope (**Figure 2.4c**). Here, the value of k_{add} would be equal to the value of k_p.

k_H dominant: $\frac{[\mathrm{HODOL_{total}}]}{[\mathrm{HPODE_{total}}]} = 1$ (eq 3)

k_{add} dominant: $\frac{[\mathrm{HODOL_{total}}]}{[\mathrm{HPODE_{total}}]} = \frac{k_{add}[\mathrm{Substrate}]}{18.7} + 1$ (eq 4)

For this new peroxyl radical clock approach, normal phase HPLC/UV was utilized to quantify the relative amounts of HPODE and HODOL products, respectively, to an internal standard, 9-anthracenemethanol (**Figure 2.5**) (see Experimental Procedures).

2.2.2 Application of the New Peroxyl Radical Clock Approach on Examining the Reactivities of Substrates that only Undergo PRA Mechanism.

We first applied the new approach to measure the rate constants of *para*- and *meta*-substituted styrenes (Fig. 4a and b). Since styrene and its *para*- and *meta*-substituted derivatives can only undergo PRA in reactions with MeLn, this series is useful not only in assessing the application of the new approach but also in determining the substituent effects on the reactivity of the PRA mechanism. The [Substrate] vs [$HODOL_{total}$]/[$HPODE_{total}$] curve for styrene and its derivatives confirmed that they are indeed k_{add} dominant (**Figure 2.6, Figure 2.7**). The value of k_{add}, which is equal to k_p, for each compound was determined and reported in **Table 2.1**. We found that the experimental k_{add} value of styrene is on the same order of magnitude to the value measured previously using the rotating-sector method at 30 °C (*195*).

Since the addition of peroxyl radical to an alkene is an electrophilic reaction (*196*), the polar transition state of PRA reaction would be opposite to the carbon-radical addition to alkenes, which was a nucleophilic process (**Figure 2.8**) (*197*). Therefore, we hypothesized that the addition rate constant of the peroxyl radical to styrene would increase as the electron density at the double bond increases. Indeed, we observed an increase in k_{add} values of styrene derivatives with strong electron donating groups at the *para*-position such as 4-MeSty and 4-MeOSty. However, the addition rate constants of styrene derivatives with electron withdrawing groups such as 4-ClSty, 4-FSty, and 4-NO_2Sty were found to have k_{add} values that are similar to that of styrene. This observation suggests that radical stabilization effects are more important than polar effects in influencing the reactivities of the addition of peroxyl radical into styrene. To provide further insights to our results, we calculated the activation energies for the addition reaction between the peroxyl radical with each of the *para*-substituted styrenes using the B3LYP/6-31++G(d,p) method

(**Table 2.1**). In the computational model of the reaction transition state, we used methyl peroxyl radical as a simplified analog for MeLn peroxyl radical to expedite the calculations. Consistent to the measured k_{add} values, we observed a decrease in the computed energy barriers for Sty, 4-MeSty, and 4-MeOSty, respectively. There was also no significant difference in the activation energies of 4-ClSty, 4-FSty, and 4-NO_2Sty from that of Sty, which agreed with our experimental data. The experimental k_{add} values also appear to align better with the trend predicted by the computed spin density than the atomic polar tensor charge, which represents the partial charge distribution (**Figure 2.9a, b**).

We then attempted to generate a Hammett correlation by plotting $\log(k_X/k_H)$ versus either the σ_{para}-scale (*198*) or the radical σ-scale (σ_{rad}) (*199*) (**Figure 2.10a, b**). However, both Hammett parameters did not allow us to derive a good linear correlation between substituent effects and the rate constant of the PRA reaction. Therefore, we utilized the extended Hammett equation:

$$\log k_X/k_H = \rho\sigma^+ + \sigma_{rad} \text{ (eq 5)}$$

to derive the correlation between the substituent effects and the computed activation energies **(Figure 2.9e**) (*200*). Note that since the reaction rates appear to be mediated primarily through radical stabilization effects and the transition state contains partial positive charge, the use of the σ^+-scale (*201*) is more appropriate than the σ-scale (*198*). The values of $\log(k_X/k_H)$, σ^+, and σ_{rad} for each substituent were fit to eq 5, giving a ρ value of -0.66. Fitting of the calculated activation energy and the combined Hammett parameters ($\sigma_{rad} - 0.66\sigma^+$) with linear regression gave eq. 6 (R^2 = 0.85):

$$E_a = -1.04(\sigma_{rad} - 0.66\sigma^+) + 19.4 \text{ (kcal/mol) (eq 6)}$$

which describes the dual radical-cationic properties of the benzylic carbon in styrene and its derivatives **(Figure 2.9c**). The negative slope of the line also confirmed that there is a partial

positive charge buildup on the benzylic carbon atom during the transition state and that the addition of peroxyl radical to alkene is indeed an electrophilic reaction. Fitting of the calculated activation energy and log (k_X/k_H) also gave a good linear correlation ($R^2 = 0.93$) with a negative slope of -1.21, which shows a good agreement between our theoretical and experimental data (**Figure 2.9d).** We then examined the *meta*-substituted styrene derivatives to investigate how the addition rate constants and activation energies would change with only contribution from the polar effects (**Table 2.1**). The small changes in both rate constants and activation energies of the *meta*-substituted styrene derivatives further suggested that contribution of polar effects to the reactivity of the PRA reaction is small. In addition, the rate constants of the *meta*-substituted styrene derivatives and σ_{meta} parameters did not give a good linear correlation in the Hammett plot (**Figure 2.10c**).

2.2.3 Application of the New Peroxyl Radical Clock Approach on Structure-reactivity Relationship Studies of Different Oxidizable Substrates.

Here, we applied the new peroxyl radical clock approach to measure the values of k_p, k_H, and k_{add} for different series of oxidizable substrates including α- and β-MeSty, conjugated dienes with different methyl substituents, and cyclic compounds (**Figure 2.2c, d, e; Figure 2.7e, f; Figure 2.11; and Figure 2.12**). The results are summarized in **Table 2.2**. Structure-reactivity relationship studies on these substrates allow us to examine the factors that affect the contribution of each mechanism into the overall propagation rate constant. For example, both α- and β-MeSty have significantly different reactivities towards the HAT mechanism due to the location of their methyl substituent. Particularly, while the proposed resulting carbon radicals formed after the abstraction of H-atom from α-MeSty span only three carbon centers, the loss of H-atom from β-MeSty potentially forms a much more delocalized radical (**Figure 2.13**). This explains why β-

MeSty has significant contribution from the HAT mechanism while α-MeSty is k_{add} dominant. However, we are surprised by the higher k_{add} value of β-MeSty compared to α-MeSty. The addition of peroxyl radical into the terminal methylene group of α-MeSty would potentially lead to the formation of a tertiary benzylic radical, which is highly stable. While the addition of the peroxyl radical at the same carbon of β-MeSty would generate a stable secondary benzylic carbon-radical, this addition position has a methyl substituent. Thus, one would expect β-MeSty to have lower k_{add} value than α-MeSty. In addition, we want to note the difference in the order of our experimental k_{add} values for Sty, α-MeSty, and β-MeSty and those reported by the rotating-sector method. The discrepancy here can be attributed to the fact that the propagation rate constants depend on the structure of not only the substrate but also the chain-propagating peroxyl radical (*23*). Specifically, in the rotating-sector method, the resulting chain-carrying species is a tertial peroxyl radical after the addition of peroxyl radical to α-MeSty, which is markedly more hindered than the secondary peroxyl radicals derived from Sty and β-MeSty (*23*). Hence, the rate constant for α-MeSty measured using the rotating sector method is much smaller than those of Sty and β-MeSty. On the other hand, in the peroxyl radical clock method, the chain-carrying species are the same secondary linoleate-based peroxyl radicals for all substrates, which means the propagation rate constants depend mostly on the structures of the substrates.

Pair-wise comparison of substrates from **Table 2.2** also confirms the electronic effects on k_{add}. For example, structures that contain additional methyl substituents on the double bond, including 3-methyl-1,3-pentadiene, 2,4-dimethyl-1,3-pentadiene, 2,4-hexadiene, and 2,5-dimethyl-2,4-hexadiene (**Figure 2.2d**), have much higher k_{add} values compared to 1,3-pentadiene. Similarly, the addition of a methyl substituent on 2-methylindene also doubles the k_{add} value of this substrate compared to indene. However, it should be noted that 2,4-dimethyl-1,3-pentadiene

has a lower k_{add} value compared to 3-methyl-1,3-pentadiene even though it has more methyl substituents. In 3-methyl-1,3-pentadiene, the peroxyl radical can be added to both carbon 1 and 4. However, in 2,4-dimethyl-1,3-pentadiene, the two methyl substituents at carbon 4 sterically hinder the attack of the peroxyl radical at this position. Comparison between 1,3-pentadiene and 1,3-hexadiene also allowed us to confirm that changes in k_H values are dependent on the stability of the radical formed after the loss of the H-atom. Specifically, after the HAT reaction, 1,3-hexadiene would yield a secondary radical that is much more stable than the primary radical formed from 1,3-pentadiene. Hence, 1,3-hexadiene has a much higher k_H value and lower k_{add}/k_H ratio than 1,3-pentadiene.

The difference in reactivities of 1,3-CHD and 1,4-CHD indicates that PRA mechanism can only significantly contribute to k_p when there is a conjugated double bond system. Specifically, 1,4-CHD has a nonconjugated double bond system with two bis-allylic positions, which have been found to be highly reactive towards H-atom transfer (*202*). Thus, 1,4-CHD is k_H dominant. In contrast, 1,3-CHD has a conjugated double bond system, which explains why there is significant contribution of k_{add} into its total propagation rate constant. It should be noted here that the k_H values measured for 1,3- and 1,4-CHD are almost identical, which is consistent with the similar C-H bond dissociation energies (BDEs) previously reported for the two compounds (*203*). We also want to note the discrepancy between our experimental k_H value for 1,4-CHD (478 M^{-1} s^{-1}) compared to the value previously reported (1480 M^{-1} s^{-1}) (*23*). Similar to the cases of Sty, α-MeSty, and β-MeSty, the difference can probably be attributed to the different propagating radicals between the rotating-sector method and our new peroxyl radical clock approach. Specifically, the chain-carrying species in the oxidation of 1,4-CHD under the rotating-sector method are mainly H-OO·

radicals, which is sterically unhindered and highly reactive, thus explaining the larger HAT rate constant (*204*).

It should be noted that our experimental k_H value for 1,4-CHD is on the same order of magnitude with the previous results in which the chain carrying species are also linoleate-based peroxyl radicals (*24, 205*). In addition, Howard and Ingold reported predominant contribution of the PRA mechanism into the propagation rate constants of 1,3-CHD, 1,2-dihydronaphthalene, and indene (*23, 203*). However, we found that the HAT mechanism contributes more significantly to the propagation step of 1,2-dihydronapthalene and indene, and both mechanisms contribute similarly to the propagation rate constant of 1,3-CHD. This discrepancy may be attributed to the fact that in the rotating-sector method, the H-atom abstracting species are polymeric peroxyl radicals, $R(OOR)_nOO\cdot$, derived from the substrate (*23*). Furthermore, the k_{add} values for 1,2-dihydronaphthalene and indene are on the same order of magnitude as those of the styrene derivatives reported here, suggesting consistency when using the radical clock method. Because of the different propagating radicals involved between the rotating-sector method and the peroxyl radical clock method, we suggest that the rate constants measured using the same method would provide better comparison of the reactivity of the oxidizable molecules.

2.2.4 Examination of Reactivities of Biologically Important Lipids

The value of k_p, k_H, and k_{add} for different biologically important lipids including sterols, lipophilic vitamins, and PUFAs were also measured using the new peroxyl radical clock and reported in **Table 2.3** (**Figure 2.2f).** Due to the low solubility of cholesterol in benzene and hexane, which caused difficulties in both the experimental setup and product analyses, we opted to use its ester analog, cholesteryl acetate, as the substrate instead. Even though cholesteryl acetate is more reactive toward free radical oxidation than cholesterol, their product distribution was reported to

be the same (*191*). The k_p values of cholesteryl acetate and 7-DHC measured by the new radical clock are 36 and 2737 M^{-1} s^{-1}, respectively. Both values are close to the previously reported values of 31.4 and 2260 M^{-1} s^{-1}, which were measured using the original peroxyl radical clock method (*25, 191*). These results validate the applicability of the new approach in examining the rate constants of lipid peroxidation.

We found the HAT mechanism to be predominant in cholesteryl acetate, which is consistent with the previous finding that cholesterol addition products only account for 12% of the total oxidation products (*191*). Due to the conjugated double bonds in the structure of 7-DHC, we expected to observe significant contribution from the PRA mechanism into the overall rate constant. However, surprisingly, we found 7-DHC to also be k_H dominant. In addition, coenzyme Q10 and lipophilic vitamins such as vitamin D_3 and retinal were all found to be highly reactive toward free radical oxidation with k_p values of 695, 1031, and 5656 M^{-1} s^{-1}, respectively. Significantly, the k_p value of retinal suggested that this compound would replace 7-DHC as the most reactive biological compound toward free radical oxidation known to date. All three compounds were found to have major contribution from the PRA mechanism, which can be attributed to their highly conjugated double bond systems. Likely due to the presence of a tertiary allylic H-atom, vitamin D_3 also has significant contribution from HAT.

We then examined the propagation rate constants of different PUFAs, including CLA 18:2, CLA 18:3, and NLA 18:3. As observed in 1,3-CHD and 1,4-CHD, conjugated PUFAs, including CLA 18:2 and CLA 18:3, have significant contribution from the PRA mechanism while nonconjugated PUFAs such as NLA 18:3 are k_H dominant. To our surprise, conjugated PUFAs appeared to be much more reactive towards lipid peroxidation compared to their nonconjugated analogs. For example, the total propagation rate constants for linoleic acid and CLA 18:2 are 62

and 118 M^{-1} s^{-1}, respectively. Similarly, CLA 18:3 was found to be highly reactive with a k_p value of 1235 M^{-1} s^{-1} compared to the k_p value of 144 M^{-1} s^{-1} for NLA 18:3.

2.3 Discussion

2.3.1 Factors Controlling the Contribution of the HAT and PRA Reactions to the Overall Propagation Step.

In this study, we report the development of a new peroxyl radical clock approach that, for the first time, simultaneously measures the rate constants of the HAT and PRA reactions for a variety of organic and lipid substrates. The structure-reactivity relationship studies through the application of this new approach has allowed us to derive five important factors that influence how each mechanism would contribute to the rate-limiting step of the free radical oxidation mechanism.

(1) *Radical stabilization effects are more important than polar effects in influencing the reactivities of PRA reaction.* Through the application of the new peroxyl radical approach to measure the k_{add} values of *para*- and *meta*-substituted styrene derivatives, we found that only substituents that allow the delocalization of electron spin via either resonance or hyperconjugation would significantly enhance the reactivities of PRA reactions. This observation is consistent with previously reported results that radical stabilization effects are more important than polar effects in influencing the stability of ring-substituted benzylic radicals (*200, 206, 207*). In addition, we found that the experimental k_{add} values and the computed activation energies of styrene and its *para*-substituted derivatives agreed better with the computed spin density than the atomic polar tensor charge distribution at the benzylic carbon as seen in **Table 2.1** and **Figure 2.9a, b.** Another example for the trend observed here is coenzyme Q10. Specifically, the methoxy moiety, which is an electron-donating substituent, can stabilize the radicals formed after the PRA reaction at C2 or C3 via resonance (**Figure 2.14a**). Computational modeling of the transition state of peroxyl radical

addition to C2 indicates that the methoxy group, C2, and C3 appear to be in the same plane in the transition state (**Figure 2.15**). On the other hand, the radicals formed after the addition of the peroxyl radical into any vinylic carbons can be delocalized into the carbonyl moiety, which is an electron-withdrawing substituent (**Figure 2.14b**). Thus, the large k_{add} value of coenzyme Q10 is further evidence that for PRA mechanism, radical stabilization effects are more important than polar effects.

The small changes in both the measured rate constants and computed activation energies of the *meta*-substituted styrenes supported our observation that polar effects do not contribute significantly to the PRA mechanism. In the transition state of the addition of peroxyl radical to styrene, there is a development of both radical characteristic and partial positive charge at the benzylic carbon. Therefore, we employed the extended Hammett equation to derive a linear correlation between the computed activation energies and substituents effects via the dual radical-cationic Hammett parameters (**Figure 2.9c**). The negative slope of -1.04 confirmed the predicted reaction mechanism.

(2) *PRA mechanism only contributes significantly to the overall propagation rate constant in structures with conjugated double bond systems, and the more conjugated the system is, the larger the increase in the total rate constant.* As an example, due to its conjugated double bond system, 1,3-CHD has significant contribution from the PRA mechanism in addition to the HAT reaction, and, thus, is much more reactive towards lipid peroxidation compared to its isomer 1,4-CHD, which is k_H dominant. The same trend was also observed in other pairs of isomers investigated in this study, such as NLA and CLA.

One of the most surprising, and important findings, in this study is how considerably more reactive the conjugated double bond structures are compared to the non-conjugated structures. For

example, the total propagation rate constant measured for CLA 18:3 is ten times higher than NLA 18:3, which is due to the combination of both PRA and HAT reactions. In addition, compounds that contain three conjugated double bonds, such as vitamin D_3 and CLA 18:3, have k_p values of over 1000 M^{-1} s^{-1} with significant contribution from both mechanisms. Significantly, retinal has a conjugated system with five double bonds and thus, has a propagation rate constant of almost 5700 M^{-1} s^{-1}, which is the largest rate constant measured for a lipid molecule to date.

To fully understand how reactive the conjugated double bond structures are, we compared the increase in the propagation rate constants of different nonconjugated and conjugated PUFAs (**Figure 2.16**). Nonconjugated PUFAs such as arachidonic acid, eicosapentaenoic acid, and docosahexaenoic acid are commonly considered highly reactive fatty acids. Their reactivities toward HAT reaction are attributed to the number of bis-allylic positions due to the weaker C-H bonds at these positions (*202, 208, 209*). Thus, the ratio of the rate constants for linoleic acid, NLA 18:3, arachidonic acid, eicosapentaenoic acid, and docosahexaenoic acid is roughly 1:2:3:4:5, which is proportional to the number of their bis-allylic positions. However, this increase in rate constant is much larger for the conjugated double bond systems. For example, CLA 18:3 has only one more double bond than CLA 18:2, but the difference in their propagation rate constants is ten times. Based on the result of retinal, we estimated that a structure with five conjugated double bonds would have a k_p value of roughly 6000 M^{-1} s^{-1} and a structure with four conjugated double bonds would have a rate constant in between 1235 and 6000 $M^{-1}s^{-1}$.

(3) *Mono-allylic positions that are adjacent to conjugated double bond system are reactive towards HAT reaction.* Mono-allylic H-atoms in acyclic structures are commonly believed to be less susceptible to abstraction compared to those at bis-allylic positions. However, once the values of k_{add} and k_H are distinguished for conjugated PUFAs using the new peroxyl radical clock, we

found that mono-allylic positions that are adjacent to a highly conjugated double bond system are also highly reactive toward HAT reactions. For example, when there is an increase in number of double bonds from CLA 18:2 to 18:3, there is a 6-fold increase in k_H values, though to a lesser extent than the increase in k_{add} values (14-fold). Our results are, in fact, consistent with the findings that C-H BDEs decreases with extended conjugation of lipids (*202*). Specifically, the lowest theoretical C-H BDEs calculated for lipids with two and three conjugated double bonds were 77.4 and 72.9 kcal/mol, respectively, comparable to the bis-allylic C-H bond BDE at 72.7 kcal/mol (*202*).

(4) *Cyclic compounds are more reactive toward lipid peroxidation than their acyclic analogs but their k_{add}/k_H ratios are the same.* The trend that cyclic compounds are more reactive toward lipid peroxidation than their acyclic analogs has previously been discussed (*4*). Indeed, we found that 1,3-CHD has a much larger k_p value compared to 1,3-hexadiene and CLA 18:2. However, after measuring the individual k_{add} and k_H, we found that all three compounds have almost the same ratio k_{add}/k_H of one. This indicates that both k_H and k_{add} values are larger in the cyclic compounds than their acyclic analogs.

(5) *Steric hindrance and the location of the substituents can potentially affect the reactivity of PRA mechanism*. Despite the opposite polar transition state, factors that affect the reactivities of carbon-radical addition to alkenes can also be applied to PRA to alkenes. The first factor is steric hindrance which can potentially dictate the regioselectivity of both reactions. Specifically, it was found that carbon radicals, and potentially peroxyl radicals, attack alkenes preferentially at carbon atoms which are the least sterically hindered (*197*). The second factor is the location of the substituents. In the addition of carbon radical to alkenes, it was found that a substituent that is bound to the α carbon, where the radical is added to, exerts markedly different effects compared

to a substituent attached to the neighboring carbon (the β carbon) (*197*), *i.e*., the β-substituent only exerts a polar effect on the rate constant while the α-substituent mostly exerts both polar and steric effects, but the polar effect is less than that of the β-substituent. Therefore, we propose that the same principle can be applied to the reaction between peroxyl radical and alkenes. In fact, even though 1,3-hexadiene, 2,4-hexadiene, and 3-methyl-1,3-pentadiene all have an additional methyl group compared to 1,3-pentadiene, only 2,4-hexadiene and 3-methyl-1,3-pentadiene have a substantial increase in k_{add} due to the polar effect of the additional methyl group on the conjugated double bonds. Replacing the methyl with an ethyl group in 1,3-hexadiene and addition of a methyl on the other end of the alkene in 2,4-hexadiene resulted in substantial k_H, but addition of the methyl at the cross-conjugation position of the alkene in 3-methyl-1,3- pentadiene did not result in an observable k_H. Furthermore, addition of two more terminal methyl groups in 2,5-dimethyl-2,4-hexadiene resulted in large increases in both k_{add} and $k_{H.}$ On the other hand, the smaller k_{add} value of 2,4-dimethyl-1,3-pentadiene relative to 3-methyl-1,3-pentadiene is likely due to the steric hindrance at one of the terminal vinyl carbons. However, for this series of dienes overall, the steric effect appears to be less important than the radical-stabilizing effect of the additional substituents. Further investigation is required to examine whether bulkier substituent on the α-carbon could exert larger steric effect for the PRA reactions.

2.3.2 Limitations of the New Peroxyl Radical Clock Approach**.**

We found that there is a threshold to which the new peroxyl radical clock approach can distinguish between k_H and k_{add} values. Since a PRA-derived epoxide product, 7-DHC 5α,6α-epoxides, was previously detected among the oxidation products of 7-DHC (*12, 191, 192*), we predicted that there should be significant contribution from the PRA mechanism into the peroxidation of 7-DHC. However, our results showed that 7-DHC is k_H dominant. This finding is

surprising as we mentioned that structures with conjugated double bonds are expected to have a large k_{add} value. We attempted to resolve this conflict in results by investigating α-terpinene, a compound that shares a cyclic diene and a tertiary mono-allylic position to 7-DHC structure (**Figure 2.2e** and **Table 2.2**). In fact, the abstraction of H-atom from the tertiary mono-allylic position of α-terpinene would yield a highly stable carbon radical. This explains the large increase in both the total propagation and HAT rate constants compared to 1,3-CHD, which only has the cyclic diene in its structure.

Significantly, the k_{add}/k_H ratio also decreases from 0.95 in 1,3-CHD to 0.28 in α-terpinene. Compared to α-terpinene, 7-DHC has two tertiary mono-allylic positions, a much more rigid structure and well-aligned axial C-H bond with the π orbitals, which requires minimum reorientation of the molecule to reach the transition of HAT (*25, 192*). Thus, it is reasonable to see that 7-DHC displays a much larger k_H than α-terpinene. On the other hand, a cholestadienol with a similar substitution pattern as α-terpinene has a k_p of 1370 $M^{-1}s^{-1}$, similar to that of α-terpinene (*210*). Although there is contribution from the PRA mechanism into the total propagation rate constant of 7-DHC, the k_{add} value may be too small to be detected by the new radical clock, which relies on accurate determination of the k_{add}/k_H ratio. Similarly, even though 12% of the total oxidation products from cholesterol or cholesteryl acetate, were addition products (*191*), our new approach was not sensitive enough to measure k_{add} of this substrate. Therefore, we concluded that there is a threshold of k_{add}/k_H ratio at which the new radical clock approach can resolve the individual k_{add} and k_H values. In the case where the contribution from one mechanism is significantly less than the other, the new approach is not sensitive enough to resolve them. The lowest k_{add}/k_H ratio that we were able to measure in this study was 0.28 of α-terpinene.

Improvement on the new radical clock approach would be needed in the future to overcome this limitation.

2.4 Experimental Procedures

2.4.1 General Methods and Materials

The radical initiator, MeOAMVN, was purchased from Wako Chemicals, dried under vacuum, and stored at -80 ℃. MeLn (Nu-Chek-Prep, Inc.) was purified through silica gel (10% ethyl acetate: 90% hexane) prior to use and stored at -80 ℃. Sty, 4-MeSty, 4-MeOSty, 4-ClSty, 4-FSty, 3-MeSty, 3-MeOSty, 3-ClSty, α-MeSty, (*trans*-)β-MeSty, 1,3-pentadiene, 3-methyl-1,3-pentadiene, 2,4-dimethyl-1,3-pentadiene, 1,3-hexadiene, 2,4-hexadiene, 2,5-dimethyl-2,4-hexadiene, 1,2-dihydronaphthalene, indene, 2-methylindene, and α-terpinene were purchased from Sigma-Aldrich Co. and were purified through a short Al_2O_3 column to remove stabilizers such as 4-*tert*-butylcatechol prior to use. 4-NO_2Sty was purchased from Thermo Fisher Scientific Inc., stored at -20 ℃, and was purified through a column to remove stabilizers prior to use. 7-DHC was purchased from Sigma-Aldrich Co., stored at -20 ℃, and purified through silica gel column prior to use. Cholesterylacetate was purchased from Thermo Fisher Scientific Inc. and used without further purification. Retinal, coenzymeQ10, and Vitamin D_3 were purchased from Chem-Impex Int'l Inc. and used without further purification. CLA 18:2 and NLA 18:3 were purchased from Nu-Chek-Prep, Inc. and used without further purification. 9(E),11(E),13(E)-CLA 18:3 was purchased from Cayman Chemical and used without further purification. The internal standard, 9-anthracenemethanol, was purchased from Sigma-Aldrich Co. $LiAlH_4$ (1 M in THF) was purchased from Sigma-Aldrich Co. Benzene (HPLC grade) was passed through a column of neutral alumina prior to use. HPLC grade hexanes and isopropanol were purchased from Thermo Fisher Scientific Inc.

2.4.2 General Procedure for the New Peroxyl Radical Clock Approach Using Methyl Linoleate

The initial experimental set up for the new approach is similar to the conventional peroxyl radical clock method (*24*). Briefly, for each reaction, stock solution of the substrate at various amount was added first to each reaction vial. Then, the same amount of stock solution of MeLn in benzene, an adjusted amount of benzene, and the same amount of stock solution of MeOAMVN in benzene were added to bring the final reaction volume in each vial to 300 μL. The final concentrations of MeLn and MeOAMVN are 0.302 M and 1.5 mM, respectively. Each reaction was carried out at 37 ℃ for an hour and then quenched by adding butylated hydroxytoluene (50 μL, 0.2 M in benzene) and 9-anthracenemethanol (6 μL, 3 mM in chloroform). The resulting mixture was vortexed for 5 seconds and left at room temperature for 30 minutes before splitting into two portions of the same volume. The first portion is diluted with 1 mL hexane for the analysis of HPODEs by HPLC-UV (Phenomenex Luna 4.6x150 mm Si column; 3 μm particle size; 1.0 ml/min; eluting solvent, Hex:Iso = 99.5:0.5). The other half of the reaction mixture was reduced by the addition of $LiAlH_4$ (90 μL, 1 M in THF). The mixture was then vortexed for 5 seconds, left at room temperature for 15 minutes, and quenched by the addition of concentrated HCl (20 μL). The final reaction mixture was diluted with 1 mL hexane, followed by filtration with Teflon syringe filter, for the analysis of HODOLs by HPLC-UV with eluting solvent of Hex:Iso = 95.5:4.5 using the same column. The measurement of rate constants for each substrate is performed in triplicates. The peak areas for HPODEs and HODOLs were integrated at 234 nm. In addition, the peak areas for the internal standard were integrated at 254nm. The ratio [*tc*-HODOLs]/[*tt*-HODOLs] is calculated as below:

$$\frac{[t,c-\text{HODOLs}]}{[t,t-\text{HODOLs}]}=\frac{(\text{total areas under all } t,c-\text{HODOLs})}{(\text{total areas under all } t,t-\text{HODOLs})}$$

The ratio $[HODOL_{total}]/[HPODE_{total}]$ is calculated as below:

$$\frac{[\mathrm{HODOL_{total}}]}{[\mathrm{HPODE_{total}}]} = \frac{(\text{total areas under all HODOLs})/(\text{total area of internal standard})}{(\text{total areas under all HPODEs})/(\text{total area of internal standard})}$$

2.4.3 General Procedure for Free Radical Oxidation of 7-DHC with the New Peroxyl Radical Clock Approach.

The oxidation, reduction, and HPLC-UV analysis for 7-DHC were carried out similarly as described above. However, the stock solution of 7-DHC was prepared in solvent mixture of equal amount of chlorobenzene and benzene (chlorobenzene:benzene = 1:1). The reaction was also carried out in chlorobenzene:benzene to increase the solubility of 7-DHC.

2.4.4 General Procedure for Free Radical Oxidation of Retinal with the New Peroxyl Radical Clock Approach.

The oxidation, reduction, and HPLC-UV analysis for retinal were carried out similarly as described above, but the experiment was carried out in only 30 minutes instead of one hour.

2.4.5 General Procedure for Free Radical Oxidation of NLA 18:2, CLA 18:2, and CLA 18:3 with the New Peroxyl Radical Clock Approach.

The oxidation, reduction, and HPLC-UV analysis for NLA 18:2, CLA 18:2, and CLA 18:3 were carried out similarly as described above. However, the -OOH moiety in these three fatty acids give a broad peak in the HPLC chromatograms that overlaps with the HPODEs product peaks. Therefore, to avoid this overlapping, the non-reduced reaction mixture of these three compounds was analyzed using eluting solvent of Hex:Iso = 99.864:0.136.

2.4.6 Preparation of HODOLs

A large-scale autoxidation was carried out using 5 g of methyl linoleate and 5 mol% of MeOAMVN at 37 °C. The product mixture was then quenched by addition of BHT and then reduced with $LiAlH_4$ at 0 °C. After quenching excess amount of $LiAlH_4$ with concentrated HCl, the solution was neutralized by addition of saturated $NaHCO_3$ solution until there is no bubble.

The resulting solution was then extracted with methylene chloride and ethyl acetate and concentrated. The product mixture was then first purified by flash column chromatography to enrich HODOL-containing fractions and remove majority of reduced methyl linoleate. Part of the HODOL mixture was then subject to purification by HPLC (250 x 10 mm Si column; 5 μm; 6 mL/min; eluting solvent, Hex:Iso = 95.5:4.5) to obtain individual HODOLs. Ag^+-coordination electrospray ionization analysis of individual HODOLs on a high-resolution QTOF mass spectrometer (Waters Synapt XS) revealed expected doublets due to the isotopes of Ag (^{107}Ag and ^{109}Ag) (**Figure 2.17**).

13-trans,trans-HODOL. ^{1}H NMR ($CDCl_3$, 300 MHz): 0.88 (t, 3H, J = 6.8 Hz), 1.30 and 1.56 (br s, 20H), 2.07 (q, 2H, J = 6.9 Hz), 3.64 (t, 2H, J = 6.6 Hz), 4.11 (q, 1H, J = 6.5 Hz), 5.57 (dd, 1H, J = 7.0 and 15.1 Hz), 5.70 (dt, 1H, J = 7.2 and 14.9 Hz), 6.02 (dd, 1H, J = 10.4 and 15.0 Hz), 6.17 (dd, 1H, J = 10.4 and 15.2 Hz). ^{13}C NMR ($CDCl_3$, 500 MHz): 14.06, 22.62, 25.15, 25.72, 29.09, 29.19, 29.36, 29.41, 31.81, 32.63, 32.81, 37.33, 63.10, 72.93, 129.50, 130.96, 133.69, 135.51. HRMS $[M+^{107}Ag]^+$ ($C_{18}H_{34}AgO_2$): observed, 389.1652; theoretical, 389.1604. UV-vis: λ_{max} (in hexanes) = 230.9 nm.

9-trans,trans-HODOL. ^{1}H NMR ($CDCl_3$): ^{1}H NMR ($CDCl_3$, 300 MHz): 0.89 (t, 3H, J = 6.8 Hz), 1.31 and 1.56 (br s, 20H), 2.07 (q, 2H, J = 6.9 Hz), 3.64 (t, 2H, J = 6.6 Hz), 4.10 (q, 1H, J = 6.5 Hz), 5.57 (dd, 1H, J = 7.0 and 15.0 Hz), 5.70 (dt, 1H, J = 7.2 and 14.9 Hz), 6.02 (dd, 1H, J = 10.4 and 14.9 Hz), 6.17 (dd, 1H, J = 10.4 and 14.9 Hz). ^{13}C NMR ($CDCl_3$, 500 MHz): 14.06, 22.54, 25.43, 25.72, 28.93, 29.36, 29.50, 29.52, 31.43, 32.63, 32.81, 37.33, 63.10, 72.91, 129.42, 131.01, 133.61, 135.66. HRMS $[M+^{107}Ag]^+$ ($C_{18}H_{34}AgO_2$): observed, 389.1652; theoretical, 389.1604. UV-vis: λ_{max} (in hexanes) = 230.9 nm.

13-trans,cis-HODOL. HRMS $[M+^{107}Ag]^+$ ($C_{18}H_{34}AgO_2$): observed, 389.1639; theoretical, 389.1604. UV-vis: λ_{max} (in hexanes) = 234.4 nm.

9-trans,cis-HODOL. HRMS $[M+^{107}Ag]^+$ ($C_{18}H_{34}AgO_2$): observed, 389.1644; theoretical, 389.1604. UV-vis: λ_{max} (in hexanes) = 234.4 nm.

2.4.7 Computational Method

All geometry optimization as performed using the Gaussian 16 software with the hybrid density functional B3LYP and the 6-31++G(d,p) basis. Transition state optimization and calculations, including activation energies, spin densities, and atomic polar tensor charge distribution, was carried out also using the B3LYP/6-31++G(d,p) with QST2 method. The activation energies were calculated by deducting the sum of total energies (electronic + thermal free energies) of styrene derivatives and methyl peroxyl radicals from the total energies (electronic + thermal free energies) of the transition state.

Figures

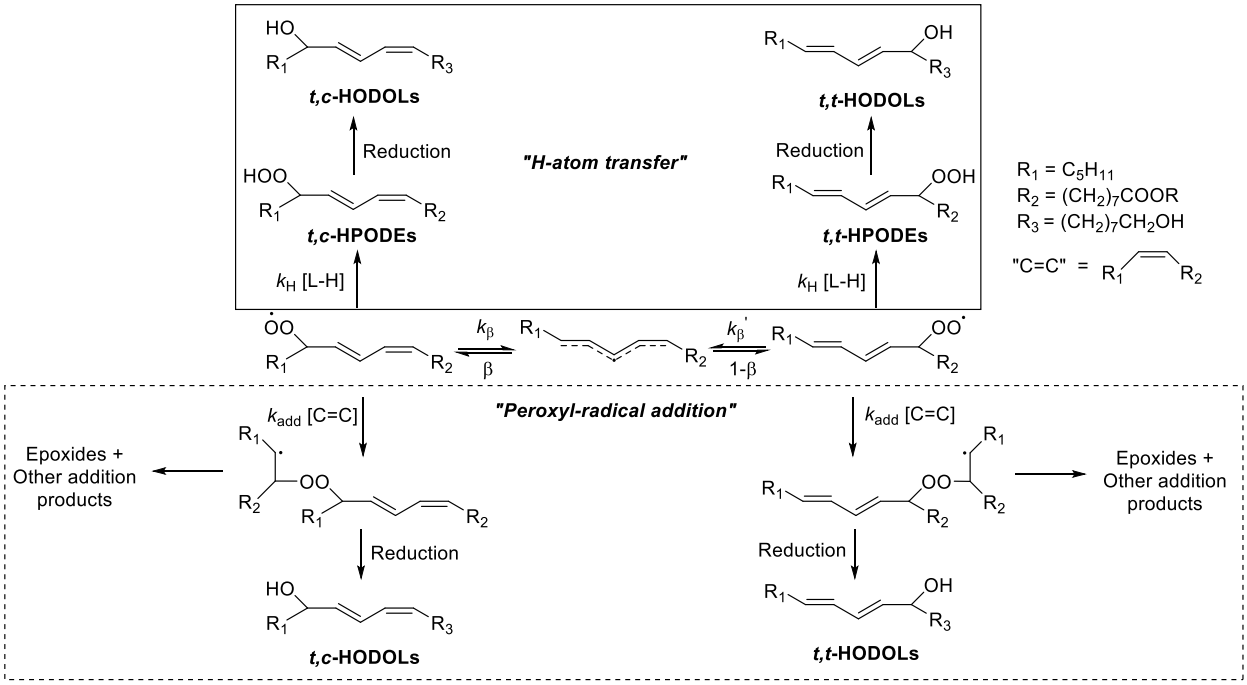

Figure 2.1 Linoleate peroxyl radical clock in the presence of both HAT and PRA reactions.

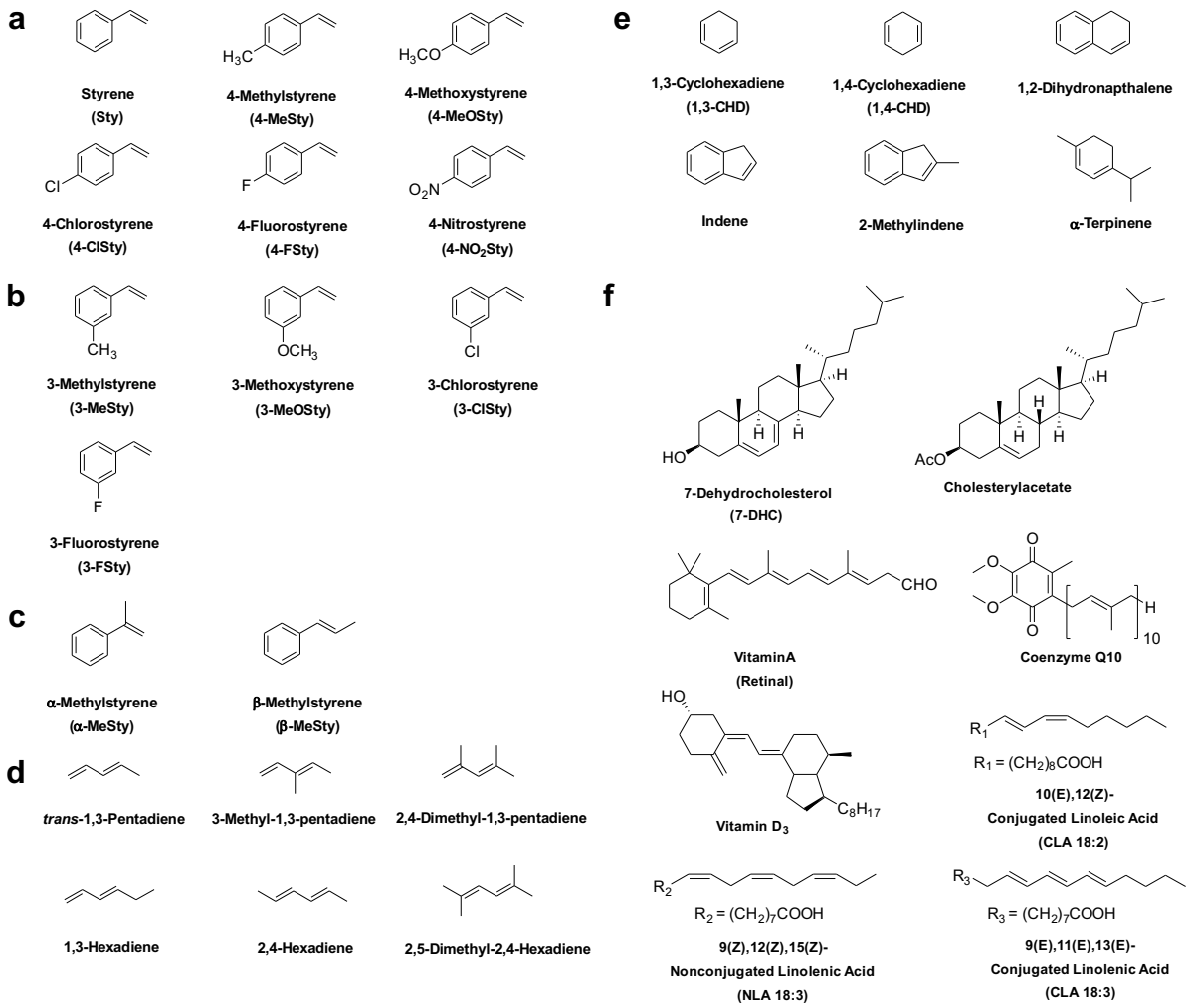

Figure 2.2 The series of substrates that are examined in this study are (a) styrene and its *para*-substituted derivatives, (b) *meta*-substituted styrene derivatives, (c) conjugated styrenes with methyl substituent at the α- and β-position, (d) conjugated dienes with different methyl substituents, (e) cyclic compounds, and (f) biologically important lipids.

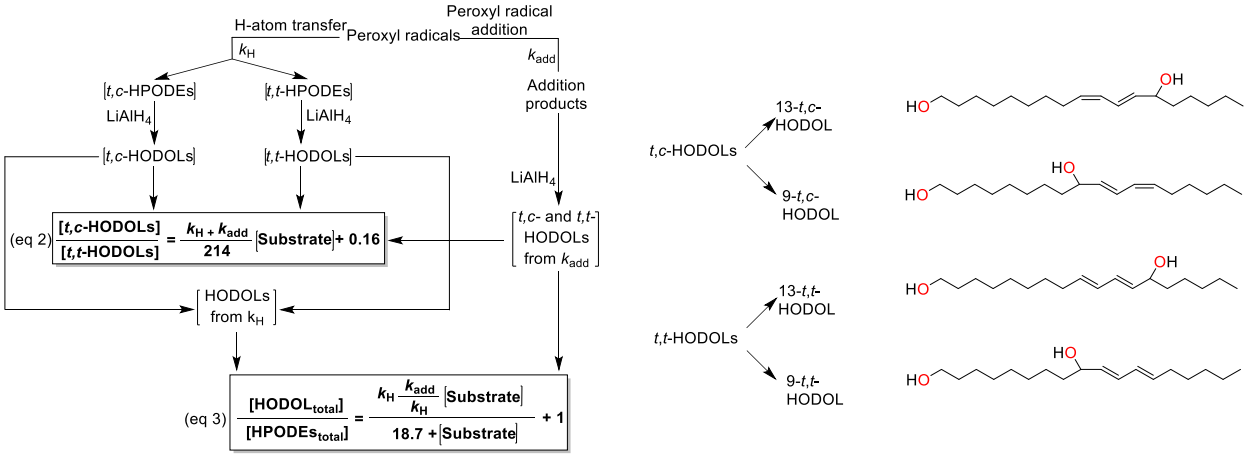

Figure 2.3 Proposed new radical clock approach and the structures of 13-*tc*-, 9-*tc*-, 13-*tt*-, and 9-*tt*-HODOL. (HPODE: hydroperoxyoctadecadienoic acid, or non-reduced products from HAT reaction; HODOL: hydroxyoctadecadienol, or reduced products from both HAT and PRA reactions; *tc: trans,cis; tt: trans,trans*; k_H: HAT rate constant; k_{add}: PRA rate constant).

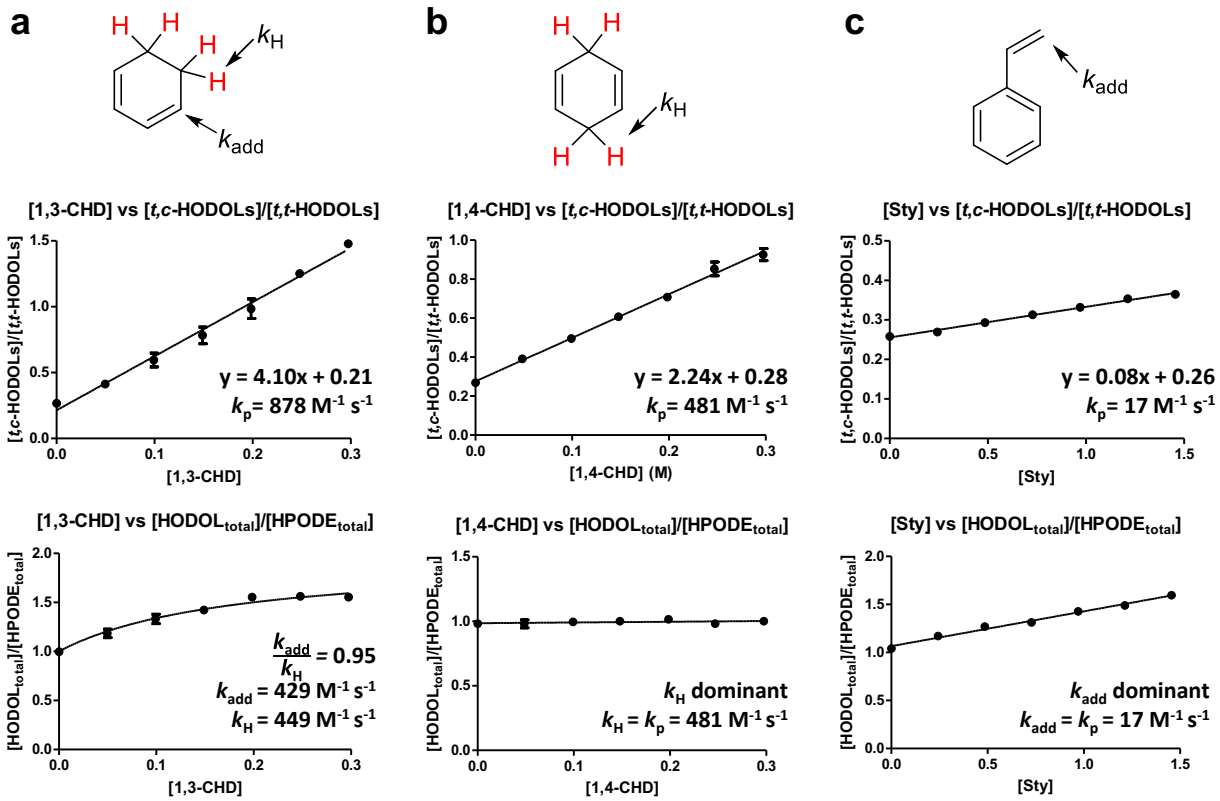

Figure 2.4 The determination of k_H and k_{add} for a substrate that can undergo (a) both reactions, (b) HAT reaction only, and (c) PRA reaction only. Here, the k_p value is calculated using the slope of the [Substrate] vs [tc-HODOLs]/[tt-HODOLs]. The ratio k_{add}/k_H is generated from the fitting of [Substrate] vs [HODOLtotal]/[HPODEtotal] plot using Prism. The measurement for each substrate was performed in triplicates.

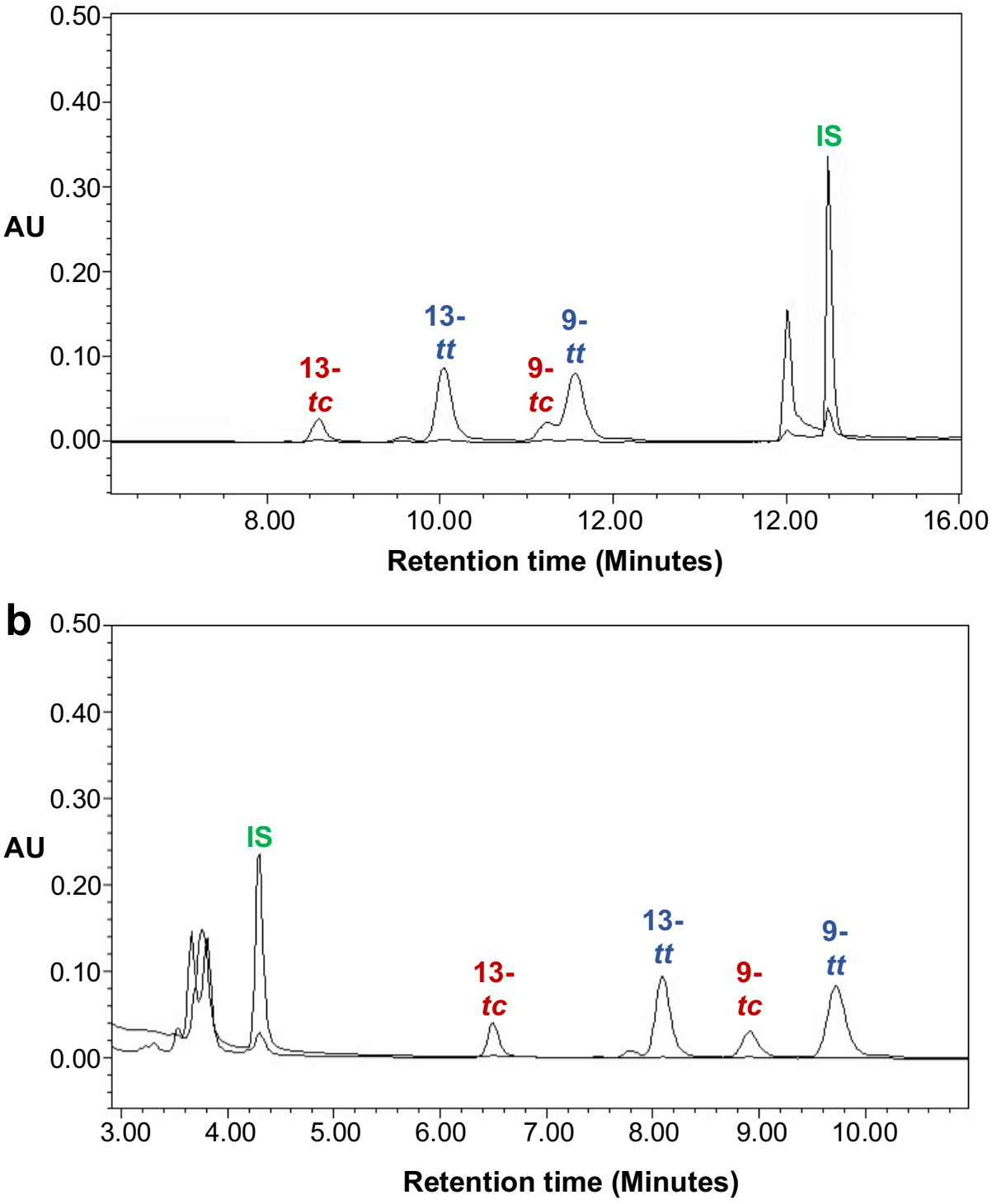

Figure 2.5 HPLC chromatogram at 234 nm for the (a) HPODE and (b) HODOL products eluting with solvent hexane:isopropanol = 99.5:0.5 and 95.5:4.5, respectively. The internal standard peak was monitored at 254 nm.

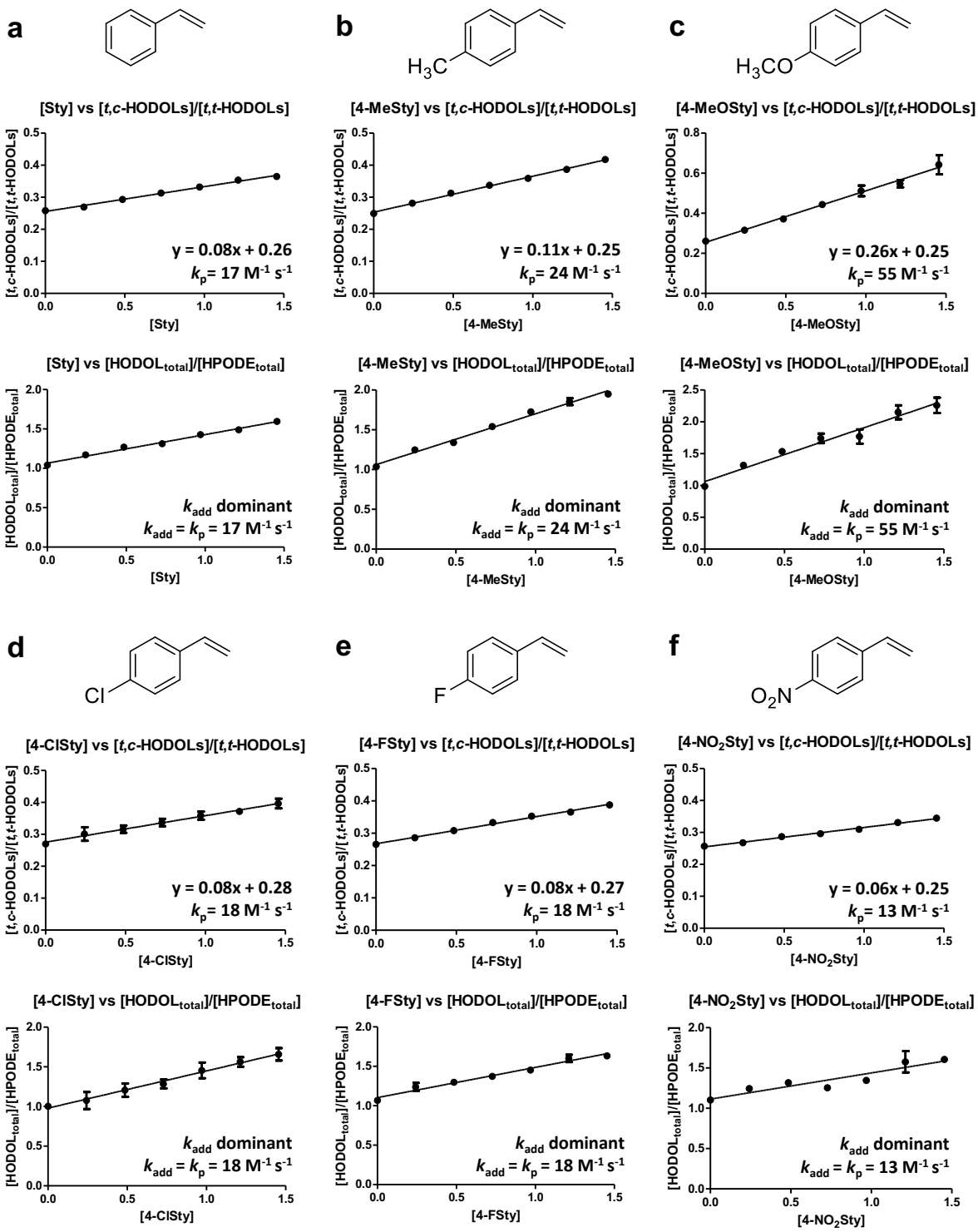

Figure 2.6 The determination of k_{add} for Sty and its *para*-substituted derivatives, including (a) Sty, (b) 4-MeSty, (c) 4-MeOSty, (d) 4-ClSty, (e) 4-FSty, and (f) 4-NO_2Sty.

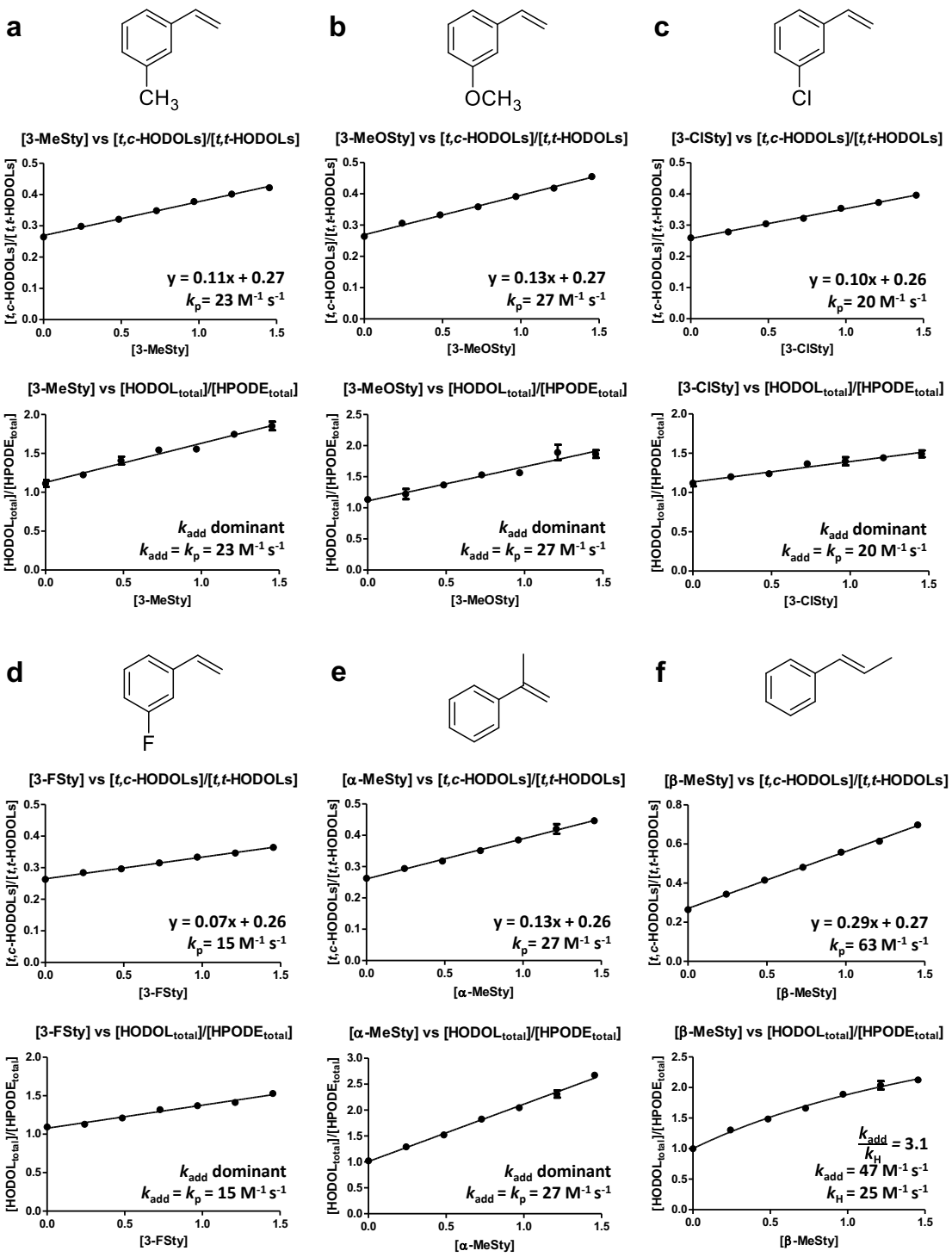

Figure 2.7 The determination of k_{add} for *meta*-substituted styrene derivatives, including (a) 3-MeSty, (b) 3-MeOSty, (c) 3-ClSty, and (d) 3-FSty, and of k_{add} and k_H for substituted conjugated styrene, including (e) α-MeSty and (f) β-MeSty.

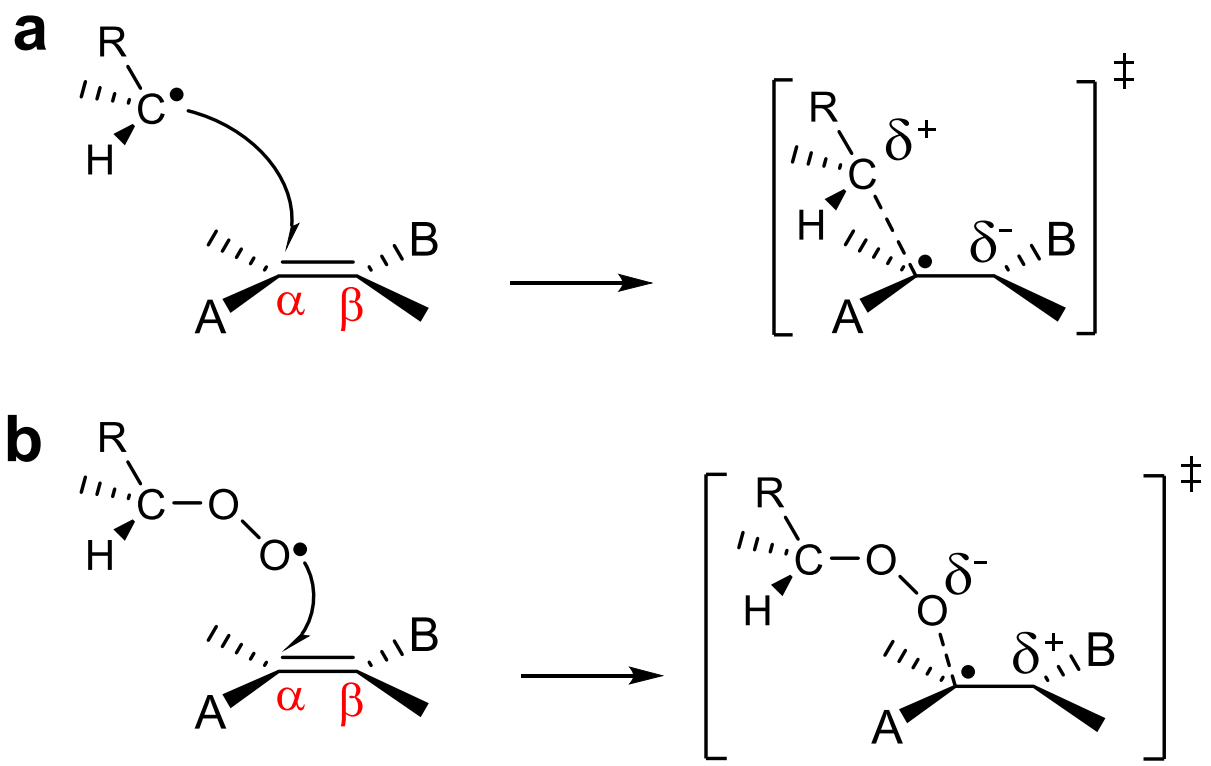

Figure 2.8 Comparison of the polar transition state between (a) carbon radical and (b) peroxyl-radical to an alkene.

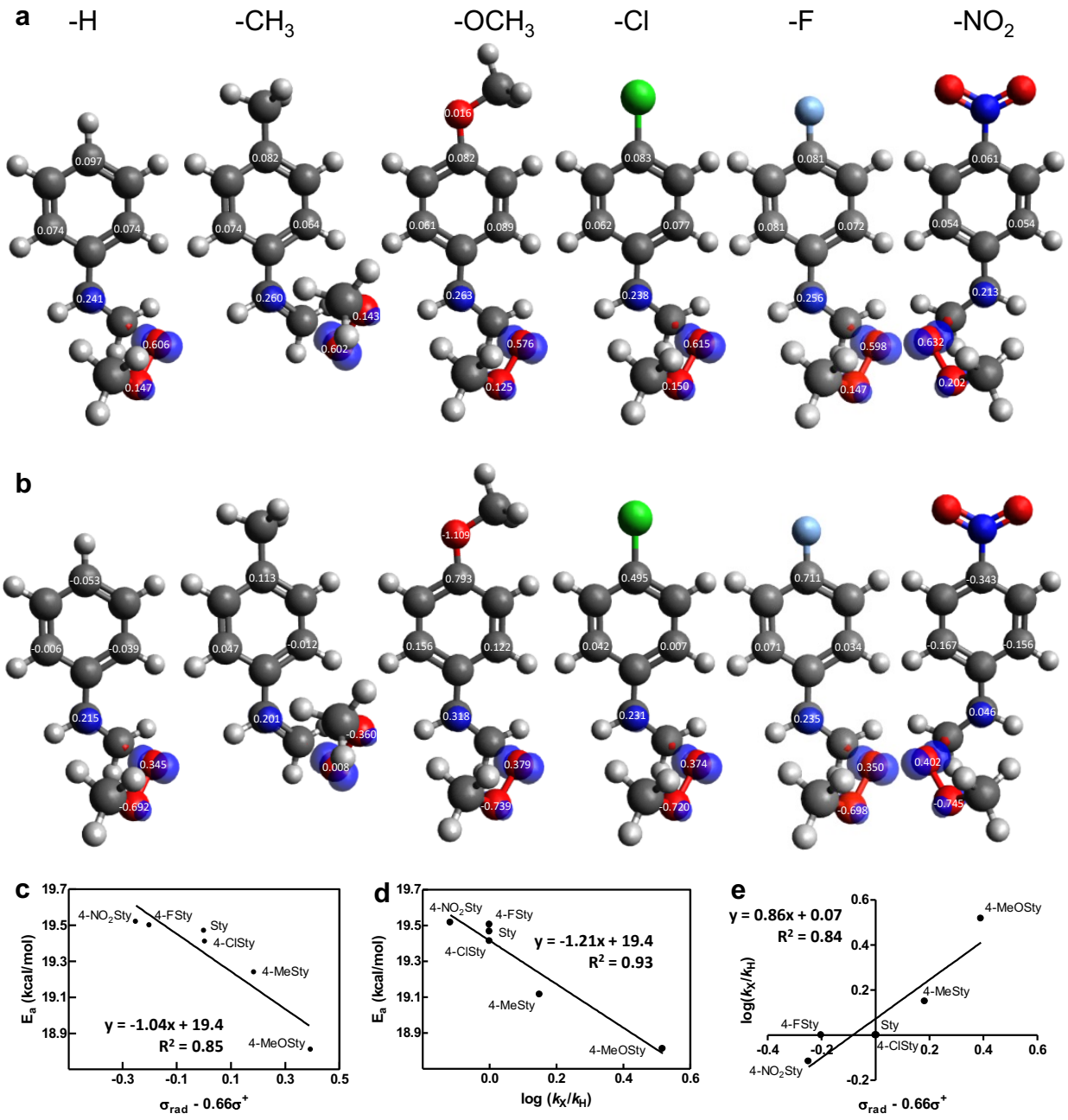

Figure 2.9 (a) Spin density, and (b) atomic polar tensor charge distribution during the transition state; activation energies versus (c) the combination of radical and cation Hammett parameters or (d) log(k_X/k_H), and (e) log(k_X/k_H) versus the combination of radical and cation Hammett parameters for the addition reaction between peroxyl radical and *para*-substituted styrene derivatives.The atoms displayed are carbon (dark grey), hydrogen (light gray), oxygen (red), chlorine (green), fluorine (light blue), and nitrogen (dark blue).

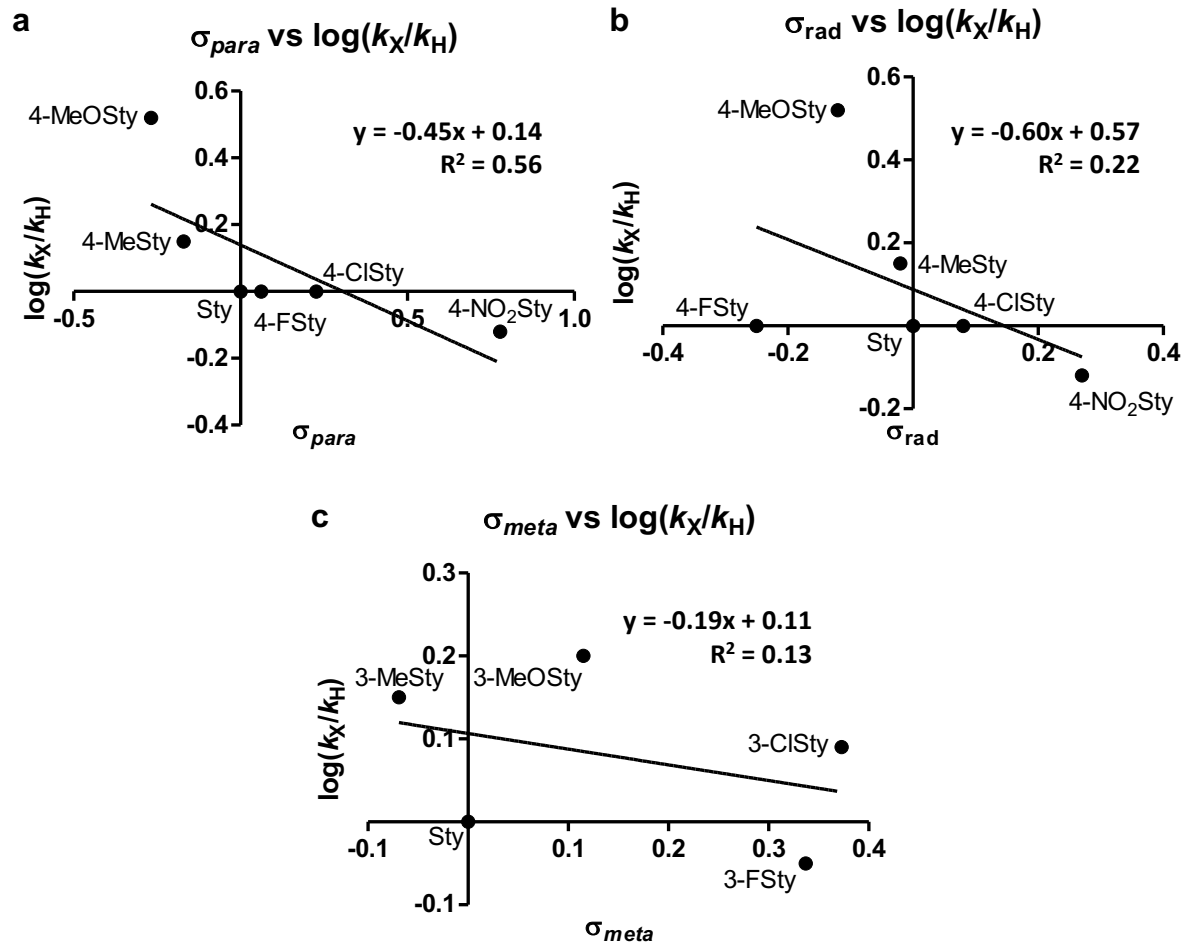

Figure 2.10 Hammett plots using (a) σ_{para} and (b) σ_{rad} for *para*-substituted styrene derivatives and (c) σ_{meta} for *meta*-substituted styrene derivatives.

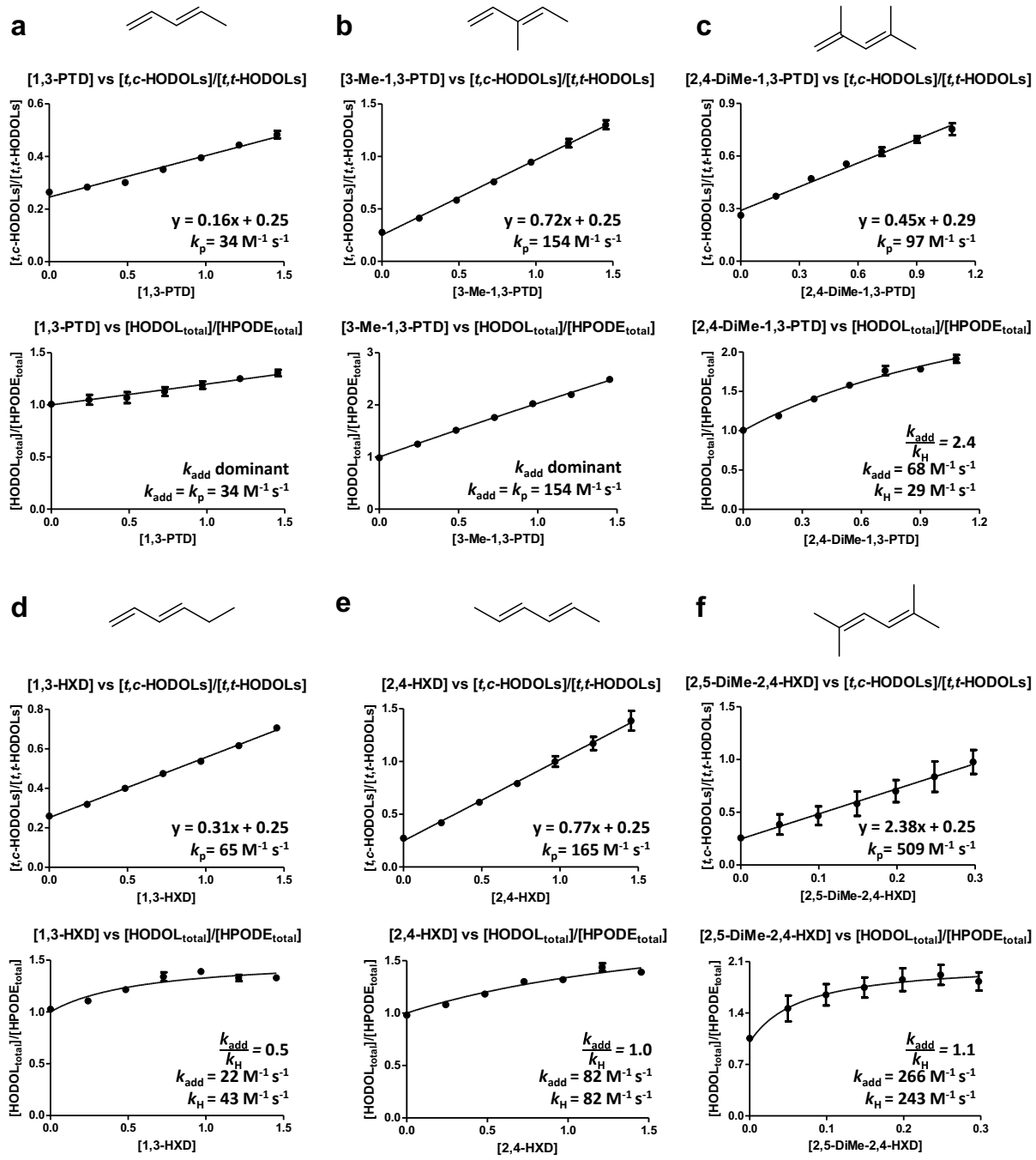

Figure 2.11 The determination of k_{add} and k_H for conjugated dienes, including (a) 1,3-PTD, (b) 3-Me-1,3-PTD, (c) 2,4-DiMe-1,3-PTD, (d) 1,3-HXD, (e) 2,4-HXD, and (f) 2,5-DiMe-2,4-HXD.

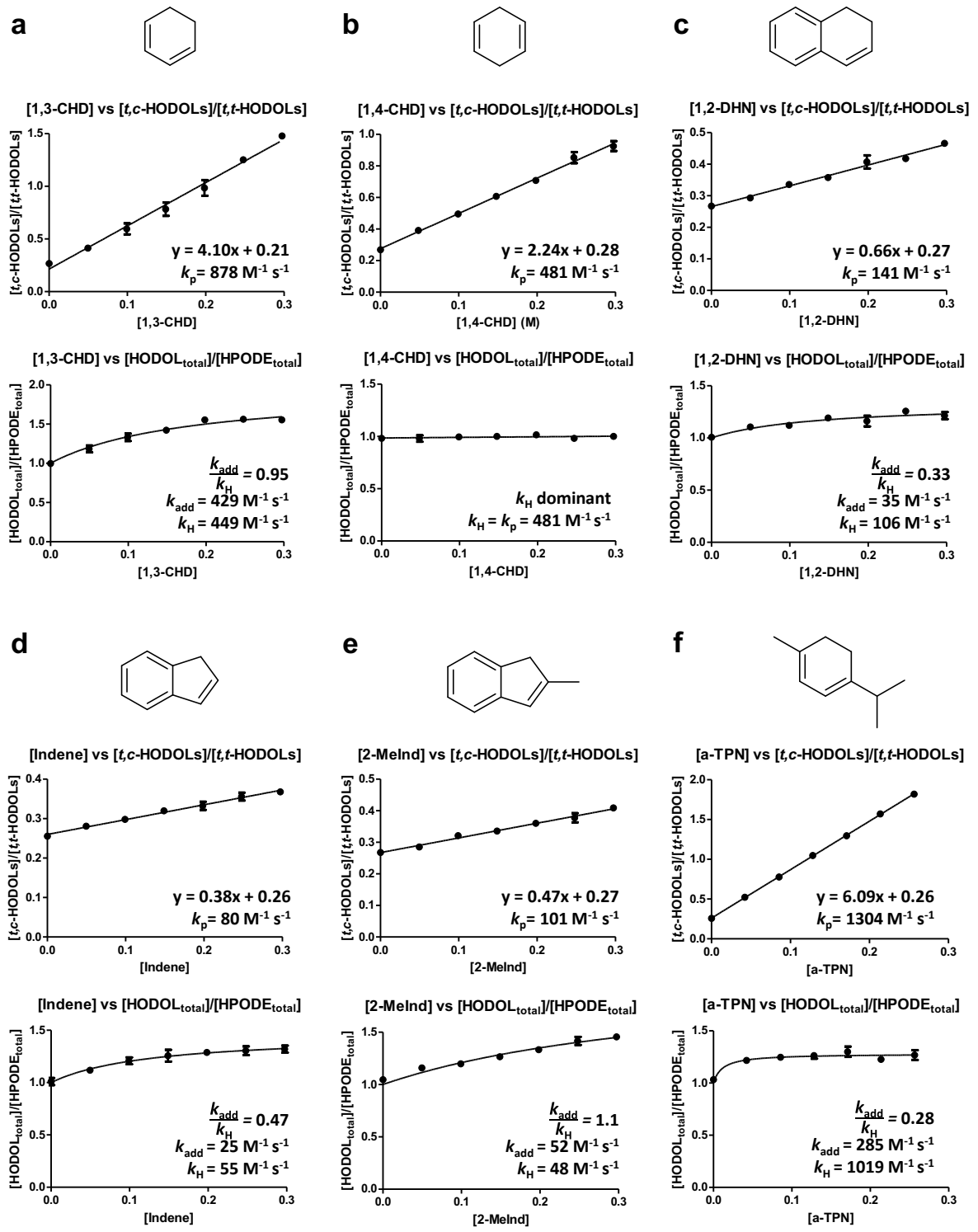

Figure 2.12 The determination of k_{add} and k_H for cyclic compounds, including (a) 1,3-CHD, (b) 1,4-CHD, (c) 1,2-DHN, (d) Ind, (e) 2-MeInd, and (f) α-TPN.

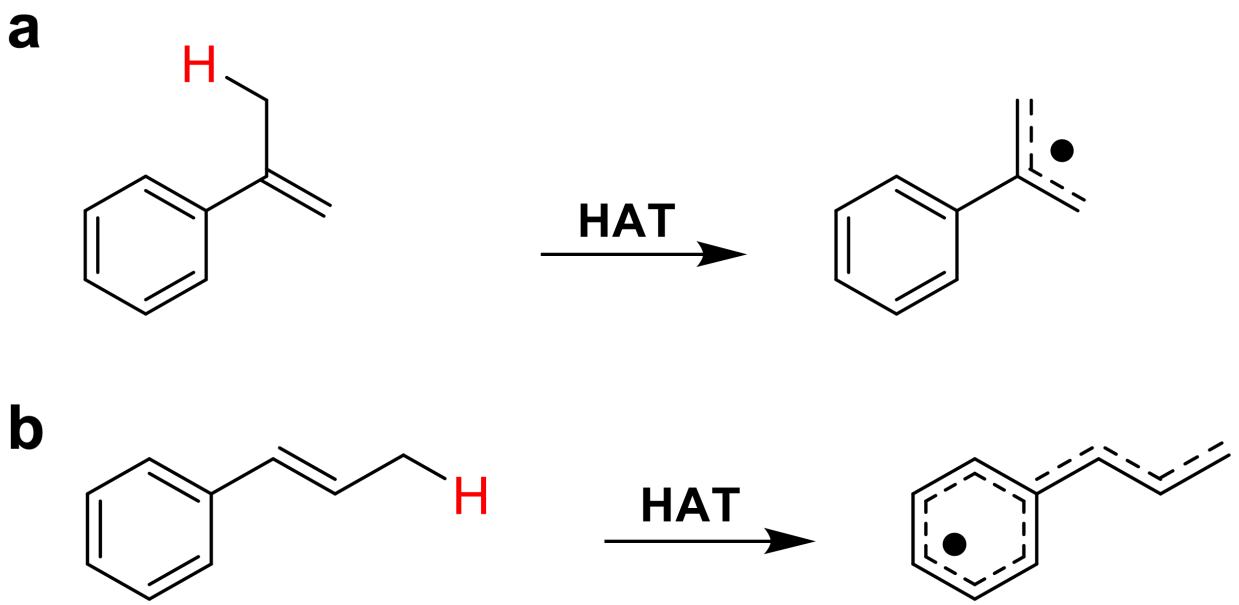

Figure 2.13 Proposed resulting carbon-radicals formed after the HAT reactions from (a) α-MeSty and (b) β-MeSty.

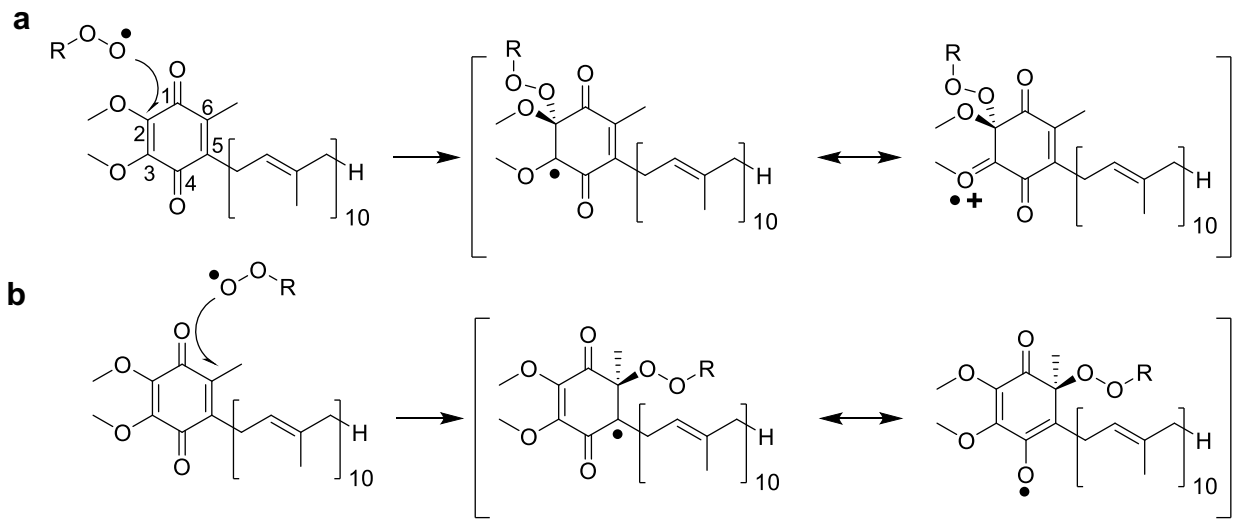

Figure 2.14 Resonance stabilization of radicals formed after the PRA reaction in coenzyme Q10 by (a) methoxy, an electron-donating substituent, and (b) alkoxyl, an electron withdrawing substituent.

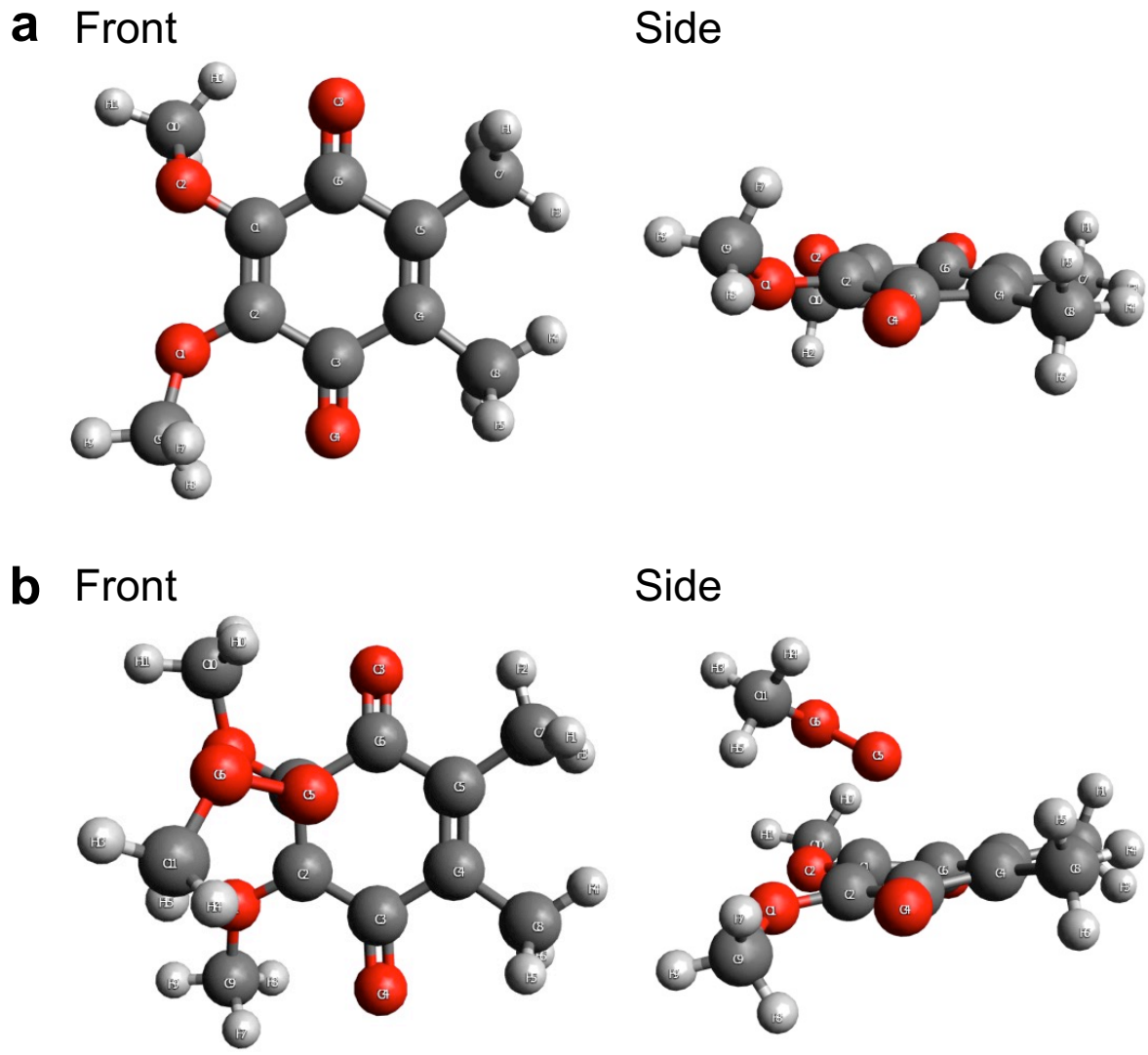

Figure 2.15 The front and side view of the computational modeling of (a) coenzyme Q10 and (b) the transition state of the addition of methyl peroxyl radical to coenzyme Q10.

Nonconjugated PUFAs

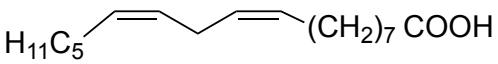

Linoleic Acid (18:2)

k_p = 62 M^{-1} s^{-1} *b*

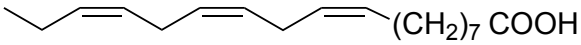

Nonconjugated Linolenic Acid (18:3)

k_p = 144 M^{-1} s^{-1} *a*

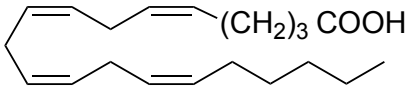

Arachidonic Acid (20:4)

k_p = 197 M^{-1} s^{-1} *c*

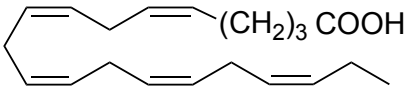

Eicosapentaenoic Acid (20:5)

k_p = 249 M^{-1} s^{-1} *c*

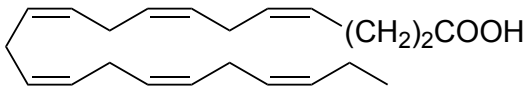

Docosahexaenoic acid (22:6)

k_p = 334 M^{-1} s^{-1} *c*

Conjugated PUFAs

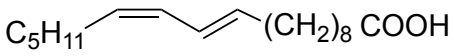

Conjugated Linoleic Acid (18:2)

k_p = 118 M^{-1} s^{-1} *a*

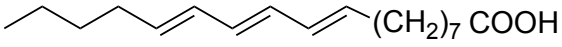

Conjugated Linolenic Acid (18:3)

k_p = 1235 M^{-1} s^{-1} *a*

Figure 2.16 The structures and rate constants of different non-conjugated and conjugated PUFAs. [a] This work. [b] From ref (*23*). [c] From ref (*25*).

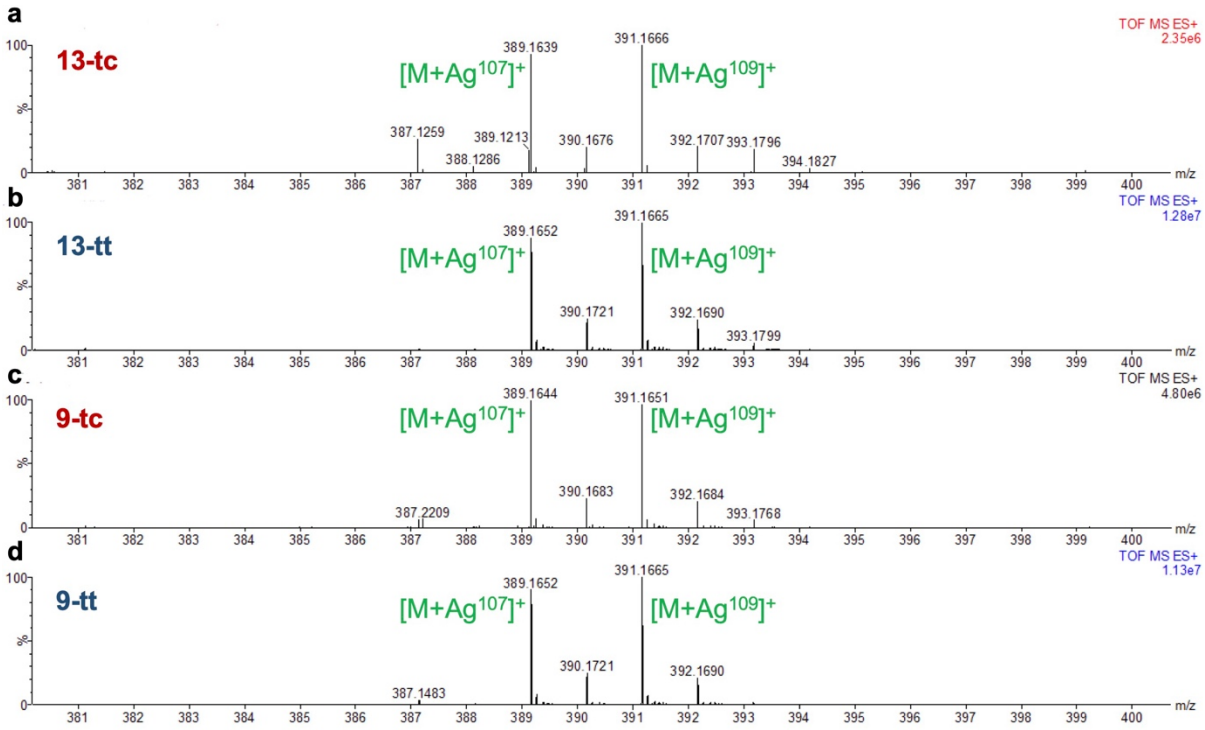

Figure 2.17 Mass spectra (TOF MS ES+) of Ag^+-coordination electrospray analysis of (a) 13-*tran,cis*-, (b) 13-*trans-trans*-, (c) 9-*trans-cis*-, and (d) 9-*trans,trans*-HODOL on a high-resolution QTOF mass spectrometer (Waters Synapt XS).

Tables

Table 2.1 PRA rate constants (k_{add}) and activation energies (E_a) of *para*- and *meta*-substituted styrene derivatives at 37 °C.

Substrate	k_{add} (M^{-1} s^{-1})	E_a (kcal/mol)	lit. k_{add} (M^{-1} s^{-1})
Sty	17 ± 1	19.5	41[a]
4-MeSty	24 ± 1	19.2	na
4-MeOSty	56 ± 3	18.8	na
4-ClSty	17 ± 2	19.4	na
4-FSty	17 ± 2	19.5	na
4-NO_2Sty	13 ± 1	19.5	na
3-MeSty	23 ± 1	19.4	na
3-MeOSty	27 ± 1	19.7	na
3-ClSty	20 ± 1	19.9	na
3-FSty	15 ± 1	19.7	na

[a] From ref (*195*), at 30 °C. na, not available.

Table 2.2 Free radical oxidation propagation (k_p), hydrogen atom transfer (k_H), and peroxyl-radical addition (k_{add}) rate constants of different organic oxidizable substrates measured by the new peroxyl radical clock at 37 °C.[a]

Substrate	k_p (M^{-1} s^{-1})	k_{add}/k_H	k_H (M^{-1} s^{-1})	k_{add} (M^{-1} s^{-1})	lit. k_H (M^{-1} s^{-1})	lit. k_{add} (M^{-1} s^{-1})
α-MeSty	27 ± 1	k_{add} dominant	na	26 ± 2	na	10[a]
β-MeSty	63 ± 1	3.1 ± 0.6	15 ± 2	48 ± 2	na	51[a]
1,3-Pentadiene	34 ± 2	k_{add} dominant	na	34 ± 2	na	na
3-Methyl-1,3-pentadiene	154 ± 4	k_{add} dominant	na	154 ± 4	na	na
2,4-Dimethyl-1,3-pentadiene	97 ± 4	2.4 ± 0.5	29 ± 4	68 ± 4	na	na
1,3-Hexadiene	65 ± 1	0.5 ± 0.1	43 ± 3	22 ± 3	na	na
2,4-Hexadiene	165 ± 7	1.0 ± 0.3	81 ± 11	84 ± 11	na	na
2,5-Dimethyl-2,4-hexadiene	509 ± 73	1.1 ± 0.2	243 ± 21	266 ± 21	na	na
1,3-Cyclohexadiene (1,3-CHD)	878 ± 35	0.95 ± 0.12	449 ± 26	429 ± 26	220[b]	na
1,4-Cyclohexadiene (1,4-CHD)	478 ± 15	k_H dominant	478 ± 15	na	1480[b] 265[c] 362[d]	na
1,2-Dihydronaphthalene	141 ± 8	0.33 ± 0.08	106 ± 6	35 ± 6	52[b]	291[a]
Indene	80 ± 5	0.47 ± 0.09	55 ± 3	25 ± 3	14[b]	128[a]
2-Methylindene	100 ± 7	1.1 ± 0.3	48 ± 6	52 ± 6	na	na
α-Terpinene	1304 ± 11	0.28 ± 0.03	1019 ± 24	285 ± 24	na	na

[a] k_H values are reported as per molecule, instead of per H-atom. [b] From ref (*23*), at 30 °C. [c] From ref (*24*), at 37 °C. [d] From ref (*205*), at 30 °C. na, not available.

Table 2.3 Radical oxidation propagation (k_p), hydrogen atom transfer (k_H), and peroxyl-radical addition rate constants (k_p) of different biologically important lipids measured by the new peroxyl radical clock approach at 37 °C.[a]

Substrate	k_p (M^{-1} s^{-1})	k_{add}/k_H	k_H (M^{-1} s^{-1})	k_{add} (M^{-1} s^{-1})	lit. k_p (M^{-1} s^{-1})
7-Dehydrocholesterol (7-DHC)	2737 ± 83	k_H dominant	2737 ± 83	na	2260[b]
Cholesterylacetate	36 ± 2	k_H dominant	36 ± 2	na	31.4[c]
Retinal	5656 ± 143	k_{add} dominant	na	5656 ± 143	na
CoenzymeQ10	695 ± 23	k_{add} dominant	na	695 ± 23	na
Vitamin D_3	1031 ± 63	1.4 ± 0.4	430 ± 63	601 ± 63	na
Conjugated linoleic acid 18:2 (CLA 18:2)	118 ± 8	1.1 ± 1.3	57 ± 21	61 ± 21	na
Conjugated linolenic acid 18:3 (CLA 18:3)	1235 ± 60	2.4 ± 1.7	359 ± 117	876 ± 117	na
Nonconjugated linolenic acid 18:3 (NLA 18:3)	144 ± 3	k_H dominant	144 ± 3	na	na

[a] k_H values are reported as per molecule, instead of per H-atom. [b] From ref (*25*), at 37 °C. [c] From ref (*191*), at 37 °C. na, not available.

Chapter 3. The Relationship Between the Reactivity of Various Biologically Important Lipids and their Ferroptosis Modulatory Effects

Portions of this chapter have been submitted as a preprint at ChemRxiv:

Quynh Do, Rutan Zhang, Gavin Hooper, and Libin Xu. Differential Contributions of Distinct Free Radical Peroxidation Mechanisms to the Induction of Ferroptosis. *ChemRxiv.* Cambridge: Cambridge Open Engage*,* (**2022**), DOI: 10.26434/chemrxiv-2022-2s60l..

3.1 Introduction

The differentiation between HAT and PRA reactions in the propagation step in Chapter 2 (*211*) would allow us to better understand not only the lipid peroxidation kinetics and mechanism but also the distribution of oxidation products of a lipid, which could translate into its biological and pathological effects. For example, a lipid that primarily undergoes the PRA mechanism would yield more addition products such as epoxides and thus, would exert very different biological effects compared to a lipid that predominantly undergoes the HAT mechanism, which generates mostly lipid hydroperoxides. Therefore, it would be interesting to compare the biological effects of nonconjugated PUFAs, which predominantly undergoes the HAT reaction, and conjugated PUFAs, which can also undergo PRA in addition to the HAT reaction. Even though the peroxidation reactivities and mechanism of nonconjugated PUFAs, such as arachidonic acid, have been studied extensively (*2, 212*), to our knowledge, the reactivities and mechanism towards lipid peroxidation of conjugated PUFAs, including CLA 18:2 and CLA 18:3, had not been studied until now.

Conjugated linoleic and linolenic acids do not occur naturally in human and can only be found in meat and dairy products from ruminants and plant-based food products, such as pomegranate seed oil and bitter gourd seed (*213-216*). However, these conjugated fatty acids have attracted many research efforts due to their health-promoting properties, such as anti-diabetic

(*217*), anti-inflammatory (*218*), anti-atherogenic (*219*) and anti-carcinogenic (*220, 221*). Interestingly, parinaric acid, an 18:4 conjugated fatty acid, is > 25 times more cytotoxic to cancer cells than corresponding non-conjugated fatty acids, and the antioxidant, butylated hydroxytoluene, abolishes its cytotoxicity, indicating a lipid peroxidation-mediated cell death mechanism (*222*). Other CLA 18:3 isomers, including α-eleostearic acid and punicic acid, were recently found to significantly sensitize triple-negative breast cancer cells to ferroptosis (*75, 146*), a type of cell death that is tightly associated with lipid peroxidation as detailed in chapter 1 (*13, 14, 63*).

Ferroptosis, also known as cell death by lipid peroxidation, is a newly discovered form of regulated cell death that is morphologically, biochemically, and genetically distinct from other types of cell death, such as apoptosis, necrosis, and autophagy (*13, 53, 223*). Specifically, due to their special metabolic needs to support the rapid differentiation and proliferation, certain cancer cell lines are constantly under high levels of oxidative stress and generate a substantial amount of ROS, resulting in a high level of lipid peroxidation (*8, 59*). Therefore, these cells rely heavily on the activities of the antioxidant network, especially those that can function at the lipid membrane, such as the enzyme glutathione peroxidase (GPX4) (*14, 78, 224*) and ferroptosis suppressor protein 1 (FSP1) (*64, 65*), for their survival. Thus, ferroptosis small-molecule inducers, such as RSL3 and erastin, which are direct and indirect inhibitors of GPX4, respectively, can lead to the accumulation of toxic lipid oxidation products and, subsequently, induction of cell death (*13, 14, 63*). The high autoxidation reactivity of conjugated PUFAs, which predominantly undergo the PRA reaction, suggests these lipids' potential to potentiate ferroptosis.

Besides conjugated PUFAs, the peroxidation reactivities and mechanism of coenzyme Q10 and lipophilic vitamins, such as retinal and vitamin D_3, were also determined in Chapter 2.

Coenzyme Q10, retinal, and vitamin D_3 have been found to play important roles in a variety of biological processes (*225-227*). However, only the reactivities and peroxidation mechanism of vitamin A precursor, β-carotene, have been studied previously (*228-233*). It would be intriguing to explore how the high reactivities of these lipid species would translate into their biological activities, especially in ferroptosis. The exceptionally large rate constant of vitamin A, retinal in this study, is of particular interest because it has been reported to act as both an antioxidant and a pro-oxidant under low and high oxygen tension, respectively (*228-231*). Given that oxygen tension varies significantly in different tissues/organs, vitamin A might play different roles in inducing or inhibiting ferroptosis in different types of cancer cells. Therefore, in this chapter, we investigate the effects of various biologically important lipids on ferroptosis induction. In addition, we then examine the ability of CLA 18:3 to act as a ferroptosis inducer in the HT-1080 cancer cell line.

3.2 Results

3.2.1 Various Biologically Important Lipids can Modulate the Sensitivity of Cancer cells to Ferroptosis.

Here, we carried out a systematic examination on the extent to which various biologically important lipids sensitize cells to cell death in the ferroptosis-sensitive cancer cell lines, including fibrosarcoma HT-1080, brain neuroblastoma SK-N-SH, and clear-cell renal carcinoma 786-O (*13, 145, 234*). We first determined the cytotoxicity of the biologically important lipids that were previously characterized, including those from chapter 2. These lipids are: 7-hydrocholesterol (7-DHC); CoQ10; vitamin D3; the two forms of vitamin A, including retinol and retinal; the nonconjugated PUFAs, including linoleic acid (LA), nonconjugated linolenic acid (NLA 18:3), arachidonic acid (AA), eicosapentaenoic acid (EPA), and docosahexaenoic acid (DHA); and the conjugated PUFAs, including the conjugated linoleic acid (CLA 18:2) and CLA 18:3. Retinoic

acid, another form of vitamin A, was not examined in this study due to its low solubility. We found that several lipid species, including 7-DHC, vitamin D_3, and retinal, were particularly toxic to all three cell lines (**Table 3.1**). The toxicity of these lipids may be related to their high reactivity towards lipid peroxidation and the formation of reactive oxidation products (See **Table 2.3**) (*211*). For example, reactive epoxides for from the oxidation of 7-DHC could lead to significant protein modifications (*192, 235, 236*). However, further investigation is needed to determine whether 7-DHC, vitamin D_3, and retinal toxicity are related to ferroptosis. In addition, the higher toxicity of retinal compared to retinol may be attributed to its aldehyde moiety. Notably, compared to other PUFAs, CLA 18:3 displayed much lower EC_{50} values of 4, 10, and 14 μM in the HT-1080, SK-N-SH, and 786-O cell lines, respectively (**Table 3.1**).

Next, we treated the cell lines with the two ferroptosis inducers imidazole ketone erastin (IKE) and RSL3 in the absence and presence of different lipid species at their non-lethal concentrations. The non-lethal concentration chosen for most lipids was 80 μM. For those that were more toxic to the cells, including 7-DHC, vitamin D_3, and retinal, the concentrations used were 10, 45, and 5 μM, respectively. In addition, CLA 18:3 was used at 1, 5, and 5 μM in the HT-1080, SK-N-SH, and 786-O cell lines, respectively. The EC_{50} values of the lipid-treated cells were then compared to the control, which was treated with the inducers only, to elucidate whether each lipid potentiates or inhibits ferroptosis. Overall, we observed similar trends among the cell lines for each lipid. First, cell death induced by RSL3 was more sensitive to the addition of exogenous lipids than IKE (**Figure 3.1**, **Figure 3.2**, and **Figure 3.3**). In addition, CoQ10 was found to suppress ferroptosis, which is consistent with its established properties as an antioxidant and a ferroptosis inhibitor (**Figure 3.1a**) (*64, 65, 111*). Despite being more toxic than other lipids, when used at non-lethal concentrations, 7-DHC, vitamin D_3, and retinal potently inhibited RSL3-induced

ferroptosis (**Figure 3.1a, b**). Moreover, between the two forms of vitamin A, retinol was more potent in inhibiting ferroptosis than retinal, which may be partially due to the 80 μM concentration of retinol used compared to the retinal concentration of 5 μM (**Figure 3.1b**).

We also found that cell death was inhibited across the three cell lines when the cells were co-treated with the ferroptosis inducers and the monounsaturated fatty acid OA (**Table 3.2**). This result is consistent with the previous findings that OA is a potent ferroptosis suppressor (*63, 77*). Among the nonconjugated PUFAs, AA was the most potent in enhancing ferroptosis in all three cancer cell lines. We also observed that the ω-6 fatty acids, including LA and AA, could sensitize cell death induced by IKE and RSL3 more potently than the ω-3 fatty acids, including EPA and DHA. Importantly, we found that the conjugated PUFAs were much more potent than the nonconjugated ones in potentiating ferroptosis (**Figure 3.1c**). For example, while displaying low toxicity when administered by itself, CLA 18:2 (EC_{50} = 3.7 nM) led to a 13-fold increase in RSL3-induced toxicity in the HT-1080 cell line (**Table 3.2**). Meanwhile, LA (EC_{50} = 18 nM) led to only a three-fold increase in RSL3 lethality. CLA 18:3 (EC_{50} = 36 nM) could also sensitize cells to ferroptosis but at a concentration 80 times lower than the concentration used for other PUFAs. Similar trends were observed in the SK-N-SH and 786-O (**Figure 3.2c**, **Figure 3.3c**, and **Table 3.2**).

3.2.2 CLA 18:3 Can Act as a Non-canonical Ferroptosis Inducer

Due to the high toxicity of CLA 18:3 in all three cancer cell lines, we next investigated whether CLA 18:3 induced ferroptosis in the HT-1080 cell line. First, we found that treating the cells with CLA 18:3 led to a dose-dependent accumulation of lipid peroxidation as assayed by flow cytometry using the fluorescent probe C11-BODIPY (**Figure 3.4a**). In contrast, the addition of the nonconjugated isomer, NLA 18:3, did not lead to changes in the lipid peroxidation level

compared to the control. Next, we confirmed that cell death induced by CLA 18:3 can be sensitized by the addition of different iron sources (**Figure 3.4b**). Last, we determined that CLA 18:3-induced cell death can be inhibited by the ferroptosis-specific inhibitors, including ferropstatin-1 (Fer-1) and liproxstatin-1 (Lip-1), the lipophilic antioxidant α-tocopherol (α-Tor), and the iron chelator deferoxamine (DFO) (**Figure 3.4c**). Moreover, the addition of either Fer-1 or DFO can reduce the lipid peroxidation level of CLA 18:3-treated cells to the same level of the control (Fig. 2d). Together, these are the evidence that CLA 18:3 induced ferroptosis in the HT-1080 cell line as a single agent.

Previously, α-eleostearic acid, a CLA 18:3 isomer, was reported to induce ferroptosis without inhibiting the function of GPX4 or affecting the cellular total glutathione level (*75*). Therefore, we next sought to determine whether the treatment with CLA 18:3 could lead to changes in the level of reduced glutathione. Reduced glutathione functions as a free radical scavenger, and a decrease in the ratio of the reduced to the oxidized form indicates an increase in cellular oxidative stress (*237-239*). Therefore, we postulated that even though the level of total cellular glutathione is not affected, the increased oxidative stress induced by CLA 18:3 can potentially lead to a decrease in the reduced glutathione level. However, we found that the reduced glutathione level was unaffected despite the decrease in cell viability upon treatment with 2.5 and 5 μM CLA 18:3 (**Figure 3.4e**). Furthermore, we only observed the reduction in reduced glutathione level when cells were treated with CLA 18:3 at the high concentrations of 10, 20, and 40 μM (**Figure 3.4f**). These results suggest that CLA 18:3-induced lethal effects happen within the cellular lipid membrane since glutathione is water soluble and cannot scavenge free radical within the lipid bilayer.

3.3 Discussion

We previously reported the autoxidation mechanism and kinetics of various biologically important lipids (*211*). The current study aimed to investigate the relationship between the autoxidation reactivity and mechanisms of these lipids to their biological effects. Specifically, this study presented the first systemic investigation on the impact of different unsaturated lipids on ferroptosis induction. We found biologically important lipids, including 7-DHC, vitamin D_3, and retinal, to be highly toxic to cancer cells (**Table 3.1**). However, when used at their non-lethal concentrations, all these lipids potently inhibited cell death triggered by the ferroptosis inducers, including IKE and RSL3 (**Figure 3.1** and **Table 3.2**). While the anti-ferroptotic properties of 7-DHC, vitamin D_3, and the precursor of vitamin A, β-carotene, were previously demonstrated (*112, 187-190*), to our knowledge, this is the first study that reports the inhibition of ferroptosis by the two forms of vitamin A including retinol and retinal. Previously, vitamin A was reported to function as either a pro-oxidant or an antioxidant, depending on oxygen tension in the tissues or organs (*228-231*). Here, vitamin A appeared to function as an antioxidant and a ferroptosis inhibitor.

The observed anti-ferroptotic properties of 7-DHC, vitamin D_3, and vitamin A highlight the importance of lipid incorporation into the cellular phospholipids to ferroptosis induction. Specifically, during the initiation of ferroptosis, fatty acids are activated and incorporated into the membrane phospholipids via the enzymes such as LPCAT3 and ACSL4 (*67, 72, 73*). Since 7-DHC, vitamin D_3, and vitamin A do not undergo such processes, at non-lethal concentrations, they can potentially "hijack" the free radical chain reaction away from the membrane phospholipids due to their high reactivity towards lipid peroxidation. Specifically, the measured autoxidation (propagation) rate constant of 7-DHC and vitamin D_3 are 2737 and 1031 $M^{-1} s^{-1}$, respectively (*211*).

Moreover, vitamin A, with the autoxidation rate constant of 5656 M^{-1} s^{-1}, is currently the most oxidizable lipid measured in solution (*211*). Therefore, 7-DHC, vitamin D_3, and vitamin A are more reactive toward lipid peroxidation than the endogenous esterified PUFAs. Indeed, 7-DHC was shown to inhibit phospholipid autoxidation and, subsequently, ferroptosis (*187*). Interestingly, the reduced form of another biologically important lipid, vitamin K, which shares similar structural properties with CoQ10, was recently found to be anti-ferroptotic (*240*). Thus, these reactive biologically important lipids represent a class of natural compounds that can act as ferroptosis suppressors.

Since fatty acids can be activated and incorporated into cellular membranes, their lipid peroxidation kinetics, mechanisms, and oxidation product profiles are correlated strongly with their ability to modulate ferroptosis. For example, the monounsaturated fatty acid OA, which can be activated by the enzyme ACSL3, has a low autoxidation rate constant of 0.9 M^{-1} s^{-1} (*4*). Thus, the addition and incorporation of exogenous OA into the cellular membrane can lead to a ferroptosis-resistant state (*63, 77*). On the other hand, the oxidation of endogenous PE containing AA and its elongation products, adrenic acid (C22:4), were found to contribute to ferroptosis induced by RSL3 (*67*). In addition, exogenous nonconjugated PUFAs, including LA and AA, were shown to sensitize cells to RSL3-induced cell death (*63*). Due to their reactive bis-allylic H atoms, nonconjugated PUFAs readily undergo the HAT reaction to initiate and carry on the free radical chain reaction (*2*). Indeed, when the bis-allylic H-atoms of LA were replaced by deuterium, ferroptosis was inhibited (*63*). Therefore, ferroptosis has been discussed extensively to be driven by the HAT mechanism and oxidation products of nonconjugated PUFAs.

In contrast, it was only recently that CLA 18:3 isomers, including α-eleostearic acid punicic acid, were shown to be pro-ferroptotic (*75, 146*), even though the anti-cancer properties of

various conjugated PUFAs have been previously recognized (*220, 221, 241-243*). We indeed found β–eleostearic acid, which is termed CLA 18:3 in this study, to be highly toxic across the three ferroptosis-sensitive cancer cell lines, including HT-1080, SK-N-SH, and 786-O (**Table 3.1**), and the CLA 18:3-induced cell death was confirmed to be ferroptosis (**Figure 3.4**). Notably, different CLA 18:3 isomers were shown to induce ferroptosis without the addition of any ferroptosis-inducing compounds in this and previous studies (*75, 146*), which has not been observed with nonconjugated PUFAs. In addition, the CLA 18:3 isomer, α-eleostearic acid, was reported to induce ferroptosis without neither directly inhibiting GPX4 nor affecting total cellular glutathione levels (*75*), suggesting its ability to act as a non-canonical ferroptosis inducer. We postulate that the large autoxidation rate constant of 1235 M^{-1} s^{-1} and the high level of toxic lipid electrophiles formed from the PRA mechanism for CLA 18:3 overwhelm the detoxification function of antioxidant enzymes such as GPX4 and FSP1 and, eventually, lead to cell death.

We also showed in this study that while displaying low toxicity when administered by itself, CLA 18:2 potently increased RSL3-induced toxicity in the HT-1080 cell line (**Table 3.2**). This observation suggests that since CLA 18:2 is not as reactive toward lipid peroxidation as CLA 18:3, functional GPX4 can effectively detoxify its oxidation products. However, when GPX4 is covalently inhibited by RSL3, CLA 18:2 can potently carry on free radical chain oxidation within the lipid membrane and lead to the significant formation of toxic oxidation products to drive ferroptosis. In addition, we demonstrated that conjugated PUFAs are significantly more potent in enhancing the lethal effects of ferroptosis inducers than their conjugated counterparts. The difference in potency of LA and CLA 18:2 can, in parts, be attributed to their difference in autoxidation mechanism and kinetics. Specifically, LA and CLA 18:2 undergo autoxidation via the HAT mechanism with similar rate constants of 62 and 57 M^{-1} s^{-1}, respectively (*211*). However,

while LA only undergoes the HAT mechanism, CLA 18:2 can also undergo the PRA reaction with a rate constant of 61 M^{-1} s^{-1}. Remarkably, the cotreatment of RSL3 with CLA 18:2 showed much higher toxicity than nonconjugated PUFAs with even more double bonds, all of which predominantly undergo lipid peroxidation via the HAT mechanism and has a larger overall rate constant, suggesting that the PRA mechanism or the resulting products more potently induce ferroptosis. In addition, at a concentration 80 times lower than the concentration used for other nonconjugated PUFAs, CLA 18:3 could also potently sensitize cells to RSL3-induced ferroptosis and showed a much more significant accumulation of lipid peroxidation compared to its nonconjugated counterpart NLA 18:3, which is nine times less reactive towards lipid peroxidation than CLA 18:3 and only undergoes the HAT mechanism (*211*). The observations that conjugated PUFAs are more potent in potentiating ferroptosis than the nonconjugated ones, which can only undergo the HAT reaction, suggest that the unusually high reactivity toward the PRA mechanism of conjugated PUFAs is underlying their high potency in enhancing ferroptosis compared to their nonconjugated counterparts.

3.4 Experimental Procedures

3.4.1 Cell lines and Culture Conditions.

HT-1080 and SK-N-SH cell lines were obtained from American Type Culture Collection (ATCC). 786-O cell line was a generous gift from the lab of Professor Rheem Totah. HT-1080 and SK-N-SH cell lines were grown in DMEM High-Glucose media (Gibco) containing 10% fetal bovine serum (FBS; Gibco), 1% MEM non-essential amino acids (Gibco), and 1% Penicillin-Streptomycin (Pen-Strep, 10,000 U/mL; Gibco). 786-O cell line was grown in RPMI-1640 media (Gibco) containing 10% FBS and 1% Pen-Strep. All cells were cultured in a humidified condition at 37 ºC with 5% CO_2.

3.4.2 Chemicals

7-DHC, ferric citrate, iron chloride hexahydrate, ferric ammonium citrate, sulfate heptahydrate, α-tocopherol, and deferoxamine mesylate salt were obtained from Sigma-Aldrich. Retinol was purchased from Thermo Fisher Scientific. Retinal, coenzyme Q10, and vitamin D3 were purchased from Chem-Impex Int'l Inc. Oleic acid (OA), linoleic acid (LA), 9,12,15-*cis,cis,cis*-octadecatrienoic acid (NLA 18:3), arachidonic acid (AA), eicosapentaenoic acid (EPA), docosahexaenoic acid (DHA), and 10,12-*trans,cis*-octadecadienoic acid (CLA 18:2) were purchased from Nu-Chek Prep, Inc. 9,11,13-*trans,trans,trans*-octadecatrienoic acid (CLA 18:3) was obtained from Sapphire North America. Imidazole ketone erastin (IKE), RSL3, liproxstatin-1 (Lip-1), and ferrostatin-1 (Fer-1) were obtained from MedChemExpress. 4-hydroxynonenal (4-HNE) was purchased from Cayman Chemical.

3.4.3 Cell Viability Assays.

Cells were seeded in 96-well plates (Corning 3598) at 5000 cells/well and treated with indicated compounds 24 h after plating. Compounds are added at the same time in co-treatments. Cell viability was assessed using CellTiter 96 Aqueous One Solution Assay (Promega) according to the manufacturer's instructions. Viability was reported as percentages relative to vehicle control, and EC_{50} curves were generated with GraphPad Prism (Version 9).

3.4.4 Analysis of Lipid Peroxidation Using Flow Cytometry.

The experiment was conducted following the protocol described by Martinez *et al. (244).* Briefly, HT-1080 cells were seeded at 1.7 x 10^5 cells/well in a 6-well plate (Corning 3506). After 24 h, cells were treated with test compounds for the indicated times and then incubated with BODIPY 581/591 C11 (Invitrogen D3861) at 37 ºC for 20 minutes. Stained cells were then washed with Hanks Balanced Salt Solution (HBSS; Gibco) and harvested by trypsinization. Harvested

cells were resuspended in HBSS, strained through a 40 μm cell strainer, and analyzed by a flow cytometer (LSR II, BD Biosciences). Flow cytometry data was analyzed using FACSDiva software, and the plots were generated using FlowJo software.

3.4.5 Reduced Glutathione Measurement.

Cells were seeded in 96-well plates at 5000 cells/well and treated with indicated concentrations of CLA 18:3 24 h after plating. After indicated treatment times, cellular reduced glutathione was measured using the GSH-Glo Glutathione Assay (Promega). CLA 18:3-treated samples were normalized to parallel cell viability measurements using CellTiter 96 Aqueous One Solution Assay (Promega)

Figures

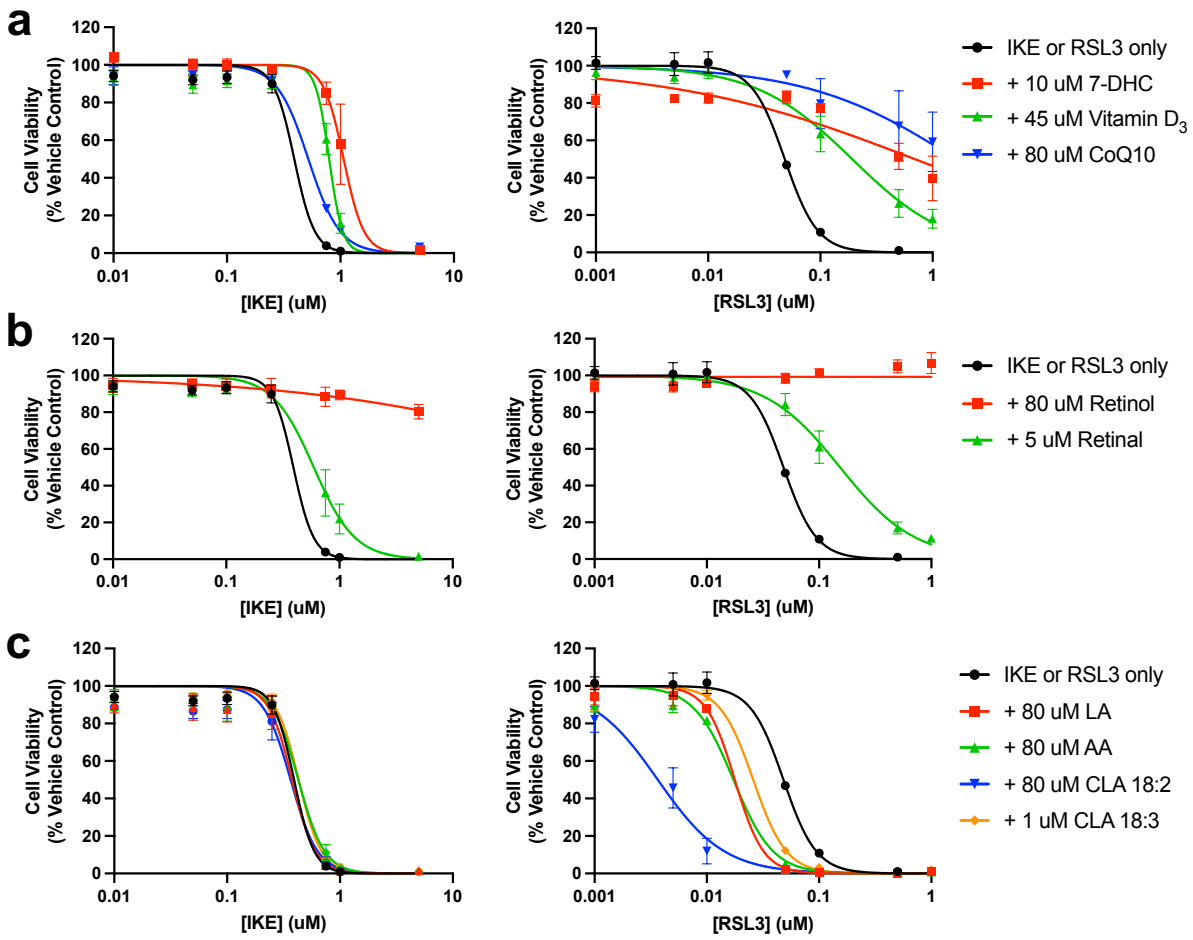

Figure 3.1 Cell viability dose-response curves of HT-1080 cells treated with ferroptosis inducers, including imidazole ketone erastin (IKE) and RSL3, in the absence and presence of a) 7-DHC, vitamin D_3, and CoQ10, b) retinol, retinal, and retinoic acid, and c) nonconjugated PUFAs, including LA and AA, and conjugated PUFAs, including CLA 18:2 and CLA 18:3. Viability is plotted as mean ± SEM of n = 3 biological replicates.

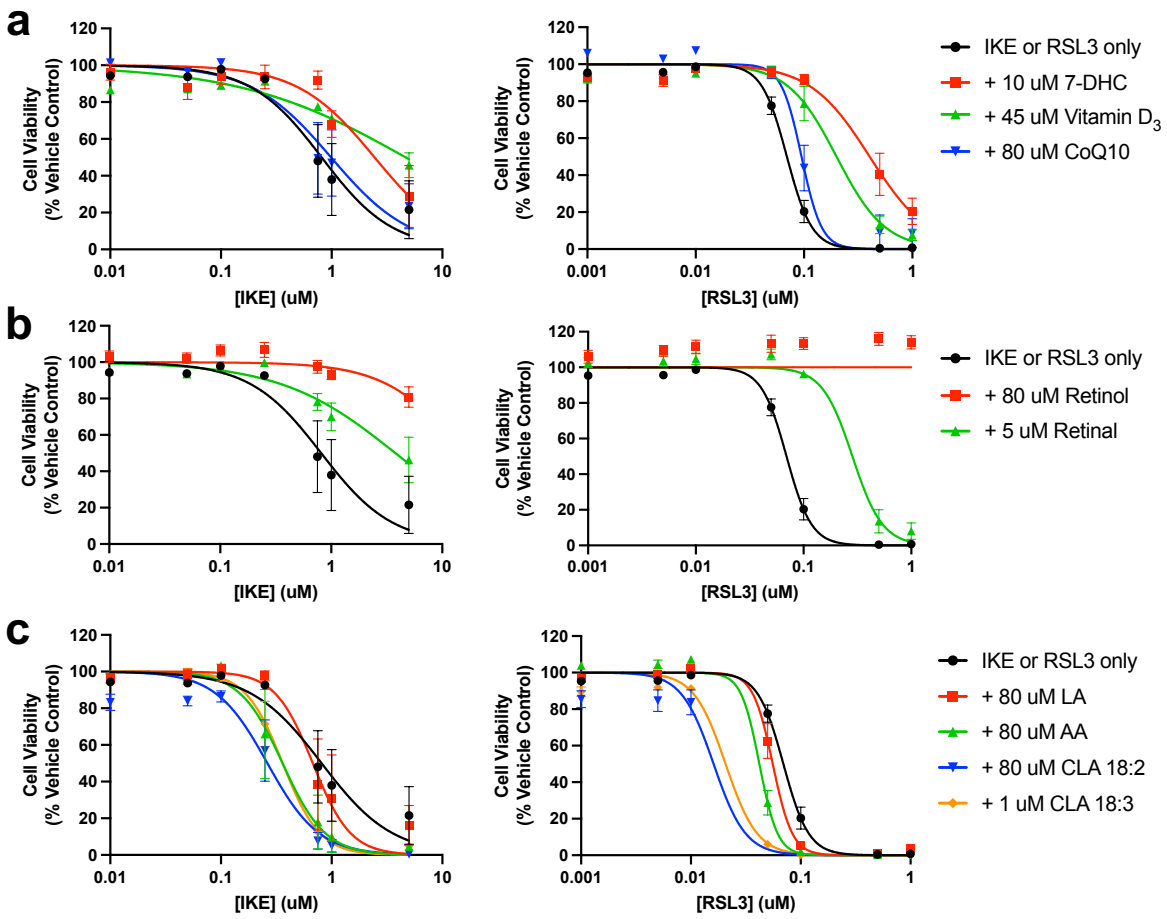

Figure 3.2 Cell viability dose-response curves of SK-NSH cells treated with ferroptosis inducers, including imidazole ketone erastin (IKE) and RSL3, in the absence and presence of a) 7-DHC, vitamin D_3, and CoQ10, b) retinol, retinal, and retinoic acid, and c) nonconjugated PUFAs, including LA, and AA, and conjugated PUFAs, including CLA 18:2 and CLA 18:3. Viability is plotted as mean ± SEM of n = 3 biological replicates.

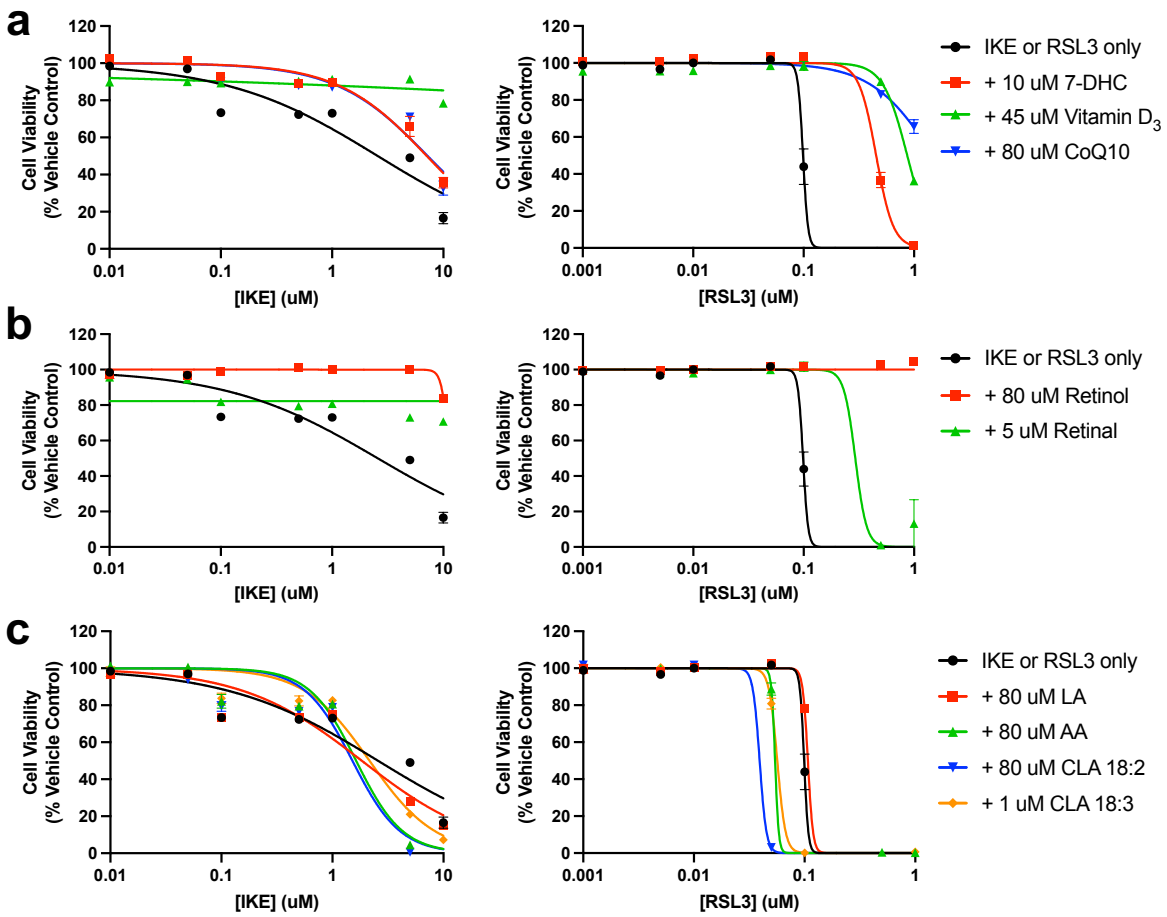

Figure 3.3 Cell viability dose-response curves of 786-O cells treated with ferroptosis inducers, including imidazole ketone erastin (IKE) and RSL3, in the absence and presence of a) 7-DHC, vitamin D_3, and CoQ10, b) retinol, retinal, and retinoic acid, and c) nonconjugated PUFAs, including LA, and AA, and conjugated PUFAs, including CLA 18:2 and CLA 18:3. Viability is plotted as mean ± SEM of n = 3 technical replicates.

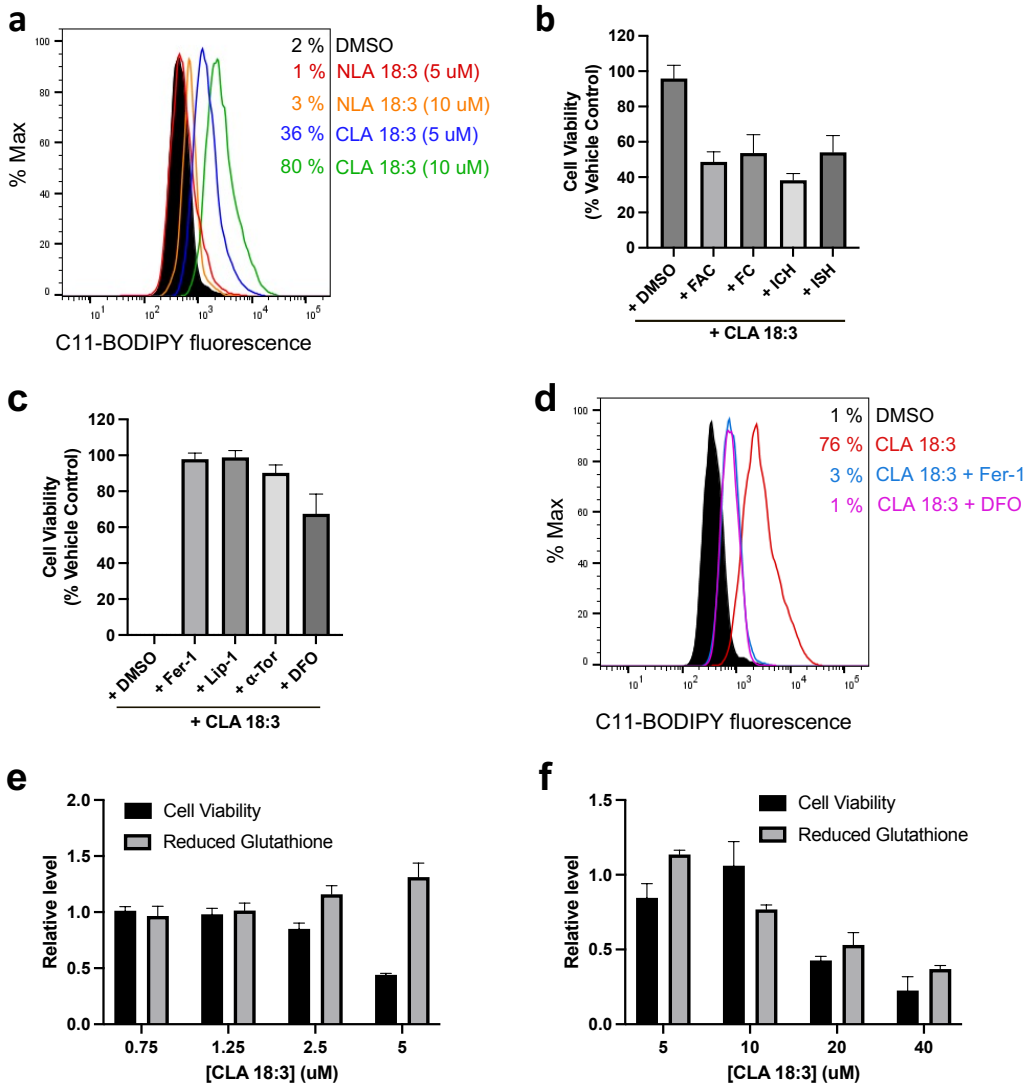

Figure 3.4 CLA 18:3 can induce ferroptosis as a single agent without affecting the level of cellular reduced glutathione in HT-1080 cell line. a) Lipid peroxidation level after 5 h of treatments with 5 and 10 μM NLA 18:3 and CLA 18:3 assayed by flow cytometry using C11-BODIPY. b) Cell viability after 3 h of treatment with 10 μM CLA 18:3 +/- ferric ammonium citrate (FAC, 38 μM), ferric citrate (FC, 25 μM), iron chloride hexahydrate (ICH, 25 μM), and iron sulfate heptahydrate (ISH, 25 μM). Viability is plotted as mean ± SD of n = 3 biological replicates. c) Cell viability after 24 h of treatment with 10 μM CLA 18:3 +/- ferrostatin-1 (Fer-1, 1 μM), liproxstatin-1 (Lip-1, 1 μM), α-tocopherol (α-Tor, 100 μM), and deferoxamine (DFO, 80 μM). Viability is plotted as mean ± SD of n = 3 biological replicates. d) Lipid peroxidation level after 5 h of treatments with 10 μM CLA 18:3 in the absence and presence of Fer-1 (1 μM) or DFO (80 μM) assayed by flow cytometry using C11-BODIPY. e) Relative viability and level of reduced glutathione after 24 h of treatments with 0.75, 1.25, 2.5, and 5 μM CLA 18:3 (n = 3 wells of 96-well plate). Relative level is plotted as mean ± SD of n = 3 technical replicates. f) Relative viability and level of reduced glutathione after 3 h of treatments with 5, 10, 20, and 40 μM CLA 18:3. Relative level is plotted as mean ± SD of n = 3 technical replicates.

Tables

Table 3.1 Cytotoxicity of various biologically important lipids in HT-1080 (n = 3 biological replicates), SK-N-SH (n = 3 biological replicates), and 786-O (n = 3 technical replicates) cell lines.

Lipids	EC_{50} ± SEM (μM)		
	HT-1080	**SK-N-SH**	**786-O**
7-DHC[f]	34 ± 2	27 ± 3	32 ± 1
CoQ10[e]	Very large[a]	Very large[a]	Very large[a]
Vitamin D_3[g]	112 ± 2	72 ± 5	143 ± 2
Retinol[d]	Very large[a]	Very large[a]	Very large[a]
Retinal[d]	13 ± 1	10 ± 6	14 ± 1
OA[g]	Very large[a]	Very large[a]	Very large[a]
LA[g]	316 ± 6	216 ± 12	Very large[a]
NLA 18:3[g]	336 ± 23	212 ± 10	365 ± 15
AA[g]	364 ± 15	195 ± 7	224 ± 1
EPA[g]	213 ± 6	188 ± 8	231[b]
DHA[g]	116 ± 2	142 ± 5	179[b]
CLA 18:2[g]	286 ± 20	Very large[a]	307 ± 5
CLA 18:3[c]	4[b]	10 ± 1	14[b]

[a] The EC_{50} values are outside the concentration range tested.
[b] No SEM calculated
[c] Concentration range = 0.05 - 20 mM
[d] Concentration range = 0.05 - 100 mM
[e] Concentration range = 13 - 100 mM
[f] Concentration range = 23 - 180 mM
[g] Concentration range = 45 - 360 mM

Table 3.2 Effects of various biologically important lipids in potentiating ferroptosis induced by imidazole ketone erastin (IKE) and RSL3 in HT-1080 (n = 3 biological replicates), SK-N-SH (n = 3 biological replicates), and 786-O (n = 3 technical replicates) cell lines.

Treatment	EC_{50} ± SEM					
	HT-1080		SH-N-SK		786-O	
	IKE (μM)	RSL3 (nM)	IKE (μM)	RSL3 (nM)	IKE (μM)	RSL3 (nM)
Inducers only	0.40 ± 0.03	48 ± 2	0.82 ± 0.12	70 ± 3	2.6 ± 0.5	99[b]
+ 10 μM 7-DHC	1.1 ± 0.1	693 ± 306	2.4 ± 0.5	560 ± 49	7.1 ± 0.7	454 ± 22
+ 80 μM CoQ10	0.52 ± 0.03	Very large[a]	0.99 ± 0.22	95 ± 6	7.2 ± 0.9	Very large[a]
+ 45 μM Vitamin D_3	0.73 ± 0.05	192 ± 26	47 ± 1	200 ± 24	Very large[a]	Very large[a]
+ 80 μM Retinol	Very large[a]	Very large[a]	Very large[a]	Very large[a]	Very large[a]	Very large[a]
+ 5 μM Retinal	0.60 ± 0.05	154 ± 15	Very large[a]	284 ± 42	Very large[a]	294[b]
+ 80 μM OA	0.77 ± 0.07	Very large[a]	Very large[a]	379 ± 48	Very large[a]	Very large[a]
+ 80 μM LA	0.38 ± 0.05	18 ± 2	0.68 ± 0.12	56 ± 2	1.8 ± 0.3	107[b]
+ 80 μM NLA 18:3	0.71 ± 0.04	29 ± 3	0.90 ± 0.15	80 ± 3	3.5 ± 0.4	99[b]
+ 80 μM AA	0.43 ± 0.04	17 ± 2	0.36 ± 0.06	42 ± 6	1.6 ± 0.2	54[b]
+ 80 μM EPA	0.77 ± 0.04	36 ± 4	0.74 ± 0.10	80 ± 5	3.1 ± 0.3	88[b]
+ 80 μM DHA	1.20 ± 0.28	30 ± 5	0.71 ± 0.13	90 ± 9	1.7 ± 0.2	57[b]
+ 80 μM CLA 18:2	0.37 ± 0.03	3.7 ± 0.5	0.26 ± 0.04	16 ± 3	1.5 ± 0.2	39[b]
+ CLA 18:3[c]	0.43 ± 0.03	26 ± 3	0.36 ± 0.03	21 ± 2	2.2 ± 0.2	57[b]

[a] The EC_{50} values are outside the concentration range tested

[b] No SEM calculated

[c] The concentrations used in the HT-1080, SK-N-SH, and 786-O were 1, 5, and 5 μM, respectively

Chapter 4. The Mechanisms Underlying the Ferroptosis Induction by Conjugated Polyunsaturated Fatty Acids

Portions of this chapter have been submitted as a preprint at ChemRxiv:

Quynh Do, Rutan Zhang, Gavin Hooper, and Libin Xu. Differential Contributions of Distinct Free Radical Peroxidation Mechanisms to the Induction of Ferroptosis. *ChemRxiv.* Cambridge: Cambridge Open Engage, (2022), DOI: 10.26434/chemrxiv-2022-2s60l.

4.1 Introduction

Due to the substantial generation of ROS and constantly being under high levels of oxidative stress (*59*), certain types of cancer cell lines rely heavily on the functions of the components in the cellular antioxidant network, including glutathione peroxidase 4 and system x_c^- for their survival (*13, 14*). Therefore, inhibition of these two components by RSL3 and erastin, respectively, leads to the accumulation of lipid oxidation products via the free radical chain reactions to lethal levels, resulting in cell death, *i.e.*, ferroptosis. Despite the establishment of several key aspects of ferroptosis throughout the ten years since its discovery, certain questions remained unanswered (*53, 158*). One of these unresolved mysteries includes the key molecular events during the execution of ferroptosis. Specifically, even though the autoxidation of polyunsaturated fatty acids (PUFAs)-containing phospholipid in the cellular membrane has been established to be the driver of ferroptosis (*17, 58, 158, 245*), it remains unknown whether the accumulation of oxidation products can lead to membrane, protein, and DNA damage and if any of these events are responsible for the point of no return in ferroptosis. In addition, while the relevance of nonconjugated PUFAs and their HAT oxidation products, such as lipid hydroperoxides in ferroptosis, have been studied intensively (*63, 67, 223, 246*), the contribution of PRA mechanism, and its oxidation products, to ferroptosis have not been characterized.

In previous chapters, we have demonstrated the relevance between the lipid peroxidation mechanism and kinetics and the modulatory effects on ferroptosis of various lipids, especially PUFAs. Specifically, we discovered that while the nonconjugated PUFAs only undergo the HAT mechanism, the conjugated species can undergo both HAT and PRA mechanisms, with a predominant contribution from the latter. In addition, the conjugated PUFAs, especially the conjugated linolenic acid (CLA 18:3), are much more reactive towards lipid peroxidation than their nonconjugated counterparts. Interestingly, with three double bonds in its structure, CLA 18:3 has a much higher peroxidation rate constant compared to those of the nonconjugated PUFAs, including arachidonic acid (AA), eicosapentaenoic acid (EPA), and docosahexaenoic acid (DHA), which have four, five, and six double bonds, respectively. Therefore, the high autoxidation reactivity of conjugated PUFAs, which predominantly undergo the PRA reaction, suggests these lipids' potential to potentiate ferroptosis. Indeed, in chapter 3, we showed that the conjugated PUFAs are much more potent than the nonconjugated PUFAs in potentiating ferroptosis.

Remarkably, despite having a smaller total propagation rate constant than AA, EPA, and DHA, CLA 18:2 displayed a much higher potency in potentiating RSL3-induced ferroptosis. This observation suggests that, in addition to autoxidation kinetics, additional mechanisms contribute to the difference in the difference in potency between conjugated and nonconjugated PUFAs. Therefore, in this chapter, we seek to elucidate the mechanisms underlying the higher potency of conjugated PUFAs in potentiating ferroptosis. Specifically, we first compare the change in the lipid composition of conjugated PUFA- and nonconjugated PUFA-treated cancer cells. Next, based on the proposed autoxidation mechanism of conjugated PUFAs, we report for the first time the detection of the highly electrophilic aldehydes formed from the PRA mechanism of conjugated PUFAs. Last, we investigate the cytotoxicity of the lipid-derived electrophiles and their lethal

mechanism via RNA-sequencing and protein pull-down assays, which suggested protein damage is one of the key steps in conjugated PUFA-induced ferroptosis. Here, the examination of the lethal mechanism and targets of these aldehydes highlights the underappreciated contribution of the PRA mechanism and its oxidation products to biological processes, especially ferroptosis. Moreover, the results from this study offer insights into the key molecular events that lead to the execution of ferroptosis.

4.2 Results

4.2.1 Nonconjugated and Conjugated PUFAs are Incorporated Into Distinct Cellular Lipid Species

To provide insights into the mechanisms underlying the difference in ferroptosis-sensitizing potency of nonconjugated and conjugated PUFAs, we first performed untargeted lipidomic analysis using our established HILIC-ion mobility-mass spectrometry method (*247, 248*) to assess the changes in the lipidome of the HT-1080 cell line upon the addition of RSL3, LA, CLA 18:2, or the combined treatment with RSL3 with either LA (RSL3-LA) or CLA 18:2 (RSL3-CLA 18:2) compared to the control treated with DMSO. Unsupervised principal component analysis (PCA score plot) showed separation in both positive and negative modes among three clusters: DMSO and RSL3, LA and RSL3-LA, and CLA 18:2 and RSL3-CLA 18:2 (**Figure 4.1**). Since the concentration used for RSL3 here was only 5 nM, its addition did not cause a significant difference in lipid composition in the treatment pairs, including RLS3 versus control, RSL3-LA versus LA, and RSL3-CLA 18:2 versus CLA 18:2.

Significantly altered lipid species (ANOVA adjusted p-value < 0.05) between treatments with either CLA 18:2 or LA only and the control were identified by *m/z*, retention time, and collision cross section (CCS) values using LiPydomics, a Python package developed by our lab

(*249*) (**Table 4.1**-**Table 4.4**). To evaluate the effects of CLA 18:2 and LA, we then compared the normalized abundance of the identified lipid species in both positive and negative modes across four groups, including treatment with DMSO, RSL3, either CLA 18:2 or LA only, and the combination of RSL3 and either CLA 18:2 or LA. We found that adding LA and CLA 18:2 either by themselves or in combination with RSL3 led to significant changes compared to DMSO- or RSL3-treated cells (**Figure 4.2**). In addition, in both CLA 18:2- and LA-treated groups, most of the altered lipids belong to two lipid classes: phosphatidylcholine (PC) and phosphatidylethanol-amine (PE) (**Table 4.1**-**Table 4.4**). Within these two classes, many long-chain and highly unsaturated lipids were found to be elevated, while there was a decrease in the abundance of shorter-chain and less unsaturated, monounsaturated, or saturated lipids. Moreover, there was a significant increase in the abundance of triacylglyceride (TAG) species in both LA and CLA 18:2 treatments (**Figure 4.3a**).

On the other hand, the lipid composition of CLA 18:2-treated cells was significantly different from LA-treated cells in both positive and negative modes. Specifically, we found that the addition of exogenous CLA 18:2 induced a more drastic increase in the normalized lipid abundance compared to the control than the addition of LA. For example, in the positive mode, in CLA 18:2-treated cells, TG (54:6) and DGDG (28:1) were the most elevated lipids compared to the control with the fold change of 25.2 and 17.5, respectively (**Table 4.1**), while in the LA versus control comparison, TG (56:8) and TG (54:6) had the highest fold changes, which were both 8.8 (**Table 4.3**). On the other hand, in the negative mode, in CLA 18:2-treated cells, PC (42:10) and PE (p40:8) had the highest fold changes of 226 and 22.2, respectively, compared to the control (**Table 4.2**). In contrast, the highest fold changes found in LA-treated cells were only 5.15 and 4.17 for PE (p34:2) and DGDG (30:3), respectively (**Table 4.4**).

Even though both the addition of LA and CLA 18:2 led to a significant increase of several TAGs, the specific elevated species were different between the two groups (**Figure 4.3a**). Specifically, the addition of LA led to a moderate increase in the normalized abundance of various TAG lipids, including very long-chain and highly unsaturated species (**Table 4.3**). In contrast, CLA 18:2 treatment led to a significant increase in the levels of shorter-chain and less unsaturated TAGs, suggesting the involvement of distinct mechanisms in the activation of LA and CLA 18:2 and their incorporation into the cellular lipidome (**Table 4.1**). Notably, while TG (54:6) was the most elevated TAG species in both LA- and CLA 18:2-treated cells, it was much more abundant upon the addition of CLA 18:2. Specifically, the fold changes of TG (54:6) upon the addition of LA and CLA 18:2 were 8.8 and 25.2, respectively (**Table 4.1** and **Table 4.3**) Fragmentation of this lipid in the positive mode confirmed the incorporation of CLA 18:2 into all three positions of the triglycerol backbone of TG (54:6) (**Figure 4.4a**). Similarly, we also observed a significant elevation of PC (36:4) and PE (36:4) in CLA 18:2-treated compared to LA-treated cells (**Figure 4.3b, c**). Fragmentation in the negative mode of PC (36:4) and PE (36:4) confirmed the incorporation of CLA 18:2 into these lipid species (**Figure 4.4b, c**).

Interestingly, the addition of CLA 18:2 was found to significantly increase the abundance of various long-chain and highly unsaturated ether-PC and ether-PE lipids compared to the control (**Figure 4.3d, e**). In contrast, the levels of these lipids were not significantly altered upon the addition of LA. Strikingly, we observed that the significantly increased ether-PEs, including PE (p40:8), PE (p40:7), and PE (p40:6), consisted of fatty acid 18:2 at the *sn*-1 position and fatty acid 22:6, 22:5, and 22:4 at the *sn*-2 position, respectively (**Figure 4.4d-f**). This observation is surprising since in endogenous plasmalogens, palmitic (16:0), stearic (18:0), and oleic (18:1) chains are almost exclusively incorporated in the *sn*-1 position, and the *sn*-2 position primarily

consists of PUFAs (*250*). Therefore, these results suggest the involvement of peroxisome in facilitating the incorporation of exogenous CLA 18:2 into ether lipids since the incorporation of activated fatty acids and vinyl-ether bond formation happen in the peroxisome (*251*). Furthermore, due to the pro-ferroptosis properties of ether phospholipids (*69, 139*), the more significant increase of these lipid species upon the addition of CLA 18:2 compared to the addition of LA can potentially contribute to the higher potency of CLA 18:2 in sensitizing cells to ferroptosis.

We also carried out lipidomic analysis for cells treated with 3 μM CLA 18:3 for 24 h and found that this treatment could also lead to a change in lipid composition compared to the control (**Figure 4.5a, b**). In addition, similar to the treatment with CLA 18:2, we observed that most altered lipids were phospholipids and ether-lipids, including ether-PEs (**Table 4.5** and **Table 4.6**). However, treatment with CLA 18:3 did not lead to as significant increase in lipid normalized abundance as CLA 18:2. For example, the fold changes of the most elevated lipid species in CLA 18:3-treated cells were 5.04 and 7.68 for PE (40:9) (positive mode) and PE (38:7) (negative mode), respectively. In addition, we found that not all highly increased lipids contain fatty acid 18:3 in their composition (**Figure 4.5c, d**), which could be due to the low concentrations of CLA 18:3 used (3 μM vs. 80 μM for CLA 18:2). Moreover, while CLA 18:2 at 80 μM is non-toxic to the cells, 3 μM CLA 18:3 can induce cell death and detachment. Therefore, the lipid composition changes in CLA 18:3-treated cells may reflect the changes in cells undergoing ferroptosis.

4.2.2 Electrophilic Lipid Aldehydes Formed from the PRA Mechanism of Conjugated PUFA are Toxic to the Cells.

Nonconjugated and conjugated PUFAs undergo lipid peroxidation via distinct mechanisms (*211*). For example, LA only undergoes the HAT mechanism to form products such as lipid hydroperoxide (HPODEs), including 9-*trans,cis*(*tc*)-, 9-*trans,trans*(*tt*)-, 13-*tt*-, and 13-*tc*-HPODE

(**Figure 4.6a**) while CLA 18:2 can undergo both HAT and PRA mechanism. The oxidation mechanism and products from nonconjugated PUFAs have been studied intensively, but the oxidation product profiles of CLA 18:2, especially those from the PRA reaction, are not well characterized.

Based on the elucidated peroxidation mechanism and kinetics of CLA 18:2 (*211*), we predicted that the oxidation product profiles of CLA 18:2 would contain two different sets of products. The first set would comprise oxidation products formed from the HAT mechanism. Specifically, abstraction of the H-atoms at either C9 or C14 positions would lead to the formation of 9-*tc*-, 10-*tt*-, 13-*tt*-, and 14-*tc*-HPODE (**Figure 4.6b**). The second set of oxidation products would comprise PRA-derived products such as 12- and 10-allylic epoxides. To elucidate the oxidation products from CLA 18:2, we carried out free radical oxidation using 2,2'-azobis(4-methoxy-2,4-dimethylvaleronitrile) (MeOAMVN) as the radical initiator, reduced the reaction mixture with triphenylphosphine, which would reduce the lipid hydroperoxides formed into corresponding alcohols (HODEs) and analyzed the products using normal phase HPLC-UV at 234 nm. Here, we identified 9-*tc*-, 10-*tt*-, 13-*tt*-, and 14-*tc*-HODE from the chromatogram of CLA 18:2 by comparing the retention times of the potential peaks to those of the HODEs from the oxidation of LA (**Figure 4.7a**). Interestingly, many additional peaks were observed in the chromatogram of CLA 18:2, suggesting a much more complex mixture of products from the oxidation of conjugated PUFAs. When the reaction mixture was reduced to dienyl diols (HODOLs) using $LiAlH_4$ (*211*), a much stronger reducing reagent than triphenylphosphine, a much cleaner chromatogram was observed for CLA 18:2, and the retention times of 9-*tc*, 10-*tt*, 13-*tt*, and 14-*tc* peaks were assigned by comparing with the peaks found from LA oxidation (**Figure 4.7b**). However, we were not able

to identify allylic epoxides from the oxidation of CLA 18:2, which could be because these products could not survive the reduction conditions.

On the other hand, peroxide dimers and polymers were previously identified as the major oxidation products of conjugated PUFAs, especially during the initial oxidation stage (*252-255*). Interestingly, volatile aldehyde compounds were also detected in CLA 18:2-rich oil and purified TAGs. using solid phase microextraction-gas chromatography (SPME-GC) (*256*). Therefore, we proposed here a schematic of the PRA mechanism for CLA 18:2 that can potentially account for the formation of lipid dimers and polymers and, subsequently, lipid aldehydes (**Figure 4.8a**). Specifically, the carbon radical formed after PRA to C13 of CLA 18:2 can undergo the homolytic substitution (S_Hi) to form allylic epoxide or react with another molecular oxygen, leading to the formation of another peroxyl radical. This radical can then abstract H-atom from another lipid, forming a di-peroxide lipid. Alternatively, this peroxyl radical can also add to the double bond of another CLA 18:2 molecule leading to peroxide dimers and polymers. The lipid dimers and polymers can then undergo "unzipping" reactions leading to the formation of the α,β-unsaturated aldehyde **1** and the saturated aldehyde **2**, which is hexanal. Such "unzipping" reactions have been well-studied using styrene-peroxide polymers (*2*). Similarly, the PRA reaction at C10 of CLA 18:2 can lead to the formation of the saturated aldehyde **3** and the α,β-unsaturated aldehyde **4**, 2-*trans*(*t*)-octenal (**Figure 4.8b**). A similar PRA mechanism can also be applied for CLA 18:3, which suggests the formation of the saturated aldehyde pentanal (**5**) and the α,β,δ,γ-unsaturated aldehyde, which we call conjugated dienal for short, aldehyde 2,4-*tt*-nonadienal as the major oxidation products (**Figure 4.9**).

To elucidate the electrophilic aldehydes formed from the oxidation of conjugated PUFAs, we carried out free radical oxidation of CLA 18:2, CLA 18:3, and CLA 18:3-rich tung oil in

benzene at 37 °C using MeOAMVN. After 2h, the reaction was quenched with butylated hydroxytoluene and triphenylphosphine. While we used β-eleostearic acid as CLA 18:3 in this study, tung oil is composed of TAGs in which 80% of the total acyl chains are esterified α-eleostearic acid. Therefore, we used tung oil as the model for the oxidation of TAG-incorporated CLA 18:3 as well as to confirm the oxidation products from both isomers. In addition, we also carried out free radical oxidation of LA to compare the aldehyde formation from LA versus CLA 18:2 oxidation. To capture the volatile aldehydes, we purged the reaction vials with N_2 gas and captured the vapor using cartridges containing 2,4-dinitrophenylhydrazine (DNPH), which derivatizes aldehydes to hydrazone, as described previously (**Figure 4.10a**) (*257-259*). The remaining mixtures in the vial was also treated with DNPH under acidic conditions. Then, both the DNPH-treated air (from the vapor) and solution (from the reaction vial) samples were analyzed using reverse-phase LC (RPLC)-MS and MS/MS fragmentation in the negative ion mode. The fragmentation spectra detected were compared to a series of commercially available aldehydes to confirm the identity of aldehydes formed from each oxidation mixture (**Figure 4.10b**).

Overall, we observed that the air samples gave much cleaner total ion chromatograms compared to the solution ones (**Figure 4.11**). From the air samples of CLA 18:2 and CLA 18:3, we detected hexanal and 2-*t*-octenal (**Figure 4.10c**) as well as pentanal and 2,4-*tt*-hexadienal (**Figure 4.10d**), which are the predicted oxidation products from the PRA mechanism of CLA 18:2 and CLA 18:3, respectively (**Figure 4.8** and **Figure 4.9**). The fragmentation patterns of these aldehydes matched those prepared from the commercially available aldehyde standards, confirming their identities (**Figure 4.12** and **Figure 4.13**). In addition, we found that both CLA 18:3 and tung oil oxidation led to the formation of 2,4-*tt*-hexadienal and the α,β–unsaturated aldehyde 2-*t*-heptenal while the levels of 2-*t*-octenal, 2-*t*-nonenal, and 4-HNE detected were

negligible in both samples (**Figure 4.14a, b**). These results suggest that similar volatile aldehydes are formed in the oxidation of both free and TAG-incorporated CLA 18:3 as well as in both CLA 18:3 isomers.

Like CLA 18:2, the oxidation of LA also led to the formation of 2-*t*-octenal, as well as other α,β-unsaturated aldehydes, including 2-*t*-heptenal and 4-HNE (**Figure 4.14c, d**). Interestingly, in the air samples, while 2-*t*-nonenal were detected from the oxidation of CLA 18:2, the detection of this aldehyde in the oxidation of LA is negligible, which is consistent with previously reported results (*256*) (**Figure 4.14c, d**). We then roughly compared the level of each aldehyde from the oxidation of CLA 18:2 versus LA by comparing the total area under the curve from both air and solution samples of the aldehyde peaks. We found that while the levels of the saturated aldehydes, including pentanal and hexanal, were comparable between LA and CLA 18:2 oxidation, the levels of the α,β-unsaturated aldehydes were significantly different between the two groups. Specifically, 4-HNE, which has been established as the most abundant stable product from the oxidation of ω-6 nonconjugated PUFAs (*2, 260*), was detected at a higher level in LA oxidation compared to CLA 18:2 oxidation (**Table 4.7**). On the other hand, the levels of 2-*t*-heptenal, 2-*t*-octenal, and 2-*t*-nonenal were higher in CLA 18:2 compared to LA.

We next sought to compare the cytotoxicity of the aldehydes by treating the cells with each aldehyde and compared their viability after 24 h. The unsaturated aldehydes, especially the conjugated dienals, are highly reactive electrophiles that can readily form adducts with nucleophiles and, thus, were predicted to be highly toxic to the cells. As expected, we found that the unsaturated aldehydes were much more toxic to the cells than the saturated ones (**Table 4.8**). In addition, the conjugated dienals were more toxic than the α,β–unsaturated ones with the same alkyl chain length; for example, 2,4-*tt*-nonadienal (EC_{50} = 13 μM) was twice more toxic than 2-*t*-

nonenal (EC_{50} = 25 μM). Importantly, we found that 2,4-*tt*-nonadienal was as toxic to the cells as 4-HNE, which is known for its high cytotoxicity and implications in various pathologies (*260, 261*). Thus, the formation of 2,4-*tt*-nonadienal from the PRA reaction of CLA 18:3 can potentially contribute to the high toxicity of this fatty acid. Moreover, we found the longer-chain aldehydes to be more toxic than the shorter-chain ones. This observation is consistent with previous findings that because longer lipid aldehydes are more hydrophobic than the shorter ones, the modification of protein side chains by these aldehydes would increase protein surface lipophilicity, leading to protein structural changes and aggregation (*262*). In addition, the higher lipophilicity of longer lipid aldehydes would allow them to diffuse more easily into the cells, making them more biologically available.

4.2.3 The Addition of Exogenous Conjugated PUFAs Leads to Increased Protein Damage and ER stress.

To elucidate the mechanism underlying the lethality of conjugated PUFAs, we carried out RNA sequencing (RNA-seq) to investigate transcriptomic changes in treatments with either CLA 18:3 or RSL3+CLA 18:2 compared with vehicle controls and cells treated with RSL3+LA. Overall, compared with the control, the addition of CLA 18:3 and RSL3-CLA 18:2 led to 318 and 560 differentially expressed genes (DEGs), respectively (adjusted p-value < 0.05, > 2-fold change) (**Figure 4.15a**). While CLA 18:3 upregulated 216 genes and downregulated 102 genes, RSL3-CLA 18:2 upregulated 295 genes and downregulated 265 genes. Among the DEGs, 182 genes were coregulated by both CLA 18:3 and RSL3-CLA 18:2, and 136 and 378 genes were uniquely regulated by CLA 18:3 and RSL3-CLA 18:2, respectively. Among the commonly upregulated genes between CLA 18:3 and RSL3- CLA 18:2, there were genes that were previously found to

associate with ferroptosis, including *DDIT4, HMOX1, SLC7A11, FTH1, FTL1,* and *GCLM* (*84, 100, 234*).

To carry out pathway analyses of DEGs in the CLA 18:3 versus control comparison, we utilized the integrated Differential Expression and Pathway (iDEP) web application and iPathwayGuide (iPG) software (*263, 264*). Only pathways that are identified to be significantly altered by both tools are reported. In iDEP, the thresholds for gene significance were set as FDR < 0.05 and minimum fold change of 2. In addition, for the pathway analysis module in iDEP, we chose the GAGE analysis method with pathway significance cutoff at 0.05 (FDR < 0.05) (*265*). For pathway analysis using iPG, the FDR *p*-value correction was applied. By applying this pathway analysis method, we identified proteasome, ribosome, and protein processing in endoplasmic reticulum (ER) among the top significantly activated KEGG pathways (**Figure 4.15c**, **Table 4.9**). We also used the network-creating function of iDEP to identify clusters of related pathways. Even though there were no significant pathways identified for the cellular component in the gene ontology (GO) enrichment analysis, we observed clusters related to proteasome, ribosome, and protein processing in the ER among the biological process and molecular function networks (FDR < 0.05) (**Figure 4.16**).

Previously, the ferrroptosis inducers erastin and sorabfenib, which inhibit system x_c^-, were found to induce significant ER stress and the activation of the unfolded protein response (*84, 133*). Therefore, we investigated whether the genes associated with ER stress and unfolded protein responses were upregulated in the treatment with CLA 18:3 compared to the control. Indeed, we observed a significant upregulation of *HSPA5* (adjusted *p*-value < 2.23E-308, fold change = 2.4) encoding for HSP70 chaperone BiP, the master regulator of the unfolded protein response (*266*). In addition, genes associated with the PERK/EIF2a/ATF4 branch of the unfolded protein response,

including *DDIT4* (padj = 3.31E-39, fold change = 5.39), *DDIT3* (padj = 1.29E-23, fold change = 3.66), and *CHAC1* (padj = 1.30E-26, fold change = 3.61) were significantly upregulated upon the addition of CLA 18:3 (*267-269*). Additionally, we further examined the expression patterns of the significant DEGs (adjusted *p*-value < 0.05, > 2-fold change) in CLA 18:3-treated cells by utilizing the Database for Annotation, Visualization and Integrated Discovery (DAVID) web server (*270*). DAVID functional clustering analysis identified the gene cluster related to unfolded protein response in the ER as the most enriched subset of genes with an enrichment score of 3.62 (**Table 4.10**). Together, the pathway analysis results from iDEP, iPG, and DAVID suggest that the addition of CLA 18:3 in HT-1080 cell line lead to increased protein damage and ER stress compared to the control.

Furthermore, we also used the upstream regulator analysis module of iPG to examine transcriptional regulators of gene expression and identified M-phase protein 6 (MPHOSPH6), C1D nuclear receptor corepressor (C1D), and DIS3 homolog, exosome endoribonuclease and 3'-5' exoribonuclease (DIS3) as the most significantly activated upstream regulators in the CLA 18:3 versus control comparison (**Figure 4.15e**). This prediction was based on combined *p*-values (2.23E-17, 2.23E-17, and 3.55E-17 for MPHOSPH6, C1D, and DIS3, respectively), which were calculated based on the number of DEGs supporting the hypothesis that the regulator is activated and the total number of DEGs downstream of the regulator. Interestingly, MPHOSPH6, C1D, and DIS3 activated similar DEG targets, which are the genes encoded for large ribosomal subunits (**Figure 4.15h** and **Table 4.11**, only the gene targets of MPHOSPH6 are shown). In addition, the following three most significantly activated upstream regulators in the CLA 18:3 versus control comparison, including eukaryotic translation initiation factor 5 (EIF5) (p = 1.85E-10), casein kinase 1 epsilon (CSNK1E) (p = 6.27E-10), and BUD23 rRNA methyltransferase and ribosome

maturation factor (BUD23) (p = 1.05E-09), also activated similar targets which are small ribosomal subunit-encoded genes (**Figure 4.15i** and **Table 4.12**, only the gene targets of EIF5 are shown). We further examined the expression patterns of the significant DEGs (adjusted p-value < 0.05, > 2-fold change) in CLA 18:3-treated cells by utilizing the Database for Annotation, Visualization and Integrated Discovery (DAVID) web server (*270*). DAVID functional clustering analysis identified the gene cluster related to unfolded protein response in the ER as the most enriched subset of genes with an enrichment score of 3.62 (**Table 4.10**). Together, the pathway analysis results from iDEP, iPG, and DAVID suggest significantly increased protein damage in CLA 18:3-treated cells compared to the control.

To identify CLA-specific transcriptomic changes, we then compared the RNA-seq results between RSL3-CLA 18:2 versus control comparison and RSL3-LA versus control comparison. Overall, the treatment with RSL3-LA only led to significant changes in 69 differentially expressed genes (DEGs) compared to the control (adjusted p-value < 0.05, > 2-fold change) (**Figure 4.15b**). Among the significantly altered genes, 33 and 36 genes were up- and downregulated, respectively. Among the significant DEGs identified in RSL3-CLA 18:2- and RSL3-LA-treated cells, only 43 genes were coregulated by both treatment groups, while 136 and 378 genes were uniquely regulated by RSL3-CLA 18:2 and RSL3-LA, respectively. Notably, pathway analyses of DEGs of the RSL3-CLA 18:2 versus control comparison using iDEP and iPG identified only two significantly activated KEGG pathways, which are protein processing in the ER and proteasome (**Figure 4.15d** and **Table 4.9**). On the other hand, no significantly altered pathways were identified by in the RSL3-LA versus control comparison. Moreover, MPHOSPH6, C1D, and DIS3 were also identified as the most activated upstream regulators in both treatments with RSL3-CLA 18:2 and RSL3-LA. However, the level of activation of these regulators was much more significant in the

RSL3-CLA18:2 versus control comparison compared to the RSL3-LA versus control comparison. Specifically, in the RSL3-CLA18:2 versus control comparison, the combined *p*-values of MPHOSPH6, C1D, and DIS3 are 1.11E-05, 1.11E-05, and 5.14E-0.5 (FDR-corrected), respectively. In contrast, in the RSL3-LA versus control comparison, the FDR-corrected combined *p*-values of MPHOSPH6 and C1D are only 0.029 for both, and the activation of DIS3 is statistically insignificant with the combined *p*-value of 0.10. Moreover, in RLS3-CLA 18:2-treated cells, the subset of genes related to unfolded protein response in the ER was identified by DAVID functional clustering analysis with an enrichment score of 1.56 (**Table 4.10**), but this subset of genes was not identified in the RLS3-LA-treated cells. In addition, genes associated with the PERK/EIF2a/ATF4 branch of the unfolded protein response, including *DDIT4* (padj = 4.73E-14, fold change = 2.65), *DDIT3* (padj = 1.29E-05, fold change = 1.82), and *CHAC1* (padj = 0.013, fold change = 1.42) were upregulated in RLS3-CLA 18:2-treated cells, albeit to a much lesser extent compared to the addition of CLA 18:3. In contrast, only *DDIT4* (padj = 0.012, fold change = 1.47) were identified among DEGs in RLS3-LA-treated cells. Therefore, the pathway analyses of the RNA-seq data suggest that protein damage is more significant in the addition of conjugated PUFAs compared to the addition of their nonconjugated counterparts.

4.2.4 Combined Treatment of RSL3 and CLA 18:2 Leads to Protein Adduct Formation

Due to the predicted high levels of lipid aldehyde formation from the oxidation of conjugated PUFAs and the suggested significant protein damage from the RNA-seq results, we predicted that the addition of conjugated PUFAs would lead to a much larger extent of protein modifications compared to their nonconjugated counterparts. In recent years, terminal alkynylated probes have been utilized to visualize and isolate protein adducts of PUFAs and their lipid electrophiles (*235, 271-274*). Therefore, here, we sought to visualize the protein modifications in

cells treated with RSL3 in the presence of either LA or CLA 182. While the alkynylated LA was previously synthesized (*235*) and is commercially available, there is currently no alkynylated CLA 18:2 available. Instead, considering the significant incorporation of LA and CLA 18:2 into TAGs (Fig. 2c), we propose the synthesis of alkynylated TAGs containing one alkynyl stearoyl chain (a18:0) and two LA (N18:2) or CLA 18:2 (C18:2) to yield TAG (a18:0/N18:2/N18:2) and TAG (a18:0/C18:2/C18:2), respectively (**Figure 4.17a**). To deliver the alkynylated TAGs into HT-1080 cells, we prepared liposomes from DMPC with either TAG (a18:0/N18:2/N18:2) (DMPC-aLA) or TAG (a18:0/N18:2/N18:2) (DMPC-aCLA) in 1-to-1 ratio (1:1 DMPC:TAG). Next, HT-1080 cells were cultured in the presence of DMPC only-liposome as control or RSL3 with either aNLA-liposome or aCLA-liposome (**Figure 4.17b**). As lipid peroxidation increased inside the cells, CLA 18:2 acyl chains on TAGs could lead to the formation of the free aldehydes **1** and **3** and the truncated lipid aldehydes **2** and **4** (as proposed in **Figure 4.8a, b**). The highly electrophilic α,β–unsaturated lipid aldehyde that remained on the TAG backbone could then modify proteins within proximity via either Michael or Schiff-base adducts (**Figure 4.17b**). The cells were then lysed, and the Michael and imine adducts were stabilized via the reduction using $NaBH_4$ prior to "Click" reaction with azide-linked biotin. The biotin-modified adducts were then detected and visualized using western blots probed with a streptavidin-conjugated fluorophore.

We were able to detect increased protein modifications in cells treated with RLS3+DMPC-aCLA and RSL3+DMPC-aLA (**Figure 4.18**). However, we noticed that DMPC-aCLA did not lead to a much higher level of protein adducts compared to DMPC-aLA. We speculate that the uptake of the CLA-TAG into the cells was efficient, leading to a reduction in lipid peroxidation and formation of oxidation products compared to the free fatty acids. Nonetheless, we still observed an increased protein adduct formation in DMPC-aCLA18:2, indicating that CLA 18:2 and its

oxidation products can indeed lead to significantly increased protein modifications under ferroptotic conditions.

4.3 Discussion

The lipidomic results suggest that distinct cellular organelles and pathways are involved in the activation and incorporation of LA and CLA 18:2 into neutral lipids and phospholipids. For example, while the addition of LA led to a moderate increase in the levels of various TAG species, the addition of 18:2 led to a much larger increase in specific TAGs (**Figure 4.3a**), especially 54:6 TAG (18:2/18:2/18:2), suggesting the potential accumulation of lipid droplets. The modulatory role of lipid droplets in ferroptosis is still under debate. Specifically, lipid droplets have been regarded as an antioxidant organelle that can sequester PUFAs away from the membrane and protect cells from oxidative damage and ferroptosis (*142-144*). On the other hand, lipid droplets can act as a reservoir that supplies PUFAs for membrane phospholipid synthesis (*141*). Indeed, the accumulation of PUFA-containing TAGs in lipid droplets, which can be catalyzed by ACSL1 or ACSL3, was shown to increase cell susceptibility to ferroptosis (*75, 76, 145*). In addition, it has been suggested that lipid droplets accumulate during the early stage of ferroptosis but break down as cell death progresses, leading to an increase in PUFA-containing membrane phospholipids and promoting ferroptosis sensitivity (*275, 276*). Furthermore, lipid droplet viscosity was shown to increase during erastin- and RSL3-induced ferroptosis in different cancer cell lines while remaining the same in the cotreatment of erastin and Fer-1 (*147*). It has been suggested that membrane viscosity is increased after lipid peroxidation due to a reduction in in the ratio of PUFAs to saturated FA in the membrane and the interaction between lipid-derived aldehydes and membrane phospholipids (*130-132, 277*). Thus, lipid droplets can potentially be additional sites where lipid peroxidation happens. Therefore, we postulate that the accumulation of highly

oxidizable conjugated PUFAs into TAGs can lead to lipid peroxidation within lipid droplets, contributing to ferroptosis sensitivity. Further investigation is necessary to elucidate whether the accumulations of conjugated PUFAs into neutral lipids and lipid droplets are essential for conjugated PUFA-induced ferroptosis.

Interestingly, we found that the addition of CLA 18:2 led to a significant increase in the normalized abundance of long-chain and highly unsaturated ether phospholipids, while the levels of these lipids were not significantly altered in LA-treated cells (**Figure 4.3d, e**). Furthermore, we observed the incorporation of fatty acid 18:2 into the *sn*-1 position of the significantly elevated ether-PEs, suggesting the involvement of peroxisome in facilitating the incorporation of exogenous CLA 18:2 into ether lipids (**Figure 4.4d-f**). Specifically, the biosynthesis of ether lipids starts in peroxisome, where fatty acids are activated into acyl-CoA, reduced into fatty alcohol, which was then used to displace the acyl chain of the *sn*-1 position of acyl-dihydroxyacetone, the precursor of ether lipid synthesis (*251*). The exchange of the acyl chain for an alkyl group leading to the formation of the ether bond at the *sn*-1 position is the rate-limiting step in ether lipid biosynthesis and is facilitated by alkylglycerone phosphate synthase (AGPS). Subsequently, the completion of ether lipid synthesis, including the acylation of fatty acids into the *sn*-2 position of the glycerol backbone, happens in the ER.

Plasmalogens were reported to inhibit iron-induced lipid peroxidation in early studies (*250, 278*) and suppress ferroptosis in both *Caenorhabditis elegans* and cancer cells in a recent study (*279*). However, ether phospholipids and their peroxisome-driven biosynthesis were also shown to promote ferroptosis recently (*69, 139*). In addition, the loss of FAR1, an essential enzyme in ether lipid synthesis, was reported to promote resistance to erastin treatment, indicating the function of ether lipids in sensitizing cells to ferroptosis (*109*). Therefore, the significant

incorporation of CLA 18:2 into the pro-ferroptotic ether lipids can potentially contribute to the difference in their potency in promoting ferroptosis compared to LA. Notably, Zou *et al.* previously concluded that the PUFA moiety, not the alkenyl ether group, which contained the non-oxidizable fatty acid 18:0 in that study, on plasmalogens is essential in potentiating ferroptosis (*69*). Perhaps, when a reactive fatty acid such as CLA 18:2 is incorporated into the *sn*-1 position, this position can contribute to membrane lipid peroxidation and ferroptosis induction. Indeed, the vinyl-ether bond was shown to disappear simultaneously during lipid peroxidation, indicating that the *sn*-1 position is also prone to radical attack (*250*). Furthermore, the proximal regions of the *sn*-1 and *sn*-2 fatty acid chains are in parallel orientation and close proximity to each other due to the *sn*-1 vinyl-ether bond of plasmalogens (*251*). Since ether lipids are the major structural component of the cellular membrane, the close alignment of *sn*-1 and *sn*-2 fatty acid chains can lead to tighter packing of membrane phospholipids (*251*), leading to the rapid propagation of lipid peroxidation among the oxidizable PUFAs. Therefore, the addition of exogenous CLA 18:2 may reorient the cellular lipidome in a manner that favors lipid peroxidation and ferroptosis. Moreover, it should be noted that the role of AGPS-dependent ether lipid synthesis in ferroptosis was recently reported to be only context-dependent since the disruption of this process was found to have little effect on erastin2- or RSL3-induced cell death (*66*). Therefore, the synthesis of ether lipids may be more relevant to the lethality of RSL3-CLA 18:2 cotreatment, which distinguishes the lethal mechanism potentiated by exogenous conjugated PUFAs from cell death induced by the canonical ferroptosis inducers. Further investigation is necessary to elucidate the importance of ether lipid biosynthesis in conjugated PUFA-induced ferroptosis.

Compared to the oxidation of LA, the oxidation of CLA 18:2 led to much more complex oxidation product profiles (**Figure 4.7a**), owing to the contribution of both the HAT and PRA

mechanisms to the propagation step. Indeed, lipid hydroperoxides, which are the major primary products from the oxidation of nonconjugated PUFAs, were shown to only be minor products during the initial stage of oxidation in conjugated PUFAs (*254, 255, 280*). Instead, peroxide dimers and polymers were detected as the major primary oxidation products of conjugated PUFAs (*252-255*). However, the mechanism leading to the formation of these products has not been provided. Here, we proposed a mechanism of PRA to the conjugated double bonds of CLA 18:2 and CLA 18:3 that accounts for the formation of such dimers and polymers (**Figure 4.8** and **Figure 4.9**).

The difference in the lipid peroxidation mechanism between the nonconjugated and conjugated PUFAs also leads to the difference in their secondary oxidation products, including the electrophilic byproducts, from the decomposition of primary peroxides. For example, the decomposition of the 9- and 13-HPODEs from the HAT mechanism of LA can lead to the formation of highly electrophilic products such as 4-HNE (*2, 281*). In contrast, since 10- and 14-HPODEs are also formed in addition to 9- and 13-HPODEs from the HAT mechanism of CLA 18:2 (**Figure 4.7a**), an isomer of 4-HNE can potentially form as a secondary product of CLA 18:2 oxidation. In addition, the decomposition of the peroxide dimers and polymers from the PRA mechanism of CLA 18:2 can potentially lead to the formation of α,β-unsaturated aldehydes such as 2-*t*-octenal and the aldehyde **3** (**Figure 4.8**). We indeed detected 2-*t*-octenal at a much higher level from the oxidation of CLA 18:2 compared to the oxidation of LA (**Figure 4.14c, d** and **Table 4.7**). In addition, 2-*t*-nonenal was detected from the oxidation mixture of CLA 18:2, but its level was negligible from the oxidation of LA (**Figure 4.14**). In line with our findings, García-Martínez *et al.* reported the formation of a much more complex mixture of volatile oxidation compounds from the oxidation of oil and TAGs rich in CLA 18:2 compared to those rich in LA (*256*). In addition, the concentration of total volatile oxidation compounds was much higher in CLA 18:2-

TAG than in LA-TAG. Importantly, García-Martínez *et al.* reported that 2-*t*-octenal and 2-*t*-nonenal were detected among the major oxidation products of CLA 18:2 and their levels were much higher in oil and TAGs rich in CLA 18:2 compared to those rich in LA (*256*), confirming the significant formation of these electrophiles from the oxidation of CLA 18:2. In the case of CLA 18:3 and tung oil rich in α-eleostearic acid, 2,4-*tt*-nonadienal, which we proposed to form from the PRA mechanism of CLA 18:3 (**Figure 4.9**), was detected as the major electrophilic aldehydes (**Figure 4.14a, b**).

We also showed that the unsaturated aldehydes, including 2-*t*-octenal, 2-*t*-nonenal, and 2,4-*tt*-nonadienal, detected from the oxidation of conjugated PUFAs are highly toxic in HT-1080 cell lines (**Table 4.8**). Notably, 2,4-*tt*-nonadienal, with its conjugated double bond system, was as toxic as 4-HNE, which is considered one of the most abundant toxic lipid peroxidation products (*260, 261*). Terminal unsaturated aldehydes are highly electrophilic and can lead to significant protein modifications via Michael adduction at cysteine, histidine, and lysine residues and Schiff base formation at lysine residue. Indeed, reactions between proteins and 2-*t*-octenal were previously reported to result in significant losses of histidine and lysine residues (*282, 283*). In addition, 2,4-*tt*-nonadienal can modify the protein side chains, leading to substantial protein structural alterations and aggregations (*262*). Moreover, it is In the context of ferroptosis, significant protein modifications by lipid-derived electrophiles were detected in HT-1080 cells treated with RSL3 (*284*). Furthermore, in addition to protein modifications, the execution phase of ferroptosis also involves pore formation in the plasma membrane, leading to increased cell swelling and calcium influx and, eventually, cell rupture (*123, 124*). Importantly, pore formation on lipid membrane was only observed for lipid-derived aldehydes, not lipid peroxides, owing to their shorter and highly mobile tails (*285*). Together, these findings highlight the importance of lipid-derived electrophiles

in the execution of ferroptosis. In fact, impaired detoxification of lipid-derived electrophiles was recently suggested to be a hallmark of ferroptosis (*286*). Thus, we hypothesize that the accumulation of the highly toxic electrophilic aldehydes contributes to the high potency of conjugated PUFAs in potentiating ferroptosis.

Indeed, pathway analysis from RNA-seq results suggests increased protein damage and ER stress in cells treated with conjugated PUFAs (Fig. 7). Specifically, in conjugated PUFA-treated cells, we observed an upregulation of unfolded protein response (**Table 4.10**), indicating the accumulation of unfolded or misfolded protein in the ER, which was previously reported for highly toxic electrophiles such as 4-HNE (*261*). Previously, ER stress and the upregulation of *CHAC1* were thought to associated specifically with ferroptosis induction via the depletion of cysteine, not other ferroptosis-inducing mechanisms (*84, 133*). However, we demonstrated in this study that the addition of conjugated PUFAs, especially CLA 18:3 can lead to significant increase in ER stress and upregulation of *CHAC1*. Notably, *DDIT3* (CHOP), the upstream regulator of *CHAC1,* acts in the opposite of the chaperone BiP to activate the apoptosis signaling pathways under prolonged ER stress (*268, 287, 288*). Here, we found a significant upregulation of *DDIT3* in CLA 18:3-treated cells. Interestingly, treatment of HT-1080 cell line with CLA 18:3 led to significant upregulation of various ribosomal large and small subunits (**Table 4.11** and **Table 4.12**) . Previous studies have shown that the ribosome is a part of the integrated stress response, which can be activated by ER stress, and that ribosomal proteins possess extraribosomal functions, including the promotion of cell death (*289, 290*). Importantly, CHOP was found to promote cell death via the activation of PPP1R15A, which we found to be significantly upregulated in CLA 18:3-treated cells (padj = 1.99E-217, fold change = 3.07), leading to the promotion of protein synthesis to further enhance ER stress and initiate cell death (*291, 292*). Therefore, we speculate that the upregulation of

ribosomal proteins is in part activated by CHOP and can potentially contribute to the execution of CLA 18:3-induced ferroptosis.

In addition, despite the CLA 18:2-containing TAGs not being the best models for the studying of conjugated PUFAs in ferroptosis, we detected an increase in protein adduction in cells treated with CLA 18:2 compared to the control (**Figure 4.18**). Furthermore, the lysine residues of KEAP1 can be modified by electrophilic lipid oxidation products, leading to its dissociation from the transcription factor NRF2, which in turn activate the transcription of the enzymes in the antioxidant-responsive elements (AREs) (*293, 294*). In fact, we detected upregulations of many gene targets of NRF2, such as *NQO1* (NADPH quinone oxidoreductase-1), *HMOX1* (heme oxygenase-1), *GCLM* (glutamate-cysteine ligase catalytic subunit), *SLC7A11* (solute carrier family 7 member 11), and *AIFM2* (ferroptosis suppressor protein 1), in both RSL3-CLA 18:2 and CLA 18:3-treated cells, suggesting significant activation of AREs in response to the accumulation of lipid-derived electrophiles from the oxidation of conjugated PUFAs. Together, these results suggest that conjugated PUFAs undergo lipid peroxidation in the cell membrane, leading to a significant accumulation of lipid-derived electrophiles, which can modify proteins and sensitize cells to ferroptosis.

4.4 Experimental Procedures

4.4.1 Cell Lines and Culture Condition**.**

HT-1080 was obtained from American Type Culture Collection (ATCC) and grown in DMEM High-Glucose media (Gibco) containing 10% fetal bovine serum (FBS; Gibco), 1% MEM non-essential amino acids (Gibco), and 1% Penicillin-Streptomycin (Pen-Strep, 10,000 U/mL; Gibco).

4.4.2 Chemicals

Pentanal, hexanal, 2-*trans*-heptenal, 2-*trans*-octenal, 2-*trans*-nonenal, 2,4-*trans,trans*-hexadienal, 2,4-*trans,trans*-nonadienal, and 2,4-*trans,trans*-decadienal were obtained from Sigma-Aldrich. 2,4-dinitrophenylhydrazine (DNPH) and LpDNPH S10L cartridges were purchased from Thermo Fisher Scientific. DMPC was obtained from Avanti Polar Lipids. RSL3 was obtained from MedChemExpress. 4-hydroxynonenal (4-HNE) was purchased from Cayman Chemical. The radical initiator, MeOAMVN, was purchased from Wako Chemicals.

4.4.3 Lipidomics Analysis

Triplicate samples of HT-1080 cells at ~60% confluence were incubated with vehicle (DMSO), 5 nM RSL3, 5 nM RSL3 + 80 μM LA, 5 nM RSL3 + 80 μM CLA 18:2, and 3 μM CLA 18:3 overnight. The cell pellets harvested were resuspended in cold PBS and lysed by sonication on ice for 30 min. Protein concentration was measured using the Bio-Rad DC protein mass assay. Lipids were extracted using the Folch method as previously described (*248*). The extracted organic layer was transferred to a Pyrex glass centrifuge tube (Corning 99502-10) and dried in a speed vacuum concentrator (Thermo Fisher Savant). The dried lipid extracted was reconstituted in methylene chloride and stored at -80 ºC until analysis.

Prior to analysis, 50 ml of the extract was transferred in LC vials, dried under argon, and reconstituted in 50 ml of 90% methanol in water with 0.1% formic acid. A pooled quality control sample was prepared by combining an equal volume from each final sample into a separate LC vial. Chromatographic separation was performed using a Waters Acquity FTN ultraperformance liquid chromatography (Waters Corp, Milford, Massachusetts) with a hydrophilic interaction column (HILIC; Phenomenex Kinetex, 100x 2.1 mm, 1.7 μm) maintained at 40 ºC at a flow rate of 0.5 ml/min. A sample injection volume of 5 mL was used for both positive and negative mode

analyses. Mobile phase A consisted of acetonitrile/water (50:50, v/v) and mobile phase B was acetonitrile/water (95:5, v/v/v), both containing 5 mM ammonium acetate. The linear gradient was as follows: 0–1 min, 100% B; 4 min, 90% B; 7–8 min, 70% B; 9–12 min, 100% B.

Ion mobility-mass spectrometry (IM-MS) analysis was performed on the Waters Synapt G2-XS platform in both positive and negative modes. Capillary voltages of +3.0 and -2.0 kV were used for positive and negative modes, respectively. Other ESI conditions were as follows: sampling cone, 40 V; extraction cone, 80 V; source temperature, 100 ºC; desolvation temperature, 350 ºC; cone gas,10 L/h; and desolvation gas, 1000 L/h. Mass calibration over *m/z* 50-1200 was performed with sodium formate. Collision cross-section calibration was performed as previously described (*248*). IM separation was performed with a traveling wave velocity of 500 m/s and wave height of 40 V. Data was acquired for *m/z* 50-1200 with a 0.5 s scan time. Leucine enkephalin was acquired as a lockspray signal for post-acquisition correction of mass and drift time.

Data alignment, peak detection, and normalization were performed in Progenesis QI (Nonlinear Dynamics). The chromatographic region between 0.4 and 8.5 min was considered for peak detection. The prepared pooled QC sample was used as reference sample for alignment and data were normalized to all compounds. The resulting data set was filtered by analysis of variance (ANOVA) p-value < 0.05. Principal components and additional multivariate statistical analyses were performed in EZInfo (Umetrics). Lipid identifications were made based on *m/z* (within 0.01 Da mass accuracy), retention time (within 0.3 min accuracy), and CCS (within 3.0 $Å^2$ accuracy), using LiPydomics (*249*). Only lipid identifications that satisfied all three levels of identification, including *m/z,* retention time, and CCS, were considered. Data are presented as mean ± standard deviation. Statistical analyses relative to control were conducted using Student's t test assuming unequal variance with a Bonferroni correction for multiple comparisons

Lipids of interest for MS/MS fragmentation were selected based on two criteria: 1) the lipids have normalized abundance over 8000 and 2) the fold increase in normalized abundance compared to the control is at least one. The targeted MS/MS fragmentation *m/z* was performed in the transfer region with a collision energy ramp of 25-40 V with 0.2 s scan time. The fragmentation and composition of lipids were confirmed using LIPID MAPS Structure Database.

4.4.4 Detection of DNPH-derivatized Aldehydes Using Reverse-phase MS and MS/MS

The DNPH-derivatized aldehydes from the oxidation mixture were separated via reverse-phase chromatography with the following conditions: C18 column (Kinetex, 100mm x 2.1mm, 1.7 μm particle diameter; Phenomenex); flow rate, 0.3 ml/min; and gradient elution method with solvent A (water) and solvent B (methanol) was used: 0 min, 80% B; 9 min, 95% B; 12-15min, 80% B. Untargeted MS and targeted MS/MS fragmentation analysis of the oxidation samples was performed on the Waters Synapt G2-XS platform in negative mode with 0.25 s scan time. Capillary voltage of -2.0 kV was used. Other ESI conditions were as follows: sampling cone, 40 V; extraction cone, 80 V; source temperature, 100 ºC; desolvation temperature, 350 ºC; cone gas,10 L/h; and desolvation gas, 1000 L/h. Mass calibration over *m/z* 50-1200 was performed with sodium formate. The commercially available aldehyde standards were also derivatized with DNPH and fragmented to obtain the reference spectrum and the optimal fixed collision energy for each DNPH-derivatized aldehyde. The transfer collision energy used for each aldehyde was as follows: pentanal, 15 V; hexanal, 11 V; 2-*t*-heptenal, 14 V; 2-*t*-octenal, 14 V; 2-*t*-nonenal, 15 V; 4-HNE, 16V; 2,4-*tt*-hexadienal, 13 V; 2,4-*tt*-nonadienal, 16 V; and 2,4-*tt*-decadienal, 17. A pooled standard sample was prepared by combining each derivatized standard into a separate LC vial. Aldehyde identifications were made based on *m/z*, retention time, and fragmentation patterns of the targeted aldehyde from the pooled standards.

4.4.5 RNA Sequencing

Quadruplicate samples of HT-1080 cells at ~60% confluence were incubated with vehicle (DMSO), 10 nM RSL3, 10 nM RSL3 + 80 mM LA, 10 nM RSL3 + 80 mM CLA 18:2, and 5 mM CLA 18:3 overnight. Total RNA was isolated from each sample using the RNeasy kit (Qiagen) and sent to Novogene to perform the cDNA library construction and sequencing using the Illumina NovaSeq 6000 platform (150 base pairs paired-end, with sequencing depth above 20 million reads per sample). Novogene confirmed the RNA integrity and purity using the Agilent 2100 BioAnalyzer (Agilent Technologies Inc). All samples met Novogene requirements of library construction and were submitted for RNA sequencing. Raw RNA sequencing reads in FASTQ format were mapped to the human genome (hg38) using HISAT algorithm (*295*) and format conversions were performed using Samtools (*296*). FeatureCounts algorithm was used to quantify the aligned RNA-seq data as raw counts (*297*). DESeq2 R package was used to determine differentially expressed genes (DEGs) from raw counts in different conditions (*298*).

4.4.6 Synthesis of Alkylated TAGs

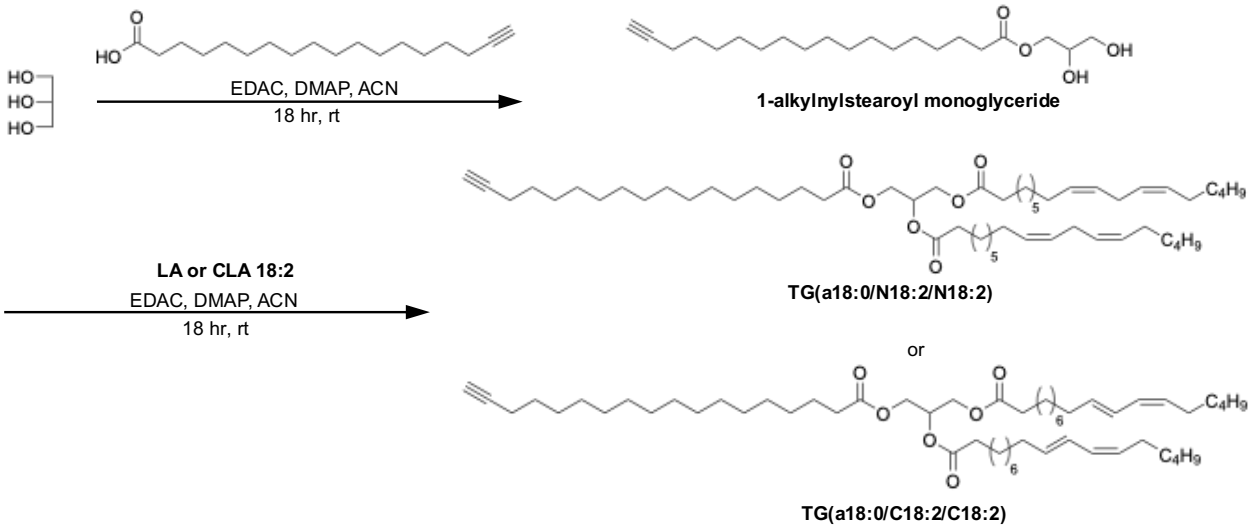

Synthesis of 1-alkynylated stearoyl monoglyceride. 1-(3-Dimethylaminopropyl)-3-ethyl-carbodiimide hydrochloride (EDAC; 98.0+ %, TCI America; 0.138 g, 0.72 mmol) was added to a

solution of alkynyl stearic acid (Click Chemistry Tool; 0.168 g, 0.6 mmol) and glycerol (99.5 %, anhydrous; ACS reagent; 0.512 g, 1.8 mmol) in 24 mL acetonitrile at 0 ºC. The reaction mixture was warmed to room temperature and stirred for 18 hr. After the reaction was completed, acetonitrile was evaporated under vacuum. Purification by column chromatography (50% ethyl acetate/hexanes) afforded the product as a white solid (0.195 g, 92 %). ^{1}H NMR (300 MHz, $CDCl_3$) δ 4.25 – 4.11 (m, 2H), 3.93 (ddd, *J* = 10.3, 5.8, 4.3 Hz, 1H), 3.74 – 3.55 (m, 2H), 2.35 (t, *J* = 7.5 Hz, 2H), 2.18 (td, *J* = 7.0, 2.6 Hz, 2H), 1.93 (t, *J* = 2.7 Hz, 1H).

Synthesis of TG(a18:0/N18:2/N18:2) and TG(a18:0/C182/C18:2). EDAC (0.032 g, 0.168 mmol) was added to a solution of LA or CLA 18:2 (0.118 g, 0.42 mmol) and 1-alkynylated stearoyl monoglyceride (0.05 g, 0.14 mmol) in 6 mL acetonitrile at 0 ºC. The reaction mixture was warmed to room temperature and stirred for 18 hr. After the reaction was completed, acetonitrile was evaporated under vacuum. Purification by column chromatography (50% ethyl acetate/hexanes) afforded the product as a white solid (0.195 g, 92 %). TG(a18:0/N18:2/N18:2) ^{1}H NMR (300 MHz, $CDCl_3$) δ 5.45 – 5.21 (m, 9H), 4.34 – 4.06 (m, 4H), 2.77 (t, *J* = 5.8 Hz, 4H), 2.31 (td, *J* = 7.5, 2.0 Hz, 6H), 2.18 (td, *J* = 7.0, 2.6 Hz, 2H), 2.05 (q, *J* = 6.7 Hz, 8H), 1.93 (t, *J* = 2.6 Hz, 1H). TG(a18:0/C182/C18:2) ^{1}H NMR (300 MHz, $CDCl_3$) δ 6.36 – 6.22 (m, 2H), 5.93 (t, J = 10.9 Hz, 2H), 5.64 (ddd, J = 14.7, 8.4, 5.6 Hz, 2H), 5.36 – 5.23 (m, 3H), 4.33 – 4.09 (m, 4H), 2.31 (td, J = 7.5, 1.8 Hz, 6H), 2.24 – 2.03 (m, 10H), 1.93 (t, J = 2.6 Hz, 1H).

4.4.7 Liposome Synthesis

53 μL chloroform solution of DMPC (4.0 μmol) was added to a 2 mL vial containing either TG(a18:0/N18:2/N18:2) or TG(a18:0/C182/C18:2) (4.0 μmol). For the DMPC liposome used as a control treatment, 109 μL chloroform solution of DMPC (4.0 μmol) was added to the vial. The solution from each vial was dried by a flow of N_2 and kept under vacuum for 10 min. 50 μL of

PBS buffer (80 mM, pH = 7.4) was added, and the mixture was sonicated for 10-20 s. The resulting milky suspension was incubated at 37 ºC for 10 min and sonicated for another 10-20 s. The liposome suspensions were stored at -80 ºC prior to usage.

4.4.8 Biotinylation of Alkynyl TAG-adducted Proteins in HT-1080 Cells

HT-1080 cells at ~60% confluence were incubated with 80 μM DMPC liposome (control), 5 nM RSL3 + 80 μM 1:1 DMPC:TG(a18:0/N18:2/N18:2) (aLA), and 5 nM RSL3 + 80 μM 1:1 DMPC: TG(a18:0/C18:2/C18:2) (aCLA) for 6 h. The cells were washed with cold PBS and harvested in 1mL cold lysis buffer supplemented with 150 mM NaCl (Fisher Chemical), 50 mM HEPES (Gibco), 0.1 % TritonX100 (Sigma Aldrich), pH = 7.0 containing protease and phosphatase inhibitors (Thermo Fisher Scientific). To stabilize adducts, sodium borohydride (5 mM) was added to the cell mixture. The cells were sonicated by pulse and lysed on ice for 20 min, then centrifuged at 10,000*g* for 10 min at 4 ºC. The supernatant was collected, and protein concentration was determined using the Bio-Rad DC protein mass assay. All protein concentrations were adjusted to 2 mg/mL. "Click" reagents were added to each sample in the following order: DADPS azido-biotin reagent (Click Chemistry Tools; 0.2 mM), TBTA ligand (Click Chemistry Tools; 0.2 mM), copper sulfate (Sigma Aldrich; 1 mM), and sodium ascorbate (Sigma Aldrich; 1 mM). The samples were vortexed and rotated at room temperature for 1 h.

4.4.9 Western Blotting of Protein Adducts

"Clicked" mixture was added to 4X LDL sample buffer (Invitrogen) containing DTT (Thermo Fisher Scientific; 0.05 M), and the mixture was boiled at 90 ºC for 5 min. The proteins from each sample were solved using 10% NuPAGE Novex BisTris gel (Invitrogen) with MES running buffer (Invitrogen). Precision Plus Protein Kaleidoscope standards (10-250 kDA; Bio-Rad) were used as reference). The proteins were dry transferred to nitrocellulose membrane using

the iBlot system (Thermo Fisher Scientific) and probed with IRDye 800 CW Streptavidin (Licor). Anti-beta actin antibody (Abcam) probed with IRDye 680LT Donkey anti-Goat IgG (Licor) was used as the loading control. Biotinylated proteins were visualized using Licor Odyssey Infrared Gel Scanner and Odyssey Software (Licor).

Figures

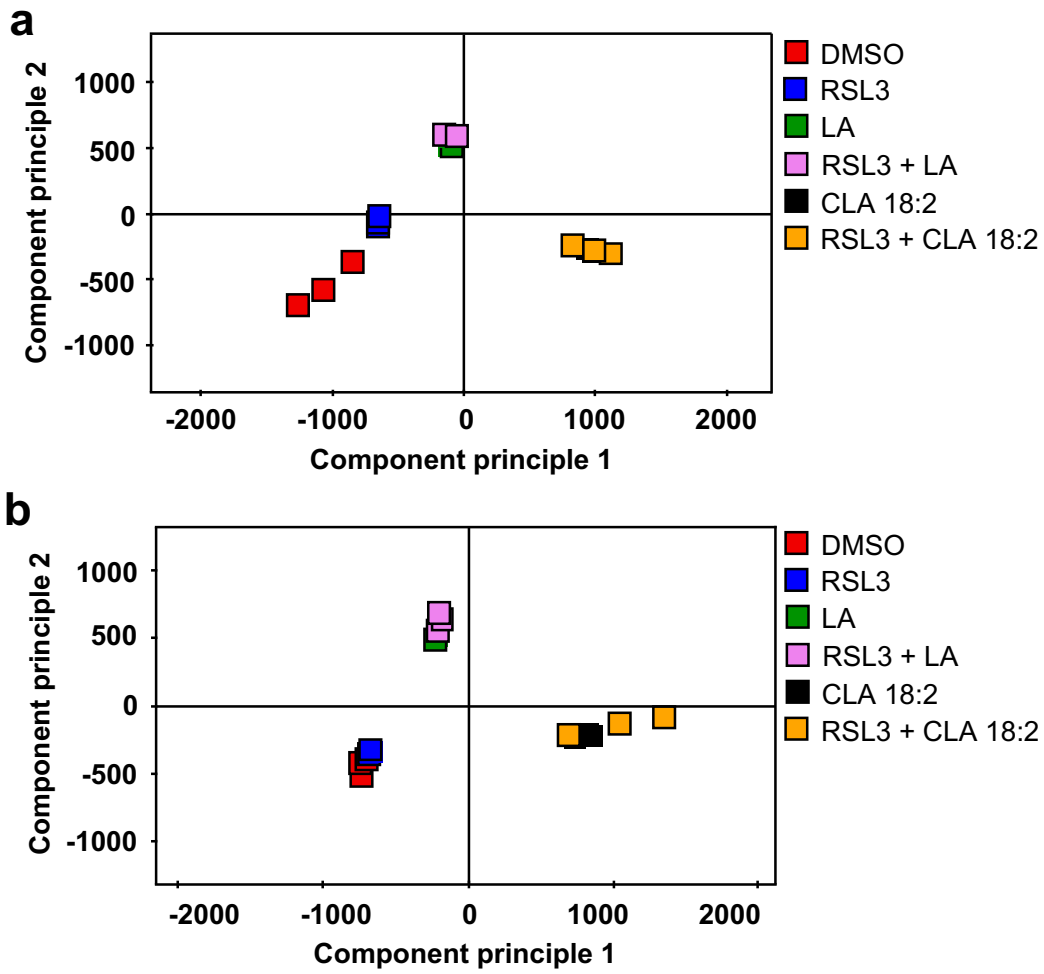

Figure 4.1 Principal component analysis score plot of the first two principal components of lipid composition among different groups of treatment in a) positive and b) negative mode.

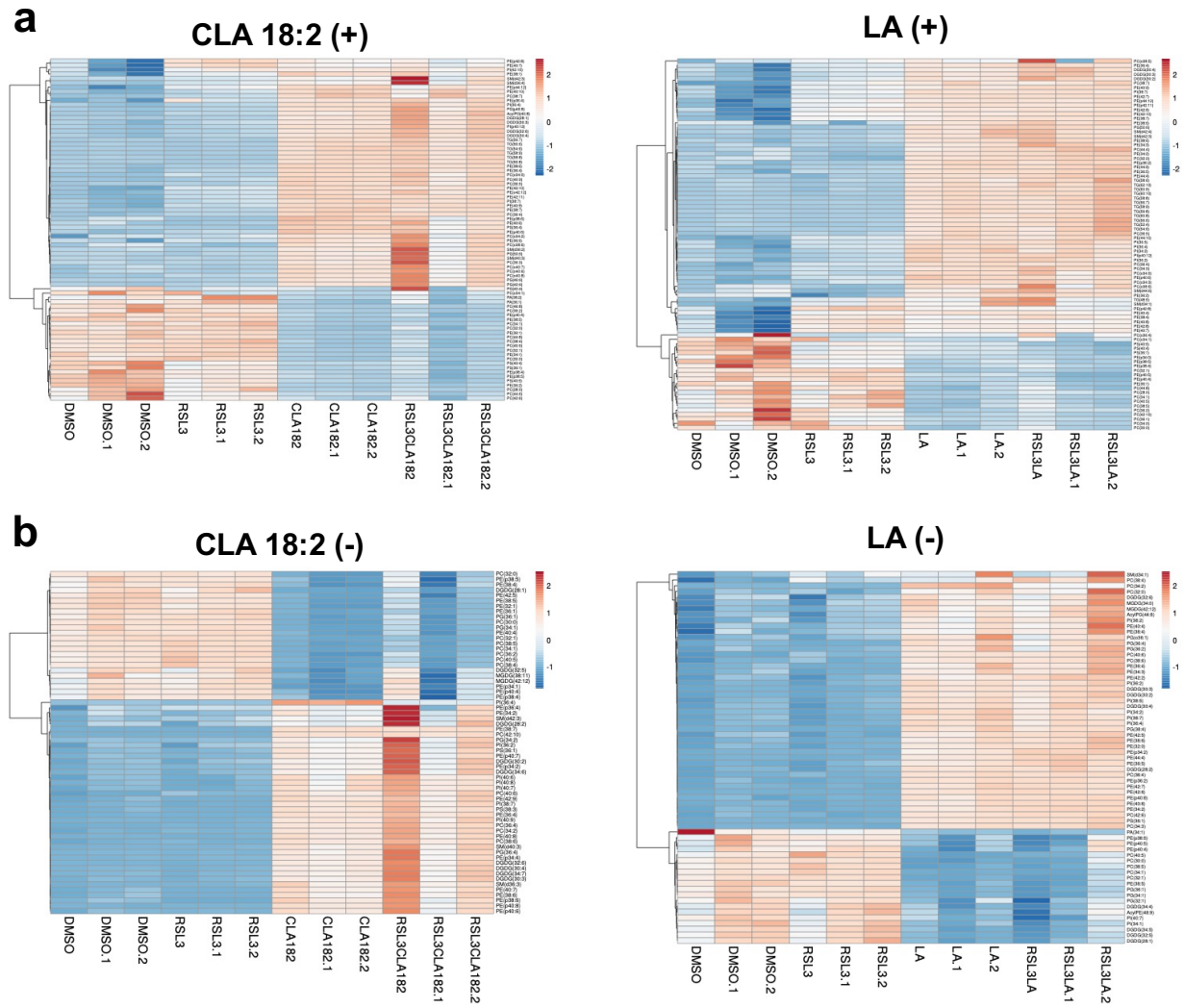

Figure 4.2 Heat map of significantly altered lipid species in the a) positive (+) and b) negative (-) modes upon the addition of CLA 18:2 and LA for 24 h.

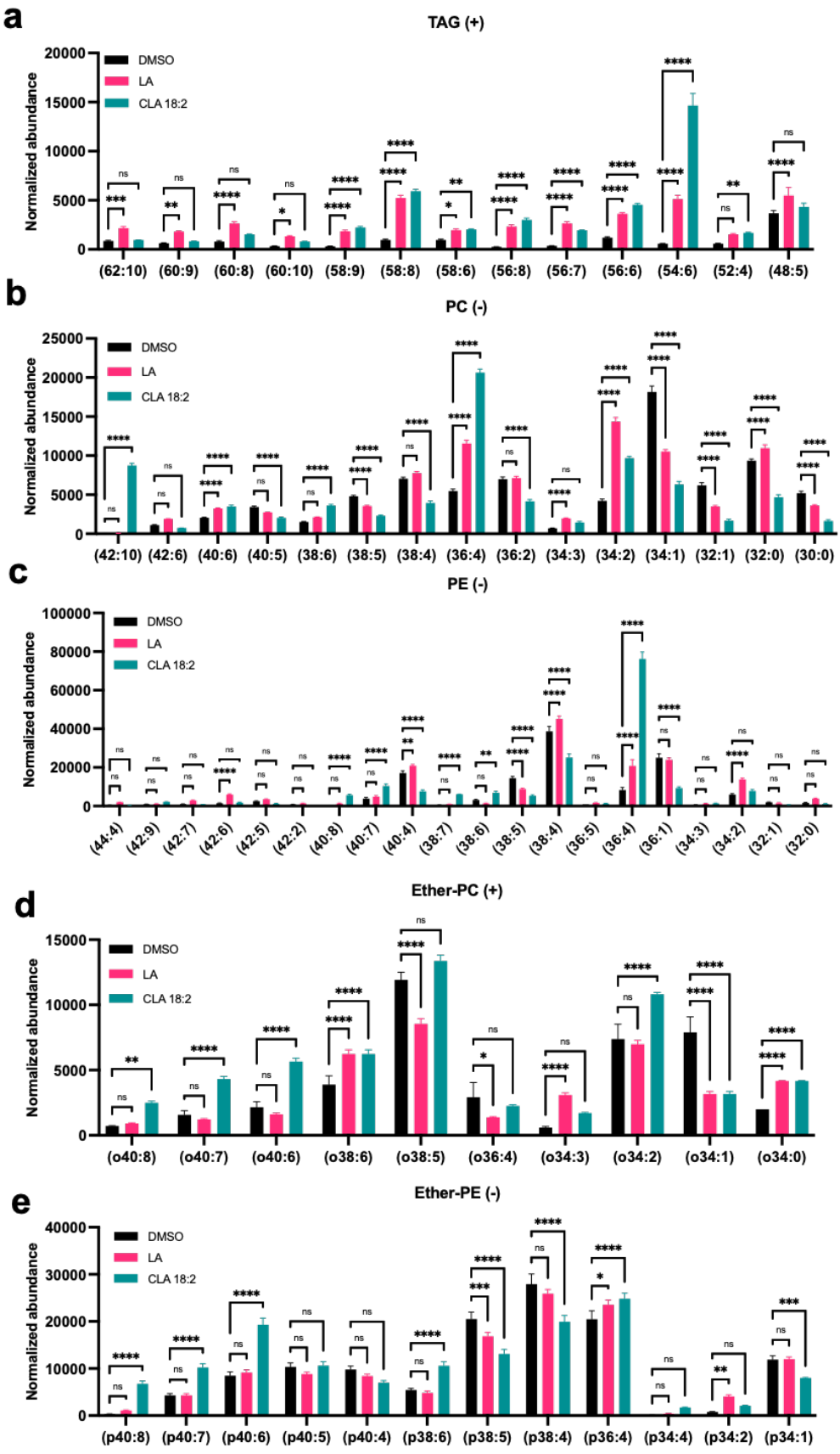
a
TAG (+)
Normalized abundance
DMSO
LA
CLA 18:2
(62:10) (60:9) (60:8) (60:10) (58:9) (58:8) (58:6) (56:8) (56:7) (56:6) (54:6) (52:4) (48:5)
b
PC (-)
(42:10) (42:6) (40:6) (40:5) (38:6) (38:5) (38:4) (36:4) (36:2) (34:3) (34:2) (34:1) (32:1) (32:0) (30:0)
c
PE (-)
(44:4) (42:9) (42:7) (42:6) (42:5) (42:2) (40:8) (40:7) (40:4) (38:7) (38:6) (38:5) (38:4) (36:5) (36:4) (36:1) (34:3) (34:2) (32:1) (32:0)
d
Ether-PC (+)
(o40:8) (o40:7) (o40:6) (o38:6) (o38:5) (o36:4) (o34:3) (o34:2) (o34:1) (o34:0)
e
Ether-PE (-)
(p40:8) (p40:7) (p40:6) (p40:5) (p40:4) (p38:6) (p38:5) (p38:4) (p36:4) (p34:4) (p34:2) (p34:1)

Figure 4.3 Untargeted lipidomics reveals distinct changes associated with the addition of nonconjugated and conjugated PUFAs in HT-1080 cell line.Normalized abundance of a) TAG, b) PC, c) PE, d) ether-PC, and e) ether-PE across specified treatments for 24 h. Normalized abundance is plotted as mean ± SD of n = 3 biological replicates for each condition. *p*-values from student's *t*-test against control with Bonferroni correction for multiple comparisons are shown; ns = non-significant, * $p < 0.032$, ** $p < 0.0021$, *** $p < 0.0002$, **** $p < 0.0001$. The concentrations of RSL3, LA, CLA 18:2 are 0.005, 80, and 80 μM, respectively. (+) = Positive mode, (-) = Negative mode. TAG = triacylglycerol, ether-PC = ether-linked phosphatidylcholine, ether-PE = ether-linked phosphatidylethanolamine.

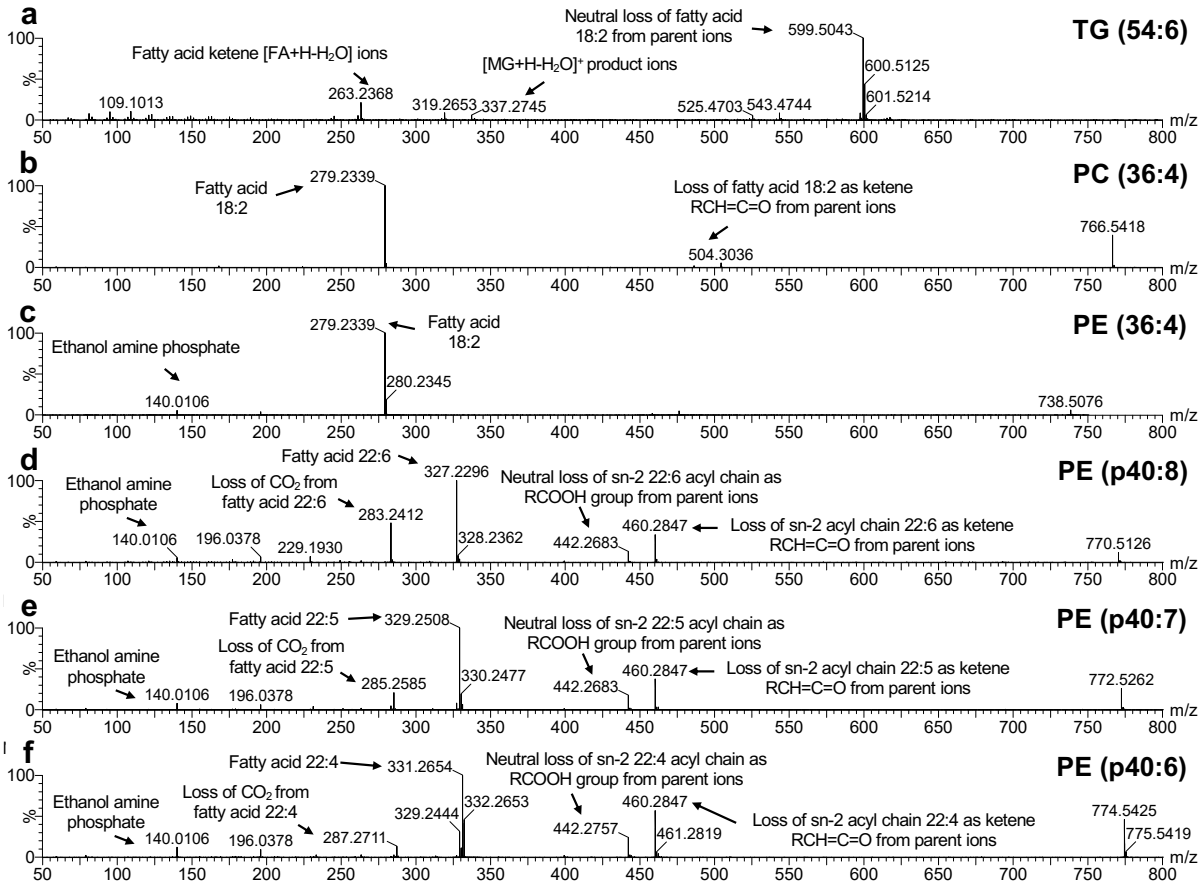

Figure 4.4 MS/MS spectra of TG (54:6), PC (36:4), PE (36:4), PE (p40:8), PE (p40:7), and PE (p40:6) indicate that the compositions of these lipids are TG (18:2/18:2/18:2), PC (18:2/18:2), PE (18:2/18:2), PE (p-18:2/22:6), PE (p-18:2/22:5), and PE (p-18:2/22:4) respectively.

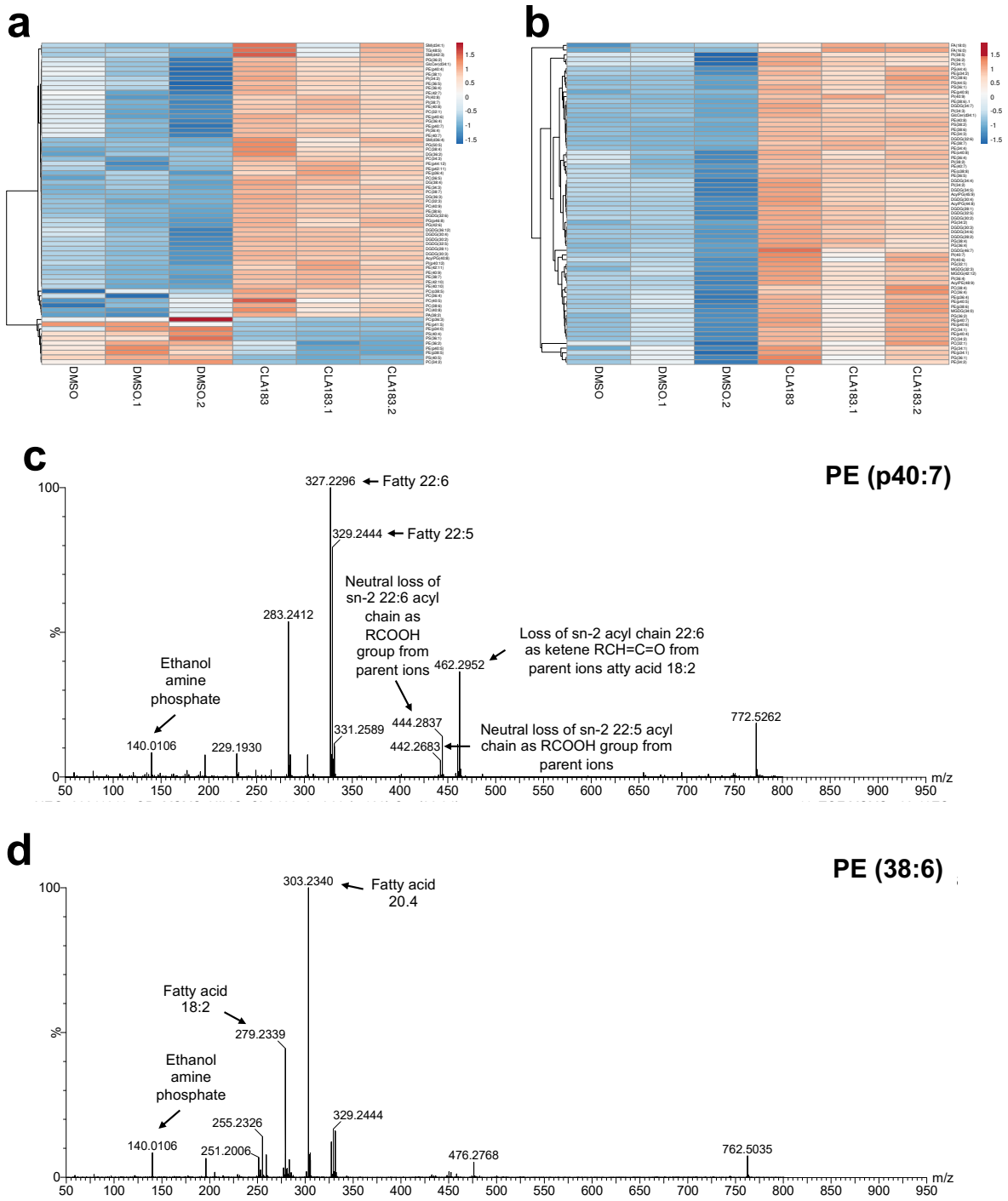

Figure 4.5 Heat map of significantly altered lipid species in the a) positive and b) negative mode upon the addition of 5 µM CLA 18:3 for 24 h (ANOVA adjusted *p*-value < 0.05, n = 3 biological replicates each condition). c) MS/MS spectra of PE (p40:7) indicates that the composition of this lipid is either PE (p-18:1/22:6) or PE (p-18:2/22:5). b) MS/ MS spectra of PE (38:6) indicates that the composition of this lipid is PE (18:2/20:4).

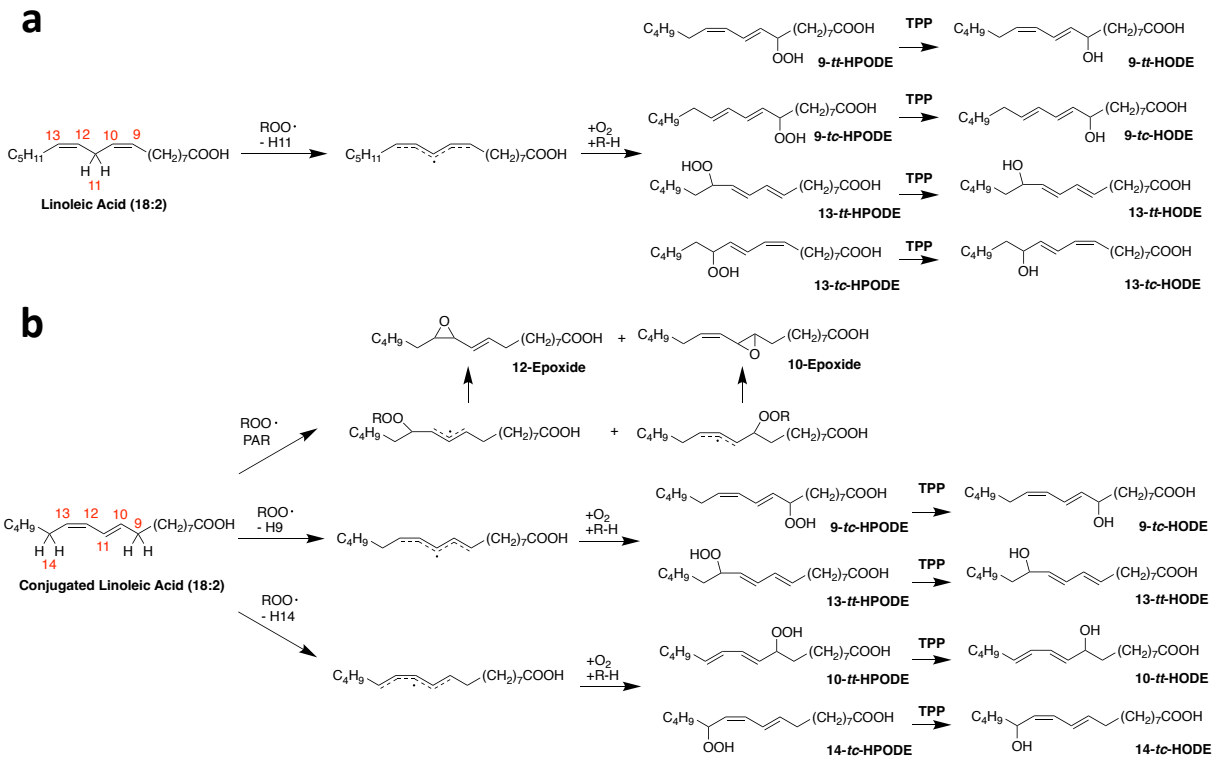

Figure 4.6 Proposed products from the free radical oxidation of a) LA and b) CLA 18:2. Reduction of lipid hydroperoxides (HPODEs) with triphenylphosphine (TPP) gives the corresponding alcohols (HODEs)

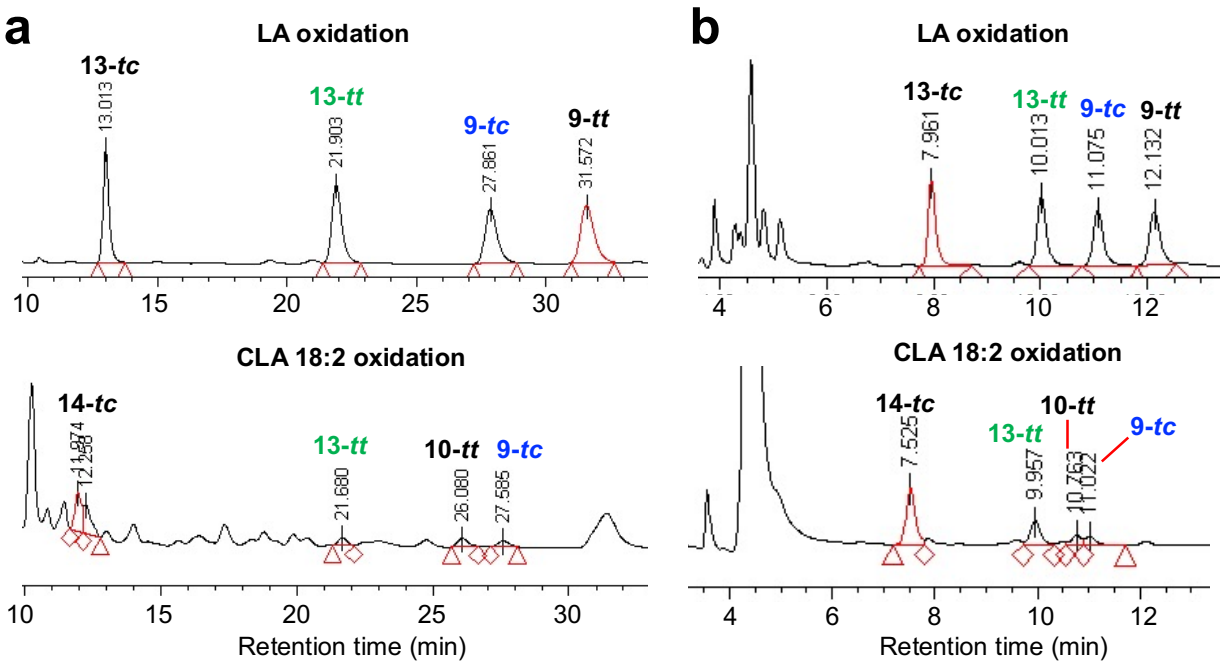

Figure 4.7 Lipid hydroperoxides detected from the oxidation of LA and CLA 18:2**.** Normal phase HPLC-UV chromatogram at 234 nm of the oxidation mixture of LA (top) and CLA 18:2 (bottom) after reduction with (a) triphenylphosphine or (b) $LiAlH_4$.

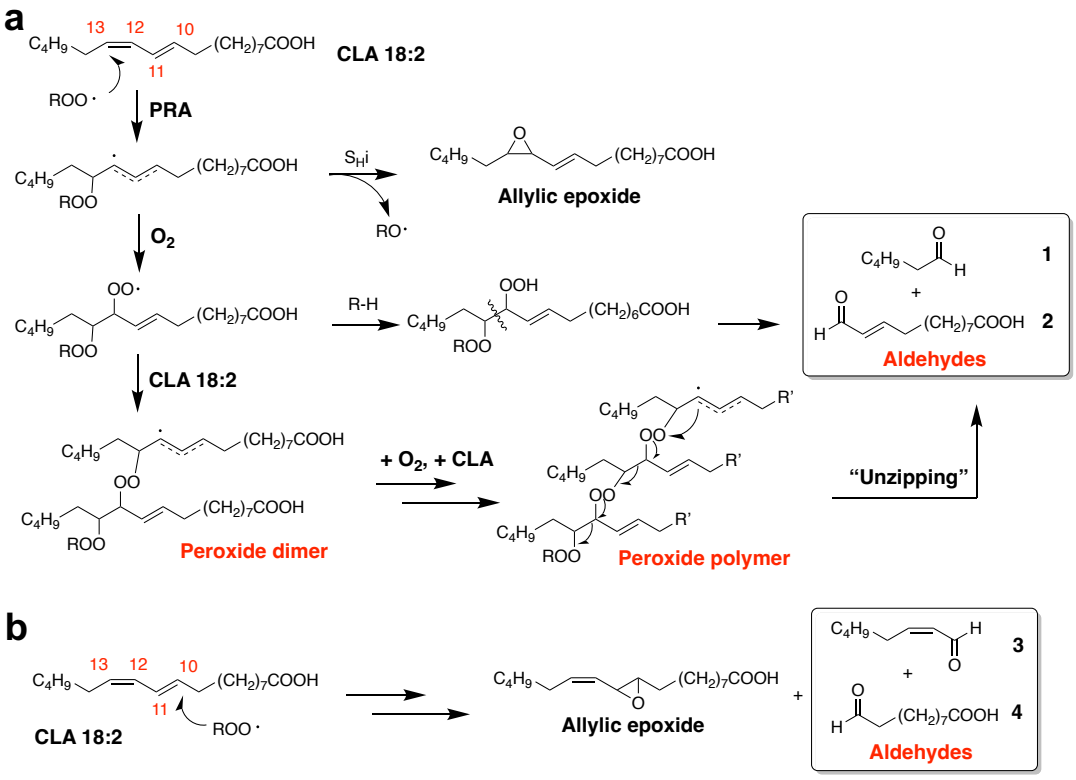

Figure 4.8 Proposed PRA mechanism of CLA 18:2 leading to the formation of peroxide dimers and polymers, and, subsequently, electrophilic aldehydes. a) Proposed PRA mechanism of CLA 18:2 at C13 leading to the formation of hexanal (**1**) and the α,β-unsaturated aldehyde **2**. b) Proposed oxidation product from PRA reaction at C10 of CLA 18:2 based on similar mechanism leading to the formation of 2-*t*-octenal (**3**) and the saturated aldehyde **4**.

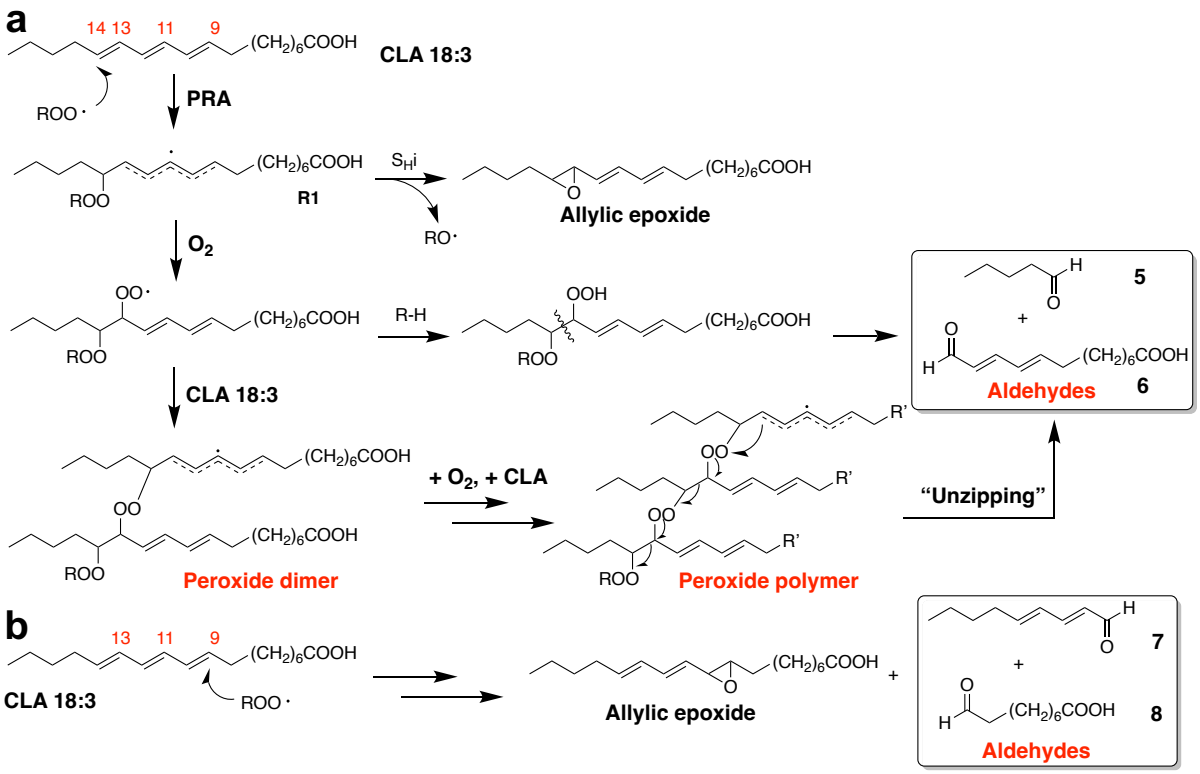

Figure 4.9 Proposed PRA mechanism of CLA 18:3 a) Proposed PRA mechanism at C14 of CLA 18:3 leading to the formation of pentanal (**5**) and the α,β,δ,γ-unsaturated (conjugated) aldehyde **6.** b) Proposed oxidation product from PRA reaction of at C9 of CLA 18:3 based on similar mechanism leading to the formation of 2,4-*tt*-nonadienal (**7**), and the saturated aldehyde.

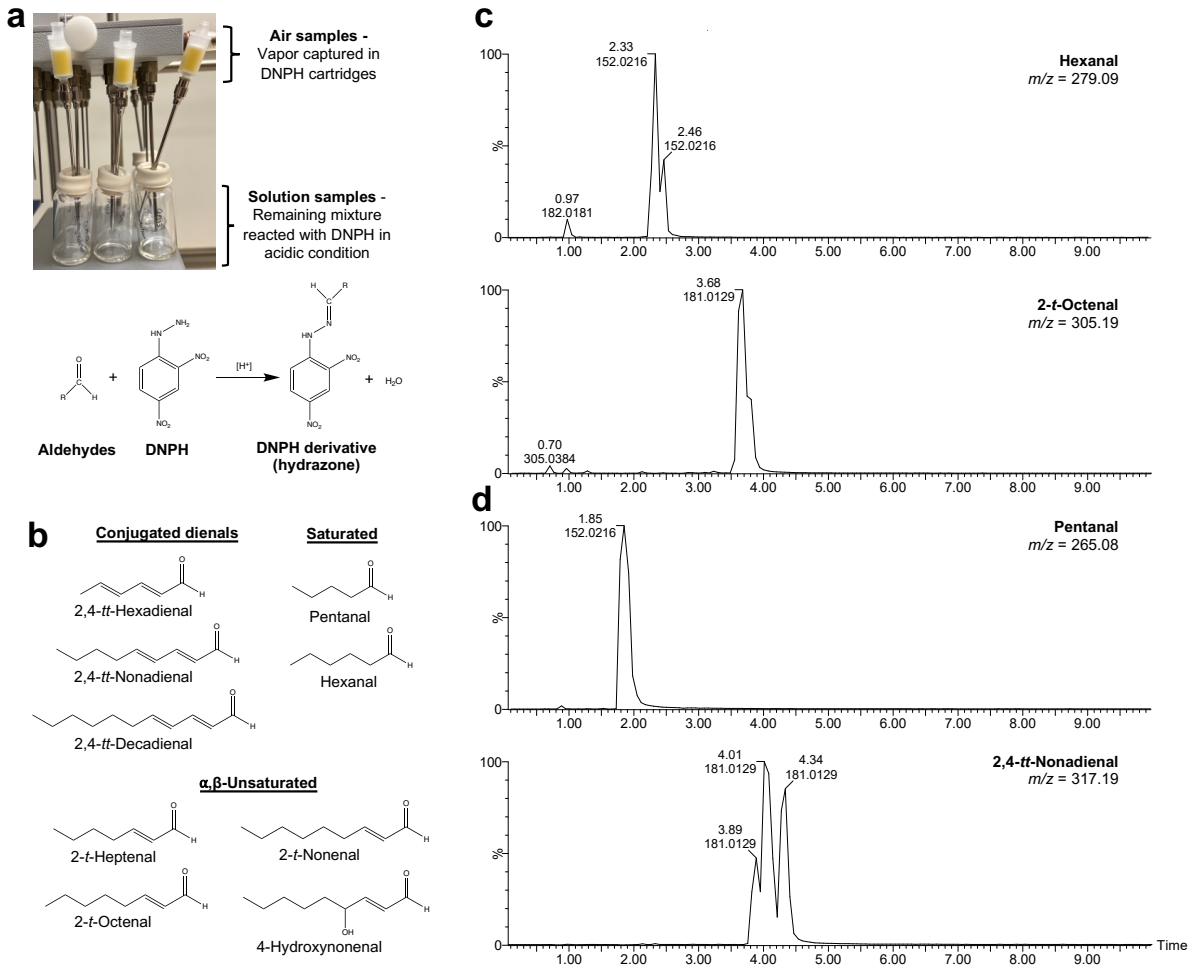

Figure 4.10 The detection of volatile aldehydes from the oxidation of conjugated PUFAs. a) Experimental setup to detect aldehydes from conjugated PUFA oxidation via derivatization using 2,4-dinitrophenylhydrazine (DNPH). The DNPH-derivatized aldehydes from both the air and solution samples were extracted using CH_2Cl_2, evaporated, and reconstituted in reverse phase-LC solvent for MS analysis. b) Structures of the aldehydes examined in this study. c) MS chromatogram of hexanal and 2-*t*-octenal detected from the air sample of CLA 18:2. d) MS chromatogram of pentanal and 2,4-*tt*-nonadienal detected from the oxidation of CLA 18:3.

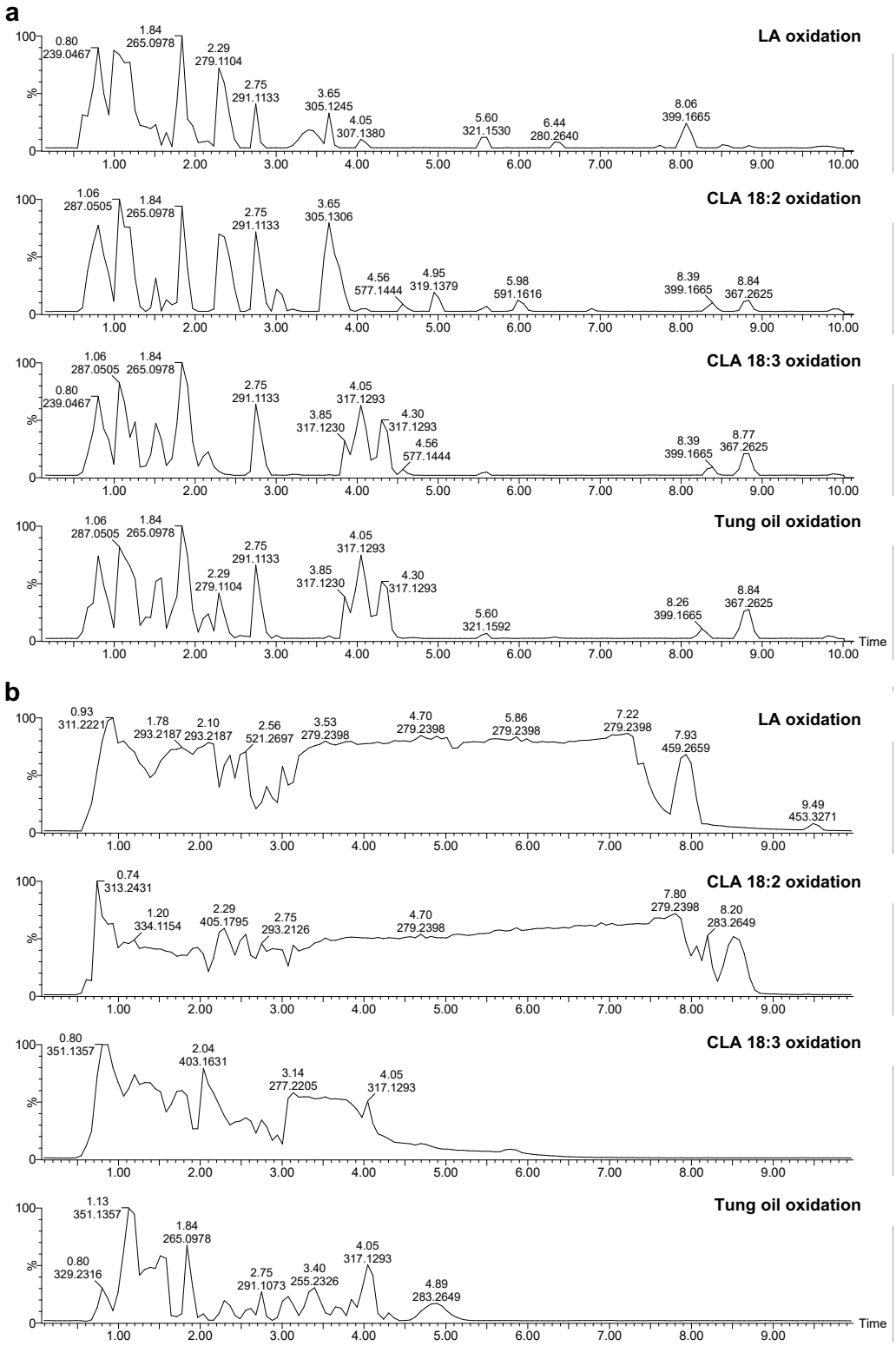

Figure 4.11 Total ion current MS chromatogram of the a) air and b) solution samples from the oxidation and derivatization with DNPH of LA, CLA 18:2, CLA 18:3, and tung oil.

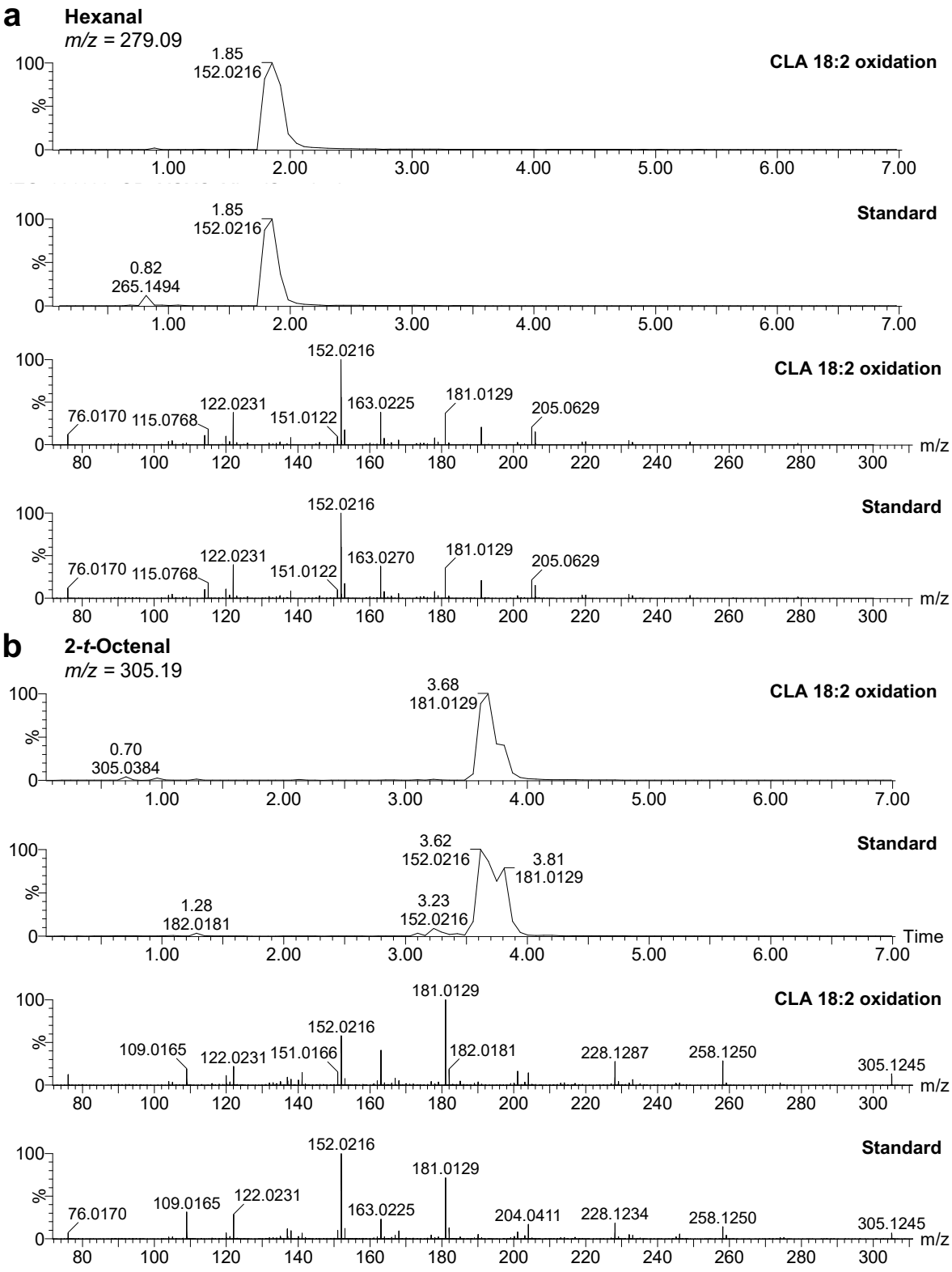

Figure 4.12 The detection of a) hexanal and b) 2-*t*-octenal from the oxidation of CLA 18:2 is confirmed by matching retention time and fragmentation patterns to those of the commercially available standards.

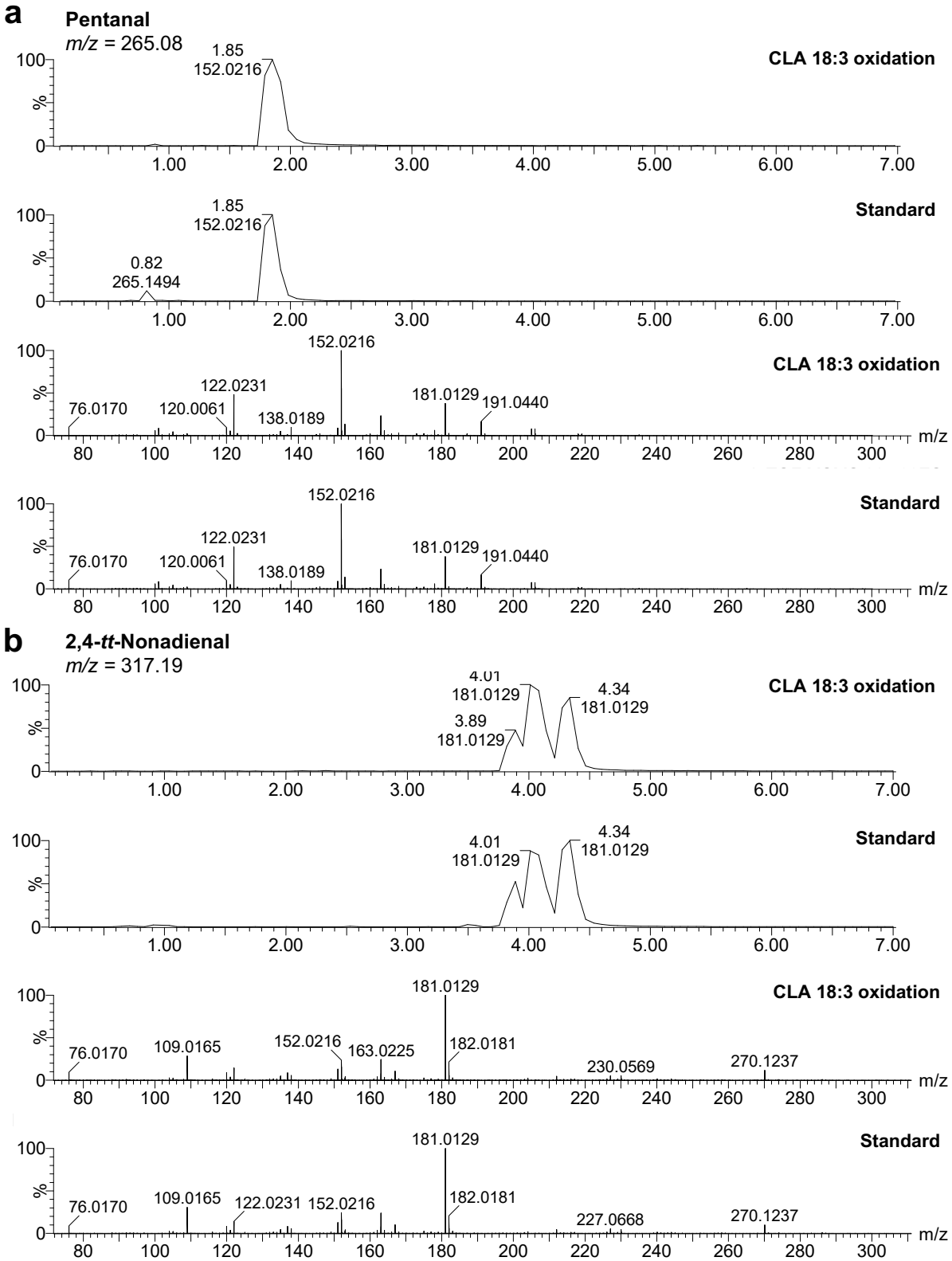

Figure 4.13 The detection of a) pentanal and b) 2,4-*tt*-nonenal from the oxidation of CLA 18:3 is confirmed by matching retention time and fragmentation patterns to those of the commercially available standards.

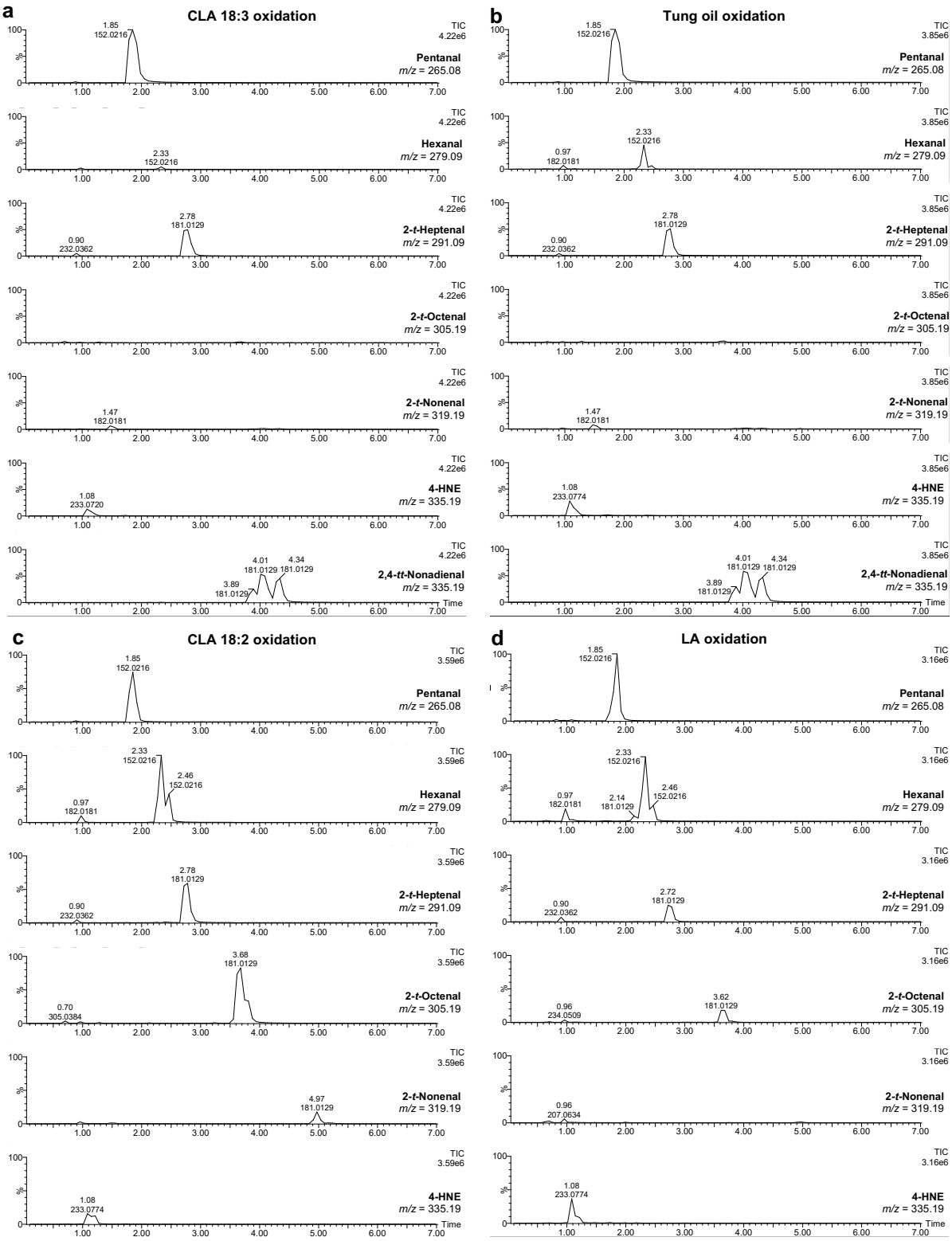

Figure 4.14 LC-MS chromatograms of indicated aldehydes from the oxidation of a) CLA 18:3, b) tung oil, c) CLA 18:2, and d) LA. All the chromatograms shown are from air sample, except for 4-hydroxynonenal, which can only be detected from the solution samples.

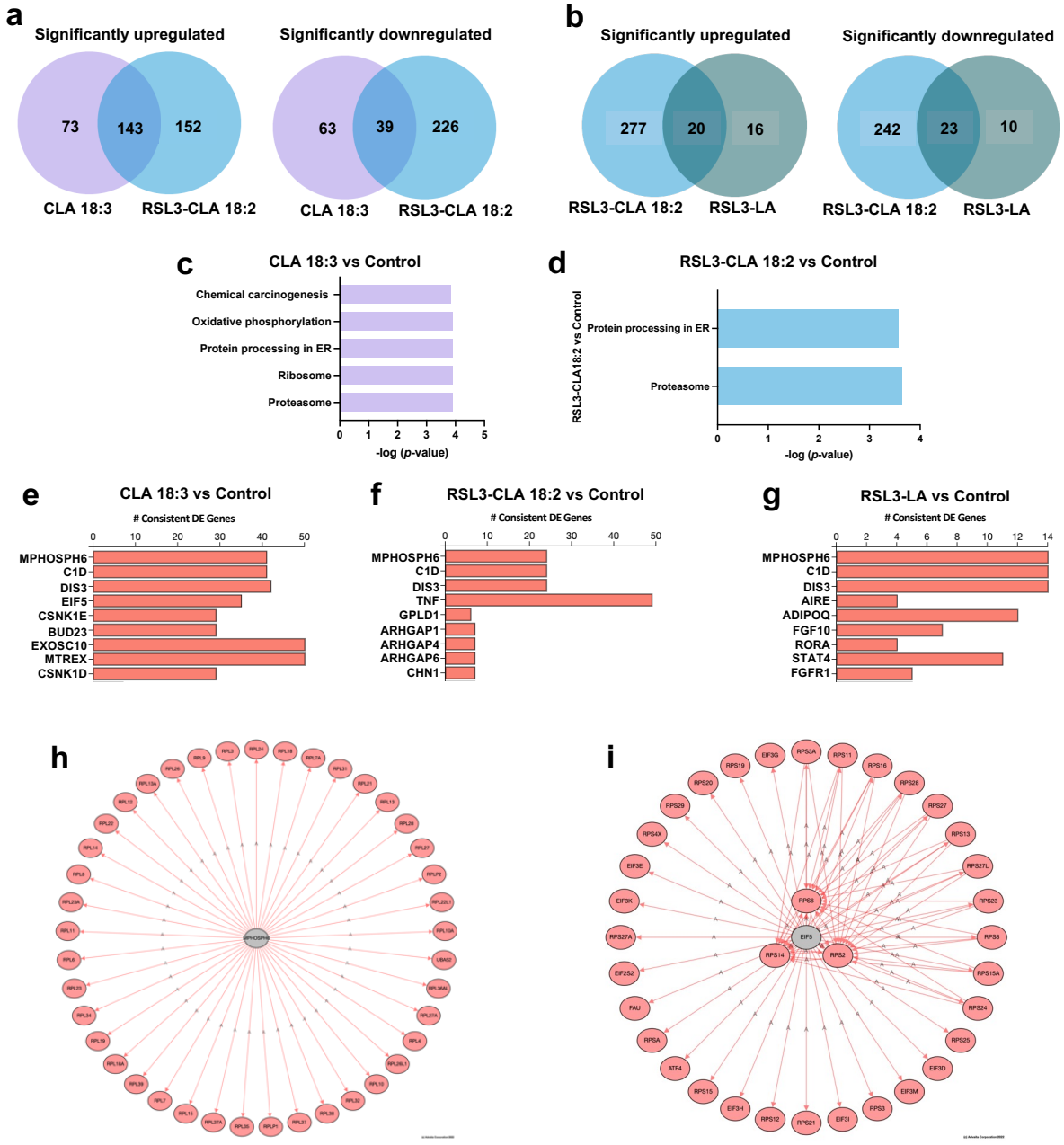

Figure 4.15 RNA sequencing data from the addition of conjugated and nonconjugated PUFAs in HT-1080 cell line**.** Venn diagram of genes commonly or uniquely up- and downregulated in cells treated with a) CLA 18:3 and RSL3-CLA 18:2, and b) RSL3-CLA 18:2 and RSL3-LA compared to the control (adjusted *p*-value < 0.05, > 2-fold change). Top significantly upregulated pathways identified by Integrated Differential Expression and Pathway (iDEP) and iPathwayGuide (iPG) analyses in cells treated with c) CLA 18:3, and d) RSL3-CLA 18:2 compared to control (the -log (-*p*-value) from iPG are shown, FDR-corrected). Top significantly activated upstream regulators identified iPathwayGuide (iPG) analysis in cells treated with e) CLA 18:3, f) RSL3-CLA 18:2, and g) RSL3-LA compared to control (combined *p*-value < 0.05). DEGs regulated by the upstream regulators h) M-phase protein 6 (MPHOSPH6) and i) eukaryotic translation initiation factor-5 (EIF5) in cells treated with CLA 18:3 compared to control (adjusted *p*-value < 0.05). n = 4

biological replicates per condition. Cells were treated for 24 h and the concentrations used for CLA 18:3, CLA 18:2, LA, and RSL3 were 5, 80, 80, and 0.01 μM, respectively.

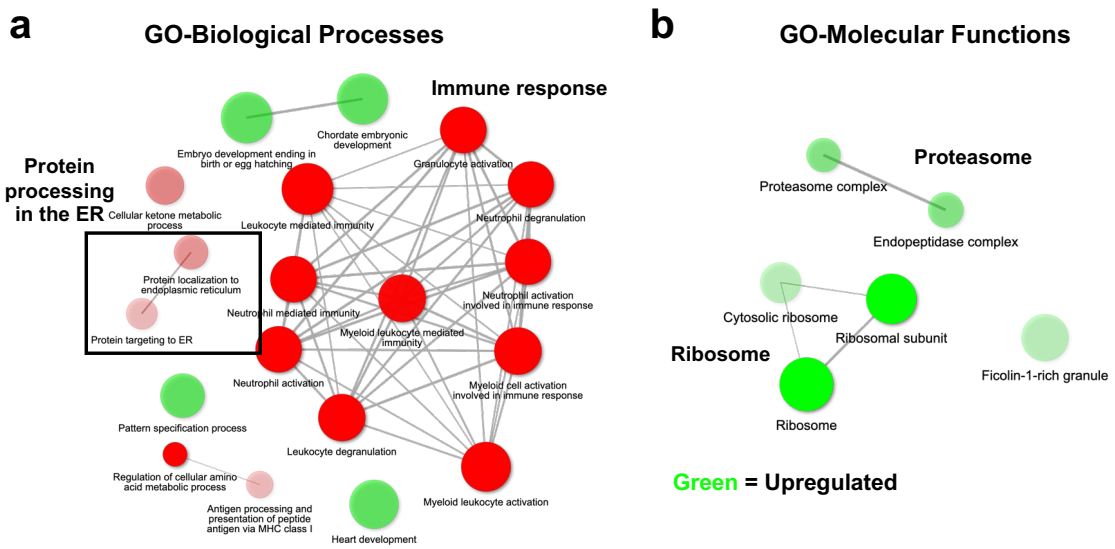

Figure 4.16 Networks of Gene Ontology (GO) associated with a) biological process and b) molecular function aspects identified by Integrated Differential Expression and Pathway (iDEP) analysis in HT-1080 cell line treated with CLA 18:3 compared to the control. Red and green nodes represent up- and downregulated pathways, respectively. When all pathways are altered in the same direction, the nodes are denoted in green as the default regardless of whether the pathway are up-or down-regulated, so in b), the green nodes represent upregulated pathways. Darker nodes represent more significantly enriched gene sets and bigger nodes represents larger gene sets. Thicker edges mean more genes are overlapped.

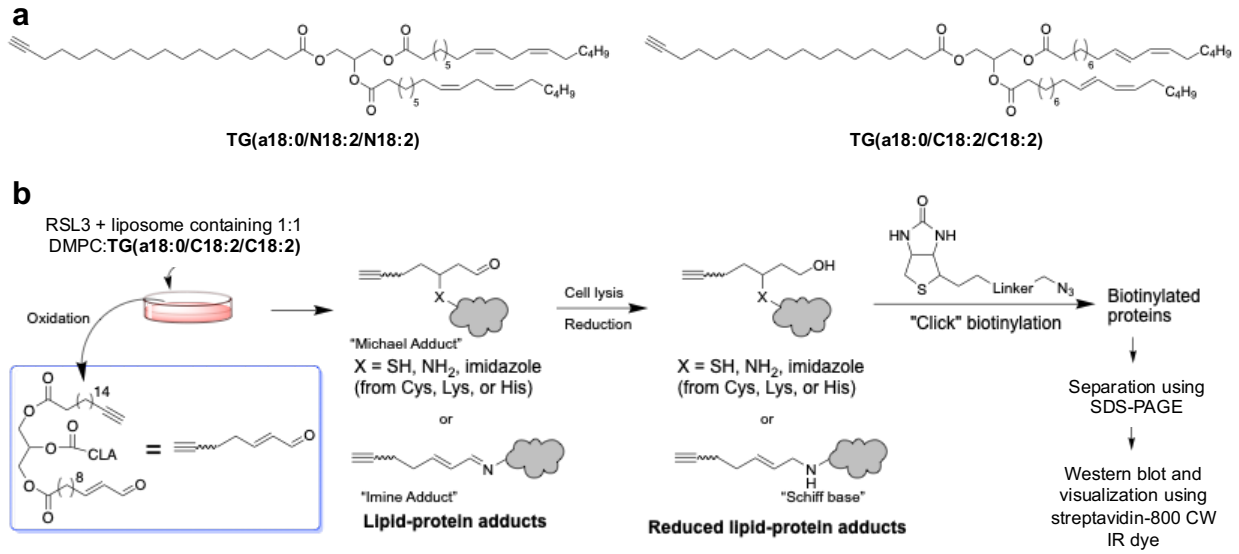

Figure 4.17 Overview of lipid-protein adduct detection utilizing alkynylated TAGs. a) Structure of alkynyl triacylglyceride probes containing LA and CLA 18:2. b) Overall workflow to label and visualize lipid-protein adducts using "Click" chemistry and western blot.

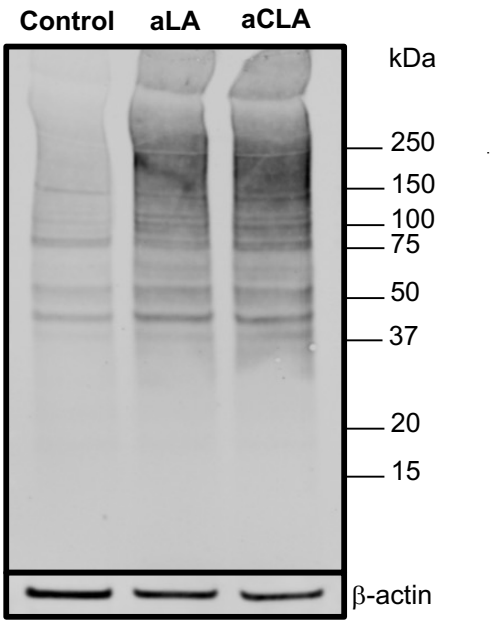

Figure 4.18 Treatment of HT-1080 cells with RSL3 in the presence of alkynylated CLA 18:2 TAG showed increased protein modifications. Western blot of cells treated with DMPC-liposome (80 μM; Control) or with RLS3 (5 nM) in the presence of either 1:1 DMPC:TAG (a18:0/N18:2/N18:2) liposome (80 μM; aLA) or 1:1 DMPC:TAG (a18:0/C18:2/C18:2) liposome (80 μM; aCLA).

Tables

Table 4.1 Altered lipids in HT-1080 cells exposed to CLA 18:2 compared to vehicle control in positive mode (p-value < 0.05).

LiPydomics identification	m/z	Retention time (min)	CCS (angstrom^2)	Abundance in Control	Fold change[a]
TG (58:9)	946.785	0.4	323.054	311 ± 36	7.14
TG (58:8)	948.801	0.4	325.464	964 ± 76	6.15
TG (56:8)	920.770	0.4	317.090	262 ± 6.1	11.5
TG (56:7)	922.784	0.4	318.303	355 ± 19	5.46
TG (56:6)	924.801	0.4	320.734	1193 ± 96	3.81
TG (54:6)	896.771	0.4	312.293	581 ± 26	25.2
SM (d42:3)	811.668	7.2	295.201	5768 ± 471	1.91
SM (d40:3)	783.636	7.2	290.249	715 ± 225	14.5
SM (d36:4)	725.556	7.3	282.857	1526 ± 184	3.06
SM (d36:2)	729.589	7.1	281.518	592 ± 132	4.79
PS (40:5)	838.561	5.8	286.048	2259 ± 95	-2.77
PS (40:4)	840.575	5.8	288.622	4509 ± 411	-2.12
PS (36:4)	784.511	5.9	273.238	1229 ± 77	3.39
PS (36:1)	790.562	5.9	282.424	5097 ± 800	-3.04
PI (p40:12)	883.470	3.2	287.106	525 ± 133	5.06
PI (42:10)	931.530	3.0	298.373	2698 ± 2109	3.00
PI (38:7)	903.506	3.2	290.867	813 ± 379	5.84
PI (36:4)	881.515	3.2	287.116	3070 ± 1451	6.88
PG (p46:8)	887.625	1.5	304.880	1045 ± 176	5.51
PG (50:6)	980.736	1.3	321.680	668 ± 35	2.99
PG (46:6)	924.679	1.3	309.674	1399 ± 89	7.18
PG (42:6)	868.615	1.4	298.688	656 ± 186	8.36
PG (40:4)	844.615	1.5	296.283	22162 ± 2073	-1.30
PE (p44:12)	820.522	4.9	284.852	555 ± 231	3.74
PE (42:8)	800.555	5.0	290.143	3300 ± 946	1.70
PE (p40:6)	776.557	5.0	285.118	9739 ± 649	2.00
PE (p40:4)	780.585	5.0	294.120	10499 ± 725	-1.72
PE (p38:6)	748.526	5.0	276.118	8541 ± 403	1.40
PE (p38:5)	750.543	5.0	280.061	19304 ± 762	-1.69
PE (p38:4)	752.558	5.0	287.872	23367 ± 2434	-1.68
PE (p36:4)	746.510	5.0	274.807	4024 ± 463	1.85
PE(o42:12)	794.508	4.9	278.468	528 ± 192	8.36
PE (42:11)	810.504	5.0	284.910	405 ± 92	6.22
PE (42:10)	812.518	5.0	287.491	1632 ± 468	3.84
PE (40:9)	786.505	5.1	278.516	882 ± 307	4.40
PE (40:7)	790.535	5.1	288.916	10531 ± 2349	1.45
PE (40:6)	792.552	5.1	282.412	11796 ± 564	1.37
PE (40:10)	784.501	5.2	278.528	1829 ± 262	2.55
PE (38:7)	762.502	5.2	278.667	3043 ± 702	8.27
PE (38:6)	764.519	5.2	281.280	3811 ± 420	2.75

PE (38:5)	766.538	5.2	285.183	14942 ± 1250	-2.15
PE (38:1)	774.605	5.0	281.215	5765 ± 1472	1.85
PE (36:5)	738.505	5.2	274.860	2653 ± 554	1.85
PE (36:4)	740.521	5.2	272.186	11388 ± 2312	4.36
PE (36:2)	744.554	5.2	277.467	15698 ± 454	-2.88
PE (36:1)	746.569	5.2	282.709	17314 ± 1466	-3.09
PE (34:1)	718.538	5.2	272.338	11456 ± 1182	-2.51
PC (o40:8)	816.589	6.4	290.047	717 ± 323	2.76
PC (o40:7)	818.604	6.4	292.603	1564 ± 426	2.63
PC (o40:6)	820.617	6.5	297.693	2151 ± 24	3.48
PC (o38:6)	792.589	6.4	287.611	3899 ± 651	1.60
PC (o34:2)	766.575	6.4	278.640	7377 ±1148	1.47
PC (o34:1)	746.601	6.7	295.630	7889 ± 1193	-2.49
PC (o34:0)	770.594	6.6	294.186	1992 ± 2.6	2.09
PC (46:8)	914.663	6.3	304.742	1806 ± 373	-15.8
PC (44:8)	886.632	6.3	297.327	3292 ± 350	-6.14
PC (44:6)	890.666	6.4	309.848	4122 ± 1099	-2.41
PC (42:6)	862.632	6.4	301.246	6791 ± 1691	-1.96
PC (40:9)	828.554	6.4	288.689	578 ± 65	5.38
PC (40:5)	858.600	6.3	291.096	6643 ± 579	-2.76
PC (38:7)	804.553	6.5	292.688	2563 ± 25	3.13
PC (38:4)	810.599	6.5	296.482	45904 ± 721	-2.07
PC (36:5)	780.554	6.5	277.235	6075 ± 134	1.67
PC (36:4)	782.568	6.5	287.674	41082 ± 3189	2.95
PC (36:3)	784.583	6.9	282.461	933 ± 289	5.83
PC (36:2)	786.601	6.6	300.440	56084 ± 11754	-2.27
PC (34:1)	760.585	6.6	295.532	90918 ± 16122	-3.11
PC (32:1)	732.554	6.6	280.184	31066 ± 2007	-4.66
PC (32:0)	734.567	6.7	287.999	46660 ± 3702	-2.51
PC (30:0)	706.540	6.7	273.758	21475 ± 3427	-4.57
PC (28:0)	678.508	6.7	265.915	2517 ± 816	-5.14
PA (38:2)	746.575	6.6	286.617	8656 ± 1867	-1.99
PA (36:1)	720.558	6.7	280.270	6125 ± 535	-1.75
DGDG (32:6)	903.502	0.7	288.297	600 ± 129	4.68
DGDG (30:4)	879.501	1.0	285.833	1880 ± 521	4.43
DGDG (30:3)	881.514	0.7	287.116	1563 ± 396	3.29
DGDG (28:1)	857.519	1.0	282.047	572 ± 189	17.5
AcylPG (40:8)	855.485	1.0	284.660	772 ± 118	4.60

[a] Fold-change relative to control

Table 4.2 Altered lipids in HT-1080 cells exposed to CLA 18:2 compared to vehicle control in negative mode (p-value < 0.05)

LiPydomics identification	m/z	Retention time (min)	CCS (angstrom^2)	Abundance in Control	Fold change[a]
SM (d42:3)	869.675	7.2	304.591	2252 ± 180	1.56
SM (d40:3)	841.644	7.2	299.075	357 ± 18	10.2
SM (d36:3)	785.581	7.2	287.915	95 ± 14	14.0
PS (38:3)	812.551	6.6	286.300	429 ± 77	5.29
PS (36:1)	788.547	6.6	282.071	1466 ± 75	1.67
PI (40:9)	963.523	3.1	313.929	103 ± 23	15.2
PI (40:8)	905.519	3.0	300.156	483 ± 71	4.23
PI (40:7)	907.534	3.1	301.564	1395 ± 250	3.61
PI (40:6)	909.550	3.0	302.970	4847 ± 822	2.52
PI (38:7)	939.523	3.2	308.456	577 ± 110	7.67
PI (36:4)	857.519	3.2	291.829	9143 ± 1117	7.29
PI (36:2)	861.550	3.2	293.245	22625 ± 2872	1.71
PG (36:4)	769.506	1.7	273.349	3582 ± 243	6.15
PG (36:1)	775.544	1.7	279.219	11491 ± 1099	-2.57
PG (34:2)	745.504	1.7	269.035	3779 ± 242	2.64
PG (34:1)	747.513	1.7	270.515	40438 ± 3762	-3.27
PE (p40:8)	770.514	4.9	273.343	305 ± 61	22.2
PE (p40:7)	772.529	4.9	274.813	4284 ± 409	2.39
PE (p40:6)	774.542	5.0	277.753	8481 ± 780	2.27
PE (p40:4)	778.571	5.0	282.133	9804 ± 718	-1.40
PE (p38:6)	746.513	5.0	269.028	5435 ± 366	1.95
PE (p38:5)	748.529	5.0	270.508	20512 ± 1485	-1.57
PE (p38:4)	750.543	5.0	274.953	27919 ± 2141	-1.40
PE (p36:4)	722.513	5.0	264.685	20460 ± 1799	1.21
PE (p34:4)	754.505	5.3	270.469	89 ± 15	19.2
PE (p34:2)	698.513	5.2	260.314	789 ± 98	2.66
PE (p34:1)	700.519	5.2	261.817	11886 ± 801	-1.48
PE (42:9)	872.542	5.1	298.904	972 ± 80	2.15
PE (42:5)	820.585	5.1	289.151	2508 ± 189	-1.93
PE (40:8)	786.508	5.1	277.680	350 ± 48	16.0
PE (40:7)	788.524	5.1	279.139	3890 ± 554	2.67
PE (40:4)	794.566	5.1	284.953	17093 ± 1163	-2.23
PE (38:7)	820.512	5.2	292.038	602 ± 40	10.2
PE (38:6)	762.510	5.1	268.926	3145 ± 365	2.19
PE (38:5)	764.524	5.1	271.895	14481 ± 928	-2.74
PE (38:4)	766.539	5.1	274.850	38704 ± 2551	-1.54
PE (36:4)	738.509	5.2	270.574	8333 ± 1331	9.15
PE (36:1)	744.551	5.2	273.510	25027 ± 2097	-2.69
PE (34:2)	714.514	5.2	260.202	5947 ± 514	1.31
PE (32:1)	688.493	5.3	255.812	1995 ± 163	-3.16
PC (42:10)	888.539	6.4	300.242	39 ± 38	226
PC (40:6)	892.607	6.4	301.640	2046 ± 65	1.71

PC (40:5)	894.622	6.4	303.045	3424 ± 136	-1.68
PC (38:6)	864.576	6.4	294.663	1512 ± 61	2.39
PC (38:5)	866.592	6.4	297.511	4792 ± 145	-2.08
PC (38:4)	868.607	6.5	300.347	7060 ± 184	-1.79
PC (36:4)	840.576	6.5	291.922	5466 ± 246	3.78
PC (36:2)	844.607	6.6	297.632	6992 ± 276	-1.68
PC (34:2)	816.576	6.6	290.619	4212 ± 228	2.30
PC (34:1)	818.592	6.6	292.049	18166 ± 732	-2.88
PC (32:1)	790.565	6.6	284.978	6206 ± 346	-3.69
PC (32:0)	792.576	6.7	287.872	9356 ± 226	-2.00
PC (30:0)	764.548	6.7	280.757	5195 ± 244	-3.19
MGDG (42:12)	845.528	0.8	289.011	5351 ± 475	-1.43
MGDG (38:11)	791.481	0.9	277.650	3735 ± 386	-1.45
DGDG (34:7)	905.518	0.9	298.735	1506 ± 83	3.00
DGDG (34:6)	907.535	0.9	298.725	3890 ± 429	2.30
DGDG (32:6)	879.506	0.9	290.274	2698 ± 274	8.70
DGDG (32:5)	881.520	0.9	290.264	13330 ± 1718	-1.63
DGDG (30:4)	855.506	1.0	286.060	9241 ± 986	6.97
DGDG (30:3)	857.519	1.0	286.050	4899 ± 563	3.68
DGDG (30:2)	859.536	1.0	288.935	20714 ± 2673	2.03
DGDG (28:2)	831.505	1.0	280.358	5425 ± 475	1.26
DGDG (28:1)	833.520	1.0	281.810	7928 ± 1015	-2.87

[a] Fold-change relative to control

Table 4.3 Altered lipids in HT-1080 cells exposed to LA compared to vehicle control in positive mode (p-value < 0.05).

LiPydomics identification	m/z	Retention time (min)	CCS (angstrom^2)	Abundance in Control	Fold change[a]
TG (62:10)	1000.832	0.4	334.804	851 ± 76	2.51
TG (60:9)	974.815	0.4	331.348	624 ± 51	2.86
TG (60:8)	976.831	0.4	331.338	787 ± 98	3.35
TG (60:10)	972.801	0.4	328.961	329 ± 31	3.99
TG (58:9)	946.785	0.4	323.054	311 ± 36	5.88
TG (58:8)	948.801	0.4	325.464	964 ± 75	5.41
TG (58:6)	952.830	0.4	327.855	962 ± 74	2.02
TG (56:8)	920.770	0.4	317.090	262 ± 6.0	8.80
TG (56:7)	922.784	0.4	318.303	355 ± 20	7.40
TG (56:6)	924.801	0.4	320.734	1193 ± 96	3.03
TG (54:6)	896.771	0.4	312.293	581 ± 26	8.78
TG (52:4)	872.768	0.4	309.945	576 ± 44	2.62
TG (48:5)	814.687	7.3	298.997	3679 ± 283	1.48
SM (d44:6)	833.649	7.2	293.795	2712 ± 654	1.57
SM (d42:4)	809.652	7.1	292.657	950 ± 116	2.53
SM (d42:3)	811.668	7.2	295.201	5768 ± 471	3.83
SM (d34:1)	703.574	7.3	280.397	18608 ± 656	1.56
PS (40:5)	838.561	5.8	286.048	2259 ± 94	-1.64
PS (40:4)	840.575	5.8	288.622	4509 ± 411	-1.55
PS (36:1)	790.562	5.9	282.424	5097 ± 800	-1.83
PI (p40:12)	883.470	3.2	287.106	525 ± 133	3.98
PI (38:7)	903.506	3.2	290.867	813 ± 379	2.68
PI (36:5)	879.502	3.2	287.126	727 ± 205	2.42
PI (36:4)	881.515	3.2	287.116	3070 ± 1450	3.11
PI (36:2)	885.547	3.2	293.515	10550 ± 2188	2.14
PI (34:2)	857.517	3.2	285.946	950 ± 298	3.64
PG (50:6)	980.736	1.3	321.680	668 ± 35	3.14
PE (p44:12)	820.522	4.9	284.852	555 ± 231	3.00
PE (p42:8)	800.555	5.0	290.143	3300 ± 946	1.61
PE (p40:6)	798.540	4.9	286.280	2914 ± 925	4.00
PE (p40:5)	778.573	5.0	290.282	10831 ± 614	-1.30
PE (p40:4)	780.585	5.0	294.120	10499 ± 725	-1.30
PE (p38:5)	750.543	5.0	280.061	19304 ± 761	-1.31
PE (p38:4)	752.558	5.0	287.872	23367 ± 2434	-1.34
PE (p36:2)	728.556	5.1	282.835	1822 ± 170	1.68
PE (p34:0)	702.542	5.1	279.088	5611 ± 1489	-2.34
PE (44:9)	842.564	5.1	295.021	1644 ± 207	2.09
PE (44:4)	852.643	5.1	298.775	1214 ± 47	1.98
PE (44:10)	840.549	5.1	293.756	505 ± 88	3.36
PE (42:9)	814.533	5.1	288.771	3181 ± 956	1.88
PE (42:8)	816.549	5.1	292.615	4982 ± 1709	1.73
PE (42:7)	818.565	5.1	296.434	5613 ± 1445	2.24

PE (42:10)	812.518	5.0	287.491	1632 ± 468	2.24
PE (40:9)	786.505	5.1	278.516	882 ± 307	2.15
PE (40:8)	788.518	5.1	283.741	4477 ± 1376	1.64
PE (40:7)	790.535	5.1	288.916	10531 ± 2349	1.53
PE (40:4)	796.584	5.1	290.168	13331 ± 2853	1.41
PE (38:7)	762.502	5.2	278.667	3043 ± 703	2.04
PE (38:6)	764.519	5.2	281.280	3811 ± 420	1.92
PE (38:5)	766.538	5.2	285.183	14942 ± 1251	1.18
PE (38:4)	806.513	5.1	290.107	3011 ± 342	1.34
PE (36:5)	738.505	5.2	274.860	2653 ± 554	2.23
PE (36:4)	740.521	5.2	272.186	11388 ± 2312	1.62
PE (36:2)	744.554	5.2	277.467	15698 ± 454	1.24
PE (36:1)	746.569	5.2	282.709	17314 ± 1467	-1.37
PE (34:3)	714.505	5.3	273.699	845 ± 104	2.16
PE (34:2)	716.523	5.2	268.332	3211 ± 675	2.10
PC (o38:6)	792.589	6.4	287.611	3899 ± 651	1.60
PC (o38:5)	794.602	6.4	290.180	11917 ± 590	1.12
PC (o36:4)	790.571	6.4	281.116	2916 ± 1123	-1.29
PC (o34:3)	742.573	6.5	278.799	590 ± 95	2.89
PC (o34:1)	746.601	6.7	295.630	7889 ± 1193	-2.49
PC (o34:0)	770.594	6.6	294.186	1992 ± 2.9	2.09
PC (44:8)	886.632	6.3	297.327	3292 ± 350	-1.54
PC (44:4)	894.694	6.5	313.538	1241 ± 229	1.91
PC (42:10)	854.572	6.4	291.118	1951 ± 344	-2.04
PC (40:5)	836.615	6.4	301.394	26593 ± 4606	-1.56
PC (38:7)	804.553	6.5	292.688	2563 ± 25	1.48
PC (38:5)	808.585	6.4	291.380	29920 ± 5039	-1.37
PC (36:5)	780.554	6.5	277.235	6075 ± 134	1.51
PC (36:4)	782.568	6.5	287.674	41082 ± 3189	1.79
PC (36:2)	786.601	6.6	300.440	56084 ± 11754	-1.41
PC (36:1)	788.614	6.8	291.504	4398 ± 1364	-3.01
PC (34:3)	756.553	6.6	277.387	6243 ± 561	2.09
PC (34:1)	760.585	6.6	295.532	90918 ± 16122	-1.69
PC (34:0)	762.597	6.8	286.508	2705 ± 717	-2.47
PC (32:2)	730.541	6.6	272.254	9074 ± 953	1.56
PC (32:1)	732.554	6.6	280.184	31066 ± 2006	-1.83
PC (30:0)	706.540	6.7	273.758	21475 ± 3427	-1.56
PC (28:0)	678.508	6.7	265.915	2517 ± 816	-1.99
DGDG (30:4)	879.501	1.0	285.833	1880 ± 521	1.76
DGDG (30:3)	881.514	0.7	287.116	1563 ± 395	2.18
DGDG (30:2)	883.533	1.0	290.966	6679 ± 1656	2.07

[a] Fold-change relative to control

Table 4.4 Altered lipids in HT-1080 cells exposed to LA compared to vehicle control in negative mode (p-value < 0.05).

LiPydomics identification	m/z	Retention time (min)	CCS (angstrom^2)	Abundance in Control	Fold change[a]
SM (d34:1)	761.581	7.3	285.163	7802 ± 372	1.29
PS (36:1)	788.547	6.6	282.071	1466 ± 75	2.15
PI (40:7)	967.554	3.1	313.911	5328 ± 350	-1.43
PI (38:7)	939.523	3.2	308.456	577 ± 110	2.86
PI (38:5)	943.553	3.2	311.235	1655 ± 318	2.90
PI (38:2)	889.575	3.2	300.237	740 ± 246	2.19
PI (36:4)	857.520	3.2	291.829	9143 ± 1117	2.88
PI (36:2)	861.550	3.2	293.245	22625 ± 2872	3.08
PI (34:2)	833.519	3.3	283.270	3499 ± 415	2.87
PI (34:1)	835.534	3.3	284.715	16866 ± 2253	-1.62
PG (o36:1)	797.548	2.3	282.016	3472 ± 461	1.81
PG (38:4)	797.534	1.6	279.085	1696 ± 106	2.69
PG (36:4)	769.506	1.7	273.349	3582 ± 243	1.94
PG (36:2)	773.531	1.7	276.285	7294 ± 636	1.61
PG (36:1)	775.544	1.7	279.219	11491 ± 1099	-2.00
PG (34:1)	747.513	1.7	270.515	40438 ± 3762	-2.12
PG (32:1)	719.488	1.8	263.197	3227 ± 204	-1.26
PE (p40:5)	776.558	5.0	279.212	10351 ± 61	3.62
PE (p40:4)	778.571	5.0	282.133	9804 ± 819	-1.17
PE (p38:5)	748.529	5.0	270.508	20512 ± 718	-1.17
PE (p36:2)	726.543	5.1	266.163	2168 ± 1485	-1.22
PE (p40:8)	770.514	4.9	273.343	305 ± 151	1.99
PE (p34:2)	698.513	5.2	260.314	789 ± 98	5.15
PE (44:4)	850.631	5.1	296.170	472 ± 41	4.12
PE (42:7)	816.554	5.1	286.276	1067 ± 82	2.72
PE (42:6)	818.569	5.1	287.715	1521 ± 131	3.92
PE (42:5)	820.585	5.1	289.151	2508 ± 189	1.43
PE (42:2)	826.630	5.2	292.002	811 ± 112	1.80
PE (40:8)	786.508	5.1	277.680	350 ± 48	4.01
PE (40:4)	794.566	5.1	284.953	17093 ± 1163	1.22
PE (38:6)	822.525	5.2	292.026	649 ± 61	2.22
PE (38:5)	764.524	5.1	271.895	14481 ± 928	-1.64
PE (38:4)	766.539	5.1	274.850	38704 ± 2551	1.17
PE (36:5)	796.511	5.3	284.941	875 ± 33	1.87
PE (36:4)	738.509	5.2	270.574	8333 ± 1331	2.49
PE (34:3)	712.493	5.2	258.696	581 ± 108	2.18
PE (34:2)	714.514	5.2	260.202	5947 ± 514	2.32
PE (32:0)	690.508	5.3	258.851	1664 ± 204	2.35
PC (42:6)	920.638	6.4	308.548	1107 ± 67	1.72
PC (40:6)	892.607	6.4	301.640	2046 ± 65	1.58
PC (40:5)	894.622	6.4	303.045	3424 ± 136	-1.25
PC (38:6)	864.576	6.4	294.663	1512 ± 61	1.39

PC (38:5)	866.592	6.4	297.511	4792 ± 145	-1.35
PC (38:4)	868.607	6.5	300.347	7060 ± 184	1.10
PC (36:4)	840.576	6.5	291.922	5466 ± 246	2.11
PC (34:3)	814.562	6.6	286.288	692 ± 46	2.83
PC (34:2)	816.576	6.6	290.619	4212 ± 228	3.41
PC (34:1)	818.592	6.6	292.049	18166 ± 732	-1.72
PC (32:1)	790.565	6.6	284.978	6206 ± 346	-1.78
PC (32:0)	792.576	6.7	287.872	9356 ± 226	1.17
PC (30:0)	764.548	6.7	280.757	5195 ± 244	-1.44
PA (34:1)	673.479	6.0	254.389	1224 ± 460	-2.83
MGDG (42:12)	845.528	0.8	289.011	5351 ± 475	1.40
MGDG (34:0)	793.560	0.9	277.637	2388 ± 223	1.46
DGDG (34:5)	909.550	0.9	298.715	6628 ± 891	-1.77
DGDG (34:4)	911.565	0.9	300.126	9125 ± 1172	-1.45
DGDG (32:6)	879.506	0.9	290.274	2698 ± 274	1.31
DGDG (32:5)	881.520	0.9	290.264	13330 ± 1718	-1.96
DGDG (30:4)	855.506	1.0	286.060	9241 ± 986	2.00
DGDG (30:3)	857.519	1.0	286.050	4899 ± 563	4.17
DGDG (30:2)	859.536	1.0	288.935	20714 ± 2673	3.53
DGDG (28:2)	831.505	1.0	280.358	5425 ± 475	2.36
DGDG (28:1)	833.520	1.0	281.810	7928 ± 1015	-1.79
AcylPG (44:8)	887.553	0.9	295.974	1447 ± 149	1.56
AcylPE (48:9)	896.585	1.5	300.201	5762 ± 703	-1.31

[a] Fold-change relative to control

Table 4.5 Altered lipids in HT-1080 cells exposed to CLA 18:3 compared to vehicle control in positive mode (p-value < 0.05).

LiPydomics identification	m/z	Retention time (min)	CCS (angstrom^2)	Abundance in Control	Fold change[a]
TG (48:5)	814.687	7.3	298.997	3679 ± 283	1.59
SM (d42:3)	811.668	7.2	295.201	5768 ± 471	1.52
SM (d36:4)	725.556	7.3	282.857	1526 ± 184	3.25
SM (d34:1)	703.574	7.3	280.397	18608 ± 656	1.39
PS (40:5)	838.561	5.8	286.048	2259 ± 94	-2.23
PS (40:4)	840.575	5.8	288.622	4509 ± 411	-1.98
PS (36:1)	790.562	5.9	282.424	5097 ± 800	-2.11
PI (p40:12)	883.470	3.2	287.106	525 ± 133	2.50
PI (40:8)	929.512	3.0	294.577	674 ± 498	2.79
PI (38:7)	903.506	3.2	290.867	813 ± 379	2.43
PI (36:4)	881.515	3.2	287.116	3070 ± 1450	2.27
PI (34:2)	857.517	3.2	285.946	950 ± 298	1.93
PG (p46:8)	887.625	1.5	304.880	1045 ± 176	1.95
PG (50:5)	982.744	1.3	322.884	1880 ± 87	1.75
PG (42:6)	868.615	1.4	298.688	656 ± 186	2.58
PG (36:4)	793.504	1.7	274.512	772 ± 297	2.24
PG (36:2)	797.529	1.7	281.074	712 ± 226	1.94
PE (p44:12)	820.522	4.9	284.852	555 ± 231	2.94
PE (p42:11)	794.508	4.9	278.468	528 ± 192	3.46
PE (p40:7)	774.541	5.0	285.131	8949 ± 2104	1.58
PE (p40:6)	798.540	4.9	286.280	2914 ± 925	1.97
PE (p40:5)	778.573	5.0	290.282	10831 ± 614	-1.28
PE (p40:4)	802.569	5.0	293.980	3773 ± 896	1.50
PE (p38:5)	750.543	5.0	280.061	19304 ± 761	-1.24
PE (p36:4)	746.510	5.0	274.807	4024 ± 463	1.79
PE (p34:0)	702.542	5.1	279.088	5611 ± 1489	-1.75
PE (42:7)	818.565	5.1	296.434	5613 ± 1445	1.53
PE (42:11)	810.504	5.0	284.910	405 ± 92	3.81
PE (42:10)	812.518	5.0	287.491	1632 ± 468	2.73
PE (40:9)	786.505	5.1	278.516	882 ± 307	5.04
PE (40:8)	788.518	5.1	283.741	4477 ± 1376	2.10
PE (40:7)	790.535	5.1	288.916	10531 ± 2349	1.64
PE (40:10)	784.501	5.2	278.528	1829 ± 263	2.08
PE (38:7)	762.502	5.2	278.667	3043 ± 703	2.76
PE (38:6)	764.519	5.2	281.280	3811 ± 420	2.63
PE (38:1)	774.605	5.0	281.215	5765 ± 1472	1.55
PE (36:5)	738.505	5.2	274.860	2653 ± 554	1.47
PE (36:4)	740.521	5.2	272.186	11388 ± 2312	1.51
PE (36:2)	744.554	5.2	277.467	15698 ± 454	-1.14
PE (34:3)	714.505	5.3	273.699	845 ± 104	2.31
PC (p36:3)	790.571	6.4	281.116	2916 ± 1123	-1.87
PC (o38:5)	794.602	6.4	290.180	11917 ± 590	1.12

PC (40:9)	828.554	6.4	288.689	578 ± 65	2.56
PC (40:8)	830.568	6.4	288.678	3723 ± 440	1.42
PC (40:5)	858.600	6.3	291.096	6643 ± 579	1.23
PC (38:7)	804.553	6.5	292.688	2563 ± 25	1.78
PC (38:6)	806.570	6.4	284.933	10180 ± 1795	1.42
PC (38:4)	810.599	6.5	296.482	45904 ± 721	1.22
PC (36:5)	780.554	6.5	277.235	6075 ± 134	1.20
PC (36:4)	782.568	6.5	287.674	41082 ± 3189	1.21
PC (34:3)	756.553	6.6	277.387	6243 ± 561	1.83
PC (34:2)	758.572	6.9	278.692	1847 ± 299	-2.20
PC (32:3)	728.522	6.7	280.213	1735 ± 189	2.72
PC (32:1)	754.538	6.6	272.094	3202 ± 736	1.76
PA (38:2)	746.575	6.6	286.617	8656 ± 1867	1.57
GlcCer (d34:1)	722.552	0.7	277.620	682 ± 255	2.01
DGDG (36:12)	907.479	0.8	292.129	2189 ± 1007	2.62
DGDG (32:6)	903.502	0.7	288.297	600 ± 129	3.41
DGDG (32:5)	905.515	0.7	290.858	1045 ± 422	2.86
DGDG (30:4)	879.501	1.0	285.833	1880 ± 521	2.00
DGDG (30:3)	881.514	0.7	287.116	1563 ± 395	2.60
DGDG (30:2)	883.533	1.0	290.966	6679 ± 1656	2.19
DGDG (28:1)	857.519	1.0	282.047	572 ± 189	2.91
DG (38:4)	627.534	0.9	262.259	12816 ± 749	1.60
DG (36:3)	601.518	0.9	257.000	831 ± 33	2.15
DG (36:2)	603.535	1.0	259.739	8528 ± 256	1.29
AcylPG (40:8)	855.485	1.0	284.660	772 ± 118	2.00

[a] Fold-change relative to control

Table 4.6 Altered lipids in HT-1080 cells exposed to CLA 18:3 compared to vehicle control in negative mode (p-value < 0.05).

LiPydomics identification	m/z	Retention time (min)	CCS (angstrom^2)	Abundance in Control	Fold change[a]
PS (44:5)	892.607	6.4	301.640	2046 ± 65	1.31
PS (44:4)	894.622	6.4	303.045	3424 ± 136	1.20
PS (38:2)	814.562	6.6	286.288	692 ± 46	2.09
PS (36:1)	788.547	6.6	282.071	1466 ± 75	1.48
PI (40:9)	963.523	3.1	313.929	103 ± 23	6.90
PI (40:7)	907.534	3.1	301.564	1395 ± 250	2.22
PI (40:6)	909.550	3.0	302.970	4847 ± 822	1.56
PI (38:5)	943.553	3.2	311.235	1655 ± 318	1.42
PI (38:2)	889.575	3.2	300.237	740 ± 246	2.24
PI (36:4)	857.520	3.2	291.829	9143 ± 1117	1.57
PI (36:2)	861.550	3.2	293.245	22625 ± 2872	1.34
PI (34:3)	831.505	3.3	283.281	774 ± 105	2.84
PI (34:2)	833.519	3.3	283.270	3499 ± 415	1.47
PI (34:1)	835.534	3.3	284.715	16866 ± 2253	1.36
PG (38:4)	797.534	1.6	279.085	1696 ± 106	1.50
PG (36:4)	769.506	1.7	273.349	3582 ± 243	1.60
PG (36:2)	773.531	1.7	276.285	7294 ± 636	1.32
PG (36:1)	775.544	1.7	279.219	11491 ± 1099	1.22
PG (34:2)	745.504	1.7	269.035	3779 ± 242	1.58
PG (34:1)	747.513	1.7	270.515	40438 ± 3762	1.20
PG (32:1)	719.488	1.8	263.197	3227 ± 204	1.32
PE (p40:8)	770.514	4.9	273.343	305 ± 61	4.38
PE (p40:7)	772.529	4.9	274.813	4284 ± 409	1.41
PE (p40:6)	774.542	5.0	277.753	8481 ± 780	1.32
PE (p40:5)	776.558	5.0	279.212	10351 ± 819	1.20
PE (p40:4)	778.571	5.0	282.133	9804 ± 718	1.26
PE (p38:6)	746.513	5.0	269.028	5435 ± 366	1.20
PE (p36:4)	722.513	5.0	264.685	20460 ± 1799	1.25
PE (p34:2)	698.513	5.2	260.314	789 ± 98	1.64
PE (p34:1)	700.519	5.2	261.817	11886 ± 801	1.13
PE (o40:8)	832.546	5.0	296.273	2970 ± 142	1.18
PE (o38:8)	804.518	5.0	290.692	2124 ± 120	1.26
PE (40:8)	786.508	5.1	277.680	350 ± 48	7.26
PE (40:7)	788.524	5.1	279.139	3890 ± 554	1.94
PE (38:7)	760.493	5.1	270.431	341 ± 59	7.68
PE (38:6)	762.510	5.1	268.926	3145 ± 365	2.88
PE (38:6)	822.525	5.2	292.026	649 ± 61	2.08
PE (36:5)	736.494	5.1	261.571	818 ± 101	1.66
PE (36:4)	738.509	5.2	270.574	8333 ± 1331	1.59
PE (34:4)	710.477	5.2	258.709	217 ± 43	4.37
PE (34:3)	712.493	5.2	258.696	581 ± 108	4.41
PE (34:2)	714.514	5.2	260.202	5947 ± 514	1.19

PC (38:6)	864.576	6.4	294.663	1512 ± 61	1.43
PC (38:4)	868.607	6.5	300.347	7060 ± 184	1.11
PC (36:4)	840.576	6.5	291.922	5466 ± 246	1.13
PC (34:2)	816.576	6.6	290.619	4212 ± 228	1.24
PC (34:1)	818.592	6.6	292.049	18166 ± 732	1.16
PC (32:1)	790.565	6.6	284.978	6206 ± 346	1.10
MGDG (42:12)	845.528	0.8	289.011	5351 ± 475	1.33
MGDG (34:0)	793.560	0.9	277.637	2388 ± 223	1.38
MGDG (32:3)	769.503	1.0	277.785	3516 ± 305	1.43
GlcCer (d34:1)	698.558	0.7	270.857	1439 ± 61	1.54
FA (18:0)	283.264	0.7	181.565	9661 ± 376	1.22
FA (16:0)	255.232	0.7	174.976	6501 ± 108	1.18
DGDG (46:7)	1073.722	1.4	334.019	1122 ± 163	1.85
DGDG (34:7)	905.518	0.9	298.735	1506 ± 83	1.96
DGDG (34:6)	907.535	0.9	298.725	3890 ± 429	1.73
DGDG (34:5)	909.550	0.9	298.715	6628 ± 891	1.51
DGDG (34:4)	911.565	0.9	300.126	9125 ± 1172	1.46
DGDG (32:6)	879.506	0.9	290.274	2698 ± 274	4.95
DGDG (32:5)	881.520	0.9	290.264	13330 ± 1718	1.59
DGDG (30:4)	855.506	1.0	286.060	9241 ± 986	1.52
DGDG (30:3)	857.519	1.0	286.050	4899 ± 563	2.03
DGDG (30:2)	859.536	1.0	288.935	20714 ± 2673	1.57
DGDG (28:2)	831.505	1.0	280.358	5425 ± 475	1.62
DGDG (28:1)	833.520	1.0	281.810	7928 ± 1015	1.65
AcylPG (45:9)	899.537	0.6	297.341	4935 ± 640	1.49
AcylPG (44:8)	887.553	0.9	295.974	1447 ± 149	1.58
AcylPE (48:9)	896.585	1.5	300.201	1447 ± 703	1.48

[a] Fold-change relative to control

Table 4.7 Area under the curve of each aldehyde from the oxidation of CLA 18:2 vs LA.

Aldehyde	LA			CLA 18:2			Ratio CLA 18:2/LA
	Air sample	Solution sample	Total	Air sample	Solution sample	Total	
Pentanal	360136	82013	442149	347753	108444	456197	1.0
Hexanal	399387	359099	758486	493005	178159	671164	0.88
2-*t*-Heptenal	95758	42366	138124	301110	100766	401876	2.9
2-*t*-Octenal	80644	203475	284119	568489	503307	1071796	3.7
2-*t*-Nonenal	4938	46131	51069	73712	82771	156483	3.1
4-HNE	-	87738	87738	-	29879	29879	0.34

Table 4.8 EC_{50} values of cells after 24 h treatment with different aldehydes (n = 3 independent experiments)

	Aldehyde	**EC_{50} ± SEM (μM)**
Saturated[b]	Pentanal	Very large[a]
	Hexanal	Very large[a]
α,β–Unsaturated[c]	2-*t*-Heptenal	59 ± 7.5
	2-*t*-Octenal	26 ± 4.1
	2-*t*-Nonenal	25 ± 3.1
	4-HNE	16 ± 1.1
Conjugated[d]	2,4-*tt*-Hexadienal	39 ± 3.2
	2,4-*tt*-Nonadienal	13 ± 1.5
	2,4-*tt*-Decadienal	6.5 ± 0.54

[a] The EC_{50} values are outside the concentration range tested.
[b] Concentration range = 10 - 1500 μM
[c] Concentration range = 1 – 400 μM
[d] Concentration range = 0.1 – 100 μM

Table 4.9 Top 10 significantly upregulated pathways in CLA 18:3-, RLS3-CLA 18:2-, RSL3-LA-treated cells compared to control treatment identified by Integrated Differential Expression and Pathway (iDEP) and iPathwayGuide (iPG) analysis. Only the top 10 differentially expressed pathway genes with highest absolute fold change are shown. (n = 4 biological replicates per condition)

Comparison Groups	iDEP Pathway	-log (*p*-value) (iDEP)	-log (*p*-value) (iPG)	Differentially Expressed Pathway Genes
CLA 18:3 vs Control	Proteasome	2.72	3.91	PSMA1, PSMC6, PSMC2, PSMA5, PSMB2, PSMB6, PSMC4, PSMD3, PSMD11, PSMD14
	Amyotrophic lateral sclerosis	2.72	3.91	RAB39B, SQSTM1, DDIT3, HSPA5, GPX3, MAPK13, PSMA1, PSMC6, SOD1, PSMC2
	Prion disease	2.72	3.78	HSPA6, IL1A, DDIT3, EGR1, IL1B, HSPA5, ITPR1, MAPK13, PSMA1, PSMC6
	Parkinson disease	2.72	3.84	DDIT3, UBC, HSPA5, ITPR1, PSMA1, PSMC6, SOD1, PSMC2, PSMA5, PSMB2
	Ribosome	2.66	3.91	MRPL23, RPL39, RPS27A, RPS27, RPL11, MRPL27, RPS21, RPS12, RPL26L1
	Protein processing in ER	2.54	3.91	HSPA6, DDIT3, PPP1R15A, HSPA5, HERPUD1, NSFL1C, UFD1, BAG2, XBP1, VCP
	Coronavirus disease	2.52	4.00	FOS, CXCL8, IL1B, C1S, MMP1, MAPK13, NFKBIA, MMP3, IL6R, C1R
	Pathways of neurodegeneration	1.68	3.82	RAB39B, HRAS, SQSTM1, L1A, DDIT3,

				IL1B, UBC, HSPA5, GPX3, ITPR1
	Chemical carcinogenesis	1.57	3.84	FOS, HMOX1, AKR1C1, AKR1C3, HRAS, NQO1, MAPK13, AKT3, NFKBIA, MGST1
	Oxidative phosphorylation	1.57	3.91	ATP6V0A4, NDUFA9, ATP6V0A1, ATP6V0E1, ATP5PO, ATP6V0B, COX6C, NDUFC2, NDUFB9, ATP6V1E1
RSL3-CLA 18:2 vs Control	Protein processing in ER	2.52	3.57	PPP1R15A, HSPA6, UBXN4, SEC24D, WFS1, NSFL1C, PLAA, HSPA5, VCP, DDIT3
	Proteasome	2.52	3.65	PSMC6, PSMB2, PSMC2, PSMD1, PSMA1, PSMD14, PSMD11, PSMB6, PSMD3, PSMD12

Table 4.10 DEGs involved in unfolded protein response in the ER identified using Database for Annotation, Visualization, and Integrated Discovery (DAVID) functional annotation clustering in HT-1080 cells treated with CLA 18:3 and RSL3-CLA18:2 (adjusted p-value < 0.05; n = 4 biological replicates per condition).

Comparison Groups	Gene ID	Description	Log2 (FC)	Adjusted p-value
CLA 18:3 vs. DMSO (Enrichment score = 3.62)	CXCL8	C-X-C motif chemokine ligand 8	3.62	8.95E-70
	CEBPB	CCAAT enhancer binding protein beta	1.35	4.27E-57
	CHAC1	ChaC glutathione specific gamma-glutamylcyclotransferase 1	1.85	1.30E-26
	DDIT3	DNA damage inducible transcript 3	1.87	1.29E-23
	DNAJB9	DnaJ heat shock protein family (Hsp40) member B9	1.86	8.72E-70
	HSPA6	heat shock protein family A (Hsp70) member 6	2.70	8.06E-26
	HERPUD1	homocysteine inducible ER protein with ubiquitin like domain 1	1.23	2.39E-68
	NIBAN1	niban apoptosis regulator 1	1.33	3.67E-39
	PPP1R15A	protein phosphatase 1 regulatory subunit 15A	1.62	1.99E-217
	THBS1	thrombospondin 1	-1.06	1.84E-130
RSL3-CLA 18:2 vs. DMSO (Enrichment score = 1.56)	CXCL8	C-X-C motif chemokine ligand 8	3.79	1.06E-102
	CEBPB	CCAAT enhancer binding protein beta	1.42	4.22E-71
	CREBRF	CREB3 regulatory factor	1.13	2.97E-11
	DNAJB9	DnaJ heat shock protein family (Hsp40) member B9	1.36	6.32E-47
	CREB3L1	cAMP responsive element binding protein 3 like 1	-1.01	2.13E-48
	HSPA6	heat shock protein family A (Hsp70) member 6	1.25	3.31E-06
	NIBAN1	niban apoptosis regulator 1	1.40	7.44E-46
	PPP1R15A	protein phosphatase 1 regulatory subunit 15A	1.32	1.36E-212
	THBS1	thrombospondin 1	-1.57	< 2.23E-308

Table 4.11 DEGs Regulated by M-Phase Phosphoprotein 6 (MPHOSPHO6) in HT-1080 cell line treated with CLA 18:3, RSL3-CLA 18:2, and RSL3-LA (n = 4 biological replicates per condition)

Gene ID	Description	CLA 18:3		RSL3-CLA 18:2		RSL3-LA	
		Log2 (FC)	Adjusted p-value	Log2(FC)	Adjusted p-value	Log2(FC)	Adjusted p-value
RPL39	60S ribosomal protein L39	1.75	1.00E-06	0.79	5.73E-04	-	-
RPL11	60S ribosomal protein L11	1.72	1.00E-06	0.75	1.00E-06	0.32	3.52E-02
RPL26L1	60S ribosomal protein L26-Like1	1.62	1.00E-06	-	-	-	-
RPL34	60S ribosomal protein L34	1.50	1.00E-06	0.83	1.00E-06	0.45	1.36E-02
RPLP1	60S acidic ribosomal protein P1	1.49	1.00E-06	0.61	1.91E-03	-	-
RPL21	60S ribosomal protein L21	1.49	1.00E-06	1.04	1.00E-06	0.43	8.75E-03
RPLP2	60S acidic ribosomal protein P2	1.45	1.00E-06	1.24	1.00E-06	0.64	7.20E-04
RPL37A	60S ribosomal protein L37a	1.43	1.00E-06	-	-	-	-
RPL19	60S ribosomal protein L19	1.42	1.00E-06	1.18	1.00E-06	0.63	1.50E-05
RPL31	60S ribosomal protein L31	1.42	1.00E-06	-	-	-	-
RPL23	60S ribosomal protein L23	1.39	1.00E-06	1.00	1.00E-06	0.58	7.64E-06
RPL9	60S ribosomal protein L9	1.32	1.00E-06	0.65	1.00E-06	0.41	5.90E-03
RPL37	60S ribosomal protein 37	1.30	1.00E-06	0.82	3.91E-06	-	-
RPL36AL	60S ribosomal protein L36a-Like	1.30	1.00E-06	0.68	7.76E-05	-	-
RPL10	60S ribosomal protein L10	1.26	1.00E-06	0.96	1.00E-06	0.41	6.98E-03
RPL24	60S ribosomal protein L24	1.24	1.00E-06	-	-	-	-
RPL27A	60S ribosomal protein L27a	1.22	1.00E-06	0.71	1.00E-06	0.34	1.38E-02
RPL32	60S ribosomal protein L32	1.21	1.00E-06	0.84	1.00E-06	0.43	1.43E-02

RPL27	60S ribosomal protein L27	1.15	1.00E-06	-	-	-	-
RPL12	60S ribosomal protein L12	1.15	1.00E-06	0.64	1.00E-06	-	-
RPL18A	60S ribosomal protein L18a	1.14	1.00E-06	-	-	-	-
RPL22L1	60S ribosomal protein L22-Like1	1.14	1.00E-06	-	-	-	-
RPL18	60S ribosomal protein L18	1.12	1.00E-06	-	-	-	-
RPL6	60S ribosomal protein L18	1.10	1.00E-06	0.50	1.75E-04	-	-
RPL35	60S ribosomal protein L35	1.10	1.00E-06	-	-	-	-
RPL13	60S ribosomal protein L13	1.06	1.00E-06	0.41	7.23E-03	-	-
RPL8	60S ribosomal protein L8	1.06	1.00E-06	-	-	-	-
RPL7A	60S ribosomal protein L7a	1.05	1.00E-06	0.59	1.00E-06	0.29	2.80E-02
RPL13A	60S ribosomal protein L13a	1.05	1.00E-06	-	-	-	-
RPL15	60S ribosomal protein L15	1.03	1.00E-06	1.09	1.00E-06	0.51	9.57E-03
RPL22	60S ribosomal protein L22	0.96	1.00E-06	-	-	-	-
RPL7	60S ribosomal protein L7	0.96	1.00E-06	-	-	-	-
RPL26	60S ribosomal protein L26	0.96	4.50E-03	-	-	-	-
RPL3	60S ribosomal protein L3	0.95	1.00E-06	0.55	1.30E-05	-	-
RPL38	60S ribosomal protein L38	0.93	1.00E-06	-	-	-	-
RPL23A	60S ribosomal protein L23a	0.91	1.00E-06	0.99	1.00E-06	-	-
RPL4	60S ribosomal protein L4	0.91	1.00E-06	0.45	6.67E-05	-	-
RPL10A	60S ribosomal protein L10a	0.89	1.00E-06	0.55	5.08E-05	0.42	5.65E-03
UBA52	Ubiquitin A-52 Residue Ribosomal Protein Fusion Product 1	0.89	1.00E-06	-	-	-	-

RPL14	60S ribosomal protein L14	0.77	1.00E-06	0.33	2.34E-03	-	-
RPL28	60S ribosomal protein L28	0.65	5.87E-04	-	-	-	-
NOL9	Nucleolar Protein 9	-	-	-	-	0.69	1.75E-03

Table 4.12 DEGs Regulated by eukaryotic translation initiation factor 5 (EIF5) in HT-1080 cell line treated with CLA 18:3 (n = 4 biological replicates per condition)

Gene ID	Description	CLA 18:3	
		Log2(FC)	Adjusted p-value
ATF4	Activating Transcription Factor 4	2.39	1.00E-06
RPS27A	40S Ribosomal Protein S27a	1.74	1.00E-06
RPS27	40S Ribosomal Protein S27	1.73	1.00E-06
RPS21	40S Ribosomal Protein S21	1.63	1.00E-06
RPS12	40S Ribosomal Protein S12	1.62	1.00E-06
RPS15A	40S Ribosomal Protein S15a	1.61	1.00E-06
RPS19	40S Ribosomal Protein S19	1.48	1.00E-06
RPS3A	40S Ribosomal Protein S3a	1.46	1.00E-06
RPS27L	40S Ribosomal Protein S27-Like	1.43	1.00E-06
RPS24	40S Ribosomal Protein S24	1.41	1.00E-06
EIF3I	Eukaryotic Translation Initiation Factor 3 Subunit I	1.32	1.00E-06
RPS25	40S Ribosomal Protein S27	1.27	1.00E-06
EIF3K	Eukaryotic Translation Initiation Factor 3 Subunit K	1.22	1.00E-06
FAU	FAU Ubiquitin Like And Ribosomal Protein S30 Fusion	1.22	1.00E-06
RPS8	40S Ribosomal Protein S8	1.21	1.00E-06
RPS13	40S Ribosomal Protein S13	1.17	1.00E-06
RPS3	40S Ribosomal Protein S3	1.17	1.00E-06
RPS11	40S Ribosomal Protein S11	1.17	1.00E-06
RPS6	40S Ribosomal Protein S6	1.16	1.00E-06
RPS15	40S Ribosomal Protein S15	1.15	1.00E-06
RPS20	40S Ribosomal Protein S20	1.13	1.00E-06
RPS16	40S Ribosomal Protein S16	1.13	1.00E-06
RPSA	40S Ribosomal Protein SA	1.10	1.00E-06
RPS29	40S Ribosomal Protein S29	1.01	3.69E-06
RPS14	40S Ribosomal Protein S14	0.91	1.00E-06
EIF3H	Eukaryotic Translation Initiation Factor 3 Subunit H	0.91	1.00E-06
EIF3D	Eukaryotic Translation Initiation Factor 3 Subunit D	0.88	1.00E-06
RPS4X	40S Ribosomal Protein S4 X-Linked	0.86	1.00E-06
EIF2S2	Eukaryotic Translation Initiation Factor 2 Subunit Beta	0.84	1.00E-06
RPS28	40S Ribosomal Protein S28	0.76	3.95E-06

EIF3M	Eukaryotic Translation Initiation Factor 3 Subunit M	0.69	6.32E-06
RPS2	40S Ribosomal Protein S2	0.69	1.00E-06
EIF3E	Eukaryotic Translation Initiation Factor 3 Subunit E	0.67	2.41E-05
RPS23	40S Ribosomal Protein S23	0.58	3.38E-03
EIFF5	Eukaryotic Translation Initiation Factor 3 Subunit G	0.52	1.38E-02

Chapter 5. The Relevance of ER Stress and the Unfolded Protein Response to Ferroptosis

1.1 Introduction

Ferroptosis is a type of regulated cell death that is driven by iron-dependent autoxidation of membrane-bound PUFAs (*13, 17, 299*). This mode of cell death was found to be morphologically, genetically, and pharmacologically distinct from other types of cell death (*13*). Recently, another point of divergence emerged between ferroptosis and other cell death mechanisms. Specifically, while other types of cell death, such as apoptosis or necroptosis, are modulated by a set of key effectors (*300*), ferroptosis is suggested not to be defined by a single, unitary lethal regulatory pathway (*66*). For example, ACSL4, an enzyme functioning in the activation of PUFAs for their incorporation into membrane phospholipids, was found to be more critical in ferroptosis induced by direct GPX4 inhibition than cystine deprivation. In addition, ether lipids and their APGS-dependent biosynthesis are also suggested to be only context-dependent.

However, instead of sharing a common regulatory network upstream from the lipid peroxidation process, the different ferroptosis induction mechanisms may converge at the membrane lipid peroxidation and downstream pathways involved in the execution of ferroptosis. Particularly, autoxidation of membrane-bound PUFAs leads to the accumulation of toxic oxidation products such as reactive lipid-derived electrophiles. These electrophilic oxidation products can modify protein side chains, leading to the accumulation of misfolded and unfolded proteins in the ER and resulting in ER stress. Indeed, previous studies have shown that oxidative stress and ER stress are strongly associated *(301, 302)*. As a result, the ER stress responses, such as the unfolded protein response (UPR), are activated. Sensing of ER stress and the activation of the UPR signaling pathways are coordinated by three ER transmembrane-bound sensors: inositol requiring

transmembrane kinase/endoribonuclease 1α (IRE1α), activating transcription factor 6 (ATF6) and protein kinase R-like ER kinase (PERK). Under ER stress conditions, activated PERK phosphorylates EIF2α, leading to the downregulation of global mRNA translation to reduce the protein folding load on the ER while promoting the transcription of approximately one-third of the UPR-associated genes, including ATF4 (*301*). Upon the initial activation of the ER stress response, ATF4 promotes the expression of the components of the adaptive response, such as ER chaperones and ER-associated degradation (ERAD) pathway, to ameliorate the accumulation of unfolded protein in the ER (*268, 287, 288*). However, when the ER stress signal is prolonged, ATF4 promotes the apoptosis signaling pathway via the activation of C/EBP homologous protein (CHOP) and its downstream targets, such as *CHAC1, PPP1R15A, TRB3* (*269, 303, 304*).

Previously, ER stress and the induction of the PERK/EIF2α/ATF4 branch of ER stress response were thought to be related to ferroptosis induced only by the system x_c^- inhibitors erastin and sorafenib (*84, 133*). Therefore, it has been suggested that the role of ER stress in ferroptosis is context-dependent (*305*). However, more ferroptosis-inducing mechanisms were found to activate the PERK/EIF2α/ATF4 branch of the ER stress response (*306-308*), suggesting the accumulation of unfolded and misfolded proteins, leading to the activation of ER stress and UPR signaling pathways may be universal downstream effects of ferroptosis-inducing mechanisms. In Chapter 4, we demonstrated that treatment with CLA 18:3, which induces ferroptosis via a non-canonical mechanism, led to increased ER stress and the upregulation of genes associated with the UPR signaling pathways. To determine whether ER stress and UPR responses are commonly activated in ferroptosis, we performed differential gene expression and pathways analyses on publicly available ferroptosis-related RNA-seq data and compared the results for each inducer to

those of CLA 18:3. The results from this chapter help provide some insight into the molecular events downstream of lipid ferroptosis and during the execution phase.

1.2 Results

To elucidate the common differentially expressed genes (DEGs) and pathways upregulated in ferroptosis induced by CLA 18:3 and other inducers, we extracted the raw ferroptosis-related RNA sequencing reads available on Gene Expression Omnibus, which is a public functional genomics data repository (*309, 310*), using the SRA toolkit (*311*). We then aligned and converted the raw RNA sequencing reads into raw counts, identified DEGs using the DEseq2 algorithm, and performed pathway analyses using the Database for Annotation, Visualization, and Integrated Discovery (DAVID) server, the integrated Differential Expression and Pathway (iDEP) web application, and iPathwayGuide (iPG) software as described in Chapter 4 to ensure that all RNA-seq data were analyzed using the same protocol as our CLA 18:3 data.

1.2.1 Repository GSE162069

1.2.1.1 Treatment with α-Eleostearic Acid

In this repository (*75*), transcriptomic changes of triple-negative breast cancer MDA-MB-231 cells cultured for 5 h with 100 μM α-eleostearic acid (α-ESA) were compared to the vehicle controls. In addition, transcriptomic changes in orthotopic MDA-MB-231 xenografts in mice treated orally with 100 μl α-ESA-rich tung oil 5 days a week for 24 days were compared to the control mice treated with high-oleic acid safflower oil. Overall, compared to the control, the addition of α-ESA and α-ESA-rich tung oil led to the significant upregulation of 88 and 130 genes, respectively (adjusted *p*-value (padj) < 0.05, > 2-fold change) (**Figure 5.1a**). Among the DEGs, 12 genes were commonly upregulated by CLA 18:3, α-ESA, and α-ESA-rich tung oil. Notably, among these 12 shared genes, DAVID functional clustering analysis identified *DNAJB9, HSPA5*,

and *HERPUD1* as genes associated with the ERAD pathway, one of the critical signaling pathways activated by ER stress (*288*), with an enrichment score of 1.42. When we removed the > 2-fold change filter, there were a total of 113 genes commonly upregulated between the three comparison groups (**Figure 5.1b**). Among them, DAVID functional clustering analysis identified the gene cluster related to the ERAD pathways among the shared genes with an enrichment score of 5.11 (**Table 5.1**). In addition, we also observed the gene cluster related to chaperone-dependent protein folding with an enrichment score of 3.28 (**Table 5.2**).

Utilizing pathway analyses by both iDEP and iPG, we found the protein processing in the ER was upregulated in treatments with α-ESA and α-ESA-rich tung oil (**Table 5.3**). Moreover, in the upstream regulator module of iPG, we observed the significant activation of ATF4 (combined *p*-values = 4.10E-8 and 1.60E-7 for treatments with ESA and ESA-rich tung oil, respectively) and other transcriptional modulators of stress responses (**Figure 5.1c-e**). In addition, we observed significant upregulations of *DDIT4*, a specific gene target of ATF4 (*267*), in α-ESA versus control (padj = 1.02E-10, log2foldchange (log2FC) = 4.26) and α-ESA-rich tung oil versus control (padj = 2.36E-16, log2FC = 4.32) comparisons. Another gene target of ATF4, *DDIT3*, was also upregulated in α-ESA versus control (padj = 1.19E-03, log2FC = 0.76) and α-ESA-rich tung oil versus control (padj = 9.78E-11, log2FC = 0.96) comparisons. In addition, *CHAC1*, which is another downstream target of the PERK/EIF2α/ATF4 and was previously considered a pharmacodynamic biomarker of system x_c^- inhibition (*84, 269*), is commonly upregulated in treatments with α-ESA (padj = 8.56E-05, log2FC = 1.07) and α-ESA-rich tung oil (padj =6.07E-08, log2FC = 1.01). Since we also found the upregulation of *DDIT4*, *DDIT3,* and *CHAC1* in our results for CLA 18:3, it appeared that increased ER stress and the activation of the

PERK/EIF2α/ATF4 branch of the UPR are common in ferroptosis induced by CLA 18:3 isomers and CLA 18:3-containing TAGs.

Notably, using the pathway network creating function of iDEP, we observed networks associated with unfolded protein response and apoptosis signaling pathway in Gene Ontology (GO)-Biological Processes enrichment analysis for both the treatments with α-ESA and α-ESA-rich tung oil (**Figure 5.2**), suggesting the activation of UPR-mediated apoptosis signaling pathways due to significant ER stress. Of note, we found that the CLA 18:3 and α-ESA induced different components of ER stress-mediated apoptosis signaling. Specifically, in our RNA-seq results of CLA 18:3 in the HT-1080 cell line, we observed the activation of the CHOP-induced apoptosis potentiators, including growth arrest and DNA damage-inducible protein GADD34 (*PPP1R15A;* padj = 1.99E-217, log2FC = 1.62) and tribbles homolog 3 TRB3 (*TRIB3*; padj = 7.12E-59, log2FC = 0.99) (*301, 312*). However, treatment of MDA-MB-231 with α-ESA only led to a mild upregulation of *PPP1R15A* (padj = 1.99E-03, log2FC = 0.46), and *TRIB3* was not observed among the significantly altered genes. Instead, in these cells, we observed significant upregulation of apoptosis-modulating genes involved in the NF-kappa B (NF-κB) signaling pathway, such as *NFKBIA* (padj = 3.15E-30, log2FC = 1.84) (*313*) and *TNFRSF10B* (padj = 2.09E-07, log2FC = 0.62) (*314*). In contrast, these genes were only slightly upregulated in CLA 18:3-treated cells. In addition, other NF-κB signaling-associated genes, including *BIRC3* (padj = 2.55E-11, log2FC = 1.43) (*315*) and *TRAF1* (padj = 2.55E-24, log2FC = 1.33) (*316*), were upregulated in α-ESA-treated cells but were not identified in our results for CLA 18:3-treated cells. In line with these findings, the NF-κB signaling pathway was identified among the most activated pathways in the treatment with ESA in MDA-MB-231 cells (**Table 5.3**) but not in our study with HT-1080 cells. Additionally, p53 upregulated modulator of apoptosis protein PUMA (*BBC3;* padj

= 1.83E-03, log2FC = 0.97) (*317*) was upregulated in α-ESA-treated cells but was not identified in our CLA 18:3-treated cells. Notably, genes that play an essential role in apoptosis, such as CASP3 or CASP7, were not identified among the DEGs, confirming that α-ESA only induces ferroptosis.

1.2.1.2 Treatment with ML162

This repository also includes the RNA-seq data for the treatment of MDA-MB-231 cells cultured for 5 h with 125 nM ML162 (*75*), a direct inhibitor of GPX4 (*14, 89*) compared to the vehicle controls. Overall, we observed that the addition of ML162 led to significant upregulation of 40 DEGs, and there were only seven genes commonly upregulated between CLA 18:3 versus control and ML162 versus control comparisons (padj < 0.05, > 2-fold change) (**Figure 5.3a**). These genes, including *HMOX1, HSPA6, DDIT4, LURAP1L, GEM, CEBPB,* and *GDF15*, were not clustered by DAVID. However, once we removed the > 2-fold change, the number of shared genes between the two comparisons increased to 25 (**Figure 5.3b**), and DAVID functional clustering analysis identified the gene cluster related to unfolded protein response in the ER as the most enriched subset of shared genes with an enrichment score of 3.55 (**Table 5.4**). However, no significantly altered pathways were identified by iDEP and iPG. Furthermore, while *DDIT4* (padj = 1.00E-22, log2FC = 4.32) was significantly upregulated in the treatment with ML162, the changes to *DDIT3* and *CHAC1* were statistically insignificant. Moreover, only INS, BMP7, and EGR2 were predicted as significantly activated upstream regulators (combined *p*-values = 0.001, 0.005, and 0.007, respectively) (**Figure 5.3c**). These results suggest a weak activation of the PERK/EIF2α/ATF4 branch of the UPR, probably due to weak ferroptosis induction since not many upregulated DEGs were identified in the treatment with ML162 compared to the control (**Figure 5.3a, b**).

1.2.2 Repository GSE135361

For this repository (*318*), we only extracted and analyzed the transcriptomic changes of HT-1080 cells treated with 10 μM erastin for 24 hr. Overall, the addition of erastin led to the significant upregulation of 34 genes, and treatments with CLA 18:3 and erastin significantly upregulated only six common genes, including *GNCT3, HMOX1, SQSTM1, GCLM, HSPB8*, and *FTH1* (padj < 0.05, > 2-fold change) (**Figure 5.4a**). When the > 2-fold change filter is removed, the number of shared genes increased to 399 (**Figure 5.4b**), and DAVID functional clustering identified chaperone-associated protein binding and ribosome biosynthesis as top two most enriched subsets of genes with enrichment scores of 12.26 and 5.34, respectively (**Table 5.5** and **Table 5.6**). While pathways analyses using iDEP and iPG did not return any significantly altered pathway in the treatment of erastin compared to the control, iDEP identified the upregulation of ribosome biogenesis network in both GO-Biological Process and Molecular Function enrichment analysis (**Figure 5.5**). In the upstream regulator module of iPG, the treatment with erastin led to the activation of the transcriptional regulators of genes associated with ribosome biosynthesis (**Figure 5.4c-e**).

When investigating whether the PERK/EIF2α/ATF4 pathway is upregulated in the treatment with erastin, we found that *CHAC1* (padj = 3.79E-74, log2FC = -2.88) and *DDIT4* (padj = 1.70E-154, log2FC = -1.98) are significantly downregulated. At the same time, *DDIT3* was not detected among the significantly altered genes. Of note, during the initiation of UPR, the phosphorylation of EIF2α leads to the suppression of global mRNA translation while promoting the expression of ATF4 (*288*). During the termination of the ER stress signals, EIF2α is dephosphorylated, leading to the downregulation of ATF4 and return to normal protein synthesis (*319*). Therefore, due to the downregulation of genes associated with the ER stress response and the activation of ribosome biogenesis, we speculate that what we observed in GSE135361 is the termination of the

PERK/EIF2α/ATF4 pathway and the recovery of protein synthesis, which is potentially due to the mitigation of ER stress in the survived cells (*319*).

The results observed here are opposite to the results in another study in which the HT-1080 cell line was treated with 10 μM erastin for a shorter period - 5 h (*84*), and the genes targets of ATF4, including *CHAC1, DDIT4*, and *DDIT3,* were significantly upregulated. Since there was no raw data available for this study, we uploaded the FPKM expression values from RNA-seq provided by the authors to iDEP for pathway analysis. Even though no significant pathways were found for gene ontology (GO) associated with cellular components and molecular functions, gene networks related to unfolded protein response and apoptotic signaling pathway in response to ER stress were found for GO terms related to biological processes (**Figure 5.6**). Additionally, we uploaded the genes that passed the authors' significance thresholds (genes with FPKM not equal to zero in any condition, FPKM≥1 for both replicates in the DMSO condition, and the difference between replicate values in the two DMSO and the two erastin-treated samples was less than 2.5) and had more than 2-fold change in expression compared to the control to DAVID web server. DAVID functional clustering analysis revealed that the genes associated with intrinsic apoptosis signaling pathway in response to ER stress as the most enriched subset of genes with an enrichment score of 3.29 (**Table 5.7**). Combining the results from this study and the results from repository GSE134361, we speculate that the addition of erastin can lead to the activation of ER stress responses, which inhibit global protein translation as part of the initiation of the UPR response and then switch to activate the UPR-dependent apoptosis signaling pathways, within 5 hours. Then, after 24 h, the normal protein synthesis is initiated again in the survived cells with subdued ER stress.

1.2.3 Repository GSE182638

In this repository (*320*), two multiple myeloma (MM) cell lines, including glucocorticoid-resistant (MM1R) and glucocorticoid-sensitive (MM1S) cell lines, were treated with 5 μM RSL3 for 3 h, and the associated transcriptomic changes were compared to the control treated with DMSO. In addition, the cells were pre-treated with 2 μM Fer-1 for 2 h before treatment with 5 μM RSL3 for 3 h and the transcriptomic changes compared to the control were also assessed.

1.2.3.1 Treatment of MM1R Cell Line with RSL3

Overall, treatment of the MM1R cell line with RSL3 led to an upregulation of 266 DEGs, and 34 of these genes are also regulated by CLA 18:3 (**Figure 5.7a**). Among the shared DEGs, DAVID functional clustering analysis identified the genes associated with unfolded protein response in the ER as the most enriched subset of genes with an enrichment score of 4.44 (padj < 0.05, > 2-fold change) (**Table 5.8**). When the > 2-fold change filter was removed, we observed a total of 192 genes commonly upregulated by CLA 18:3 and RSL3 (**Figure 5.7b**), and ER stress response was the most enriched subset of genes identified by DAVID functional clustering with an enrichment score of 3.84. However, no significantly altered pathways were identified in pathway analyses using iDEP and iPG. On the other hand, the gene targets of ATF4, including *CHAC1* (padj = 4.13E-39, log2FC = 3.04), *DDIT3* (padj = 2.02E-04, log2FC = 2.18), and *DDIT4* (padj = 1.83E-05, log2FC = 2.39), were all significantly upregulated.

Pre-treating the cells with Fer-1 for 2 h prior to the addition of RSL3 led to the significant downregulation of 28 genes and upregulation of one gene compared to the cells treated with RSL3 alone (padj < 0.05, > 2-fold change). Among the downregulated DEGs, genes associated with protein damage or ER stress, such as *CHAC1, DDIT4,* and *DDIT3*, were not observed. Instead, transcription regulation is identified by DAVID functional clustering as one of the most enriched

among the significantly downregulated gene in the combined treatment with RSL3 and Fer-1 compared to the treatment with RSL3 with an enrichment score of 1.42 (**Table 5.9**). This result is consistent with the findings from the original study that treating MM1R cells with RSL3 led to epigenomic stress responses, and the pre-treatment with Fer-1 could revert these responses (*320*).

1.2.3.2 Treatment of MM1S Cell Line with RSL3

Overall, the treatment with RSL3 in MM1S cell lines led to the significant upregulation of 159 DEGs, and 26 genes among those were also co-regulated by CLA 18:3 (padj < 0.05, > 2-fold change) (**Figure 5.8a**). Similar to the treatment with RSL3 in the MM1R cell line, among the shared genes, DAVID functional clustering identified unfolded protein response to be the most enriched subset of genes with an enrichment score of 3.08 in the treatment with RSL3 in the MM1S cell line (**Table 5.10**). When the > 2-fold change filter is removed, the number of shared DEGs between treatments with CLA 18:3 and RSL3 increased to 112 (**Figure 5.8b**), and multiple enriched subsets of genes related to unfolded protein responses were identified by DAVID functional clustering. While no pathways were determined to be significantly altered by iDEP and iPG for the treatment of the MM1S cell line with RSL3, we observed a network associated with unfolded protein response in the GO-Biological Process enrichment analysis (**Figure 5.8c**). Additionally, *DDIT4* (padj = 2.48E-03, log2FC = 2.25) and *DDIT3* (padj = 3.13E-08, log2FC = 2.45) were identified among the significant upregulated DEGs. On the other hand, pre-treating the cells with Fer-1 for 2 h prior to the treatment with RSL3 led to significant changes in the expression of only two genes, including *LY6E* (padj = 3.72E-02, log2FC = -2.29) and *TMEM50B* (padj = 3.72E-02, log2FC = -2.37).

1.2.4 Repository GSE164267

In this repository (*321*), the diffuse large B-cell lymphoma (DLBCL) cell line HBL-1 was treated with 20 μM dimethyl fumarate (DMF), which is an electrophile and depletes GSH, and the transcriptomic changes compared to the control were assessed at different time points, including 6, 12, 24, and 48 h. Of note, since iPG software can only analyze 5000 genes at a time and there were over 5000 DEGs identified with padj < 0.05 as a significant threshold, to lower the number of genes, we reduced the padj threshold to 0.00048 for all time points.

1.2.4.1 Treatment of HBL-1 Cell Line with DMF for 6 h

Overall, the treatment of the HBL-1 cell line with DMF for 6 h led to the significant upregulation of 199 genes, and among these DEGs, among which 36 genes were commonly upregulated by CLA 18:3 and DMF (padj < 0.05, > 2-fold change) (**Figure 5.9a**). Functional clustering analysis by DAVID on these shared genes revealed ferroptosis and iron homeostasis as the most enriched gene cluster with an enrichment score of 2.24. When we removed the > 2-fold change filter, the number of shared DEGs increased to 1085 (**Figure 5.9b**), and DAVID functional clustering identified ribosome, chaperone-mediated protein folding, and proteasome as the three most enriched subsets of genes with the enrichment scores of 38.9, 24.5, and 17.6, respectively (**Table 5.11Table 5.13**).

Furthermore, protein processing in the ER was identified among the most significantly upregulated pathways in HBL-1 cells treated with DMF for 6 h by iDEP and iPG analyses (**Table 5.14**). In addition, unfolded protein response was observed among the biological process and molecular function networks in the gene ontology (GO) enrichment analysis (FDR < 0.05) (**Figure 5.10**). In the upstream regulator module of iPG, the transcription regulators of the large ribosomal subunits, including EXOSC10, MTREX, MPHOSPH6, C1D, and DIS3 (combined p = 4.88E-12

for all regulators), were predicted to be the most significantly activated upstream regulators in the DMF-treated cells (**Figure 5.9c, d**). Additionally, the transcription regulators of the small ribosomal subunits, including EIF5 (p = 8.68E-07), CSNK1E (p = 4.48E-06), and BUD23 (p = 5.68E-06), were predicted as the following three most activated upstream regulators (**Figure 5.9c, d**). Of note, MPHOSPH6, C1D, DIS3, EIF5, CSNK1E, and BUD23 are also the most activated upstream regulators in our treatment of the HT-1080 cell line with CLA 18:3 (**Figure 4.15**). Furthermore, the gene targets of ATF4, including *CHAC1* (padj = 1.28E-28, log2FC = 1.43), *DDIT3* (padj = 7.73E-05, log2FC = 0.57), and *DDIT4* (padj = 7.73E-05, log2FC = 0.71), were found to be upregulated in the treatment with DMF compared to the control. Together, these results suggest that treatment of the HBL-1 cell line with DMF for 6 h led to increased protein damage and ER stress.

Additionally, we noticed the upregulation of many gene targets of NRF2, the activator of the transcriptions of the enzymes associated with the AREs, such as *NQO1* (padj = 1.11E-162, log2FC = 2.22), *HMOX1* (padj < 2.23E-308, log2FC = 2.08), *GCLM* (padj < 2.23E-308, log2FC = 2.14), *SLC7A11* (padj = 3.29E-110, log2FC = 2.12), and *AIFM2* (padj = 6.27E-45, log2FC = 0.79). Since the modification lysine residues of KEAP1 leads to its dissociation from NRF2 and the activation of NRF2 (*293, 294*), the activation of the transcription targets of NRF2 is probability due to the modification of KEAP1 by DMF, which is a strong electrophile.

1.2.4.2 Treatment of HBL-1 Cell Line with DMF for 12 h

To our surprise, treatment with DMF for 12 h led to a much small number of significantly changed genes in the HBL-1 cell line. Specifically, overall, we observed that treatment of HBL-1 cells with DMF for 12 h led to the significant upregulation of only 69 genes (padj < 0.05, > 2-fold change) (**Figure 5.11a**). Among these DEGs, 14 genes were also upregulated in our treatment of

HT-1080 cell with CLA 18:3, and DAVID functional clustering identified the shared genes associated with response to oxidative stress, including *NQO1, GCLM*, and *HMOX1*, to be the most enriched subsets of genes with an enrichment score of 1.63. When the > 2-fold change filter was removed, the number of shared DEGs increased to 50 (**Figure 5.11b**), and the subset of genes associated with oxidoreductase and lysosome were identified by DAVID functional clustering to be the most enriched in cells treated with DMF for 12 with the enrichment scores of 2.40 and 2.01, respectively. However, we could not identify many significantly altered pathways with iDEP and iPG in this dataset.

1.2.4.3 Treatment of HBL-1 Cell Line with DMF for 24 h

Overall, after treatment of the HBL-1 cell line with DMF for 24 h, there were significant upregulations in the expression of 363 genes, and 20 of those genes were also upregulated in our treatment of the HT-1080 cell line with CLA 18:3 for 24 h (padj < 0.05, > 2-fold change) (**Figure 5.12a**). Among the shared DEGs, DAVID functional clustering identified genes associated with ferroptosis and iron homeostasis as the most enriched subset of genes with an enrichment score of 2.11. However, without the > 2-fold change filter, there were a total of 1034 shared genes between the two treatments **Figure 5.12b**), and DAVID functional clustering still identified genes associated with ribosome and proteasome among the most enriched subset of genes with the enrichment scores of 5.47 and 8.31, respectively.

Using iDEP and iPG, we identified lysosome as the only significantly upregulated pathway. In line with this observation, we found the pathway network associated with lysosome to be upregulated in GO enrichment analysis using iDEP (**Figure 5.12c**). On the other hand, no transcription modulators were found to be significantly upregulated using iPG upstream regulator module. Furthermore, while the expression of *DDIT3* (padj = 1.07E-11, log2FC = 0.81) was

upregulated compared to the control, *CHAC1* (padj = 1.05E-11, log2FC = -0.88) was downregulated, and *DDIT4* were not identified among the significantly altered genes.

Interestingly, many gene targets of NRF2, including *NQO1* (padj < 2.23E-308, log2FC = 3.59), *HMOX1* (padj = 3.25E-214, log2FC = 1.88), *GCLM* (padj = 1.65E-10, log2FC = 0.49), and *AIFM2* (padj = 7.17E-24, log2FC = 0.73), were still significantly upregulated compared to the control after 24 h of treatment with DMF.

1.2.4.4 Treatment of HBL-1 Cell Line with DMF for 48 h

Overall, after the treatment of the HBL-1 cell line with DMF for 48 h, there were a total of 758 significantly upregulated genes (padj < 0.05, > 2-fold change) (**Figure 5.13a**). Among these DEGs, 33 were commonly upregulated in our results with CLA 18:3 in the HT-1080 cell line, and the subsets of genes associated with oxidoreductase and ferroptosis were identified as the most enriched clusters by DAVID functional clustering with the enrichment scores of 3.38 and 2.09. When the > 2-fold change filter was removed, the number of shared DEGs increased to 861 (**Figure 5.13b**), and genes associated with proteasome were identified by DAVID functional clustering as the most enriched subset of genes with an enrichment score of 12.18.

Interestingly, while lysosome was identified as significantly upregulated by iDEP and iPG, the ribosome-associated pathway was downregulated. Similarly, pathway networks associated with protein translation and ribosome components were found to be downregulated in GO enrichment analysis (**Figure 5.13c**). In the upstream regulator module of iPG, we did not find any significantly activated transcription modulators. Furthermore, while *DDIT4* (padj = 1.03E-37, log2FC = -1.03) were found to be significantly downregulated, *CHAC1* is upregulated (padj = 1.11E-03, log2FC = 0.82), and *DDIT3* were not identified among the DEGs.

Furthermore, the gene targets of NRF2, such as *NQO1* (padj < 2.23E-308, log2FC = 4.51), *HMOX1* (padj < 2.23E-308, log2FC = 2.55), *GCLM* (padj = 8.94E-51, log2FC = 1.23), *SLC7A11* (padj = 8.77E-14, log2FC = 1.20), and *AIFM2* (padj = 5.51E-30, log2FC = 1.11), are strongly activated in DMF-treated cells after treatment for 48 h.

1.3 Discussion

In Chapter 4, we observed that the treatment of HT-1080 cells with CLA 18:3 led to increased ER stress and activation of the UPR. The elevated ER stress can result from increased lipid peroxidation and the accumulation of lipid-derived electrophiles, which can modify the protein side chains, leading to an increase in misfolded and unfolded protein load. Since ferroptosis is associated tightly with lipid peroxidation and the oxidation products formed, in this chapter, we aim to elucidate whether the activation of ER stress responses is commonly observed in cell death induced by different ferroptosis agents. We indeed observed an upregulation of the UPR in the treatments with different ferroptosis inducers, including α-ESA, α-ESA-rich tung oil, and ML162 in triple-negative breast cancer MDA-MB-231 cells and mice xenografts (GSE162069) (*75*); RSL3 in multiple myeloma MM1S and MM1R cell lines (GSE182638) (*320*); and DMF in the diffuse large B-cell lymphoma HBL-1 cell line (GSE164267) (*321*). However, the degree of UPR activation and the specific responses activated vary among the data sets. For example, in repository GSE162069 (*75*), while the treatment of MDA-MB-231 cells with the conjugated PUFA α-ESA led to significant transcriptomic changes, the addition of the GPX4 direct inhibitor ML162 did not alter the expression of many genes.

Here, we proposed some factors that can affect the observed UPR activation. First, the time point at which the cells are collected after the administration of the inducers will have an effect on the RNA-seq results. For example, in repository GSE135361 (*318*), we observed the

downregulation of the PERK/EIF2α/ATF4 pathway and the recovery of translation initiation 24 h after HT-1080 cells were treated with 10 μM erastin. In contrast, in another study, treatment of the HT-1080 cell line with 10 μM erastin for 5 h led to the upregulation of genes associated with the PERK/EIF2α/ATF4 pathway, including *DDIT3, DDIT4*, and *CHAC1* (*84*). Therefore, we hypothesize that erastin can rapidly induce ER stress and UPR within 5 h, during which global mRNA translation is inhibited while mRNA encoding ATF4 is preferentially translated. After 24h, the UPR signaling is terminated after the cells recover from the ER stress, and protein synthesis and normal cell functioning are restored.

Notably, it was found that while treatment of HT-180 cell line with the inhibitors of system x_c^-, including erastin, sulfasalazine, and sorafenib, for 5 h can lead to significant upregulation of *CHAC1*, treatment with RSL3 and artesunate, the direct and indirect inhibitors of GPX4 (*63, 98*), also for 5h did not lead to the change in expression of *CHAC1* compared to the control (*84*). Thus, at the time, *CHAC1* was considered a pharmacodynamic marker for cysteine deprivation-induced ferroptosis. In contrast, we found that *CHAC1* is significantly upregulated in the treatment of the MM1R cell line with RSL3 for 24 h (GSE182638) (*320*). Besides the treatment with RSL3, *CHAC1* is also found to be upregulated in treatments with CLA 18:3 isomers (both α- and β-ESA) and DMF. Thus, we speculate that erastin, sorafenib, and sulfasalazine can induce ER stress and the activation of the UPR at a faster rate than RSL3 artesunate due to the depletion of the amino acid cysteine induced by system x_c^- inhibitors. Indeed, amino acid starvation was previously found to induce the expression of CHOP (*DDIT3*), the upstream regulator of *CHAC1*, by both UPR-dependent and independent pathways (*322-324*).

In addition, we propose that the sensitivity of cell lines to ferroptosis and different ferroptosis inducers may play a role in how strongly the UPR is activated. For example, the HBL-1 cell line

was found to be sensitive to RSL3 but was classified as moderately resistant to erastin (*68, 148*). Therefore, this cell line may exhibit stronger ER stress responses upon the addition of RSL3 than erastin. In repository GSE164267 (*321*), within 6 h treatment of the HBL-1 cell line with DMF led to significant upregulation of the UPR and the components of the PERK/EIF2α/ATF4 branch. Interestingly, the treatment with DMF at the 6 h time point led to the significant upregulation of the upstream regulators of ribosome large and small subunits, which is similar to the results observed from our results for the treatment of HT-1080 cell line with CLA 18:3 for 24 h. However, we noticed that the upregulation of the ribosome subunits in DMF-treated cells is not as significant as our results for CLA 18:3 (**Table 5.11**). As an α,β-unsaturated dimethyl ester, DMF is highly electrophilic and can modify various cellular nucleophiles like the lipid-derived electrophiles formed from the peroxidation of conjugated PUFAs. Therefore, the stress responses observed in treatments with CLA 18:3 and DMF, including the upregulation of the ribosome subunits, may result from the presence of a high concentration of reactive electrophiles inside the cells. Notably, we did not observe the upregulation of the ribosome subunits and treatment of MDA-MB-231 cells with α-ESA for 5 h. Thus, the upregulation of the ribosome subunits can be cell type-dependent. Another possible explanation is that the increase in expression of ribosome subunits is only induced when the intracellular level of electrophiles reaches a certain threshold.

Interestingly, while the transcription targets of the AREs, which are activated by the KEAP1-NRF2-pathway, are strongly activated after treatments for 6, 24, and 48 h, the genes associated with the ER stress responses and the ribosome biogenesis are either not significantly changed in expression or downregulated. Perhaps, for the ER stress signaling and the activation of the ribosomal subunits to prolong, there should be continuous generation of electrophiles inside the cells. For example, the levels of DMF may reduce over time after the initial administration due to

the antioxidant responses, such as the reaction with GSH or the activation of the AREs. In contrast, CLA 18:3 can carry on the free radical chain oxidation, leading to a more continuous generation of toxic electrophiles inside the cells and a more prolonged activation of the UPR and the biogenesis of ribosomal subunits.

While the electrophile DMF is uptake into the cells directly, it may take some time for the electrophiles to build up from the lipid peroxidation of conjugated PUFAs. Other factors, including the cells' internal pH level and cell permeability to different ferroptosis inducers, can also potentially play a role in the differences in ER stress responses. Furthermore, we realized that MM1S and MM1R cell lines used in the treatment with RSL3 in repository GSE182638 (*320*) are not sensitive to ferroptosis. Particularly, the EC_{50} values of erastin and RSL3 in MM1S and MM1R cell lines are > 50 μM and > 1 μM, respectively (*320*). In contrast, in the ferroptosis-sensitive HT-1080 cell lines, the EC_{50} values of erastin and RSL3 are < 10 μM and between 0.01-0.1 μM, respectively (*13, 68, 84*). Indeed, the EC_{50} measured for the HT-1080 cell line from our data is 0.048 μM (**Table 3.2**). Thus, MM2S and MM1R are not highly sensitive to ferroptosis, which may explain why we did not identify any altered pathways in these data sets.

Importantly, we confirmed that both CLA 18:3 isomers, including α- and β-ESA (our CLA 18:3), led to significant activation of both the pro-survival (ERAD pathway) and pro-death (ATF4/CHOP-mediated pathway) responses of the UPR, suggesting that the formation of toxic electrophiles can lead to the accumulation of unfolded and misfolded proteins in conjugated PUFA-treated cells. Interestingly, CLA 18:3 and α-ESA also activated distinct ER stress-mediated apoptosis signaling components. Specifically, CLA 18:3 activated CHOP-induced apoptosis potentiators GADD34 and TRB3 in the HT-1080 cell line (*301, 312*) while treatment of MDA-MB-231 cells with ESA led to the significant activation of the NF-κB signaling pathway, which

was shown to promote the induction of anti-apoptotic genes (*325, 326*). Notably, the activation of the NF-κB signaling pathway suggests the involvement of the second branch of the UPR, the IRE1α pathway, in addition to the PERK/EIF2α/ATF4 branch (*287, 302, 327, 328*). The involvement of the IRE1α pathway observed for treatment with α-ESA suggests that the ER stress is still in the early phase compared to prolonged ER stress. Specifically, the activity of IRE1α was shown to be attenuated early, while PERK and its downstream target CHOP remained active until cell death (*329, 330*). However, we want to note that XBP1, the direct downstream target of IRE1α, is upregulated in treatments with CLA 18:3 (padj = 2.12E-34, log2FC = 0.77) and α-ESA (padj = 9.20E-08, log2FC = 0.80), suggesting that IRE1α is still active in both treatments. Perhaps, in the context of conjugated PUFA-induced ferroptosis, both PERK and IRE1α stay activated during the entire progression of cell death, but the activity of IRE1α is more relevant in early UPR. Indeed, PUMA, which we observed to be upregulated in α-ESA-treated cells but was not identified in treatment with CLA 18:3, was shown to interact with IRE1α (*331*). While PUMA was previously considered a pro-apoptotic protein (*332, 333*), it was also shown to possess non-apoptotic functions and contribute to the early adaptive ER stress response (*331*). Additionally, PUMA was shown to be a downstream target of CHOP protein (*334*).

Even though the analyses in this chapter suggest the relevance between ER stress and ferroptosis, we were only able to analyze the RNA-seq results from four repositories, therefore, more studies are needed to elucidate the contribution of the UPR components to ferroptosis execution. Recently, the involvement of ER stress response to ferroptosis has gained more research efforts (*306, 335-337*). Interestingly, the activation of UPR by ferroptosis inducers suggests a cross-talking point between ferroptosis and apoptosis (*338, 339*). Specifically, the ferroptosis inducer erastin and artesunate were shown to induce ER stress and the p53-independent expression

of PUMA (*338*), which was also upregulated in the treatment with α-ESA (GSE162069). Here, we want to emphasize the ferroptosis agent-induced upregulation of pro-apoptotic genes does not lead to apoptosis. For example, artesunate leads to the increased expression of PUMA but not other apoptosis regulators such as NOXA and BIM (*338*). Indeed, we did not observe the upregulation of canonical apoptosis genes, such as *BAX, BAK, BIM*, or executioner caspase genes, in our results for CLA 18:3 and the treatment with α-ESA. In addition, even though the combined treatment between ferroptosis inducers and the apoptosis agent tumor necrosis factor-related apoptosis-inducing ligand (TRAIL), which induces apoptosis by binding to death receptor 5 (DR5), enhanced apoptosis, the treatments with ferroptosis inducers alone failed to induce apoptosis (*339*). In addition, the addition of ferroptosis inhibitors Fer-1 and Lip-1 into the combined treatment of ferroptosis inducers and apoptosis agent TRAIL only suppressed ferroptosis but not apoptosis (*338*). These results emphasize that ferroptosis and apoptosis are indeed distinct from each other but with the possibility of cross talk between the two mechanisms. In addition, the activation of ER stress responses induced by ferroptosis inducers leads to an increase in the expression of PUMA and DR5, making the cells more susceptible to apoptosis inducers. In addition, while autophagy was previously shown to increase ferroptosis sensitivity via ferritin degradation, leading to the increase in intracellular iron level (*54, 57*), ferroptosis and autophagy were shown to share some cell death characteristics via ER stress responses (*340*). Therefore, ER stress represents an important cross-talk point between ferroptosis and other cell death pathways and, thus, merits further investigation regarding its role in ferroptosis execution.

Figures

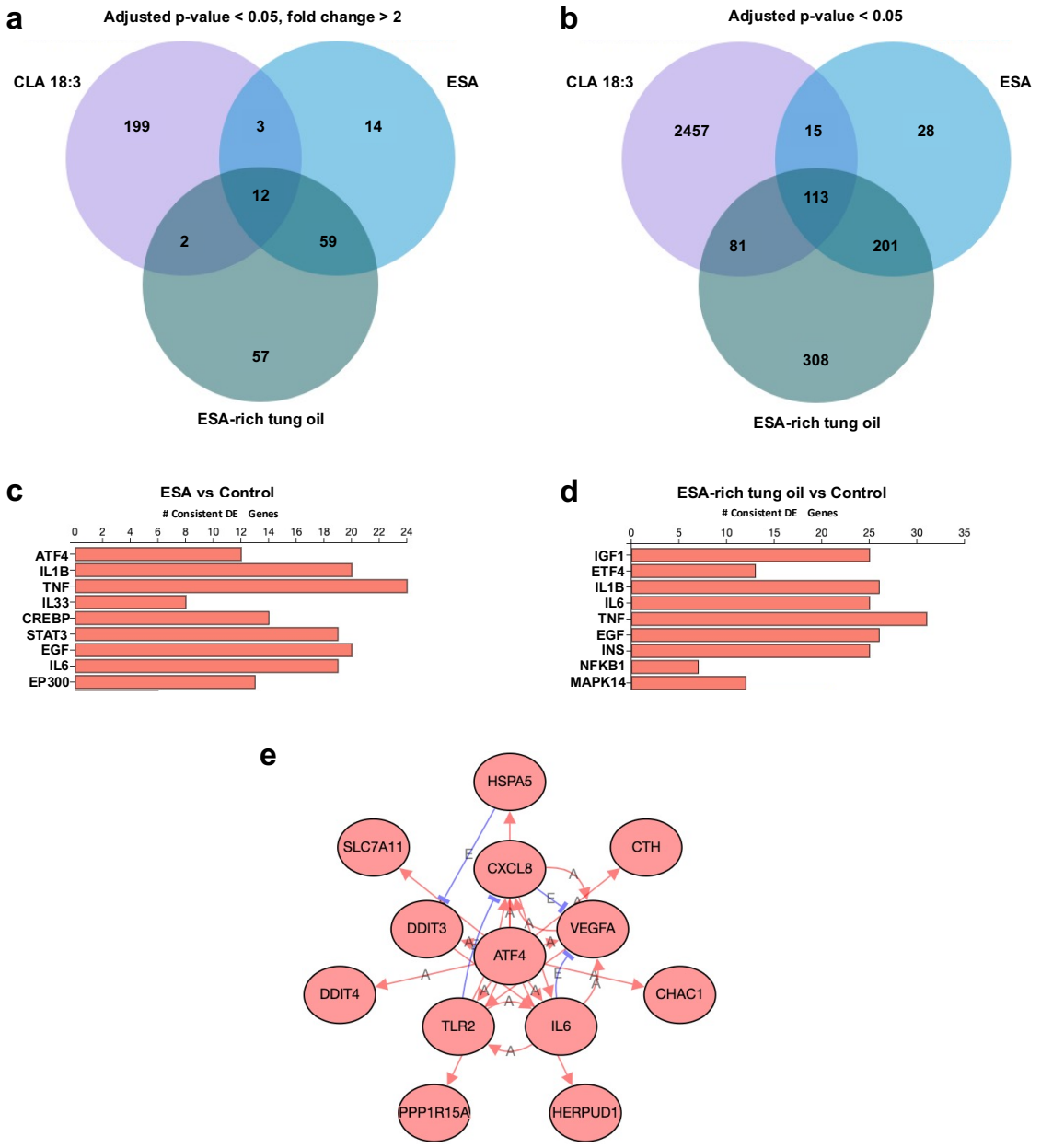

Figure 5.1 RNA-seq results of α-ESA versus control and α-ESA-rich tung oil versus control comparisons in MDA-MB-231 cell line and in orthotopic MDA-MB-231 xenografts (GSE162069).a) Venn diagram of genes commonly upregulated in treatments with CLA 18:3, α-ESA, and α-ESA-rich tung oil compared to the control (adjusted *p*-value < 0.05, fold change > 2). b) Venn diagram of extended genes commonly upregulated in treatments with CLA 18:3, α-ESA, and α-ESA-rich tung oil compared to the control (adjusted *p*-value < 0.05). Top significantly activated upstream regulators identified iPathwayGuide (iPG) analysis in cells treated with c) α-ESA and d) α-ESA-rich tung oil compared to the control. e) DEGs regulated by the upstream regulator ATF4 in cells treated with α-ESA compared to the control.

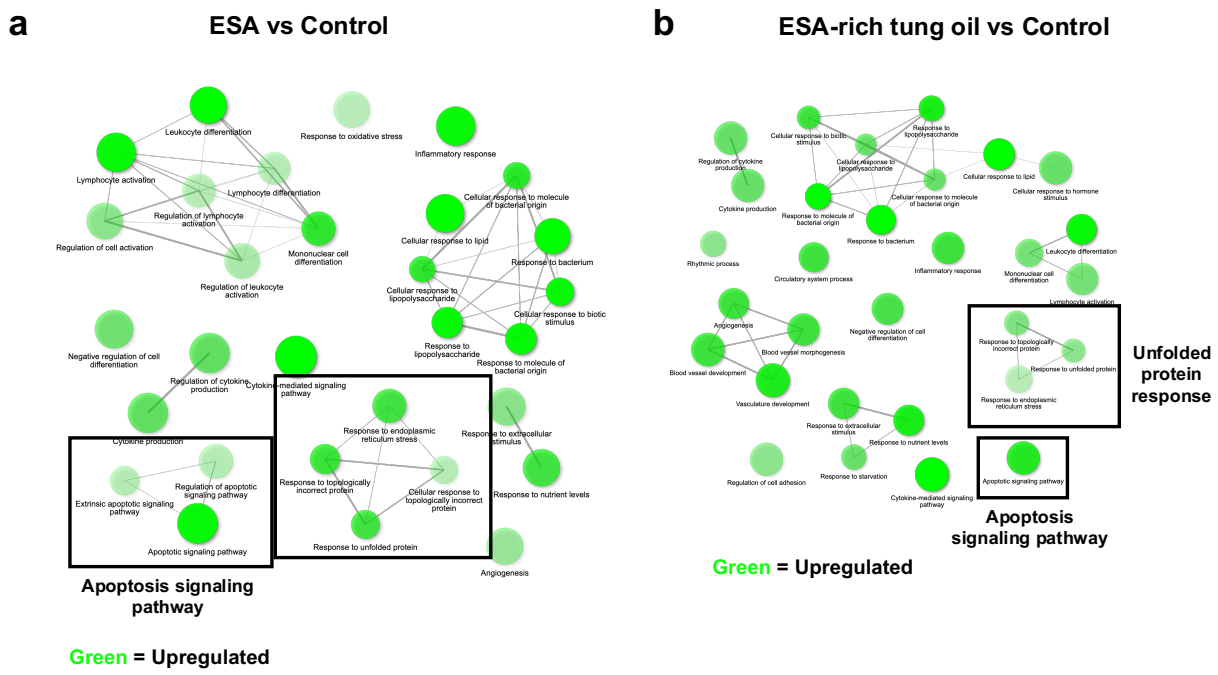

Figure 5.2 Networks of Gene Ontology (GO) terms associated with biological process aspect identified by Integrated Differential Expression and Pathway (iDEP) analysis α-ESA versus control and α-ESA-rich tung oil versus control comparisons in MDA-MB-231 cell line and in orthotopic MDA-MB-231 xenografts (GSE162069). When all pathways are regulated in the same direction, the nodes are denoted in green as the default regardless of whether the pathway are up- or down-regulated, so, here, the green nodes represent upregulated pathways. Darker nodes represent more significantly enriched gene sets and bigger nodes represents larger gene sets. Thicker edges mean more genes are overlapped.

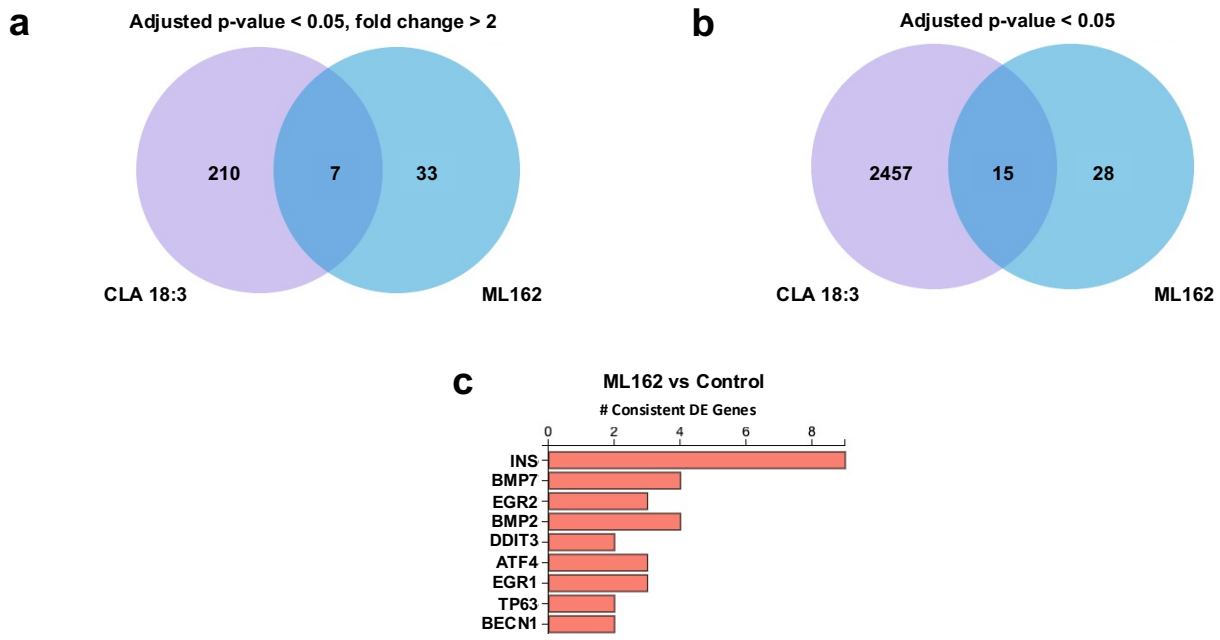

Figure 5.3 RNA-seq results of ML162 versus control comparison in MDA-MB-231 cell line (GSE162069).a) Venn diagram of genes commonly upregulated in treatments with CLA 18:3 and ML162 compared to the control (adjusted *p*-value < 0.05, fold change > 2). b) Venn diagram of extended genes commonly upregulated in treatments with CLA 18:3 and ML162 compared to the control (adjusted *p*-value < 0.05). c) Top significantly activated upstream regulators identified iPG analysis in cells treated with ML162 compared to the control.

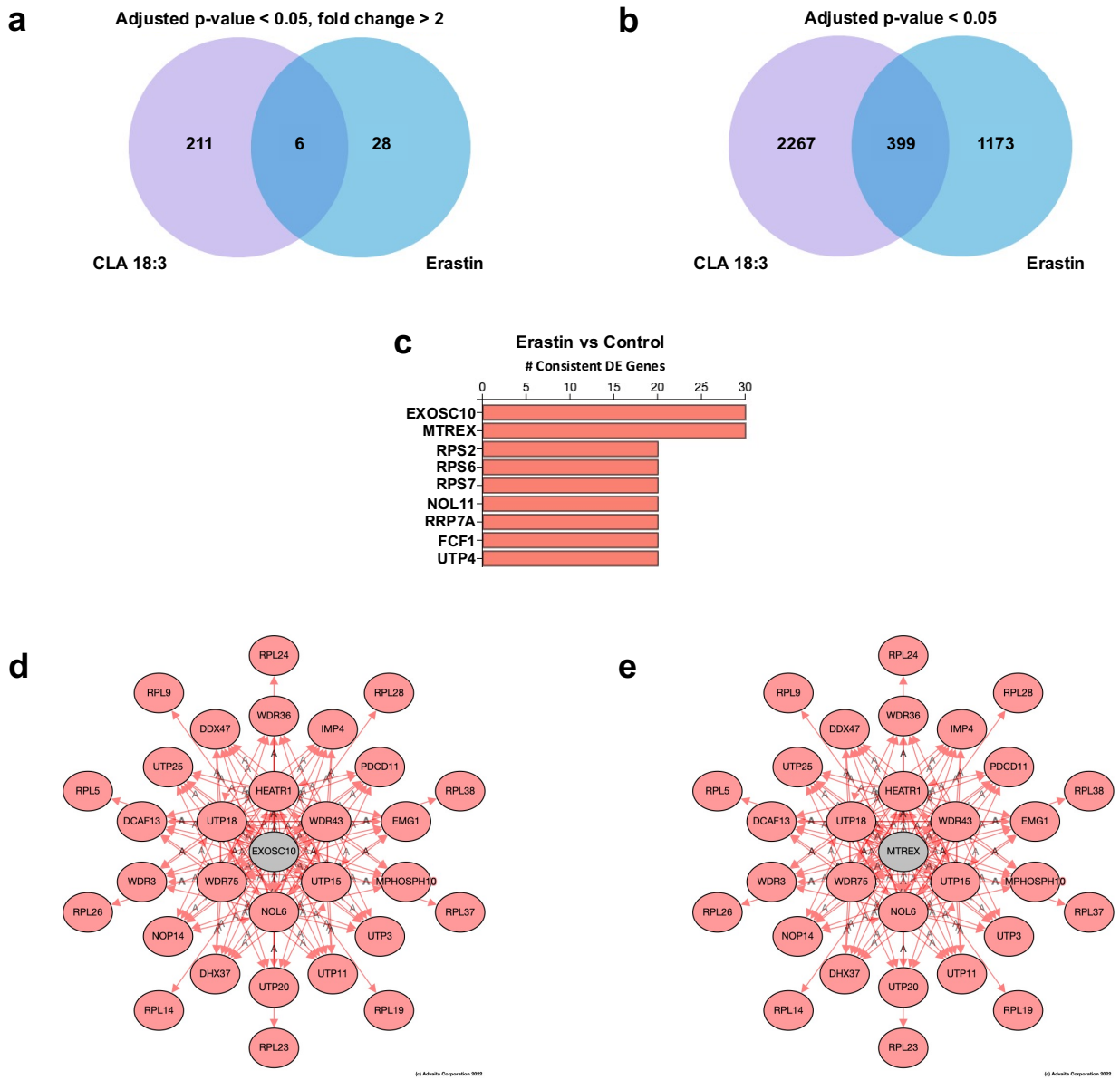

Figure 5.4 RNA-seq results of erastin versus control comparison in HT-1080 cell line (GSE135361).a) Venn diagram of genes commonly upregulated in treatments with CLA 18:3 and erastin compared to the control (adjusted *p*-value < 0.05, fold change > 2). b) Venn diagram of extended genes commonly upregulated in treatments with CLA 18:3 and erastin compared to the control (adjusted *p*-value < 0.05). c) Top significantly activated upstream regulators identified iPG analysis in cells treated with erastin compared to the control. d) DEGs regulated by the upstream regulator EXOSC10 in cells treated with DMF for compared to the control. e) DEGs regulated by the upstream regulator MTREX in cells treated with DMF compared to the control.

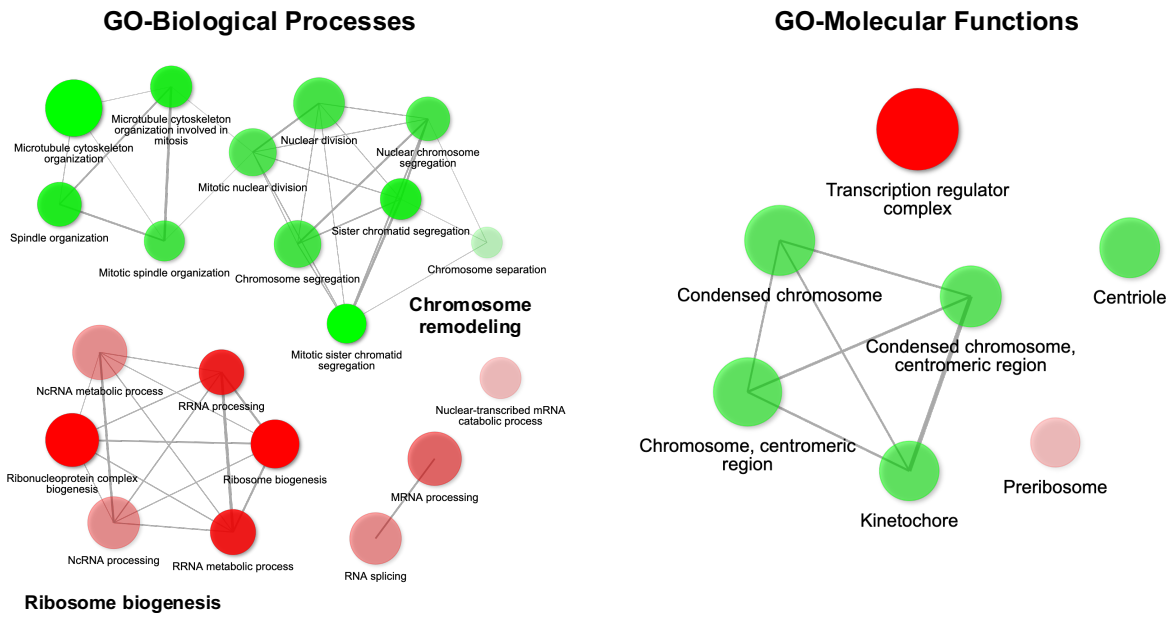

Red = Upregulated
Green = Downregulated

Figure 5.5 Networks of GO terms associated with biological process and molecular function aspects identified by iDEP analysis for HT-1080 cells treated with erastin. Red and green nodes represent up- and downregulated pathways, respectively. Darker nodes represent more significantly enriched gene sets and bigger nodes represents larger gene sets. Thicker edges mean more genes are overlapped.

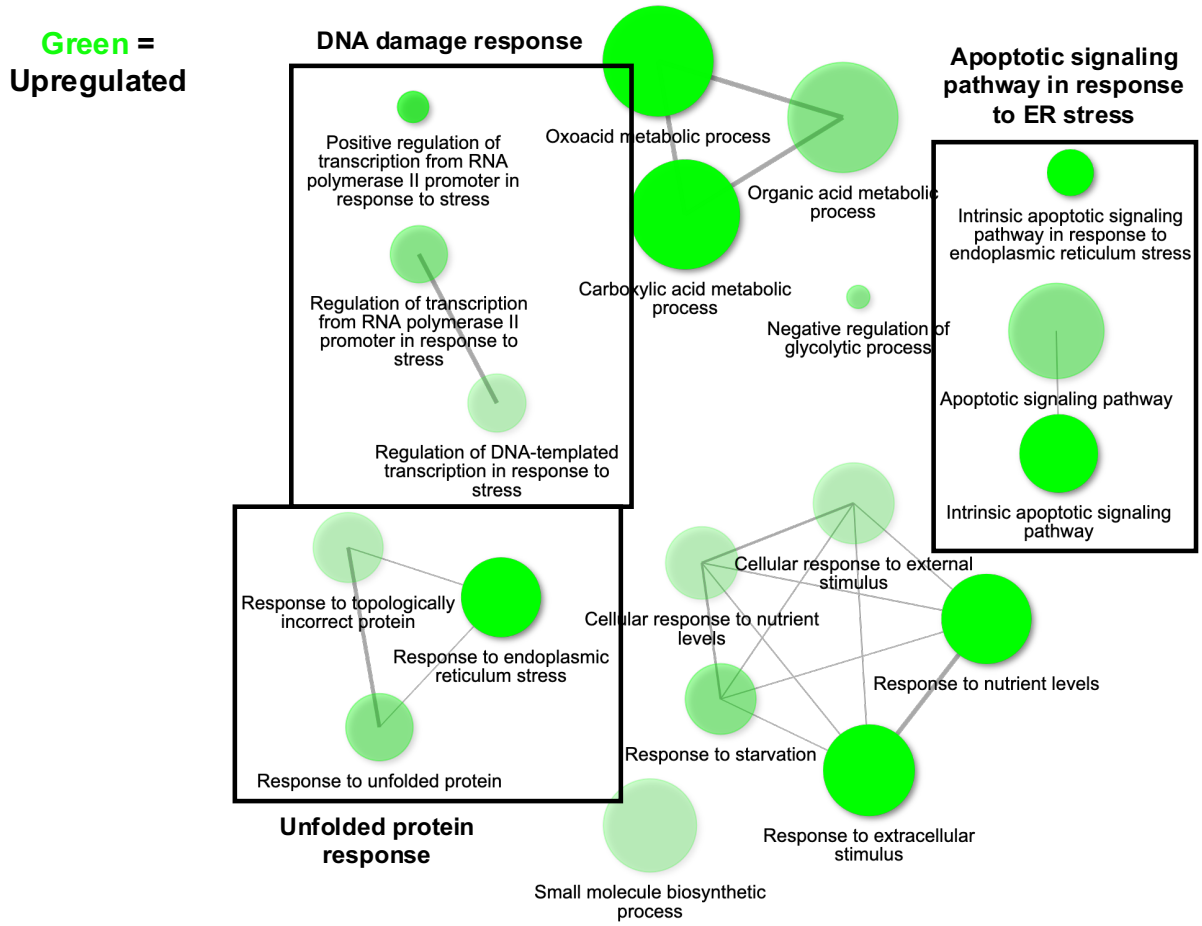

Figure 5.6 Networks of GO terms associated with biological process aspect identified by iDEP analysis for HT-1080 cells treated with erastin (from reference (*84*)). When all pathways are regulated in the same direction, the nodes are denoted in green as the default regardless of whether the pathway are up-or down-regulated, so, here, the green nodes represent upregulated pathways. Darker nodes represent more significantly enriched gene sets and bigger nodes represents larger gene sets. Thicker edges mean more genes are overlapped.

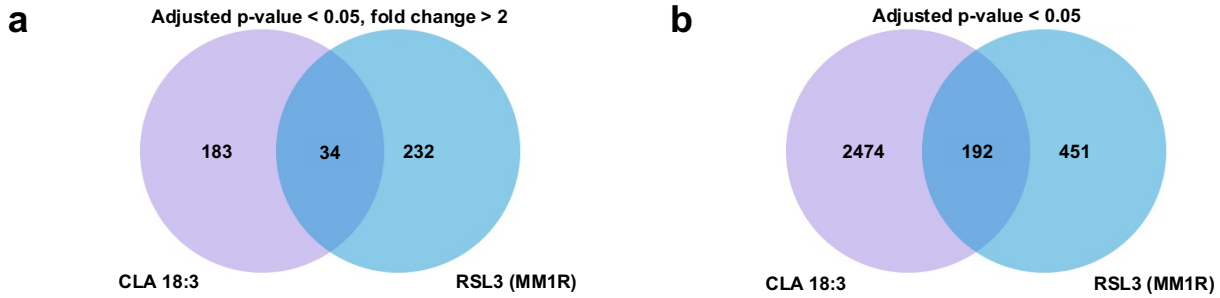

Figure 5.7 RNA-seq results of RSL3 versus control comparison in MM1R cell line (GSE182638).a) Venn diagram of genes commonly upregulated in treatments with CLA 18:3 and RSL3 compared to the control (adjusted *p*-value < 0.05, fold change > 2). b) Venn diagram of extended genes commonly upregulated in treatments with CLA 18:3 and RSL3 compared to the control (adjusted *p*-value < 0.05).

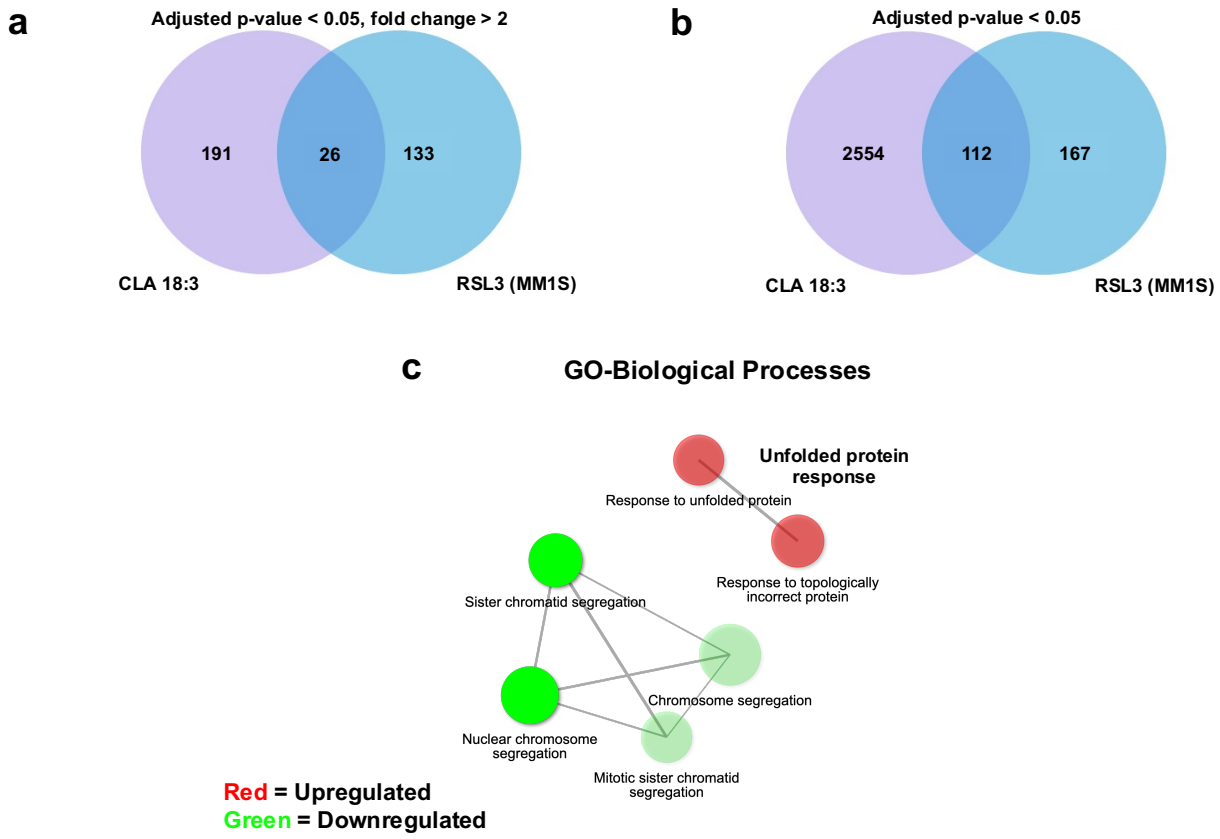

Figure 5.8 RNA-seq results of RSL3 versus control comparison in MM1S cell line (GSE182638).a) Venn diagram of genes commonly upregulated in treatments with CLA 18:3 and RSL3 compared to the control (adjusted *p*-value < 0.05, fold change > 2). b) Venn diagram of extended genes commonly upregulated in treatments with CLA 18:3 and RSL3 compared to the control (adjusted *p*-value < 0.05). c) Networks of Gene Ontology (GO) associated with biological process aspects identified by iDEP analysis. Red and green nodes represent up- and downregulated pathways, respectively. Darker nodes represent more significantly enriched gene sets and bigger nodes represents larger gene sets. Thicker edges mean more genes are overlapped.

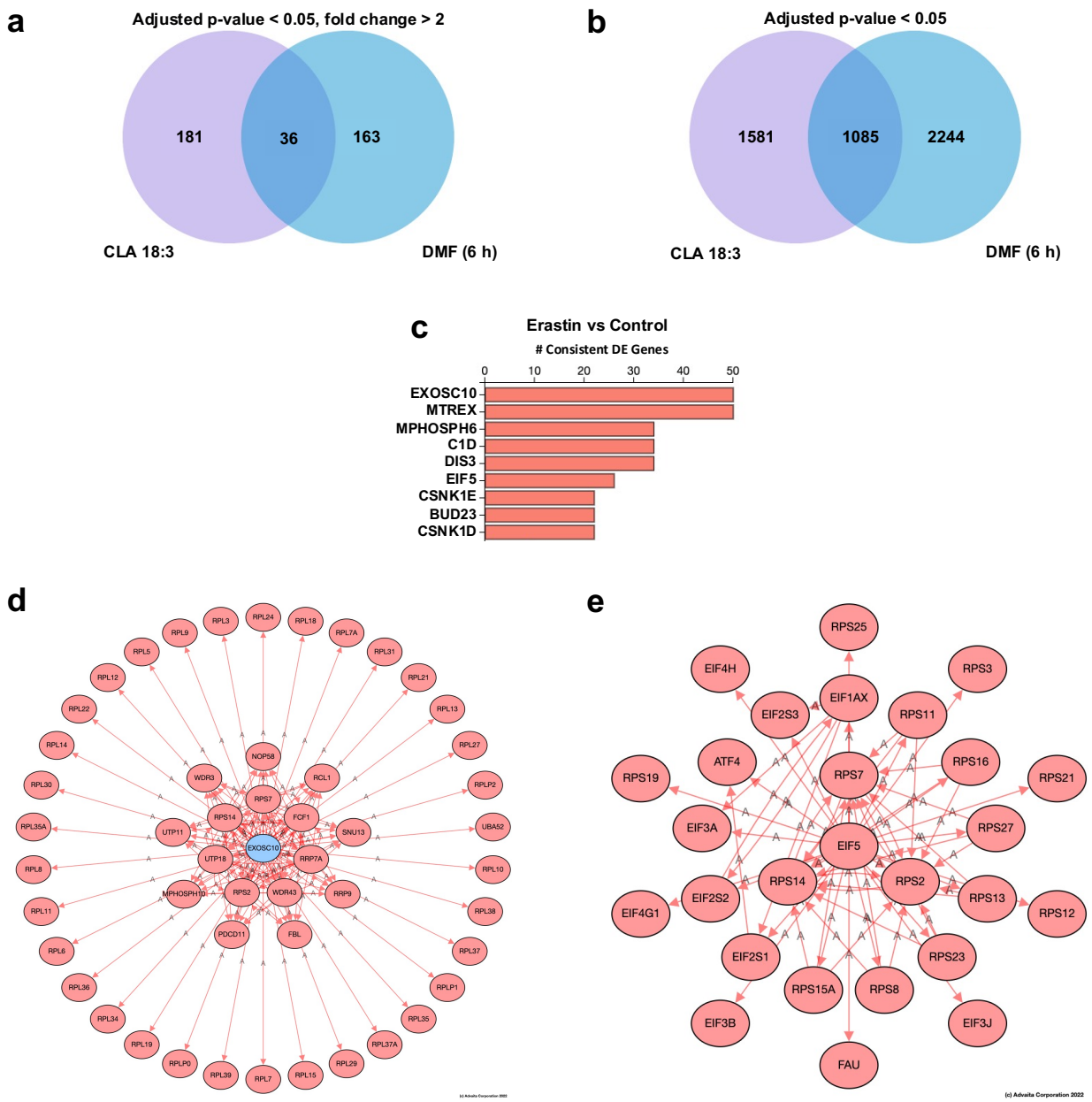

Figure 5.9 RNA-seq results of DMF versus control comparison (6 h) in HBL-1 cell line (GSE164267).a) Venn diagram of genes commonly upregulated in treatments with CLA 18:3 and DMF compared to the control (adjusted *p*-value < 0.05, fold change > 2). b) Venn diagram of extended genes commonly upregulated in treatments with CLA 18:3 and DMF compared to the control (adjusted *p*-value < 0.05). c) Top significantly activated upstream regulators identified iPG analysis in cells treated with erastin compared to the control. d) DEGs regulated by the upstream regulator EXOSC10 in cells treated with DMF for compared to the control. e) DEGs regulated by the upstream regulator EIF5 in cells treated with DMF compared to the control.

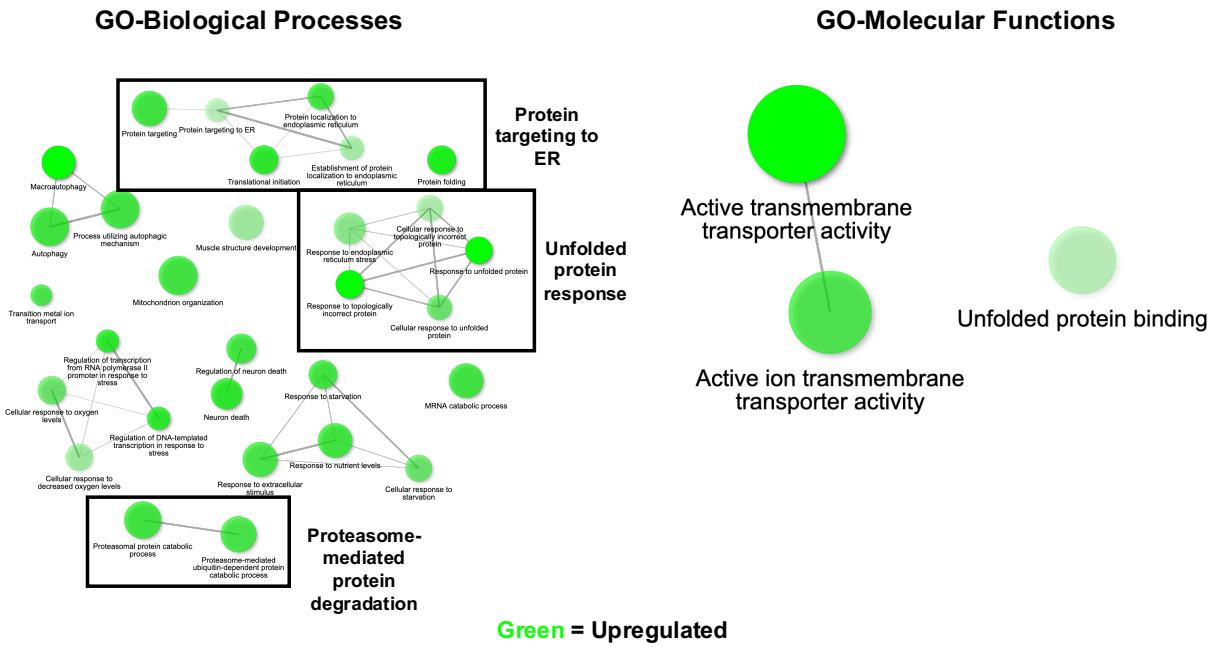

Figure 5.10 Networks of GO terms associated with biological process and molecular functions aspects identified by iDEP analysis for HBL-1 cells treated with DMF for 6 h.When all pathways are regulated in the same direction, the nodes are denoted in green as the default regardless of whether the pathway are up-or down-regulated, so, here, the green nodes represent upregulated pathways. Darker nodes represent more significantly enriched gene sets and bigger nodes represents larger gene sets. Thicker edges mean more genes are overlapped.

.

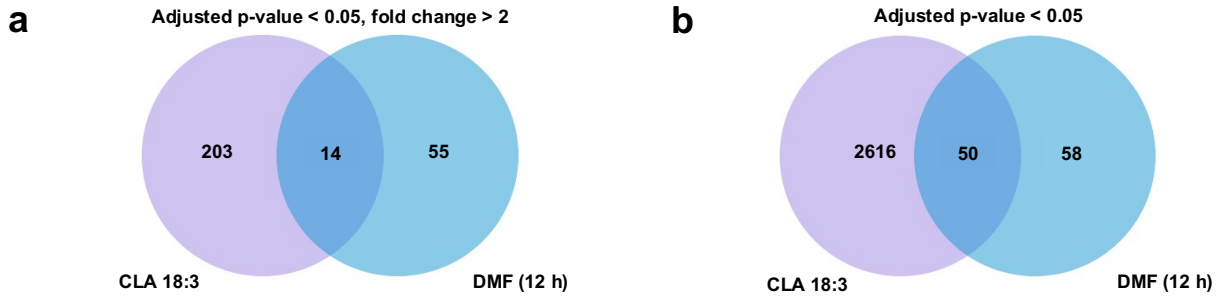

Figure 5.11 RNA-seq results of DMF versus control comparison (12 h) in HBL-1 cell line (GSE164267).a) Venn diagram of genes commonly upregulated in treatments with CLA 18:3 and DMF compared to the control (adjusted *p*-value < 0.05, fold change > 2). b) Venn diagram of extended genes commonly upregulated in treatments with CLA 18:3 and DMF compared to the control (adjusted *p*-value < 0.05).

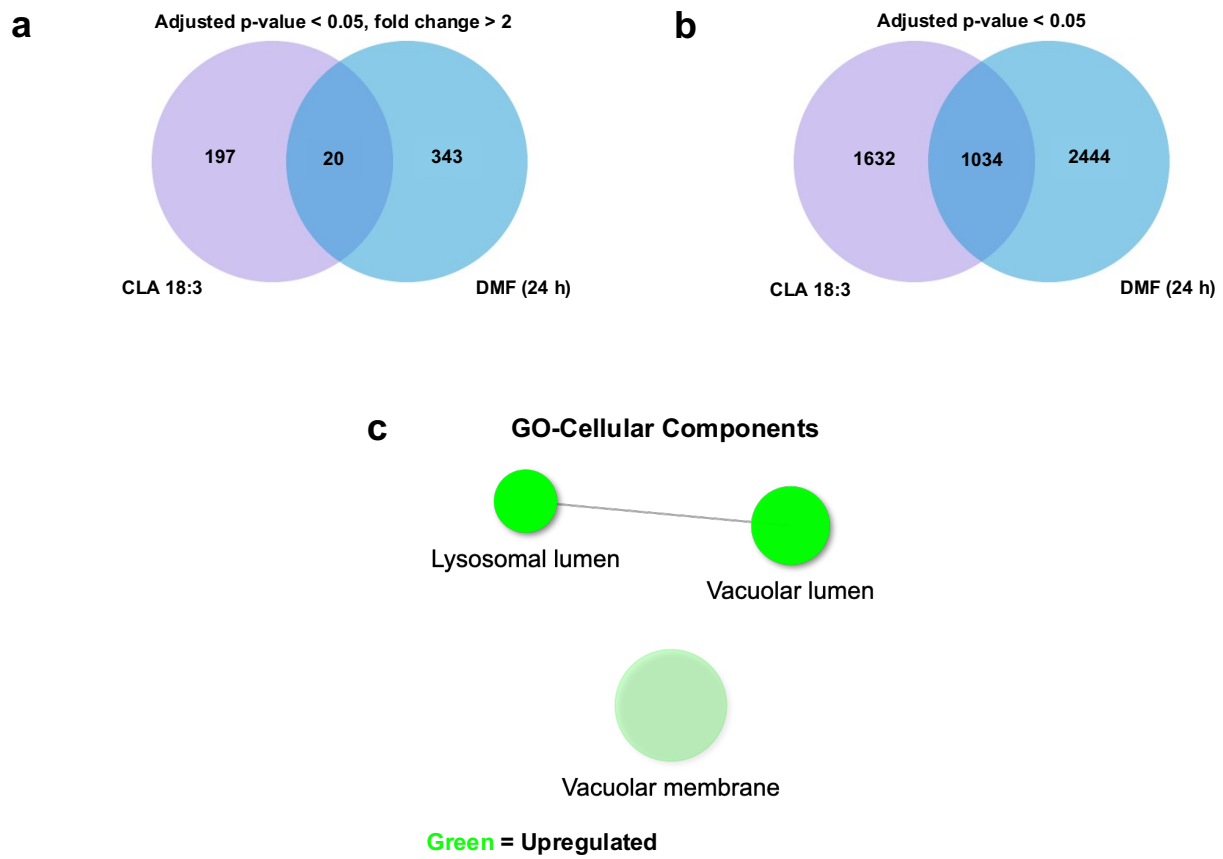

Figure 5.12 RNA-seq results of DMF versus control comparison (24 h) in HBL-1 cell line (GSE164267).a) Venn diagram of genes commonly upregulated in treatments with CLA 18:3 and DMF compared to the control (adjusted *p*-value < 0.05, fold change > 2). b) Venn diagram of extended genes commonly upregulated in treatments with CLA 18:3 and DMF compared to the control (adjusted *p*-value < 0.05). c) Networks of GO terms associated with biological process and molecular functions aspects identified by iDEP analysis.When all pathways are regulated in the same direction, the nodes are denoted in green as the default regardless of whether the pathway are up-or down-regulated, so, here, the green nodes represent upregulated pathways. Darker nodes represent more significantly enriched gene sets and bigger nodes represents larger gene sets. Thicker edges mean more genes are overlapped.

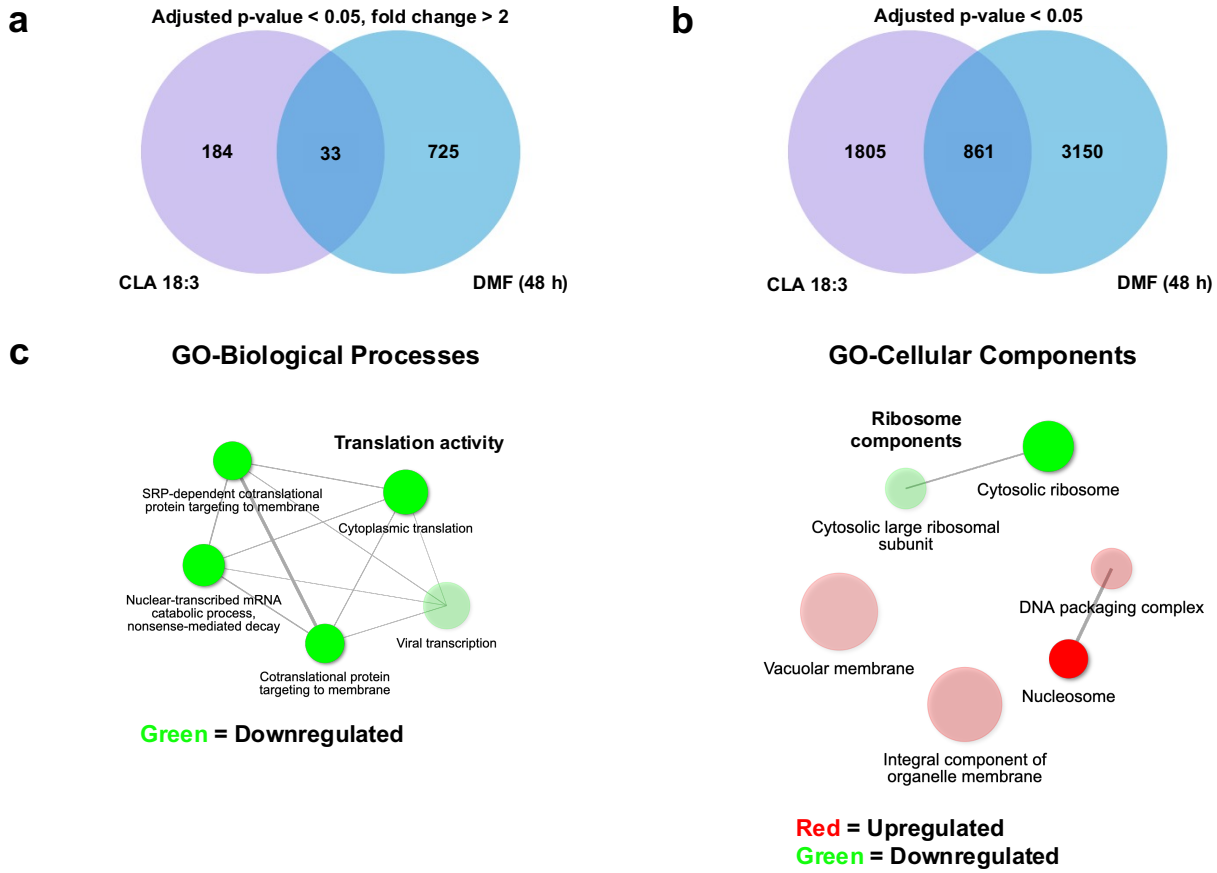

Figure 5.13 RNA-seq results of DMF versus control comparison (48 h) in HBL-1 cell line (GSE164267).a) Venn diagram of genes commonly upregulated in treatments with CLA 18:3 and DMF compared to the control (adjusted *p*-value < 0.05, fold change > 2). b) Venn diagram of extended genes commonly upregulated in treatments with CLA 18:3 and DMF compared to the control (adjusted *p*-value < 0.05). c) Networks of GO terms associated with biological process and cellular components aspects identified by iDEP analysis. Red and green nodes represent up- and downregulated pathways, respectively. When all pathways are regulated in the same direction, the nodes are denoted in green as the default regardless of whether the pathway are up-or down-regulated, so in GO-Biological Processes, the green nodes represent downregulated pathways. Darker nodes represent more significantly enriched gene sets and bigger nodes represents larger gene sets. Thicker edges mean more genes are overlapped.

Tables

Table 5.1 Shared DEGs involved in ERAD pathway (enrichment score = 5.11) identified using Database for Annotation, Visualization, and Integrated Discovery (DAVID) functional annotation clustering for treatments with CLA 18:3 in HT-1080 and α-ESA in MDA-MB-231 cell line (GSE162069) and α-ESA-rich tung oil in orthotopic MDA-MB-231 xenografts (GSE162069) (adjusted *p*-value < 0.05).

Gene ID	Description	CLA 18:3 vs control		α-ESA vs control		α-ESA-rich tung oil vs control	
		Log2 FC	Adjusted *p*-value	Log2 FC	Adjusted *p*-value	Log2 FC	Adjusted *p*-value
DDIT3	DNA damage inducible transcript 3	1.87	1.29E-23	0.76	1.19E-03	0.96	9.78E-11
DNAJB11	DnaJ heat shock protein family (Hsp40) member B11	0.45	2.58E-14	0.42	4.51E-03	0.37	4.60E-03
DNAJB9	DnaJ heat shock protein family (Hsp40) member B9	1.86	8.72E-70	1.74	1.46E-12	1.75	2.82E-28
EDEM1	ER degradation enhancing alpha-mannosidase like protein 1	0.27	8.56E-10	0.35	1.07E-02	0.52	7.20E-06
SEC24D	SEC24 homolog D, COPII coat complex component	0.56	2.43E-17	0.39	7.78E-03	0.51	1.51E-05
XBP1	X-box binding protein 1	0.77	2.12E-34	0.80	9.20E-08	0.95	2.86E-11
CTH	Cystathionine gamma-lyase	1.39	1.76E-07	0.62	4.59E-02	0.88	1.70E-04
EIF2AK3	Eukaryotic translation initiation factor 2 alpha kinase 3	0.68	3.14E-06	0.78	3.44E-04	0.97	4.37E-09
HSP90B1	Heat shock protein 90 beta family member 1	0.72	7.40E-73	0.26	3.45E-02	0.29	1.69E-02

HSPA5	Heat shock protein family A (Hsp70) member 5	1.27	0	1.02	2.34E-08	1.12	2.66E-13
HSPA6	Heat shock protein family A (Hsp70) member 6	2.70	8.06E-26	1.33	6.48E-03	2.27	8.42E-09
HERPUD1	Homocysteine inducible ER protein with ubiquitin like domain 1	1.23	2.39E-68	1.98	3.37E-22	2.08	1.11E-33
HYOU1	Hypoxia up-regulated 1	0.43	2.32E-28	0.42	9.71E-04	0.37	9.06E-03
SELENOS	Selenoprotein S	0.55	2.82E-13	0.34	2.87E-02	0.31	2.32E-02
SYVN1	Synoviolin 1	0.42	7.27E-08	0.34	2.10E-03	0.36	2.91E-03

Table 5.2 Shared DEGs involved in chaperone-dependent protein folding (enrichment score = 3.28) identified using DAVID functional annotation clustering for treatments with CLA 18:3 in HT-1080 cell line, α-ESA in MDA-MB-231 cell line (GSE162069) and α-ESA-rich tung oil in orthotopic MDA-MB-231 xenografts (GSE162069) (adjusted *p*-value < 0.05).

Gene ID	Description	CLA 18:3 vs Control		α-ESA vs Control		α-ESA-rich tung oil vs Control	
		Log2 (FC)	Adjusted *p*-value	Log2 (FC)	Adjusted *p*-value	Log2 (FC)	Adjusted *p*-value
DNAJB11	DnaJ heat shock protein family (Hsp40) member B11	0.45	2.58E-14	0.42	4.51E-03	0.37	4.60E-03
DNAJB9	DnaJ heat shock protein family (Hsp40) member B9	1.86	8.72E-70	1.74	1.46E-12	1.75	2.82E-28
EDEM1	ER degradation enhancing alpha-mannosidase like protein 1	0.27	8.56E-10	0.35	1.07E-02	0.52	7.20E-06
GRPEL1	GrpE like 1, mitochondrial	0.16	1.17E-02	0.27	2.37E-02	0.24	4.80E-02
HSP90B1	Heat shock protein 90 beta family member 1	0.72	7.40E-73	0.26	3.45E-02	0.29	1.69E-02
HSPA5	Heat shock protein family A (Hsp70) member 5	1.27	0	1.02	2.34E-08	1.12	2.66E-13
HSPA6	Heat shock protein family A (Hsp70) member 6	2.70	8.06E-26	1.33	6.48E-03	2.27	8.42E-09
HYOU1	Hypoxia up-regulated 1	0.43	2.32E-28	0.42	9.71E-04	0.37	9.06E-03
MANF	Mesencephalic astrocyte derived neurotrophic factor	0.92	3.49E-45	0.67	6.91E-04	0.74	3.98E-06

PPIF	Peptidylprolyl isomerase	0.41	6.12E-18	0.49	9.50E-05	0.36	1.92E-02
PLAUR	Plasminogen activator, urokinase receptor	0.70	3.95E-59	0.93	5.84E-11	0.87	4.94E-08
P4HA1	Prolyl 4-hydroxylase subunit alpha 1	0.23	1.08E-02	0.45	3.12E-02	0.58	3.55E-05
SDF2L1	Stromal cell derived factor 2 like 1	1.16	6.18E-43	0.73	2.14E-04	0.60	3.14E-03
SYVN1	Synoviolin 1	0.42	7.27E-08	0.34	2.10E-03	0.36	2.91E-03
YWHAG	Tyrosine 3-monooxygenase/tryptophan 5-monooxygenase activation protein gamma	0.19	1.71E-07	0.31	4.46E-02	0.32	1.48E-02

Table 5.3 Top 10 significantly upregulated pathways in treatments with α-ESA in MDA-MB-231 cell line and α-ESA-rich tung oil in orthotopic MDA-MB-231 xenografts (GSE162069) identified by both Integrated Differential Expression and Pathway (iDEP) (FDR < 0.05) and iPathwayGuide (iPG) (FDR-corrected) analyses. Only the top 10 differentially expressed pathway genes with highest fold change are shown (adjusted *p*-value < 0.05).

Comparison Groups	Pathway	-log (*p*-value) (iDEP)	log (*p*-value) (iPG)	Differentially Expressed Pathway Genes
α-ESA vs Control	Cytokine-cytokine receptor interaction	2.49	5.55	CXCL8, CXCL2, CXCL3, CXCL1, CLCF1, LIF, BMP4, TNFRSF10B, IL24, TNFRSF10D
	TNF signaling pathway	2.10	3.89	ATF4, CSF1, BCL3, CREB3L3, NFKB1, TNFRSF1A, CREB5, MAP2K3, CSF2, IL6
	Lipid and atherosclerosis	2.10	3.89	CXCL8, CXCL2, CXCL3, CXCL1, ABCA1, NFKBIA, HSPA5, XBP1, TNFRSF10B, CYP1A1
	Viral protein interaction with cytokine and cytokine receptor	1.62	5.55	CXCL8, CXCL2, IL6, CXCL3, CXCL1, IL24, IL6R, TNFRSF10D, TNFRSF10B, TNFRSF10A
	MAPK signaling pathway	1.74	4.38	VEGFA, EPHA2, NFKB2,RELB, DUSP6, NR4A1, DUSP4, JUN, TGFA, DUSP5
	Protein processing in the ER	1.74	4.14	HERPUD1, HSPA6, HSPA5, XBP1, EIF2AK3, YOD1, DDIT3, ERN1, PPP1R15A, HYOU1
	PI3K-Akt signaling pathway	1.74	5.34	DDIT4, VEGFA, MCL1, EPHA2, NR4A1, TGFA, IL6, IL6R TLR2, CREB5
	NF-kappa B signaling pathway	1.66	3.89	CXCL8, CXCL2, CXCL3, CXCL1, NFKBIA, TNFAIP3, BIRC3, TRAF1, ICAM1, NFKB2

	Kaposi sarcoma-associated herpesvirus infection	1.66	3.89	CXCL8, CXCL2, IL6, CXCL3, CXCL1, NFKBIA, CSF2, VEGFA, CDKN1A, ICAM1
	JAK-STAT signaling pathway	1.62	2.70	IL6, IL11, IL24, CSF2, IL6R, LIF, CDKN1A, SOCS1, MCL1, MYC
α-ESA-rich tung oil vs Control	Cytokine-cytokine receptor interaction	2.57	5.48	CXCL2, IL6, CXCL8, CXCL3, CXCL1, LIF, BMP4, CLCF1, TNFRSF10B, TNFRSF10D
	TNF signaling pathway	2.32	3.70	CXCL2, IL6, CXCL3, CXCL1, NFKBIA, BIRC3, TNFAIP3, TRAF1, LIF, JUN
	Viral protein interaction with cytokine and cytokine receptor	1.41	5.39	CXCL2, IL6, CXCL8, CXCL3, CXCL1, TNFRSF10D, TNFRSF10B, TNFRSF10A, TNFRSF1A
	Rheumatoid arthritis	1.41	3.73	CXCL2, IL6, CXCL8, CXCL3, CXCL1, VEGFA, IL11, JUN, IL1A, CSF2
	Protein processing in endoplasmic reticulum	1.41	3.75	HSPA6, HERPUD1, HSPA5, YOD1, EIF2AK3, DDIT3, XBP1, ERN1, ERO1B, HSPA4L
	IL-17 signaling pathway	1.32	3.73	CXCL2, IL6, CXCL8, CXCL3, CXCL1, NFKBIA, TNFAIP3, JUN, CEBPB, TRAF4

Table 5.4 Shared DEGs involved in unfolded protein response in the ER (enrichment score = 3.55) identified using DAVID functional annotation clustering for treatments with CLA 18:3 in HT-1080 and ML162 in MDA-MB-231 cell line (GSE162069) (adjusted *p*-value < 0.05).

Gene ID	Description	CLA 18:3 vs Control		ML162 vs Control	
		Log2 FC	Adjusted *p*-value	Log2 FC	Adjusted *p*-value
CEBPB	CCAAT enhancer binding protein beta	1.35	4.27E-57	1.33	2.66E-08
CREBRF	CREB3 regulatory factor	0.89	4.80E-05	1.02	2.65E-05
DNAJB9	DnaJ heat shock protein family (Hsp40) member B9	1.86	8.72E-70	0.52	3.86E-02
HSPA6	Heat shock protein family A (Hsp70) member 6	2.70	8.06E-26	2.02	1.34E-03
HERPUD1	Homocysteine inducible ER protein with ubiquitin like domain 1	1.23	2.39E-68	0.44	1.16E-02
PPP1R15A	Protein phosphatase 1 regulatory subunit 15	1.62	1.99E-217	0.60	1.86E-02

Table 5.5 Shared DEGs involved in chaperone-associated protein folding (enrichment score = 12.26) identified using DAVID functional annotation clustering for treatments with CLA 18:3 in HT-1080 and ML162 in MDA-MB-231 cell line (GSE162069) (adjusted *p*-value < 0.05).

Gene ID	Description	CLA 18:3 vs Control		Erastin vs Control	
		Log2 FC	Adjusted *p*-value	Log2 FC	Adjusted *p*-value
AHSA1	Activator of HSP90 ATPase activity 1	0.51	3.12E-41	0.29	3.35E-04
APP	Amyloid beta precursor protein	0.10	4.10E-03	0.14	1.48E-02
ASF1A	Anti-silencing function 1A histone chaperone	1.08	2.11E-32	0.39	1.19E-02
BAG2	BAG cochaperone 2	0.78	8.09E-31	0.58	7.01E-09
BAG3	BAG cochaperone 3	0.50	3.25E-28	0.46	3.74E-09
BTF3	Basic transcription factor 3	0.36	1.55E-21	0.13	2.83E-02
CANX	Calnexin	0.25	2.91E-21	0.13	1.98E-02
CCT2	Chaperonin containing TCP1 subunit 2	0.09	1.31E-02	0.15	4.10E-02
CHORDC1	Cysteine and histidine rich domain containing 1	0.47	3.51E-10	0.54	2.87E-07
COTL1	Coactosin like F-actin binding protein 1	0.12	3.44E-02	0.57	1.30E-16
DNAJA1	DnaJ heat shock protein family (Hsp40) member A1	0.44	1.52E-29	0.36	2.52E-05
DNAJA2	DnaJ heat shock protein family (Hsp40) member A2	0.14	4.54E-02	0.31	1.08E-03
DNAJB1	DnaJ heat shock protein family (Hsp40) member B1	0.40	2.60E-22	0.51	1.87E-07
DNAJC2	DnaJ heat shock protein family (Hsp40) member C2	0.36	6.70E-06	0.77	3.59E-10

DNAJC21	DnaJ heat shock protein family (Hsp40) member C21	0.18	1.62E-02	0.25	9.01E-03
DNAJC3	DnaJ heat shock protein family (Hsp40) member C3	0.47	2.86E-16	0.35	5.16E-05
ERP44	Endoplasmic reticulum protein 44	0.50	2.16E-14	0.29	1.20E-02
FKBP4	FKBP prolyl isomerase 4	0.11	2.41E-02	0.40	2.91E-06
GRPEL1	GrpE like 1, mitochondrial	0.16	1.17E-02	0.29	9.48E-03
HSP90AA1	Heat shock protein 90 alpha family class A member 1	0.52	1.04E-44	0.38	2.50E-10
HSP90AB1	Heat shock protein 90 alpha family class B member 1	0.19	6.11E-10	0.27	3.28E-08
HSP90B1	Heat shock protein 90 beta family member 1	0.72	7.40E-73	0.46	1.71E-13
HSPA5	heat shock protein family A (Hsp70) member 5	1.27	0.00E+00	0.76	4.20E-04
HSPA8	Heat shock protein family A (Hsp70) member 8	0.57	4.96E-67	0.58	1.25E-30
HSPB8	Heat shock protein family B (small) member 8	1.64	9.06E-73	1.19	3.14E-31
HSPD1	Heat shock protein family D (Hsp60) member 1	0.20	2.76E-08	0.31	1.06E-06
HSPH1	Heat shock protein family H (Hsp110) member 1	0.55	6.75E-29	1.03	8.16E-39
NACA	Nascent polypeptide associated complex subunit alpha	0.43	8.64E-23	0.18	4.41E-03
NGLY1	N-glycanase 1	0.46	2.64E-05	0.27	1.44E-02
PDIA3	Protein disulfide isomerase family A member 3	0.55	1.51E-80	0.29	7.00E-05

POMP	Proteasome maturation protein	0.52	1.43E-31	0.21	4.87E-02
PPIF	Peptidylprolyl isomerase F	0.41	6.12E-18	0.53	3.55E-13
PTGES3	Prostaglandin E synthase 3	0.30	2.85E-19	0.20	1.28E-02
SDF2L1	Stromal cell derived factor 2 like 1	1.16	6.18E-43	0.72	5.40E-05
ST13	ST13 Hsp70 interacting protein	0.33	5.47E-16	0.20	1.74E-02
STIP1	Stress induced phosphoprotein 1	0.31	1.79E-12	0.31	8.10E-07
TBCA	Tubulin folding cofactor A	0.68	1.29E-24	0.27	6.29E-03
TCP1	T-complex 1	0.13	1.28E-03	0.18	1.30E-02
TTC1	Tetratricopeptide repeat domain 1	0.76	1.08E-45	0.22	4.11E-02

Table 5.6 Shared DEGs involved in ribosome biogenesis (enrichment score = 5.34) identified using DAVID functional annotation clustering for treatments with CLA 18:3 in HT-1080 and erastin in HT-1080 cell line (GSE135361) (adjusted *p*-value < 0.05).

Gene ID	Description	CLA 18:3 vs Control		Erastin vs Control	
		Log2 FC	Adjusted *p*-value	Log2 FC	Adjusted *p*-value
CANX	Calnexin	0.25	2.91E-21	0.13	1.98E-02
DCAF13	DDB1 and CUL4 associated factor 13	0.14	6.94E-03	0.29	3.95E-04
DNAJC21	DnaJ heat shock protein family	0.18	1.62E-02	0.25	9.01E-03
EEF1A1	Eukaryotic translation elongation factor 1 alpha 1	0.24	1.30E-17	0.13	1.92E-02
IL12A	Interleukin 12A	0.52	3.89E-03	0.98	2.01E-23
IL6R	Interleukin 6 receptor	0.85	1.90E-04	1.14	5.69E-05
MPHOSPH10	M-phase phosphoprotein 10	0.23	3.35E-03	0.55	1.33E-05
MRPS22	Mitochondrial ribosomal protein S22	0.15	4.41E-02	0.22	4.78E-02
MRPS30	Mitochondrial ribosomal protein S30	0.21	5.08E-03	0.39	2.87E-04
MRPS6	Mitochondrial ribosomal protein S6	0.42	2.23E-03	0.41	9.43E-03
NACA	Nascent polypeptide associated complex subunit alpha	0.43	8.64E-23	0.18	4.41E-03
RELA	RELA proto-oncogene, NF-kB subunit	0.14	1.02E-02	0.25	1.28E-02
RPL14	Ribosomal protein L14	0.23	4.21E-18	0.18	1.93E-03
RPL19	Ribosomal protein L19	0.43	2.00E-37	0.14	1.43E-02
RPL23	Ribosomal protein L23	0.42	1.06E-36	0.17	3.82E-03
RPL24	Ribosomal protein L24	0.37	1.11E-20	0.20	2.34E-03
RPL26	Ribosomal protein L26	0.29	4.50E-03	0.39	6.40E-06

RPL28	Ribosomal protein L28	0.20	5.87E-04	0.16	2.14E-02
RPL37	Ribosomal protein L37	0.39	4.25E-17	0.20	4.13E-04
RPL38	Ribosomal protein L38	0.28	1.16E-09	0.18	5.23E-03
RPL5	Ribosomal protein L5	0.23	8.09E-11	0.16	3.18E-03
RPL9	Ribosomal protein L9	0.40	1.54E-30	0.24	6.71E-04
RPS24	Ribosomal protein S24	0.42	7.91E-33	0.18	1.35E-03
RPS27L	Ribosomal protein S27 like	0.43	5.14E-13	0.25	5.53E-05
RPS3A	Ribosomal protein S3A	0.44	3.64E-28	0.23	7.10E-03
SERP1	Stress associated endoplasmic reticulum protein 1	0.47	6.56E-32	0.25	1.10E-04
SNRPB2	Small nuclear ribonucleoprotein polypeptide B2	0.24	6.61E-07	0.26	1.28E-02
TBK1	TANK binding kinase 1	0.41	2.77E-07	0.45	7.72E-05
TNIP1	TNFAIP3 interacting protein 1	0.47	2.77E-15	0.36	3.16E-07
WARS1	Tryptophanyl-tRNA synthetase 1	0.43	1.66E-16	0.43	2.10E-08

Table 5.7 Significantly altered genes involved in intrinsic apoptosis signaling in response to ER stres (enrichment score = 3.29) identified using DAVID functional annotation clustering for treatments with erastin in HT-1080 (FPKM expression data from reference (*84*)) (fold change >2).

Gene ID	Description	Fold change
CHAC1	ChaC glutathione specific gamma-glutamylcyclotransferase 1	24.0
DDIT3	DNA damage inducible transcript 3	21.6
DDIT4	DNA damage inducible transcript 4	3.52
XBP1	X-box binding protein 1	2.49
ATF4	Activating transcription factor 4	2.46
HERPUD1	Homocysteine inducible ER protein with ubiquitin like domain 1	2.20
TRIB3	Tribbles pseudokinase 3	2.19

Table 5.8 Shared DEGs involved in unfolded protein response (enrichment score = 4.44) identified using DAVID functional annotation clustering for treatments with CLA 18:3 in HT-1080 and RSL3 in MM1R cell line (GSE182638) (adjusted *p*-value < 0.05, > 2-fold change).

Gene ID	Description	CLA 18:3 vs Control		RSL3 vs Control	
		Log2 (FC)	Adjusted *p*-value	Log2 (FC)	Adjusted *p*-value
CEBPB	CCAAT enhancer binding protein beta	1.35	4.27E-57	1.60	5.04E-11
CHAC1	ChaC glutathione specific gamma-glutamylcyclotransferase 1	1.85	1.30E-26	3.04	4.13E-39
DDIT3	DNA damage inducible transcript 3	1.87	1.29E-23	2.18	2.02E-04
DNAJB9	DnaJ heat shock protein family	1.86	8.72E-70	1.25	1.91E-10
HSPA1B	Heat shock protein family A	1.23	2.39E-68	1.25	1.26E-08
HSPA6	Heat shock protein family A	2.43	1.02E-02	5.31	5.89E-08
HERPUD1	Homocysteine inducible ER protein with ubiquitin like domain 1	2.70	8.06E-26	7.51	3.95E-10
PPP1R15A	Protein phosphatase 1 regulatory subunit 15A	1.62	1.99E-217	2.66	1.20E-03

Table 5.9 DEGs involved in transcription regulation (enrichment score = 1.42) identified using DAVID functional annotation clustering for combined treatment with RSL3 and Fer-1 compared to the treatment with RSL3 only in MM1R cell line (GSE182638) (adjusted *p*-value < 0.05, > 2-fold change).

Gene ID	Description	Log2(FC)	Adjusted *p*-value
BCL3	BCL3 transcription coactivator	-1.26	6.04E-06
BHLHE41	Basic helix-loop-helix family member e41	-1.00	1.08E-04
CCN1	Cellular communication network factor 1	-2.01	1.67E-02
CSRNP1	Cysteine and serine rich nuclear protein 1	-1.07	5.30E-04
CXCL10	C-X-C motif chemokine ligand 10	-1.58	1.74E-09
DMBT1	Deleted in malignant brain tumors 1	-1.87	2.13E-03
DUSP4	Dual specificity phosphatase 4	-1.70	7.27E-03
DUSP5	Dual specificity phosphatase 5	-1.85	1.18E-11
DUSP8	Dual specificity phosphatase 8	-2.22	9.72E-03
FOXA1	Forkhead box A1	-1.17	5.91E-04
HES1	Hes family bHLH transcription factor 1	-1.44	6.67E-08
KLF3	KLF transcription factor 3	-1.21	8.20E-05
MAFB	MAF bZIP transcription factor B	-1.32	2.90E-02
SIK1	Salt inducible kinase 1	-1.31	3.01E-04

Table 5.10 Shared DEGs involved in unfolded protein response (enrichment score = 3.08) identified using DAVID functional annotation clustering for treatments with CLA 18:3 in HT-1080 and RSL3 in MM1S cell line (GSE182638) (adjusted *p*-value < 0.05, > 2-fold change).

Gene ID	Description	Log2(FC)	Adjusted *p*-value
CEBPB	CCAAT enhancer binding protein beta	2.45	3.13E-08
DDIT3	DNA damage inducible transcript 3	1.41	4.98E-04
DNAJB9	DnaJ heat shock protein family	1.25	7.68E-03
HERPUD1	Homocysteine inducible ER protein with ubiquitin like domain 1	1.20	4.37E-03

Table 5.11 Shared DEGs involved in ribosome (enrichment score = 38.9) identified using DAVID functional annotation clustering for treatments with CLA 18:3 in HT-1080 and DMF in HBL-1 cell line for 6 h (GSE164267) (only top 30 genes with the highest values of log2FC in CLA 18:3 vs Control comparison are shown)

Gene ID	Description	CLA 18:3 vs Control		DMF vs Control	
		Log2 (FC)	Adjusted *p*-value	Log2 (FC)	Adjusted *p*-value
C1S	Complement C1s	1.26	1.53E-24	0.93	1.13E-05
FOS	Fos proto-oncogene, AP-1 transcription factor subunit	6.04	2.19E-113	1.06	6.80E-04
MRPL14	Mitochondrial ribosomal protein L14	0.42	1.99E-09	0.19	1.43E-05
MRPL52	Mitochondrial ribosomal protein L52	0.4	1.28E-09	0.32	9.35E-09
MRPS6	Mitochondrial ribosomal protein S6	0.42	2.23E-03	0.30	3.61E-07
NACA	Nascent polypeptide associated complex subunit alpha	0.43	8.64E-23	0.17	1.62E-09
RPL11	Ribosomal protein L11	0.52	2.31E-72	0.15	2.79E-05
RPL19	Ribosomal protein L19	0.43	2.00E-37	0.11	2.92E-04
RPL21	Ribosomal protein L21	0.45	9.40E-23	0.13	1.62E-06
RPL31	Ribosomal protein L31	0.43	9.27E-17	0.26	4.80E-10
RPL34	Ribosomal protein L34	0.45	2.42E-22	0.21	6.18E-11
RPL37A	Ribosomal protein L37a	0.43	4.90E-30	0.20	1.46E-09
RPL39	Ribosomal protein L39	0.53	3.06E-23	0.40	5.08E-26
RPL41	Ribosomal protein L41	0.41	3.16E-20	0.21	2.06E-08
RPL9	Ribosomal protein L9	0.4	1.54E-30	0.31	2.53E-20
RPLP0P6	Ribosomal protein lateral stalk subunit P0 pseudogene 6	0.41	3.04E-10	0.28	1.51E-06
RPLP1	Ribosomal protein lateral stalk subunit P1	0.45	3.68E-46	0.44	1.60E-11

RPLP2	Ribosomal protein lateral stalk subunit P2	0.44	2.18E-34	0.23	1.27E-08
RPS12	Ribosomal protein S12	0.49	1.28E-32	0.35	1.68E-18
RPS15A	Ribosomal protein S15a	0.48	9.08E-20	0.29	4.35E-08
RPS19	Ribosomal protein S19	0.45	2.16E-36	0.14	1.27E-05
RPS19BP1	Ribosomal protein S19 binding protein 1	0.42	8.28E-12	0.14	7.97E-04
RPS21	Ribosomal protein S21	0.49	1.73E-21	0.29	2.95E-12
RPS27	Ribosomal protein S27	0.52	3.03E-31	0.11	2.80E-04
RPS27A	Ribosomal protein S27a	0.52	7.43E-24	0.10	2.88E-02
SARS1	Seryl-tRNA synthetase 1	0.4	2.99E-22	0.36	2.11E-25
SERP1	Stress associated endoplasmic reticulum protein 1	0.47	6.56E-32	0.57	4.84E-87
SRP19	Signal recognition particle 19	0.48	1.52E-06	0.32	1.57E-04
TBK1	TANK binding kinase 1	0.41	2.77E-07	0.14	6.55E-03
WARS1	Tryptophanyl-tRNA synthetase 1	0.43	1.66E-16	0.39	5.79E-34

Table 5.12 Shared DEGs involved in chaperone-mediated protein folding (enrichment score = 24.5) identified using DAVID functional annotation clustering for treatments with CLA 18:3 in HT-1080 and DMF in HBL-1 cell line for 6 h (GSE164267) (only top 30 genes with the highest values of log2FC in CLA 18:3 vs control comparison are shown)

Gene ID	Description	CLA 18:3 vs Control		DMF vs Control	
		Log2 (FC)	Adjusted *p*-value	Log2 (FC)	Adjusted *p*-value
AHSA1	Activator of HSP90 ATPase activity 1	0.51	3.12E-41	0.48	4.43E-45
ASF1A	Anti-silencing function 1A histone chaperone	1.08	2.11E-32	0.40	1.61E-06
BAG2	BAG cochaperone 2	0.78	8.09E-31	0.48	3.15E-25
BAG3	BAG cochaperone 3	0.5	3.25E-28	1.36	9.42E-111
CHORDC1	Cysteine and histidine rich domain containing 1	0.47	3.51E-10	0.53	1.81E-57
COX17	Cytochrome c oxidase copper chaperone COX17	0.45	5.08E-10	0.22	7.44E-03
DNAJA1	DnaJ heat shock protein family	0.44	1.52E-29	0.54	8.44E-94
DNAJB11	DnaJ heat shock protein family	0.45	2.58E-14	0.39	9.78E-15
DNAJB9	DnaJ heat shock protein family	1.86	8.72E-70	0.89	1.05E-27
DNAJC3	DnaJ heat shock protein family	0.47	2.86E-16	0.68	7.34E-54
ERP29	Endoplasmic reticulum protein 29	0.47	9.93E-17	0.20	5.37E-07
ERP44	Endoplasmic reticulum protein 44	0.5	2.16E-14	0.23	1.42E-05
HSP90AA1	Heat shock protein 90 alpha family class A member 1	0.52	1.04E-44	0.71	2.19E-163
HSP90B1	Heat shock protein 90 beta family member 1	0.72	7.40E-73	0.15	8.39E-09
HSPA5	Heat shock protein family A	1.27	0	0.61	4.21E-124
HSPA6	Heat shock protein family A	2.7	8.06E-26	3.12	7.00E-08
HSPA8	Heat shock protein family A	0.57	4.96E-67	0.48	7.89E-57

HSPA9	Heat shock protein family A	0.47	6.28E-32	0.30	2.09E-34
HSPE1	Heat shock protein family E	0.49	6.75E-09	0.59	3.19E-22
HSPH1	Heat shock protein family H	0.55	6.75E-29	0.66	3.61E-131
HYOU1	Hypoxia up-regulated 1	0.43	2.32E-28	0.22	1.38E-15
NACA	Nascent polypeptide associated complex subunit alpha	0.43	8.64E-23	0.17	1.62E-09
NDUFAF2	NADH:ubiquinone oxidoreductase complex assembly factor 2	0.56	2.13E-06	0.35	6.77E-08
NPLOC4	NPL4 homolog, ubiquitin recognition factor	0.51	6.01E-35	0.33	2.90E-25
PDIA3	Protein disulfide isomerase family A member 3	0.55	1.51E-80	0.09	2.17E-02
PDIA4	Protein disulfide isomerase family A member 4	0.55	1.57E-55	0.20	6.18E-09
POMP	Proteasome maturation protein	0.52	1.43E-31	0.38	1.10E-19
PPIB	Peptidylprolyl isomerase B	0.5	4.56E-23	0.37	1.65E-26
TBCA	Tubulin folding cofactor A	0.68	1.29E-24	0.41	6.78E-18
UNC45A	Unc-45 myosin chaperone A	0.46	1.01E-16	0.16	2.33E-04

Table 5.13 Shared DEGs involved in proteasome (enrichment score = 17.6) identified using DAVID functional annotation clustering for treatments with CLA 18:3 in HT-1080 and DMF in HBL-1 cell line for 6 h (GSE164267) (only top 30 genes with the highest values of log2FC in CLA 18:3 vs control comparison are shown)

Gene ID	Description	CLA 18:3 vs Control		DMF vs Control	
		Log2 (FC)	Adjusted *p*-value	Log2 (FC)	Adjusted *p*-value
ATF4	Activating transcription factor 4	0.72	1.07E-65	0.55	2.90E-83
CBR1	Carbonyl reductase 1	0.93	3.33E-34	0.44	5.16E-09
CTSD	Cathepsin D	1.26	2.99E-91	0.70	4.74E-18
DDIT3	DNA damage inducible transcript 3	1.87	1.29E-23	0.57	7.73E-05
EGR1	Early growth response 1	1.76	6.92E-18	0.50	3.93E-13
FOS	Fos proto-oncogene, AP-1 transcription factor subunit	6.04	2.19E-113	1.06	6.80E-04
GSR	Glutathione-disulfide reductase	0.97	3.42E-51	1.49	0
HMOX1	Heme oxygenase 1	5.14	0	2.08	0
HSPA5	Heat shock protein family A	1.27	0	0.61	4.21E-124
HSPA6	Heat shock protein family A	2.70	8.06E-26	3.12	7.00E-08
MAP1LC3B	Microtubule associated protein 1 light chain 3 beta	0.73	3.33E-48	0.80	2.92E-63
NQO1	NAD	1.07	3.26E-45	2.22	1.11E-162
NSFL1C	NSFL1 cofactor	0.91	2.30E-54	0.17	7.24E-06
PSMA1	Proteasome 20S subunit alpha 1	0.92	6.62E-18	0.28	1.44E-05
PSMA5	Proteasome 20S subunit alpha 5	0.84	1.68E-88	0.22	6.11E-08
PSMB2	Proteasome 20S subunit beta 2	0.83	8.61E-123	0.12	4.26E-03
PSMB6	Proteasome 20S subunit beta 6	0.78	2.12E-53	0.24	8.19E-06
PSMC2	Proteasome 26S subunit, ATPase 2	0.86	3.52E-79	0.28	4.53E-16
PSMC4	Proteasome 26S subunit, ATPase 4	0.77	4.41E-77	0.15	9.10E-04

PSMC6	Proteasome 26S subunit, ATPase 6	0.90	2.52E-45	0.17	5.76E-06
PSMD11	Proteasome 26S subunit, non-ATPase 11	0.75	2.81E-82	0.48	5.89E-54
PSMD14	Proteasome 26S subunit, non-ATPase 14	0.74	1.24E-98	0.52	1.96E-35
PSMD3	Proteasome 26S subunit, non-ATPase 3	0.77	1.84E-51	0.20	4.86E-09
RAB39B	RAB39B, member RAS oncogene family	2.14	6.65E-04	0.61	6.62E-13
SOD1	Superoxide dismutase 1	0.87	1.11E-89	0.52	1.32E-47
SQSTM1	Sequestosome 1	1.97	0	1.26	0
TXNL1	Thioredoxin like 1	0.89	1.19E-64	0.32	4.22E-23
UBC	Ubiquitin C	1.43	0.00E+00	0.77	3.09E-132
VCP	Valosin containing protein	0.76	1.63E-132	0.42	8.00E-56
XBP1	X-box binding protein 1	0.77	2.12E-34	0.77	3.25E-80
ZFAND2A	Zinc finger AN1-type containing 2A	2.00	7.33E-81	0.79	2.92E-27

Table 5.14 Top significantly upregulated pathways in treatments with DMF for 6 h in HBL-1 cell line (GSE164267) identified by iDEP analysis (FDR < 0.05) and iPG (FDR-corrected) analyses. Only the top 10 differentially expressed pathway genes with highest fold change are shown (adjusted *p*-value < 0.05)

Pathway	-log (*p*-value) (iDEP)	log (*p*-value) (iPG)	Differentially Expressed Pathway Genes
Protein processing in endoplasmic reticulum	3.60	3.44	HSPA6, DNAJB1, PPP1R15A, XBP1, NFE2L2, HSP90AA1, EDEM1, DNAJC3, TXNDC5, HSPH1
Ferroptosis	2.27	2.52	GCLM, SLC7A11, HMOX1, FTH1, FTL, MAP1LC3A, SLC3A2, GCLC, MAP1LC3B, PRNP
Amyotrophic lateral sclerosis	2.27	3.60	DNAH7, MAP1LC3A, SQSTM1, MAP1LC3B, XBP1, PPP3R1, HSPA5, RAB39B, ALS2, DDIT3
Parkinson disease	2.27	3.38	KEAP1, UBC, XBP1, NFE2L2, TXN, ADORA2A, HSPA5, DDIT3, ATF4. SOD1
Huntington disease	1.92	1.36	DNAH7, MAP3K5, ITPR1, SOD1, PSMD14, CLTC, ATG101, CASP3, NDUFA1, PSMD11
Collecting duct acid secretion	1.62	3.02	SLC12A7, ATP6V0C, ATP6V1C1 ATP6V0A1, ATP6V0A2, ATP6V1G1, ATP6V0D1, ATP6V1D, ATP6V1A, ATP6V0E1
Pathways of neurodegeneration	1.82	3.43	DNAH7, WNT6, MAP1LC3A, SQSTM1, FZD2, MAP1LC3B, UBC, XBP1, WNT10A, PRNP
Synaptic vesicle cycle	1.62	1.59	STX3, SLC6A9, ATP6V0C, ATP6V1C1, ATP6V0B,

			ATP6V0A1, ATP6V0A2, ATP6V1H, ATP6V1G1, CLTC
Prion disease	1.64	2.52	HSPA6, CAV1, FYN, NCF1, PRNP, PPP3R1, PIK3CD, NCF2, HSPA5, CACNA1D

Chapter 6. Summary, Perspectives, and Future Directions

The propagation of the free radical chain oxidation (autoxidation) of a lipid molecule can proceed via both the HAT and PRA mechanisms. However, the conventional peroxyl radical method only reflects the contribution of the HAT mechanism to the propagation step. Therefore, the development of a new radical clock approach is important. The elucidation of the autoxidation mechanism and kinetics would allow for the prediction of oxidation products from a lipid and the explanation of its biological effects. Particularly, this dissertation investigates the relevance between the lipid peroxidation mechanisms and their contribution to the modulatory effects of lipids on ferroptosis, a distinct type of cell death driven by iron-dependent autoxidation of membrane-incorporated PUFAs.

Chapter 2 discussed the development and validation of a new peroxyl radical clock approach that can elucidate the propagation mechanisms and kinetics of various biologically important lipids. Here, we reported that the lipids with highly conjugated double bonds are particularly reactive to lipid peroxidation with significant contributions from the PRA mechanism. Importantly, we discovered that the conjugated PUFAs are much more reactive to lipid peroxidation than the nonconjugated ones. Chapter 3 examined the reactivity of various lipids in inhibiting or potentiating ferroptosis. We found that although isoprenoid-derived non-fatty acid lipids, such as CoQ10, vitamins A and D_3, and 7-DHC, are reactive toward lipid peroxidation, they act as inhibitors of ferroptosis. We further found that the conjugated PUFAs are much more potent in inducing ferroptosis than their nonconjugated counterparts. We then demonstrated that CLA 18:3 could act as a ferroptosis inducer via a noncanonical pathway. In Chapter 4, we investigated the mechanisms underlying the potency of conjugated PUFAs in ferroptosis induction. Here, we discovered that the conjugated PUFAs are preferentially incorporated into TAGs and ether lipids,

suggesting the contribution of these two lipid species to the potency of conjugated PUFAs. Additionally, we detected the formation of highly reactive lipid-derived aldehydes from the oxidation of conjugated PUFAs. We also observed a significant increase in ER stress and the activation of the UPR in cells treated with conjugated PUFAs, which likely results from the modifications of protein side chains by lipid-derived electrophiles. Finally, in Chapter 5, we investigated the relevance of the ER stress responses in ferroptosis induced by different agents and discussed how some of the UPR components could contribute to the ferroptosis execution.

The results from this work highlight the underappreciated contribution of the PRA reaction to lipid peroxidation and ferroptosis. This work also helps explain the mechanism underlying the anti-tumor and pro-ferroptotic properties of the conjugated PUFAs. Moreover, this work also provides some insight into the molecular events that happen during the execution of ferroptosis. Furthermore, some findings from this work merit further investigation. For example, the role of ether lipids and lipid droplets in conjugated PUFA-induced ferroptosis required additional investigation. In addition, due to the variation in ER stress responses across treatments observed in Chapter 5, we propose a systematic study in which the changes in gene expression of the same ferroptosis-sensitive cell lines are examined. Specifically, these cell lines should be treated with different ferroptosis inducers within the same time frame, and the concentrations of the inducers should be chosen carefully so that the numbers of viable cells are similar across different treatments.

References

1. P. D. Ray, B. W. Huang, Y. Tsuji, Reactive oxygen species (ROS) homeostasis and redox regulation in cellular signaling. *Cell Signal* **24**, 981-990 (2012).
2. H. Yin, L. Xu, N. A. Porter, Free Radical Lipid Peroxidation: Mechanisms and Analysis. *Chemical Reviews* **111**, 5944-5972 (2011).
3. B. Halliwell, S. Chirico, Lipid peroxidation: its mechanism, measurement, and significance. *Am J Clin Nutr* **57**, 715S-724S; discussion 724S-725S (1993).
4. L. Xu, N. A. Porter, Free radical oxidation of cholesterol and its precursors: Implications in cholesterol biosynthesis disorders. *Free Radic Res* **49**, 835-849 (2015).
5. A. J. Brown, W. Jessup, Oxysterols and atherosclerosis. *Atherosclerosis* **142**, 1-28 (1999).
6. G. Davi, A. Falco, C. Patrono, Lipid peroxidation in diabetes mellitus. *Antioxid Redox Signal* **7**, 256-268 (2005).
7. B. N. Ames, DNA damage from micronutrient deficiencies is likely to be a major cause of cancer. *Mutat. Res.* **475**, 7-20 (2001).
8. G. Barrera, Oxidative stress and lipid peroxidation products in cancer progression and therapy. *ISRN Oncol* **2012**, 137289 (2012).
9. N. A. Simonian, J. T. Coyle, Oxidative stress in neurodegenerative diseases. *Annu. Rev. Pharmacol. Toxicol.* **36**, 83-106 (1996).
10. L. M. Sayre *et al.*, 4-Hydroxynonenal-derived advanced lipid peroxidation end products are increased in Alzheimer's disease. *J Neurochem* **68**, 2092-2097 (1997).
11. F. D. Porter *et al.*, Cholesterol oxidation products are sensitive and specific blood-based biomarkers for Niemann-Pick C1 disease. *Sci. Transl. Med.* **2**, 56ra81 (2010).

12. L. Xu *et al.*, An oxysterol biomarker for 7-dehydrocholesterol oxidation in cell/mouse models for Smith-Lemli-Opitz syndrome. *J. Lipid Res.* **52**, 1222-1233 (2011).

13. S. J. Dixon *et al.*, Ferroptosis: an iron-dependent form of nonapoptotic cell death. *Cell* **149**, 1060-1072 (2012).

14. W. S. Yang *et al.*, Regulation of ferroptotic cancer cell death by GPX4. *Cell* **156**, 317-331 (2014).

15. P. Tsvetkov *et al.*, Copper induces cell death by targeting lipoylated TCA cycle proteins. *Science* **375**, 1254-1261 (2022).

16. O. Zilka *et al.*, On the Mechanism of Cytoprotection by Ferrostatin-1 and Liproxstatin-1 and the Role of Lipid Peroxidation in Ferroptotic Cell Death. *ACS Central Science* **3**, 232-243 (2017).

17. R. Shah, M. S. Shchepinov, D. A. Pratt, Resolving the Role of Lipoxygenases in the Initiation and Execution of Ferroptosis. *ACS Central Science* **4**, 387-396 (2018).

18. M. Conrad, D. A. Pratt, The chemical basis of ferroptosis. *Nature Chemical Biology* **15**, 1137-1147 (2019).

19. N. A. Porter, A Perspective on Free Radical Autoxidation: The Physical Organic Chemistry of Polyunsaturated Fatty Acid and Sterol Peroxidation. *The Journal of Organic Chemistry* **78**, 3511-3524 (2013).

20. Z. A. M. Zielinski, D. A. Pratt, Lipid Peroxidation: Kinetics, Mechanisms, and Products. *The Journal of Organic Chemistry* **82**, 2817-2825 (2017).

21. J. Howard, K. Ingold, ABSOLUTE RATE CONSTANTS FOR HYDROCARBON AUTOXIDATION: IV. TETRALIN, CYCLOHEXENE, DIPHENYLMETHANE,

ETHYLBENZENE, AND ALLYLBENZENE. *Canadian Journal of Chemistry* **44**, 1119-1130 (1966).

22. J. A. Howard, K. U. Ingold, M. Symonds, Absolute rate constants for hydrocarbon oxidation. VIII. The reactions of cumylperoxy radicals. *Canadian Journal of Chemistry* **46**, 1017-1022 (1968).

23. J. Howard, K. Ingold, Absolute rate constants for hydrocarbon autoxidation. VI. Alkyl aromatic and olefinic hydrocarbons. *Canadian Journal of Chemistry* **45**, 793-802 (1967).

24. B. Roschek *et al.*, Peroxyl Radical Clocks. *The Journal of Organic Chemistry* **71**, 3527-3532 (2006).

25. L. Xu, T. A. Davis, N. A. Porter, Rate Constants for Peroxidation of Polyunsaturated Fatty Acids and Sterols in Solution and in Liposomes. *Journal of the American Chemical Society* **131**, 13037-13044 (2009).

26. C. R. Lamberson *et al.*, Propagation rate constants for the peroxidation of sterols on the biosynthetic pathway to cholesterol. *Chemistry and Physics of Lipids* **207**, 51-58 (2017).

27. D. A. Pratt, K. A. Tallman, N. A. Porter, Free Radical Oxidation of Polyunsaturated Lipids: New Mechanistic Insights and the Development of Peroxyl Radical Clocks. *Accounts of Chemical Research* **44**, 458-467 (2011).

28. N. Kresge, R. D. Simoni, R. L. Hill, The Biosynthetic Pathway for Cholesterol: Konrad Bloch. *Journal of Biological Chemistry* **280**, e7-e7 (2005).

29. M. F. Holick *et al.*, Photometabolism of 7-dehydrocholesterol to previtamin D3 in skin. *Biochem Biophys Res Commun* **76**, 107-114 (1977).

30. L. Galluzzi *et al.*, Molecular mechanisms of cell death: recommendations of the Nomenclature Committee on Cell Death 2018. *Cell Death & Differentiation* **25**, 486-541 (2018).

31. A. Degterev *et al.*, Chemical inhibitor of nonapoptotic cell death with therapeutic potential for ischemic brain injury. *Nature Chemical Biology* **1**, 112-119 (2005).

32. B. T. Cookson, M. A. Brennan, Pro-inflammatory programmed cell death. *Trends in Microbiology* **9**, 113-114 (2001).

33. H. Eagle, Nutrition Needs of Mammalian Cells in Tissue Culture. *Science* **122**, 501-504 (1955).

34. H. Eagle, The specific amino acid requirements of a human carcinoma cell (Stain HeLa) in tissue culture. *J Exp Med* **102**, 37-48 (1955).

35. H. Eagle, Amino Acid Metabolism in Mammalian Cell Cultures. *Science* **130**, 432-437 (1959).

36. S. Bannai, H. Tsukeda, H. Okumura, Effect of antioxidants on cultured human diploid fibroblasts exposed to cystine-free medium. *Biochemical and Biophysical Research Communications* **74**, 1582-1588 (1977).

37. R. R. Ratan, J. M. Baraban, APOPTOTIC AN IN AN IN VITRO MODEL OF NEURONAL OXIDATIVE STRESS. *Clinical and Experimental Pharmacology and Physiology* **22**, 309-310 (1995).

38. M. Yonezawa, S. A. Back, X. Gan, P. A. Rosenberg, J. J. Volpe, Cystine deprivation induces oligodendroglial death: rescue by free radical scavengers and by a diffusible glial factor. *J Neurochem* **67**, 566-573 (1996).

39. T. H. Murphy, R. L. Schnaar, J. T. Coyle, Immature cortical neurons are uniquely sensitive to glutamate toxicity by inhibition of cystine uptake. *The FASEB Journal* **4**, 1624-1633 (1990).

40. T. H. Murphy, M. Miyamoto, A. Sastre, R. L. Schnaar, J. T. Coyle, Glutamate toxicity in a neuronal cell line involves inhibition of cystine transport leading to oxidative stress. *Neuron* **2**, 1547-1558 (1989).

41. F. Ursini, M. Maiorino, M. Valente, L. Ferri, C. Gregolin, Purification from pig liver of a protein which protects liposomes and biomembranes from peroxidative degradation and exhibits glutathione peroxidase activity on phosphatidylcholine hydroperoxides. *Biochimica et Biophysica Acta (BBA) - Lipids and Lipid Metabolism* **710**, 197-211 (1982).

42. A. Roveri, M. Maiorino, C. Nisii, F. Ursini, Purification and characterization of phospholipid hydroperoxide glutathione peroxidase from rat testis mitochondrial membranes. *Biochim Biophys Acta* **1208**, 211-221 (1994).

43. J. P. Thomas, P. G. Geiger, M. Maiorino, F. Ursini, A. W. Girotti, Enzymatic reduction of phospholipid and cholesterol hydroperoxides in artificial bilayers and lipoproteins. *Biochim Biophys Acta* **1045**, 252-260 (1990).

44. M. Arai *et al.*, Mitochondrial Phospholipid Hydroperoxide Glutathione Peroxidase Plays a Major Role in Preventing Oxidative Injury to Cells *. *Journal of Biological Chemistry* **274**, 4924-4933 (1999).

45. R. Hurst *et al.*, Hyperresistance to cholesterol hydroperoxide-induced peroxidative injury and apoptotic death in a tumor cell line that overexpresses glutathione peroxidase isotype-4. *Free Radical Biology and Medicine* **31**, 1051-1065 (2001).

46. H. Imai *et al.*, Overexpression of phospholipid hydroperoxide glutathione peroxidase suppressed cell death due to oxidative damage in rat basophile leukemia cells (RBL-2H3). *Biochem Biophys Res Commun* **222**, 432-438 (1996).

47. K. Yagi *et al.*, Expression of Human Phospholipid Hydroperoxide Glutathione Peroxidase Gene for Protection of Host Cells from Lipid Hydroperoxide-Mediated Injury. *Biochemical and Biophysical Research Communications* **219**, 486-491 (1996).

48. A. Seiler *et al.*, Glutathione Peroxidase 4 Senses and Translates Oxidative Stress into 12/15-Lipoxygenase Dependent- and AIF-Mediated Cell Death. *Cell Metabolism* **8**, 237-248 (2008).

49. W. H. Kim, C. H. Choi, S. K. Kang, C. H. Kwon, Y. K. Kim, Ceramide Induces Non-Apoptotic Cell Death in Human Glioma Cells. *Neurochemical Research* **30**, 969-979 (2005).

50. S. Dolma, S. L. Lessnick, W. C. Hahn, B. R. Stockwell, Identification of genotype-selective antitumor agents using synthetic lethal chemical screening in engineered human tumor cells. *Cancer Cell* **3**, 285-296 (2003).

51. W. S. Yang, B. R. Stockwell, Synthetic Lethal Screening Identifies Compounds Activating Iron-Dependent, Nonapoptotic Cell Death in Oncogenic-RAS-Harboring Cancer Cells. *Chemistry & Biology* **15**, 234-245 (2008).

52. N. Yagoda *et al.*, RAS–RAF–MEK-dependent oxidative cell death involving voltage-dependent anion channels. *Nature* **447**, 865-869 (2007).

53. B. R. Stockwell, Ferroptosis turns 10: Emerging mechanisms, physiological functions, and therapeutic applications. *Cell* **185**, 2401-2421 (2022).

54. M. Gao, P. Monian, N. Quadri, R. Ramasamy, X. Jiang, Glutaminolysis and Transferrin Regulate Ferroptosis. *Molecular Cell* **59**, 298-308 (2015).

55. W. Breuer, M. Shvartsman, Z. I. Cabantchik, Intracellular labile iron. *Int J Biochem Cell Biol* **40**, 350-354 (2008).

56. D. Basuli *et al.*, Iron addiction: a novel therapeutic target in ovarian cancer. *Oncogene* **36**, 4089-4099 (2017).

57. W. Hou *et al.*, Autophagy promotes ferroptosis by degradation of ferritin. *Autophagy* **12**, 1425-1428 (2016).

58. B. R. Stockwell, X. Jiang, The Chemistry and Biology of Ferroptosis. *Cell Chem Biol* **27**, 365-375 (2020).

59. T. P. Szatrowski, C. F. Nathan, Production of Large Amounts of Hydrogen Peroxide by Human Tumor Cells. *Cancer Research* **51**, 794 (1991).

60. R. Brigelius-Flohé, M. Maiorino, Glutathione peroxidases. *Biochimica et Biophysica Acta (BBA) - General Subjects* **1830**, 3289-3303 (2013).

61. G. J. McBean, The transsulfuration pathway: a source of cysteine for glutathione in astrocytes. *Amino Acids* **42**, 199-205 (2012).

62. M. Hayano, W. S. Yang, C. K. Corn, N. C. Pagano, B. R. Stockwell, Loss of cysteinyl-tRNA synthetase (CARS) induces the transsulfuration pathway and inhibits ferroptosis induced by cystine deprivation. *Cell Death Differ* **23**, 270-278 (2016).

63. W. S. Yang *et al.*, Peroxidation of polyunsaturated fatty acids by lipoxygenases drives ferroptosis. *Proc Natl Acad Sci U S A* **113**, E4966-4975 (2016).

64. K. Bersuker *et al.*, The CoQ oxidoreductase FSP1 acts parallel to GPX4 to inhibit ferroptosis. *Nature* **575**, 688-692 (2019).

65. S. Doll *et al.*, FSP1 is a glutathione-independent ferroptosis suppressor. *Nature* **575**, 693-698 (2019).

66. L. Magtanong *et al.*, Context-dependent regulation of ferroptosis sensitivity. *Cell Chemical Biology* **29**, 1409-1418.e1406 (2022).

67. V. E. Kagan *et al.*, Oxidized arachidonic and adrenic PEs navigate cells to ferroptosis. *Nat Chem Biol* **13**, 81-90 (2017).

68. V. A. N. Kraft *et al.*, GTP Cyclohydrolase 1/Tetrahydrobiopterin Counteract Ferroptosis through Lipid Remodeling. *ACS Cent Sci* **6**, 41-53 (2020).

69. Y. Zou *et al.*, Plasticity of ether lipids promotes ferroptosis susceptibility and evasion. *Nature* **585**, 603-608 (2020).

70. S. G. Kathman, J. Boshart, H. Jing, B. F. Cravatt, Blockade of the Lysophosphatidylserine Lipase ABHD12 Potentiates Ferroptosis in Cancer Cells. *ACS Chemical Biology* **15**, 871-877 (2020).

71. D. Chen *et al.*, iPLA2β-mediated lipid detoxification controls p53-driven ferroptosis independent of GPX4. *Nature Communications* **12**, 3644 (2021).

72. S. Doll *et al.*, ACSL4 dictates ferroptosis sensitivity by shaping cellular lipid composition. *Nature Chemical Biology* **13**, 91-98 (2017).

73. S. J. Dixon *et al.*, Human Haploid Cell Genetics Reveals Roles for Lipid Metabolism Genes in Nonapoptotic Cell Death. *ACS Chemical Biology* **10**, 1604-1609 (2015).

74. H. Yuan, X. Li, X. Zhang, R. Kang, D. Tang, Identification of ACSL4 as a biomarker and contributor of ferroptosis. *Biochemical and Biophysical Research Communications* **478**, 1338-1343 (2016).

75. A. Beatty *et al.*, Ferroptotic cell death triggered by conjugated linolenic acids is mediated by ACSL1. *Nature Communications* **12**, 2244 (2021).

76. T. D. Klasson *et al.*, ACSL3 regulates lipid droplet biogenesis and ferroptosis sensitivity in clear cell renal cell carcinoma. *Cancer & Metabolism* **10**, 14 (2022).

77. L. Magtanong *et al.*, Exogenous Monounsaturated Fatty Acids Promote a Ferroptosis-Resistant Cell State. *Cell Chem Biol* **26**, 420-432.e429 (2019).

78. J. P. Friedmann Angeli *et al.*, Inactivation of the ferroptosis regulator Gpx4 triggers acute renal failure in mice. *Nat Cell Biol* **16**, 1180-1191 (2014).

79. Y. Xie *et al.*, Identification of baicalein as a ferroptosis inhibitor by natural product library screening. *Biochemical and Biophysical Research Communications* **473**, 775-780 (2016).

80. M. Matsushita *et al.*, T cell lipid peroxidation induces ferroptosis and prevents immunity to infection. *Journal of Experimental Medicine* **212**, 555-568 (2015).

81. S. H. Brütsch *et al.*, Expression of Inactive Glutathione Peroxidase 4 Leads to Embryonic Lethality, and Inactivation of the Alox15 Gene Does Not Rescue Such Knock-In Mice. *Antioxidants & Redox Signaling* **22**, 281-293 (2014).

82. M. Conrad, H. Sato, The oxidative stress-inducible cystine/glutamate antiporter, system xc−: cystine supplier and beyond. *Amino Acids* **42**, 231-246 (2012).

83. H. Sato, M. Tamba, T. Ishii, S. Bannai, Cloning and Expression of a Plasma Membrane Cystine/Glutamate Exchange Transporter Composed of Two Distinct Proteins *. *Journal of Biological Chemistry* **274**, 11455-11458 (1999).

84. S. J. Dixon *et al.*, Pharmacological inhibition of cystine-glutamate exchange induces endoplasmic reticulum stress and ferroptosis. *Elife* **3**, e02523 (2014).

85. M.-H. Larraufie *et al.*, Incorporation of metabolically stable ketones into a small molecule probe to increase potency and water solubility. *Bioorganic & Medicinal Chemistry Letters* **25**, 4787-4792 (2015).

86. P. W. Gout, A. R. Buckley, C. R. Simms, N. Bruchovsky, Sulfasalazine, a potent suppressor of lymphoma growth by inhibition of the xc− cystine transporter: a new action for an old drug. *Leukemia* **15**, 1633-1640 (2001).

87. C. Louandre *et al.*, Iron-dependent cell death of hepatocellular carcinoma cells exposed to sorafenib. *International Journal of Cancer* **133**, 1732-1742 (2013).

88. C. Louandre *et al.*, The retinoblastoma (Rb) protein regulates ferroptosis induced by sorafenib in human hepatocellular carcinoma cells. *Cancer Letters* **356**, 971-977 (2015).

89. M. Weïwer *et al.*, Development of small-molecule probes that selectively kill cells induced to express mutant RAS. *Bioorg Med Chem Lett* **22**, 1822-1826 (2012).

90. J. K. Eaton *et al.*, Targeting a Therapy-Resistant Cancer Cell State Using Masked Electrophiles as GPX4 Inhibitors. *bioRxiv*, 376764 (2018).

91. K. Shimada *et al.*, Global survey of cell death mechanisms reveals metabolic regulation of ferroptosis. *Nat Chem Biol* **12**, 497-503 (2016).

92. N. Fradejas *et al.*, Mammalian Trit1 is a tRNA([Ser]Sec)-isopentenyl transferase required for full selenoprotein expression. *Biochem J* **450**, 427-432 (2013).

93. V. S. Viswanathan *et al.*, Dependency of a therapy-resistant state of cancer cells on a lipid peroxidase pathway. *Nature* **547**, 453-457 (2017).

94. Q. Zhang *et al.*, Atorvastatin Induces Mitochondria-Dependent Ferroptosis via the Modulation of Nrf2-xCT/GPx4 Axis. *Front Cell Dev Biol* **10**, 806081 (2022).

95. M. M. Gaschler *et al.*, FINO2 initiates ferroptosis through GPX4 inactivation and iron oxidation. *Nature Chemical Biology* **14**, 507-515 (2018).

96. R. P. Abrams, W. L. Carroll, K. A. Woerpel, Five-Membered Ring Peroxide Selectively Initiates Ferroptosis in Cancer Cells. *ACS Chemical Biology* **11**, 1305-1312 (2016).

97. T. Lőrincz, K. Jemnitz, T. Kardon, J. Mandl, A. Szarka, Ferroptosis is Involved in Acetaminophen Induced Cell Death. *Pathology & Oncology Research* **21**, 1115-1121 (2015).

98. N. Eling, L. Reuter, J. Hazin, A. Hamacher-Brady, N. R. Brady, Identification of artesunate as a specific activator of ferroptosis in pancreatic cancer cells. *Oncoscience* **2**, 517-532 (2015).

99. H. Yamaguchi *et al.*, Caspase-Independent Cell Death Is Involved in the Negative Effect of EGF Receptor Inhibitors on Cisplatin in Non–Small Cell Lung Cancer Cells. *Clinical Cancer Research* **19**, 845-854 (2013).

100. H. Nishizawa *et al.*, Ferroptosis is controlled by the coordinated transcriptional regulation of glutathione and labile iron metabolism by the transcription factor BACH1. *J Biol Chem* **295**, 69-82 (2020).

101. M. Y. Kwon, E. Park, S. J. Lee, S. W. Chung, Heme oxygenase-1 accelerates erastin-induced ferroptotic cell death. *Oncotarget* **6**, 24393-24403 (2015).

102. X. Fang *et al.*, Ferroptosis as a target for protection against cardiomyopathy. *Proceedings of the National Academy of Sciences* **116**, 2672-2680 (2019).

103. X. Sun *et al.*, Activation of the p62-Keap1-NRF2 pathway protects against ferroptosis in hepatocellular carcinoma cells. *Hepatology* **63**, 173-184 (2016).

104. O. Adedoyin *et al.*, Heme oxygenase-1 mitigates ferroptosis in renal proximal tubule cells. *Am J Physiol Renal Physiol* **314**, F702-f714 (2018).

105. L. Jiang *et al.*, Ferroptosis as a p53-mediated activity during tumour suppression. *Nature* **520**, 57-62 (2015).

106. M. Jennis *et al.*, An African-specific polymorphism in the TP53 gene impairs p53 tumor suppressor function in a mouse model. *Genes Dev* **30**, 918-930 (2016).

107. K. Gnanapradeepan *et al.*, The p53 Tumor Suppressor in the Control of Metabolism and Ferroptosis. *Frontiers in Endocrinology* **9**, (2018).

108. Y. Zou *et al.*, Cytochrome P450 oxidoreductase contributes tophospholipid peroxidation in ferroptosis. *Nature Chemical Biology* **16**, 302-309 (2020).

109. M. Soula *et al.*, Metabolic determinants of cancer cell sensitivity to canonical ferroptosis inducers. *Nature Chemical Biology* **16**, 1351-1360 (2020).

110. C. Mao *et al.*, DHODH-mediated ferroptosis defence is a targetable vulnerability in cancer. *Nature* **593**, 586-590 (2021).

111. B. R. Stockwell, A powerful cell-protection system prevents cell death by ferroptosis. *Nature* **575**, 597-598 (2019).

112. N. Yagoda *et al.*, RAS-RAF-MEK-dependent oxidative cell death involving voltage-dependent anion channels. *Nature* **447**, 864-868 (2007).

113. R. Shah, K. Margison, D. A. Pratt, The Potency of Diarylamine Radical-Trapping Antioxidants as Inhibitors of Ferroptosis Underscores the Role of Autoxidation in the Mechanism of Cell Death. *ACS Chemical Biology* **12**, 2538-2545 (2017).

114. L. A. Farmer, E. A. Haidasz, M. Griesser, D. A. Pratt, Phenoxazine: A Privileged Scaffold for Radical-Trapping Antioxidants. *The Journal of Organic Chemistry* **82**, 10523-10536 (2017).

115. T. Krainz *et al.*, A Mitochondrial-Targeted Nitroxide Is a Potent Inhibitor of Ferroptosis. *ACS Cent Sci* **2**, 653-659 (2016).

116. M. Griesser *et al.*, The Catalytic Reaction of Nitroxides with Peroxyl Radicals and Its Relevance to Their Cytoprotective Properties. *Journal of the American Chemical Society* **140**, 3798-3808 (2018).

117. J.-H. Kim, T. M. Lewin, R. A. Coleman, Expression and Characterization of Recombinant Rat Acyl-CoA Synthetases 1, 4, and 5: SELECTIVE INHIBITION BY TRIACSIN C AND THIAZOLIDINEDIONES*. *Journal of Biological Chemistry* **276**, 24667-24673 (2001).

118. J. Wong-ekkabut *et al.*, Effect of Lipid Peroxidation on the Properties of Lipid Bilayers: A Molecular Dynamics Study. *Biophysical Journal* **93**, 4225-4236 (2007).

119. A. Catalá, M. Díaz, Editorial: Impact of Lipid Peroxidation on the Physiology and Pathophysiology of Cell Membranes. *Frontiers in Physiology* **7**, (2016).

120. C. T. R. Heffern *et al.*, Thermodynamic and kinetic investigations of the release of oxidized phospholipids from lipid membranes and its effect on vascular integrity. *Chemistry and Physics of Lipids* **175-176**, 9-19 (2013).

121. J. W. Borst, N. V. Visser, O. Kouptsova, A. J. Visser, Oxidation of unsaturated phospholipids in membrane bilayer mixtures is accompanied by membrane fluidity changes. *Biochim Biophys Acta* **1487**, 61-73 (2000).

122. E. Agmon, J. Solon, P. Bassereau, B. R. Stockwell, Modeling the effects of lipid peroxidation during ferroptosis on membrane properties. *Sci Rep* **8**, 5155 (2018).

123. M. Riegman *et al.*, Ferroptosis occurs through an osmotic mechanism and propagates independently of cell rupture. *Nat Cell Biol* **22**, 1042-1048 (2020).

124. L. Pedrera *et al.*, Ferroptotic pores induce Ca(2+) fluxes and ESCRT-III activation to modulate cell death kinetics. *Cell Death Differ* **28**, 1644-1657 (2021).

125. E. Agmon, B. R. Stockwell, Lipid homeostasis and regulated cell death. *Curr Opin Chem Biol* **39**, 83-89 (2017).

126. Ü. Coskun, K. Simons, Cell Membranes: The Lipid Perspective. *Structure* **19**, 1543-1548 (2011).

127. M. M. Gaschler *et al.*, Determination of the Subcellular Localization and Mechanism of Action of Ferrostatins in Suppressing Ferroptosis. *ACS Chem Biol* **13**, 1013-1020 (2018).

128. L. Hao, Y.-M. Zhong, C.-P. Tan, Z.-W. Mao, Quantitative tracking of endoplasmic reticulum viscosity during ferroptosis by an iridium complex via TPPLM. *Chemical Communications* **57**, 5040-5042 (2021).

129. C.-P. Chng, Y. Sadovsky, K. J. Hsia, C. Huang, Site-specific peroxidation modulates lipid bilayer mechanics. *Extreme Mechanics Letters* **42**, 101148 (2021).

130. J. J. Chen, B. P. Yu, Alterations in mitochondrial membrane fluidity by lipid peroxidation products. *Free Radical Biology and Medicine* **17**, 411-418 (1994).

131. M. T. Curtis, D. Gilfor, J. L. Farber, Lipid peroxidation increases the molecular order of microsomal membranes. *Arch Biochem Biophys* **235**, 644-649 (1984).

132. G. E. Dobretsov, T. A. Borschevskaya, V. A. Petrov, Y. A. Vladimirov, The increase of phospholipid bilayer rigidity after lipid peroxidation. *FEBS Letters* **84**, 125-128 (1977).

133. M. Rahmani *et al.*, The kinase inhibitor sorafenib induces cell death through a process involving induction of endoplasmic reticulum stress. *Mol Cell Biol* **27**, 5499-5513 (2007).

134. H. Liang *et al.*, Short form glutathione peroxidase 4 is the essential isoform required for survival and somatic mitochondrial functions. *J Biol Chem* **284**, 30836-30844 (2009).

135. L. Plecitá-Hlavatá, J. Jezek, P. Jezek, Pro-oxidant mitochondrial matrix-targeted ubiquinone MitoQ10 acts as anti-oxidant at retarded electron transport or proton pumping within Complex I. *Int J Biochem Cell Biol* **41**, 1697-1707 (2009).

136. M. Luo *et al.*, miR-137 regulates ferroptosis by targeting glutamine transporter SLC1A5 in melanoma. *Cell Death Differ* **25**, 1457-1472 (2018).

137. M. Gao *et al.*, Role of Mitochondria in Ferroptosis. *Mol Cell* **73**, 354-363.e353 (2019).

138. T. Tadokoro *et al.*, Mitochondria-dependent ferroptosis plays a pivotal role in doxorubicin cardiotoxicity. *JCI Insight* **5**, (2020).

139. W. Cui, D. Liu, W. Gu, B. Chu, Peroxisome-driven ether-linked phospholipids biosynthesis is essential for ferroptosis. *Cell Death Differ* **28**, 2536-2551 (2021).

140. S. Torii *et al.*, An essential role for functional lysosomes in ferroptosis of cancer cells. *Biochemical Journal* **473**, 769-777 (2016).

141. T. Petan, Lipid Droplets in Cancer. *Reviews of Physiology, Biochemistry and Pharmacology*, (2020).

142. A. P. Bailey *et al.*, Antioxidant Role for Lipid Droplets in a Stem Cell Niche of Drosophila. *Cell* **163**, 340-353 (2015).

143. E. Dierge *et al.*, Peroxidation of n-3 and n-6 polyunsaturated fatty acids in the acidic tumor environment leads to ferroptosis-mediated anticancer effects. *Cell Metabolism* **33**, 1701-1715.e1705 (2021).

144. E. Jarc *et al.*, Lipid droplets induced by secreted phospholipase A2 and unsaturated fatty acids protect breast cancer cells from nutrient and lipotoxic stress. *Biochimica et Biophysica Acta (BBA) - Molecular and Cell Biology of Lipids* **1863**, 247-265 (2018).

145. Y. Zou *et al.*, A GPX4-dependent cancer cell state underlies the clear-cell morphology and confers sensitivity to ferroptosis. *Nat Commun* **10**, 1617 (2019).

146. P. Vermonden *et al.*, Punicic Acid Triggers Ferroptotic Cell Death in Carcinoma Cells. *Nutrients* **13**, (2021).

147. B. Dong, W. Song, Y. Lu, Y. Sun, W. Lin, Revealing the Viscosity Changes in Lipid Droplets during Ferroptosis by the Real-Time and In Situ Near-Infrared Imaging. *ACS Sensors* **6**, 22-26 (2021).

148. Y. Zhang *et al.*, Imidazole Ketone Erastin Induces Ferroptosis and Slows Tumor Growth in a Mouse Lymphoma Model. *Cell Chem Biol* **26**, 623-633.e629 (2019).

149. W. Cao *et al.*, Oxidized Lipids Block Antigen Cross-Presentation by Dendritic Cells in Cancer. *The Journal of Immunology* **192**, 2920-2931 (2014).

150. F. Veglia *et al.*, Lipid bodies containing oxidatively truncated lipids block antigen cross-presentation by dendritic cells in cancer. *Nature Communications* **8**, 2122 (2017).

151. S. J. Wang *et al.*, Acetylation Is Crucial for p53-Mediated Ferroptosis and Tumor Suppression. *Cell Rep* **17**, 366-373 (2016).

152. S. Egolf *et al.*, MLL4 mediates differentiation and tumor suppression through ferroptosis. *Science Advances* **7**, eabj9141 (2021).

153. Y. Zhang *et al.*, BAP1 links metabolic regulation of ferroptosis to tumour suppression. *Nature Cell Biology* **20**, 1181-1192 (2018).

154. S. W. Alvarez *et al.*, NFS1 undergoes positive selection in lung tumours and protects cells from ferroptosis. *Nature* **551**, 639-643 (2017).

155. W. Wang *et al.*, CD8+ T cells regulate tumour ferroptosis during cancer immunotherapy. *Nature* **569**, 270-274 (2019).

156. P. Liao *et al.*, CD8+ T cells and fatty acids orchestrate tumor ferroptosis and immunity via ACSL4. *Cancer Cell* **40**, 365-378.e366 (2022).

157. K. Schnurr, A. Borchert, H. Kuhn, Inverse regulation of lipid-peroxidizing and hydroperoxyl lipid-reducing enzymes by interleukins 4 and 13. *Faseb j* **13**, 143-154 (1999).

158. X. Jiang, B. R. Stockwell, M. Conrad, Ferroptosis: mechanisms, biology and role in disease. *Nat Rev Mol Cell Biol* **22**, 266-282 (2021).

159. H. Zheng, L. Jiang, T. Tsuduki, M. Conrad, S. Toyokuni, Embryonal erythropoiesis and aging exploit ferroptosis. *Redox Biol* **48**, 102175 (2021).

160. N. L. Jenkins *et al.*, Changes in ferrous iron and glutathione promote ferroptosis and frailty in aging Caenorhabditis elegans. *eLife* **9**, e56580 (2020).

161. Q. Shen, M. Liang, F. Yang, Y. Z. Deng, N. I. Naqvi, Ferroptosis contributes to developmental cell death in rice blast. *New Phytol* **227**, 1831-1846 (2020).

162. X. Bosch, E. Poch, J. M. Grau, Rhabdomyolysis and acute kidney injury. *N Engl J Med* **361**, 62-72 (2009).

163. O. Boutaud, L. J. Roberts, 2nd, Mechanism-based therapeutic approaches to rhabdomyolysis-induced renal failure. *Free Radic Biol Med* **51**, 1062-1067 (2011).

164. J. J. Volpe, Neurobiology of periventricular leukomalacia in the premature infant. *Pediatr Res* **50**, 553-562 (2001).

165. T. Inder *et al.*, Elevated Free Radical Products in the Cerebrospinal Fluid of VLBW Infants with Cerebral White Matter Injury. *Pediatric Research* **52**, 213-218 (2002).

166. W. M. Johnson, A. L. Wilson-Delfosse, J. J. Mieyal, Dysregulation of glutathione homeostasis in neurodegenerative diseases. *Nutrients* **4**, 1399-1440 (2012).

167. M. Muller, B. R. Leavitt, Iron dysregulation in Huntington's disease. *J Neurochem* **130**, 328-350 (2014).

168. M. Sadagurski *et al.*, IRS2 increases mitochondrial dysfunction and oxidative stress in a mouse model of Huntington disease. *J Clin Invest* **121**, 4070-4081 (2011).

169. R. Skouta *et al.*, Ferrostatins inhibit oxidative lipid damage and cell death in diverse disease models. *Journal of the American Chemical Society* **136**, 4551-4556 (2014).

170. A. Linkermann *et al.*, Synchronized renal tubular cell death involves ferroptosis. *Proc Natl Acad Sci U S A* **111**, 16836-16841 (2014).

171. S. A. Back, X. Gan, Y. Li, P. A. Rosenberg, J. J. Volpe, Maturation-dependent vulnerability of oligodendrocytes to oxidative stress-induced death caused by glutathione depletion. *J Neurosci* **18**, 6241-6253 (1998).

172. J. Chen *et al.*, Iron accumulates in Huntington's disease neurons: protection by deferoxamine. *PLoS One* **8**, e77023 (2013).

173. Q. Li *et al.*, Inhibition of neuronal ferroptosis protects hemorrhagic brain. *JCI Insight* **2**, e90777 (2017).

174. A. Linkermann *et al.*, Two independent pathways of regulated necrosis mediate ischemia–reperfusion injury. *Proceedings of the National Academy of Sciences* **110**, 12024-12029 (2013).

175. D. C. Bueno *et al.*, New Probucol Analogues Inhibit Ferroptosis, Improve Mitochondrial Parameters, and Induce Glutathione Peroxidase in HT22 Cells. *Molecular Neurobiology* **57**, 3273-3290 (2020).

176. I. Alim *et al.*, Selenium Drives a Transcriptional Adaptive Program to Block Ferroptosis and Treat Stroke. *Cell* **177**, 1262-1279.e1225 (2019).

177. M. A. Badgley *et al.*, Cysteine depletion induces pancreatic tumor ferroptosis in mice. *Science* **368**, 85-89 (2020).

178. J. K. Iglehart, R. M. York, A. P. Modest, H. Lazarus, D. M. Livingston, Cystine requirement of continuous human lymphoid cell lines of normal and leukemic origin. *J Biol Chem* **252**, 7184-7191 (1977).

179. S. K. Tickoo, M. B. Amin, R. J. Zarbo, Colloidal iron staining in renal epithelial neoplasms, including chromophobe renal cell carcinoma: emphasis on technique and patterns of staining. *Am J Surg Pathol* **22**, 419-424 (1998).

180. P. W. Gout, C. R. Simms, M. C. Robertson, In vitro studies on the lymphoma growth-inhibitory activity of sulfasalazine. *Anticancer Drugs* **14**, 21-29 (2003).

181. M. J. Hangauer *et al.*, Drug-tolerant persister cancer cells are vulnerable to GPX4 inhibition. *Nature* **551**, 247-250 (2017).

182. J. Tsoi *et al.*, Multi-stage Differentiation Defines Melanoma Subtypes with Differential Vulnerability to Drug-Induced Iron-Dependent Oxidative Stress. *Cancer Cell* **33**, 890-904.e895 (2018).

183. J. P. Friedmann Angeli, D. V. Krysko, M. Conrad, Ferroptosis at the crossroads of cancer-acquired drug resistance and immune evasion. *Nature Reviews Cancer* **19**, 405-414 (2019).

184. G. Lei *et al.*, The role of ferroptosis in ionizing radiation-induced cell death and tumor suppression. *Cell Research* **30**, 146-162 (2020).

185. L. F. Ye *et al.*, Radiation-Induced Lipid Peroxidation Triggers Ferroptosis and Synergizes with Ferroptosis Inducers. *ACS Chem Biol* **15**, 469-484 (2020).

186. X. Lang *et al.*, Radiotherapy and Immunotherapy Promote Tumoral Lipid Oxidation and Ferroptosis via Synergistic Repression of SLC7A11. *Cancer Discovery* **9**, 1673-1685 (2019).

187. J. P. F. Angeli, *e. al.*, 7-Dehydrocholesterol is an endogenous suppressor of ferroptosis. *Research Square*, (2021).

188. N. Yamada *et al.*, DHCR7 as a novel regulator of ferroptosis in hepatocytes. *bioRxiv*, 2022.2006.2015.496212 (2022).

189. X. Liu, S. Wang, S. Jin, S. Huang, Y. Liu, Vitamin D3 attenuates cisplatin-induced intestinal injury by inhibiting ferroptosis, oxidative stress, and ROS-mediated excessive mitochondrial fission. *Food & Function* **13**, 10210-10224 (2022).

190. Y. Cai *et al.*, Vitamin D suppresses ferroptosis and protects against neonatal hypoxic-ischemic encephalopathy by activating the Nrf2/HO-1 pathway. *Translational Pediatrics*, (2022).

191. Z. A. M. Zielinski, D. A. Pratt, H-Atom Abstraction vs Addition: Accounting for the Diverse Product Distribution in the Autoxidation of Cholesterol and Its Esters. *Journal of the American Chemical Society* **141**, 3037-3051 (2019).

192. L. Xu, Z. Korade, N. A. Porter, Oxysterols from Free Radical Chain Oxidation of 7-Dehydrocholesterol: Product and Mechanistic Studies. *Journal of the American Chemical Society* **132**, 2222-2232 (2010).

193. W. Liu, N. A. Porter, C. Schneider, A. R. Brash, H. Yin, Formation of 4-hydroxynonenal from cardiolipin oxidation: Intramolecular peroxyl radical addition and decomposition. *Free Radic Biol Med* **50**, 166-178 (2011).

194. A. Baschieri, R. Pizzol, Y. Guo, R. Amorati, L. Valgimigli, Calibration of Squalene, p-Cymene, and Sunflower Oil as Standard Oxidizable Substrates for Quantitative Antioxidant Testing. *Journal of Agricultural and Food Chemistry* **67**, 6902-6910 (2019).

195. J. A. Howard, K. U. Ingold, ABSOLUTE RATE CONSTANTS FOR HYDROCARBON AUTOXIDATION: I. STYRENE. *Canadian Journal of Chemistry* **43**, 2729-2736 (1965).

196. M. S. Stark, Addition of Peroxyl Radicals to Alkenes and the Reaction of Oxygen with Alkyl Radicals. *Journal of the American Chemical Society* **122**, 4162-4170 (2000).

197. B. Giese, Formation of CC Bonds by Addition of Free Radicals to Alkenes. *Angewandte Chemie International Edition in English* **22**, 753-764 (1983).

198. D. H. McDaniel, H. C. Brown, An Extended Table of Hammett Substitutent Constants Based on the Ionization of Substituted Benzoic Acids. *The Journal of Organic Chemistry* **23**, 420-427 (1958).

199. T. H. Fisher, A. W. Meierhoefer, Substituent effects in free-radical reactions. A study of 4-substituted 3-cyanobenzyl free radicals. *The Journal of Organic Chemistry* **43**, 224-228 (1978).

200. S. Dinçtürk, R. A. Jackson, M. Townson, An improved σ· scale. The thermal decomposition of substituted dibenzylmercury compounds in alkane solutions. *J. Chem. Soc., Chem. Commun.*, 172-174 (1979).

201. R. Taylor, *Electrophilic aromatic substitution*. (J. Wiley, Chichester, West Sussex, England ; New York, 1990), pp. xvi, 513 p.

202. D. A. Pratt, J. H. Mills, N. A. Porter, Theoretical Calculations of Carbon−Oxygen Bond Dissociation Enthalpies of Peroxyl Radicals Formed in the Autoxidation of Lipids. *Journal of the American Chemical Society* **125**, 5801-5810 (2003).

203. S. Korcek, J. Chenier, J. Howard, K. Ingold, Absolute Rate Constants for Hydrocarbon Autoxidation. XXI. Activation Energies for Propagation and the Correlation of Propagation Rate Constants with Carbon–Hydrogen Bond Strengths. *Canadian Journal of Chemistry* **50**, 2285-2297 (1972).

204. J. A. Howard, K. U. Ingold, Absolute rate constants for hydrocarbon autoxidation. V. The hydroperoxy radical in chain propagation and termination. *Canadian Journal of Chemistry* **45**, 785-792 (1967).

205. N. A. Porter, L. S. Lehman, B. A. Weber, K. J. Smith, Unified mechanism for polyunsaturated fatty acid autoxidation. Competition of peroxy radical hydrogen atom abstraction, .beta.-scission, and cyclization. *Journal of the American Chemical Society* **103**, 6447-6455 (1981).

206. D. A. Pratt, G. A. DiLabio, P. Mulder, K. U. Ingold, Bond Strengths of Toluenes, Anilines, and Phenols: To Hammett or Not. *Accounts of Chemical Research* **37**, 334-340 (2004).

207. C. M. Bathelt, L. Ridder, A. J. Mulholland, J. N. Harvey, Aromatic Hydroxylation by Cytochrome P450: Model Calculations of Mechanism and Substituent Effects. *Journal of the American Chemical Society* **125**, 15004-15005 (2003).

208. A. B. Trenwith, Dissociation of 3-methylpenta-1, 4-diene and the resonance energy of the pentadienyl radical. *Journal of the Chemical Society, Faraday Transactions 1: Physical Chemistry in Condensed Phases* **78**, 3131-3136 (1982).

209. J. Berkowitz, G. B. Ellison, D. Gutman, Three methods to measure RH bond energies. *The Journal of Physical Chemistry* **98**, 2744-2765 (1994).

210. L. Xu, N. A. Porter, Reactivities and Products of Free Radical Oxidation of Cholestadienols. *Journal of the American Chemical Society* **136**, 5443-5450 (2014).

211. Q. Do *et al.*, Development and Application of a Peroxyl Radical Clock Approach for Measuring Both Hydrogen-Atom Transfer and Peroxyl Radical Addition Rate Constants. *J Org Chem* **86**, 153-168 (2021).

212. T. Aliwarga *et al.*, Enzymatic and free radical formation of cis- and trans-epoxyeicosatrienoic acids in vitro and in vivo. *Free Radical Biol. Med.* **112**, 131-140 (2017).

213. T. R. Dhiman, G. R. Anand, L. D. Satter, M. W. Pariza, Conjugated linoleic acid content of milk from cows fed different diets. *J Dairy Sci* **82**, 2146-2156 (1999).

214. F. Destaillats, J. P. Trottier, J. M. Galvez, P. Angers, Analysis of alpha-linolenic acid biohydrogenation intermediates in milk fat with emphasis on conjugated linolenic acids. *J Dairy Sci* **88**, 3231-3239 (2005).

215. R. Suzuki *et al.*, Cytotoxic effect of conjugated trienoic fatty acids on mouse tumor and human monocytic leukemia cells. *Lipids* **36**, 477-482 (2001).

216. H. Kohno *et al.*, Dietary conjugated linolenic acid inhibits azoxymethane-induced colonic aberrant crypt foci in rats. *Jpn J Cancer Res* **93**, 133-142 (2002).

217. F. Moloney *et al.*, Antidiabetic effects of cis-9, trans-11-conjugated linoleic acid may be mediated via anti-inflammatory effects in white adipose tissue. *Diabetes* **56**, 574-582 (2007).

218. D. Dipasquale *et al.*, Anti-inflammatory effects of conjugated linoleic acid isomers and essential fatty acids in bovine mammary epithelial cells. *Animal* **12**, 2108-2114 (2018).

219. R. J. Nicolosi, E. J. Rogers, D. Kritchevsky, J. A. Scimeca, P. J. Huth, Dietary conjugated linoleic acid reduces plasma lipoproteins and early aortic atherosclerosis in hypercholesterolemic hamsters. *Artery* **22**, 266-277 (1997).

220. J. A. Scimeca, H. J. Thompson, C. Ip, in *Diet and Breast Cancer,* E. K. Weisburger, Ed. (Springer US, Boston, MA, 1994), pp. 59-65.

221. M. Igarashi, T. Miyazawa, Newly recognized cytotoxic effect of conjugated trienoic fatty acids on cultured human tumor cells. *Cancer Lett* **148**, 173-179 (2000).

222. A. S. Cornelius, N. R. Yerram, D. A. Kratz, A. A. Spector, Cytotoxic effect of cis-parinaric acid in cultured malignant cells. *Cancer Res* **51**, 6025-6030 (1991).

223. W. S. Yang, B. R. Stockwell, Ferroptosis: Death by Lipid Peroxidation. *Trends Cell Biol* **26**, 165-176 (2016).

224. T. M. Seibt, B. Proneth, M. Conrad, Role of GPX4 in ferroptosis and its pharmacological implication. *Free Radical Biology and Medicine* **133**, 144-152 (2019).

225. M. H. Zile, Function of vitamin A in vertebrate embryonic development. *J Nutr* **131**, 705-708 (2001).

226. M. F. Holick, Vitamin D: importance in the prevention of cancers, type 1 diabetes, heart disease, and osteoporosis. *Am J Clin Nutr* **79**, 362-371 (2004).

227. G. Lenaz, R. Fato, G. Formiggini, M. L. Genova, The role of Coenzyme Q in mitochondrial electron transport. *Mitochondrion* **7 Suppl**, S8-33 (2007).

228. G. W. Burton, K. U. Ingold, beta-Carotene: an unusual type of lipid antioxidant. *Science* **224**, 569-573 (1984).

229. T. A. Kennedy, D. C. Liebler, Peroxyl radical scavenging by beta-carotene in lipid bilayers. Effect of oxygen partial pressure. *J Biol Chem* **267**, 4658-4663 (1992).

230. P. Palozza, G. Calviello, G. M. Bartoli, Prooxidant activity of beta-carotene under 100% oxygen pressure in rat liver microsomes. *Free Radic Biol Med* **19**, 887-892 (1995).

231. H. Tsuchihashi, M. Kigoshi, M. Iwatsuki, E. Niki, Action of beta-carotene as an antioxidant against lipid peroxidation. *Arch Biochem Biophys* **323**, 137-147 (1995).

232. R. C. Mordi *et al.*, Exploratory study of β-carotene autoxidation. *Tetrahedron Letters* **32**, 4203-4206 (1991).

233. R. C. Mordi *et al.*, Oxidative degradation of β-carotene and β-apo-8′-carotenal. *Tetrahedron* **49**, 911-928 (1993).

234. B. Hassannia *et al.*, Nano-targeted induction of dual ferroptotic mechanisms eradicates high-risk neuroblastoma. *J Clin Invest* **128**, 3341-3355 (2018).

235. K. Windsor *et al.*, Probing lipid-protein adduction with alkynyl surrogates: application to Smith-Lemli-Opitz syndrome. *Journal of lipid research* **54**, 2842-2850 (2013).

236. Z. Korade, L. Xu, R. Shelton, N. A. Porter, Biological activities of 7-dehydrocholesterol-derived oxysterols: implications for Smith-Lemli-Opitz syndrome. *J Lipid Res* **51**, 3259-3269 (2010).

237. O. Zitka *et al.*, Redox status expressed as GSH:GSSG ratio as a marker for oxidative stress in paediatric tumour patients. *Oncol Lett* **4**, 1247-1253 (2012).

238. I. Rebrin, R. S. Sohal, Pro-oxidant shift in glutathione redox state during aging. *Adv Drug Deliv Rev* **60**, 1545-1552 (2008).

239. P. Ghezzi, Regulation of protein function by glutathionylation. *Free Radic Res* **39**, 573-580 (2005).

240. E. Mishima *et al.*, A non-canonical vitamin K cycle is a potent ferroptosis suppressor. *Nature* **608**, 778-783 (2022).

241. K. K. Dhar Dubey, G. Sharma, A. Kumar, Conjugated Linolenic Acids: Implication in Cancer. *J Agric Food Chem* **67**, 6091-6101 (2019).

242. T. Tsuzuki, Y. Tokuyama, M. Igarashi, T. Miyazawa, Tumor growth suppression by alpha-eleostearic acid, a linolenic acid isomer with a conjugated triene system, via lipid peroxidation. *Carcinogenesis* **25**, 1417-1425 (2004).

243. A. S. Cornelius, N. R. Yerram, D. A. Kratz, A. A. Spector, Cytotoxic Effect of *cis*-Parinaric Acid in Cultured Malignant Cells. *Cancer Research* **51**, 6025 (1991).

244. A. M. Martinez, A. Kim, W. S. Yang, Detection of Ferroptosis by BODIPY™ 581/591 C11. *Methods Mol Biol* **2108**, 125-130 (2020).

245. B. R. Stockwell, X. Jiang, W. Gu, Emerging Mechanisms and Disease Relevance of Ferroptosis. *Trends Cell Biol* **30**, 478-490 (2020).

246. N. Yamada *et al.*, Ferroptosis driven by radical oxidation of n-6 polyunsaturated fatty acids mediates acetaminophen-induced acute liver failure. *Cell Death Dis* **11**, 144 (2020).

247. A. Li, K. M. Hines, L. Xu, in *Ion Mobility-Mass Spectrometry : Methods and Protocols,* G. Paglia, G. Astarita, Eds. (Springer US, New York, NY, 2020), pp. 119-132.

248. K. M. Hines, J. Herron, L. Xu, Assessment of altered lipid homeostasis by HILIC-ion mobility-mass spectrometry-based lipidomics. *J Lipid Res* **58**, 809-819 (2017).

249. D. H. Ross, J. H. Cho, R. Zhang, K. M. Hines, L. Xu, LiPydomics: A Python Package for Comprehensive Prediction of Lipid Collision Cross Sections and Retention Times and Analysis of Ion Mobility-Mass Spectrometry-Based Lipidomics Data. *Anal Chem* **92**, 14967-14975 (2020).

250. P. J. Sindelar, Z. Guan, G. Dallner, L. Ernster, The protective role of plasmalogens in iron-induced lipid peroxidation. *Free Radic Biol Med* **26**, 318-324 (1999).

251. J. M. Dean, I. J. Lodhi, Structural and functional roles of ether lipids. *Protein & Cell* **9**, 196-206 (2018).

252. P. Luna, M. A. de la Fuente, D. Salvador, G. Márquez-Ruiz, Differences in Oxidation Kinetics between Conjugated and Non-conjugated Methyl Linoleate. *Lipids* **42**, 1085-1092 (2007).

253. R. Suzuki, M. Abe, K. Miyashita, Comparative Study of the Autoxidation of TAG Containing Conjugated and Nonconjugated C 18 PUFA. *J Amer Oil Chem Soc* **81**, 563-569 (2004).

254. R. T. Holman, Autoxidation of Fat and Related Substances. *Progress in the Chemistry of Fats and Other Lipid* **2**, 51-98 (1954).

255. U. I. Brimberg, A. Kama-Eldin, On the kinetics of the autoxidation of fats: substrates with conjugated double bonds. *Eur. J. Lipid Sci. Technol.* **105**, 17-22 (2003).

256. M. C. García-Martínez, G. Márquez-Ruiz , J. Fontecha, M. H. Gordon, Volatile Oxidation Compounds in a Conjugated Linoleic Acid-rich Oil. *Food Chemistry* **119**, 926-931 (2009).

257. S. Kolliker, M. Oehme, C. Dye, Structure Elucidation of 2,4-Dinitrophenylhydrazone Derivatives of Carbonyl Compounds in Ambient Air by HPLC/MS and Multiple MS/MS Using Atmospheric Chemical Ionization in the Negative Ion Mode. *Anal Chem* **70**, 1979-1985 (1998).

258. E. V. Berdyshev, Mass spectrometry of fatty aldehydes. *Biochim Biophys Acta* **1811**, 680-693 (2011).

259. G. Spiteller, W. Kern, P. Spiteller, Investigation of aldehydic lipid peroxidation products by gas chromatography–mass spectrometry. *Journal of Chromatography A* **843**, 29-98 (1999).

260. M. Shoeb, N. H. Ansari, S. K. Srivastava, K. V. Ramana, 4-Hydroxynonenal in the pathogenesis and progression of human diseases. *Curr Med Chem* **21**, 230-237 (2014).

261. M. Csala *et al.*, On the role of 4-hydroxynonenal in health and disease. *Biochimica et Biophysica Acta (BBA) - Molecular Basis of Disease* **1852**, 826-838 (2015).

262. L. S. Dantas *et al.*, Lipid aldehyde hydrophobicity affects apo-SOD1 modification and aggregation. *Free Radical Biology and Medicine* **156**, 157-167 (2020).

263. S. X. Ge, E. W. Son, R. Yao, iDEP: an integrated web application for differential expression and pathway analysis of RNA-Seq data. *BMC Bioinformatics* **19**, 534 (2018).

264. S. Ahsan, S. Drăghici, Identifying Significantly Impacted Pathways and Putative Mechanisms with iPathwayGuide. *Current Protocols in Bioinformatics* **57**, 7.15.11-17.15.30 (2017).

265. W. Luo, M. S. Friedman, K. Shedden, K. D. Hankenson, P. J. Woolf, GAGE: generally applicable gene set enrichment for pathway analysis. *BMC Bioinformatics* **10**, 161 (2009).

266. J. Wang, J. Lee, D. Liem, P. Ping, HSPA5 Gene encoding Hsp70 chaperone BiP in the endoplasmic reticulum. *Gene* **618**, 14-23 (2017).

267. M. L. Whitney, L. S. Jefferson, S. R. Kimball, ATF4 is necessary and sufficient for ER stress-induced upregulation of REDD1 expression. *Biochem Biophys Res Commun* **379**, 451-455 (2009).

268. W. Rozpedek *et al.*, The Role of the PERK/eIF2α/ATF4/CHOP Signaling Pathway in Tumor Progression During Endoplasmic Reticulum Stress. *Curr Mol Med* **16**, 533-544 (2016).

269. I. N. Mungrue, J. Pagnon, O. Kohannim, P. S. Gargalovic, A. J. Lusis, CHAC1/MGC4504 is a novel proapoptotic component of the unfolded protein response, downstream of the ATF4-ATF3-CHOP cascade. *J Immunol* **182**, 466-476 (2009).

270. B. T. Sherman *et al.*, DAVID: a web server for functional enrichment analysis and functional annotation of gene lists (2021 update). *Nucleic Acids Res* **50**, W216-221 (2022).

271. A. Vila *et al.*, Identification of protein targets of 4-hydroxynonenal using click chemistry for ex vivo biotinylation of azido and alkynyl derivatives. *Chem Res Toxicol* **21**, 432-444 (2008).

272. H. Y. Kim, K. A. Tallman, D. C. Liebler, N. A. Porter, An azido-biotin reagent for use in the isolation of protein adducts of lipid-derived electrophiles by streptavidin catch and photorelease. *Mol Cell Proteomics* **8**, 2080-2089 (2009).

273. K. A. Tallman *et al.*, Phospholipid−Protein Adducts of Lipid Peroxidation: Synthesis and Study of New Biotinylated Phosphatidylcholines. *Chemical Research in Toxicology* **20**, 227-234 (2007).

274. K. A. Tallman *et al.*, Probes for protein adduction in cholesterol biosynthesis disorders: Alkynyl lanosterol as a viable sterol precursor. *Redox Biol* **12**, 182-190 (2017).

275. K. D. Tousignant *et al.*, Therapy-induced lipid uptake and remodeling underpin ferroptosis hypersensitivity in prostate cancer. *Cancer & Metabolism* **8**, 11 (2020).

276. Y. Bai *et al.*, Lipid storage and lipophagy regulates ferroptosis. *Biochem Biophys Res Commun* **508**, 997-1003 (2019).

277. J. J. García *et al.*, Protective effects of melatonin in reducing oxidative stress and in preserving the fluidity of biological membranes: a review. *J Pineal Res* **56**, 225-237 (2014).

278. M. Zommara *et al.*, Inhibitory effect of ethanolamine plasmalogen on iron- and copper-dependent lipid peroxidation. *Free Radical Biology and Medicine* **18**, 599-602 (1995).

279. M. A. Perez, L. Magtanong, S. J. Dixon, J. L. Watts, Dietary Lipids Induce Ferroptosis in Caenorhabditiselegans and Human Cancer Cells. *Developmental Cell* **54**, 447-454.e444 (2020).

280. R. R. Allen, A. Jackson, F. A. Kummerow, Factors which affect the stability of highly unsaturated fatty acids. I. Differences in the oxidation of conjugated and nonconjugated linoleic acid. *Journal of the American Oil Chemists' Society* **26**, 395-399 (1949).

281. R. J. Schaur, Basic aspects of the biochemical reactivity of 4-hydroxynonenal. *Molecular Aspects of Medicine* **24**, 149-159 (2003).

282. M. Alaiz, M. Beppu, K. Ohishi, K. Kikugawa, Modification of Delipidated Apoprotein B of Low Density Lipoprotein by Lipid Oxidation Products in Relation to Macrophage Scavenger Receptor Binding. *Biological & Pharmaceutical Bulletin* **17**, 51-57 (1994).

283. M. Alaiz, S. Barragán, Reaction of a lysyl residue analogue with E-2-octenal. *Chemistry and Physics of Lipids* **75**, 43-49 (1995).

284. Y. Chen *et al.*, Quantitative Profiling of Protein Carbonylations in Ferroptosis by an Aniline-Derived Probe. *Journal of the American Chemical Society* **140**, 4712-4720 (2018).

285. P. Boonnoy, V. Jarerattanachat, M. Karttunen, J. Wong-ekkabut, Bilayer Deformation, Pores, and Micellation Induced by Oxidized Lipids. *The Journal of Physical Chemistry Letters* **6**, 4884-4888 (2015).

286. A. T. M. Van Kessel, R. Karimi, G. Cosa, Live-cell imaging reveals impaired detoxification of lipid-derived electrophiles is a hallmark of ferroptosis. *Chemical Science* **13**, 9727-9738 (2022).

287. A. H. Schönthal, Endoplasmic reticulum stress: its role in disease and novel prospects for therapy. *Scientifica (Cairo)* **2012**, 857516 (2012).

288. I. Kim, W. Xu, J. C. Reed, Cell death and endoplasmic reticulum stress: disease relevance and therapeutic opportunities. *Nature Reviews Drug Discovery* **7**, 1013-1030 (2008).

289. W. Wang *et al.*, Ribosomal proteins and human diseases: pathogenesis, molecular mechanisms, and therapeutic implications. *Med Res Rev* **35**, 225-285 (2015).

290. A. C. Vind, A. V. Genzor, S. Bekker-Jensen, Ribosomal stress-surveillance: three pathways is a magic number. *Nucleic Acids Res* **48**, 10648-10661 (2020).

291. S. J. Marciniak *et al.*, CHOP induces death by promoting protein synthesis and oxidation in the stressed endoplasmic reticulum. *Genes Dev* **18**, 3066-3077 (2004).

292. I. Novoa, H. Zeng, H. P. Harding, D. Ron, Feedback inhibition of the unfolded protein response by GADD34-mediated dephosphorylation of eIF2alpha. *J Cell Biol* **153**, 1011-1022 (2001).

293. A.-L. Levonen *et al.*, Cellular mechanisms of redox cell signalling: role of cysteine modification in controlling antioxidant defences in response to electrophilic lipid oxidation products. *Biochemical Journal* **378**, 373-382 (2004).

294. A. T. Dinkova-Kostova *et al.*, Direct evidence that sulfhydryl groups of Keap1 are the sensors regulating induction of phase 2 enzymes that protect against carcinogens and oxidants. *Proc Natl Acad Sci U S A* **99**, 11908-11913 (2002).

295. D. Kim, B. Langmead, S. L. Salzberg, HISAT: a fast spliced aligner with low memory requirements. *Nature Methods* **12**, 357-360 (2015).

296. H. Li *et al.*, The Sequence Alignment/Map format and SAMtools. *Bioinformatics* **25**, 2078-2079 (2009).

297. Y. Liao, G. K. Smyth, W. Shi, featureCounts: an efficient general purpose program for assigning sequence reads to genomic features. *Bioinformatics* **30**, 923-930 (2013).

298. M. I. Love, W. Huber, S. Anders, Moderated estimation of fold change and dispersion for RNA-seq data with DESeq2. *Genome Biology* **15**, 550 (2014).

299. S. Dixon, B. Stockwell, The hallmarks of ferroptosis. *Annual Review of Cancer Biology* **3**, 35-54 (2019).

300. D. R. Green, The Coming Decade of Cell Death Research: Five Riddles. *Cell* **177**, 1094-1107 (2019).

301. J. D. Malhotra, R. J. Kaufman, Endoplasmic reticulum stress and oxidative stress: a vicious cycle or a double-edged sword? *Antioxid Redox Signal* **9**, 2277-2293 (2007).

302. S. S. Cao, R. J. Kaufman, Endoplasmic reticulum stress and oxidative stress in cell fate decision and human disease. *Antioxid Redox Signal* **21**, 396-413 (2014).

303. M. H. Brush, D. C. Weiser, S. Shenolikar, Growth arrest and DNA damage-inducible protein GADD34 targets protein phosphatase 1 alpha to the endoplasmic reticulum and promotes dephosphorylation of the alpha subunit of eukaryotic translation initiation factor 2. *Mol Cell Biol* **23**, 1292-1303 (2003).

304. N. Ohoka, S. Yoshii, T. Hattori, K. Onozaki, H. Hayashi, TRB3, a novel ER stress-inducible gene, is induced via ATF4-CHOP pathway and is involved in cell death. *Embo j* **24**, 1243-1255 (2005).

305. D. Tang, X. Chen, R. Kang, G. Kroemer, Ferroptosis: molecular mechanisms and health implications. *Cell Research* **31**, 107-125 (2021).

306. C. Zhao *et al.*, Endoplasmic reticulum stress-mediated autophagy activation is involved in cadmium-induced ferroptosis of renal tubular epithelial cells. *Free Radical Biology and Medicine* **175**, 236-248 (2021).

307. Y. Xu *et al.*, Sevoflurane Induces Ferroptosis of Glioma Cells Through Activating the ATF4-CHAC1 Pathway. *Front Oncol* **12**, 859621 (2022).

308. C.-C. Lin *et al.*, The regulation of ferroptosis by MESH1 through the activation of the integrative stress response. *Cell Death & Disease* **12**, 727 (2021).

309. R. Edgar, M. Domrachev, A. E. Lash, Gene Expression Omnibus: NCBI gene expression and hybridization array data repository. *Nucleic Acids Res* **30**, 207-210 (2002).

310. T. Barrett *et al.*, NCBI GEO: archive for functional genomics data sets--update. *Nucleic Acids Res* **41**, D991-995 (2013).

311. R. Leinonen, H. Sugawara, M. Shumway, The sequence read archive. *Nucleic Acids Res* **39**, D19-21 (2011).

312. I. Tabas, D. Ron, Integrating the mechanisms of apoptosis induced by endoplasmic reticulum stress. *Nat Cell Biol* **13**, 184-190 (2011).

313. M. Kolesnichenko *et al.*, Transcriptional repression of NFKBIA triggers constitutive IKK- and proteasome-independent p65/RelA activation in senescence. *Embo j* **40**, e104296 (2021).

314. S. Shetty *et al.*, Transcription factor NF-kappaB differentially regulates death receptor 5 expression involving histone deacetylase 1. *Mol Cell Biol* **25**, 5404-5416 (2005).

315. P. Simon, R. Sargent, A. Rabson, Inhibitor of apoptosis protein BIRC3 (API2, cIAP2, AIP1) is upregulated by the non-canonical NFKB pathway. *Cancer Research* **67**, 5327-5327 (2007).

316. F. Guo *et al.*, TRAF1 is involved in the classical NF-kappaB activation and CD30-induced alternative activity in Hodgkin's lymphoma cells. *Mol Immunol* **46**, 2441-2448 (2009).

317. J. Yu, L. Zhang, PUMA, a potent killer with or without p53. *Oncogene* **27 Suppl 1**, S71-83 (2008).

318. D. Huang *et al.*, CRL4(DCAF8) dependent opposing stability control over the chromatin remodeler LSH orchestrates epigenetic dynamics in ferroptosis. *Cell Death Differ* **28**, 1593-1609 (2021).

319. K. Pakos-Zebrucka *et al.*, The integrated stress response. *EMBO reports* **17**, 1374-1395 (2016).

320. E. Logie *et al.*, Ferroptosis Induction in Multiple Myeloma Cells Triggers DNA Methylation and Histone Modification Changes Associated with Cellular Senescence. *Int J Mol Sci* **22**, (2021).

321. A. Schmitt *et al.*, Dimethyl fumarate induces ferroptosis and impairs NF-κB/STAT3 signaling in DLBCL. *Blood* **138**, 871-884 (2021).

322. J. Averous *et al.*, Induction of CHOP Expression by Amino Acid Limitation Requires Both ATF4 Expression and ATF2 Phosphorylation*. *Journal of Biological Chemistry* **279**, 5288-5297 (2004).

323. C. Jousse *et al.*, Amino acid limitation regulates CHOP expression through a specific pathway independent of the unfolded protein response. *FEBS Lett* **448**, 211-216 (1999).

324. A. Bruhat *et al.*, Amino Acid Limitation Induces Expression of CHOP, a CCAAT/Enhancer Binding Protein-related Gene, at Both Transcriptional and Post-transcriptional Levels*. *Journal of Biological Chemistry* **272**, 17588-17593 (1997).

325. J. L. Luo, H. Kamata, M. Karin, IKK/NF-kappaB signaling: balancing life and death--a new approach to cancer therapy. *J Clin Invest* **115**, 2625-2632 (2005).

326. Z. B. Xia *et al.*, Inhibition of NF-κB signaling pathway induces apoptosis and suppresses proliferation and angiogenesis of human fibroblast-like synovial cells in rheumatoid arthritis. *Medicine (Baltimore)* **97**, e10920 (2018).

327. A. B. Tam, E. L. Mercado, A. Hoffmann, M. Niwa, ER stress activates NF-κB by integrating functions of basal IKK activity, IRE1 and PERK. *PLoS One* **7**, e45078 (2012).

328. P. Hu, Z. Han, A. D. Couvillon, R. J. Kaufman, J. H. Exton, Autocrine tumor necrosis factor alpha links endoplasmic reticulum stress to the membrane death receptor pathway through IRE1alpha-mediated NF-kappaB activation and down-regulation of TRAF2 expression. *Mol Cell Biol* **26**, 3071-3084 (2006).

329. J. H. Lin *et al.*, IRE1 signaling affects cell fate during the unfolded protein response. *Science* **318**, 944-949 (2007).

330. H. Yoshida, T. Matsui, A. Yamamoto, T. Okada, K. Mori, XBP1 mRNA is induced by ATF6 and spliced by IRE1 in response to ER stress to produce a highly active transcription factor. *Cell* **107**, 881-891 (2001).

331. D. A. Rodriguez *et al.*, BH3-only proteins are part of a regulatory network that control the sustained signalling of the unfolded protein response sensor IRE1α. *Embo j* **31**, 2322-2335 (2012).

332. C. Reimertz, D. Kögel, A. Rami, T. Chittenden, J. H. Prehn, Gene expression during ER stress-induced apoptosis in neurons: induction of the BH3-only protein Bbc3/PUMA and activation of the mitochondrial apoptosis pathway. *J Cell Biol* **162**, 587-597 (2003).

333. J. Li, B. Lee, A. S. Lee, Endoplasmic reticulum stress-induced apoptosis: multiple pathways and activation of p53-up-regulated modulator of apoptosis (PUMA) and NOXA by p53. *J Biol Chem* **281**, 7260-7270 (2006).

334. A. P. Ghosh, B. J. Klocke, M. E. Ballestas, K. A. Roth, CHOP potentially co-operates with FOXO3a in neuronal cells to regulate PUMA and BIM expression in response to ER stress. *PLoS One* **7**, e39586 (2012).

335. Y. Peng *et al.*, Corosolic acid sensitizes ferroptosis by upregulating HERPUD1 in liver cancer cells. *Cell Death Discovery* **8**, 376 (2022).

336. L. Wang *et al.*, ATF3 promotes erastin-induced ferroptosis by suppressing system Xc–. *Cell Death & Differentiation* **27**, 662-675 (2020).

337. Y. Chen *et al.*, Dihydroartemisinin-induced unfolded protein response feedback attenuates ferroptosis via PERK/ATF4/HSPA5 pathway in glioma cells. *Journal of Experimental & Clinical Cancer Research* **38**, 402 (2019).

338. S. H. Hong *et al.*, Molecular crosstalk between ferroptosis and apoptosis: emerging role of ER stress-induced p53-independent PUMA expression. *Oncotarget* **8**, 115164-115178 (2017).

339. Y. S. Lee *et al.*, Ferroptosis-inducing agents enhance TRAIL-induced apoptosis through upregulation of death receptor 5. *J Cell Biochem* **120**, 928-939 (2019).

340. Y.-S. Lee *et al.*, Ferroptotic agent-induced endoplasmic reticulum stress response plays a pivotal role in the autophagic process outcome. *Journal of Cellular Physiology* **235**, 6767-6778 (2020).